1-1-1987

Molecular gas in Virgo Cluster spiral galaxies.

Jeffrey D. Kenney
University of Massachusetts Amherst

MOLECULAR GAS IN VIRGO CLUSTER SPIRAL GALAXIES

A Dissertation Presented

by

Jeffrey D. Kenney

Submitted to the Graduate School of the
University of Massachusetts in partial fulfillment
of the requirements for the degree of

DOCTOR OF PHILOSOPHY

May 1987

Department of Physics and Astronomy

Molecular Gas in Virgo Cluster Spiral Galaxies

A Dissertation Presented

by

Jeffrey D. Kenney

Approved as to style and content by:

Judith S. Young, Chairperson

William A. Dent, Member

F. Peter Schloerb, Member

Steven E. Strom, Member

Robert V. Krotkov, Outside Member

Martha P. Haynes, Outside Member

Robert B. Hallock, Department Head
Department of Physics and Astronomy

ACKNOWLEDGEMENTS

First and foremost, I'd like to thank Judy Young, who suggested this project (really), and then made me do it (not really). Judy served as advisor extraordinaire and friend. Her willingness to discuss matters, her prompt feedback, and her continual encouragement made writing this thesis almost a pleasure.

Steve Strom, Bill Dent, Martha Haynes, Pete Schloerb, and Bob Krotkov all served on my committee, all read the entire 930 page thesis (or so it must have seemed), and all provided valuable input. Steve has taught me a lot about galaxies and science. His uncontained enthusiasm when presented with some surprising fact exemplifies what science should be. It was Bill who gave me a start in radio astronomy and tutored me in the ancient art of data calibration. Bill has given me advice on a variety of subjects during the six years I have known him, for which I am grateful. Martha deserves thanks for her correspondence and visits to Amherst. Her careful work on the HI properties of galaxies has been a source of inspiration. I appreciate Pete's insightful feedback which helped to strengthen several flimsy areas of the tome which follows.

Many others in the UMass Astronomy department have helped me write this thesis, although they may not have known it. Discussions of a stimulating nature were had with Steve Lord, John Kwan, and Ron Snell. Linda Tacconi, Lowell Garman, Mark Claussen, Steve Lord, as well as both of the Tacconi-Garmans were kind enough to observe Virgo galaxies

for me when I was out of town on important business, sick with exotic tropical diseases, or just wanted to play softball. Dave Taylor and Shuding Xie are to be thanked for their work on the calibration of Quabbin and IRAS data. Particular thanks go to Sally Rule, Jackie Golonka, and Denise Kuzmeskus for their continual help in accomplishing an infinite number of necessary tasks. Their pleasant demeanor made daily visits to the GRC bearable. I am indebted to the FCRAO Scheduling Committees, whose generous allotments of telescope time enabled this project to be completed.

Several individuals outside of Amherst are to be acknowledged. Rein Warmels, Jacqueline van Gorkom and Chris Kotanyi supplied HI data prior to publication. John Stauffer provided helpful criticism of a paper describing some preliminary results of this thesis. Rob Kennicutt did the same, and took the time to explain some essential facts about Hα emission from galaxies. Conversations with Greg Bothun clarified a couple of pertinent issues. The Boston Red Sox of 1986 kept my adrenaline flowing at unprecedented levels during a critical period of this work.

It is hard to believe that people can actually be paid to do astronomy. FCRAO supported me with a stipend and travel money for most of "the thesis years". Judy (remember Judy?) stepped in with financial support during a time in which I would otherwise have been left homeless and starving. I owe even more to my parents, Phil and Ellie, who have been paying for me to become an astronomer for nearly 3 decades.

My time as a graduate student will be fondly remembered for as long

as my memory lasts. Amherst has been a great place to live, largely because of the people I've come to know and enjoy. Friendships within the department have made the last six years a rich experience. I can only hope to find myself in another place where the people are as amiable and lively as you folks.

And then there's Jo, who suggested this project (not really) and has been so encouraging and supportive that it's hard to believe (really). Not only has Jo generally made life a pleasure for me, but she has spent several hundred hours typing (even this acknowledgement), making figures, and preparing the text (which she couldn't understand). Her love has provided the emotional sustenance necessary to complete this undertaking.

ABSTRACT

Molecular Gas in Virgo Cluster Spiral Galaxies

(May 1987)

Jeffrey D. Kenney

B.S. Bates College

Ph.D. University of Massachusetts

Directed by: Judith S. Young

We have obtained CO(J=1→0) observations with 45" resolution at over 200 positions along the major axes of 42 Virgo cluster spiral galaxies, using the FCRAO 14-meter telescope. Although there is a general correlation between the CO flux of a galaxy and its optical diameter, the S_{CO}/D_{opt}^2 ratio is found to depend on both the morphological type and the HI content. Analyses indicate that for the Sa-Sb and highest luminosity Sc Virgo galaxies, the molecular gas contents and distributions have not been strongly affected by the cluster environment.

There is a population of HI-rich, lower-luminosity ($10.9<B_T^o<12.0$) Sc galaxies in the outer cluster with a mean S_{CO}/D_{opt}^2 ratio a factor of 5 less than the other Sc's. While it also may be that the conversion of HI into H_2 is enhanced in low mass galaxies by an interaction with the intracluster medium, these results strongly suggest that the attainment of an H_2-dominated ISM is a function of galaxy mass. These

outer cluster low mass Virgo Sc galaxies have large massive star formation rates and high central HI surface densities, indicating that atomic gas plays a direct role in star formation in these systems.

Galaxies which are HI-deficient by a factor of 10 are gas-deficient ($HI+H_2$) by only a factor of 2-3, due to the survival of large quantities of molecular gas. The massive-star formation rates, as indicated by Hα, radio continuum and far-infrared emission, are also lower by factors of ~2-3 in galaxies which are HI-deficient by a factor of 10. Comparison of the radial distributions of HI and H_2 indicate that the total gas deficiency is manifested largely by a lack of HI in the outer galaxy. The inner disk regions, although HI-deficient, are not significantly gas-deficient since the ISM in the inner regions of most of the galaxies in this sample are H_2-dominated. The large H_2/HI ratios in the inner regions of Virgo spirals indicate that either the lifetime of the molecular phase or the lifetime of GMC complexes is $\sim 2 \times 10^9$ years in H_2-dominated environments.

CO emission has been detected in the center of 2 small-bulge S0-S0/a Virgo galaxies which remain undetected in HI. These galaxies exhibit the expected aftereffects of a severe stripping event which occurred $\sim 2 \times 10^9$ years ago, and may be the first known examples of stripped spirals in the process of turning into S0-like systems.

TABLE OF CONTENTS

V. MOLECULAR AND ATOMIC GAS PROPERTIES OF VIRGO SPIRALS

VI. STAR FORMATION IN VIRGO GALAXIES AND THE EVOLUTION OF STRIPPED SPIRALS

VII. THE ROLES OF MOLECULAR AND ATOMIC GAS IN STAR FORMATION

LIST OF TABLES

LIST OF FIGURES

CHAPTER I

INTRODUCTION

§1. Introduction to the Introduction

Molecular gas in galaxies is important because it is the medium from which stars form. Furthermore, molecular gas comprises a large fraction of the total interstellar gas mass in many galaxies, and dominates the mass of the interstellar medium (ISM) in the central regions of most luminous spiral galaxies. In order to understand the evolution of galaxies, which proceeds as gas turns into stars, it is therefore imperative to have a quantitative knowledge of both the distributions and relative amounts of atomic and molecular gas within galaxies.

For practical and historical reasons, numerous studies during the last two decades have attempted to understand star formation and galactic evolution with a quantitative knowledge of only the atomic gas component. The presence of atomic gas is revealed by radiation from the 21 cm (1.42 GHz) hyperfine transition of neutral hydrogen (HI). Since the discovery in the early 1950's of widespread 21 cm emission throughout the Milky Way, centimeter wave radio astronomy technology has progressed to the stage where it is possible to efficiently survey HI emission in galaxies as distant as $z=0.03$ ($v=10{,}000$ km s^{-1}). On the other hand, the presence of molecular gas is currently best revealed by radiation from the 2.60 mm (115 GHz) rotational transition of carbon monoxide (CO). Cold interstellar molecular clouds were not discovered

in our own galaxy until the early 1970's with the advent of millimeter wave radio astronomy technology. Although CO emission has been detected in many galaxies since that time, the work reported in this thesis represents the first large-scale, systematic survey of CO emission in the disks of spiral galaxies in a large cluster of galaxies. The 600 painstaking hours of telescope time needed to complete this survey illustrates why there is so little molecular gas data on galaxies today, compared with the large data base of atomic gas in galaxies.

Three general themes are addressed with the CO data on 42 Virgo Cluster spiral galaxies: the evolution of galaxies within clusters; the molecular gas properties of galaxies as a function of mass, morphological type, and environment; and the roles of atomic and molecular gas in the star formation process. These topics are interrelated, and are consequently discussed together throughout the thesis.

§2. Evolution of Galaxies Within Clusters

The evolution of galaxies is not independent of their environment. The Virgo cluster was chosen for study because it is the nearest large cluster of galaxies, and it exhibits evidence for environmental modification of the galaxies within it. The three-dimensional structure and dynamical state of the Virgo cluster have been clarified by recent redshift and HI linewidth studies. The cluster is evidently still in the process of formation. While the distribution of radial velocities for the Virgo elliptical population can be characterized by a Gaussian,

that of the spiral population is flatter and broader, with several peaks (Huchra 1985). This has been interpreted to mean that the ellipticals have existed in the cluster long enough to dynamically relax, and that many of the spirals are recent arrivals which have not crossed the cluster core more than once. Support for this scenario comes from dynamical studies of the Local Supercluster near the Virgo cluster region. Tully and Shaya (1984) find that the infalling motion of supercluster spirals toward Virgo should double the number of galaxies in the cluster over the next 10^{10} years.

Most of the new arrivals are gas-rich spiral galaxies which are encountering a new environment for the first time in their existence. In rich clusters, the large density of galaxies, their high relative velocities, and the existence of intracluster gas yield the potential for galaxian modification. Several nearby clusters of galaxies are found to contain large numbers of spiral galaxies which are deficient in atomic gas, relative to more isolated galaxies (Giovanelli and Haynes 1985). The fraction of HI-deficient galaxies in a particular cluster is well correlated with the strength of the x-ray emission from the cluster's intracluster gas, which strongly suggests that the interaction between the intracluster medium (ICM) and the galaxy's ISM strips away the atomic gas. The magnitude of the HI-deficiency can be severe: many galaxies have an order of magnitude less atomic gas than their more isolated counterparts.

Since interstellar gas is the raw material for star formation, the star-forming ability and future evolution of HI-deficient galaxies are

unquestionably altered by their interaction with the ICM. What is unknown is the severity of the alteration. The answers to 2 important questions depend upon the severity of the modification. 1) Do cluster spirals evolve much more rapidly than isolated spirals? 2) Can the fact that most SO galaxies are located in clusters be partially or fully explained by the stripping of spiral galaxies?

One measure of the impact of HI-deficiency is the massive star formation rate, as measured by the Hα equivalent width. To date, surveys of the Hα emission have been performed for four clusters containing large fractions of HI-deficient galaxies. In the Coma, Cancer, and Abell 1367 clusters, no correlation between the Hα emission and HI deficiency is evident (Kennicutt, Bothun, and Schommer 1984). In the Virgo cluster, HI-deficient galaxies do have less Hα emission, on average, than the HI-normal galaxies (Kennicutt 1983), yet it is shown in this thesis that the magnitude of the 'Hα-deficiency' is much smaller than the magnitude of the HI-deficiency. A likely explanation for the small impact of the HI-deficiency on star formation in the Virgo cluster (and other clusters) is the existence of molecular gas. Evidence is presented here that the molecular gas in Virgo cluster spirals survives the interaction which causes the HI-deficiency. Global star formation rates in Virgo spirals remain relatively high because molecular clouds, the phase of the ISM in which stars form, remain abundant.

Although the survival of large amounts of molecular gas mitigates the impact of HI-deficiency on star formation and subsequent galactic

evolution, it does not spare the galaxies from altered evolutionary paths. The evolutionary fate of cluster spirals can now be considered for the first time with full awareness of both atomic and molecular gas components.

§3. CO as a Function of Type and Mass and the Role of Molecular Gas in Star Formation

Knowledge of the CO properties of galaxies as a function of mass (or luminosity) and morphological type can help answer questions about galactic structure and star formation, as well as elucidate the role of molecular gas in star formation and galactic evolution. The large number of Virgo galaxies mapped here, and the fact that it is a complete, magnitude-limited sample, make this a valuable data base for mass and type comparisons, although care must be taken with possible environmental effects.

Various tracers of star formation (e.g. B-V colors, Hα emission line) indicate that the Hubble morphological type sequence of elliptical through Sc spiral galaxies is one of increasing current-day star formation rate (e.g. Kennicutt and Kent 1983). The disks of Sa galaxies generally have lower ratios of new to old stars than the disks of Sc galaxies. This suggests that Sa galaxies have converted a larger fraction of their original gas supply into stars than have Sc galaxies. If so, then Sa galaxies would be expected to have less gas per disk star than Sc galaxies. To date, only one study has addressed the morphological type dependence of CO emission in galaxies. Young,

Scoville, and Brady (1985) observed CO emission in the central 45" of 25 Virgo Sa-Sc galaxies, and found that the ratios of CO luminosity to blue luminosity in the central regions were lower in the early-type galaxies. However, since the light from the central regions of early type galaxies is dominated by the bulge, and only the central regions were observed in CO, the study of Young, Scoville, and Brady could not address the morphological dependence of the gas mass to disk stars ratio. This issue is addressed in the present study, with particular attention paid to possible environmental effects.

An early comparison of CO emission with blue light in a small sample of Sc galaxies showed that the two quantities were well correlated (Young and Scoville 1982b), which could be taken as evidence that the quantity of molecular gas in a galaxy was directly proportional either to its mass, or the star-formation rate during the last 2×10^9 years. However, several studies (Elmegreen, Elmegreen and Morris 1980; Young, Gallagher and Hunter 1984; Tacconi and Young 1985; Israel et al. 1986) have shown that dwarf irregular galaxies have CO to blue light ratios at least an order of magnitude lower than the more massive spiral galaxies. Thus, a constant CO to blue light ratio does not extend down to the smallest galaxies.

There are three schools of thought on the reason for the difference between the massive spirals and the less massive dwarf irrregulars. One school proposes that the relation between CO intensity and H_2 surface density is not a universal constant, and that the H_2 mass to blue light ratio is actually similar in dwarf irregulars and spirals

(Israel et al.). A second school suggests that episodic bursts of star formation create dwarf irregular galaxies with both high and low H_2 mass to blue light ratios: actively star-forming dwarf irregulars have low CO to blue light ratios because they have used up their supply of star forming molecular gas in a galaxy-wide burst of star formation (Tacconi and Young 1987). Bursts of star formation in spirals do not envelope the entire galaxy, because of their larger size. Under this hypothesis, populations of CO-rich, yet optically faint dwarf irregular galaxies should exist. The third camp believes that dwarf irregular galaxies simply never form a large steady-state supply of molecular gas (Hunter, Gallagher and Rauzenkrantz 1982). If so, then the relatively high star forming rates in some of these galaxies indicate that the role of molecular gas in star formation is not fully understood.

In order to determine the real reason that spirals and dwarf irregulars have different CO properties, it would be valuable to observe galaxies with small bulge-to-disk ratios (B/D) over a large mass range to determine at what galaxy mass the CO properties begin to change. After all, the fundamental difference between spirals and dwarf irregulars is mass: there are no dwarf spiral galaxies (Sandage, Binggeli and Tammann 1985). Among the sample of Virgo spiral galaxies studied here, we have discovered that some of the lower mass spiral galaxies have little CO emission per unit mass, relative to the more massive spirals. This similarity between the CO properties of the dwarf irregulars and the lower mass spirals indicates that the weak CO emission is related to galaxy mass. The HI-richness of these CO-poor,

low mass Virgo spirals suggests that the reason for their feeble CO emission is an actual dearth of molecular gas.

Previous studies have shown that the radial distributions of young stars in several luminous spiral galaxies follow the CO emission more closely than the HI emission, indicating that molecular gas plays an important role in star formation (e.g. Talbot 1980; Scoville and Young 1983). Yet because of the dominance of molecular gas in the inner regions of these galaxies, it has not been possible to discern whether the star formation rate is more dependent upon the surface density of H_2, or the total gas surface density ($HI+H_2$). The discovery reported here of HI-rich, CO-poor spirals with high massive star formation rates indicates that atomic gas, as well as molecular gas, may play a direct role in star formation.

§4. Summary of Chapters

In the first part of Chapter II, the FCRAO telescope system and observational methods are described. In the later half of this chapter, the selection criteria and properties of the Virgo galaxy sample are detailed.

In Chapter III, the CO data for 42 Virgo galaxies is presented. From this data, both global CO fluxes and radial distributions are obtained. The derivations of the CO fluxes, CO diameters, and CO asymmetry parameters, which are used in the subsequent analysis, are summarized. Some of the calibration details are included in 2 appendices.

Chapter IV presents a discussion on the relationship between CO

emission and molecular mass. Recent observational and theoretical studies which are relevant to this important topic are reviewed.

A detailed analysis of the CO properties of the Virgo spirals appears in Chapter V. CO emission is first compared with starlight and galaxy mass. Much of this chapter then focusses on the comparison of CO and HI emission, including analysis of both global properties and radial distributions. For most of the Virgo galaxies, CO and HI emission are uncorrelated, indicating that there is no molecular gas deficiency in the HI-deficient galaxies. As a result, the total gas deficiency is only a small fraction of the HI-deficiency. There is, however, a population of HIrich, Sc galaxies in the outer cluster with low mass ratios of CO luminosity to optical diameter a factor of $\gtrsim 5$ less than the other Sc galaxies. These galaxies are among the least massive in the sample -- their existence indicates that the formation of an H_2-dominated ISM is a function of galaxy mass. However, it also may be that conversion of HI into H_2 is enhanced in low mass Sc galaxies by an interaction with the intra-cluster medium. The susceptibility of atomic and moleculr gas to removal, and the possibility of enhanced conversion of HI into H_2 by an ISM-ICM interaction is examined theoretically.

Star formation in Virgo spirals is discussed in Chapter VI. Hα line emission, B-V colors, radio contiuum emission, and far-infrared emission are all utilized as tracers of star forming activity. The far-infrared data is composed of previously unpublished CO-added data from the IRAS satellite. A description of this data is followed by a

discussion on the origin of far-infrared emission from "normal" galaxies. A comparison of these various tracers reveals that global star formation is reduced in the HI-deficient galaxies by an amount comparable to the total gas deficiency. The chapter concludes with a section on the evolutionary fate of stripped spirals. It is argued the CO and other data on 3 S0-Sa Virgo galaxies indicate that the transformation of spirals into S0s is accelerated by stripping.

Chapter VII includes 2 topics which pertain to the roles of atomic and molecular gas in star formation. A discourse on the lifetime of the molecular phase in galaxies is motivated by the observation that the inner regions of the HI-deficient spirals have systematically larger H_2/HI mass ratios. Finally, we address the implications of the CO-poor, HI-rich low mass spirals for the roles of atomic and molecular gas in the star formation process. It is put forth that the distinction between H_2 and HI as 'star-forming clouds' and 'clouds that form the star-forming clouds' is inappropriate for all galaxies.

Appendices A and B delve into details on the data calibration. Appendix A describes the analysis of 200 calibration measurements, which we used to determine an elevation correction and an absolute calibration scale for the CO data. Appendix B describes the method used for calculating global CO line fluxes from major axis maps, a procedure which accounts for the coupling between the beam and the source, and for the undersampling of emission.

CHAPTER II

CO OBSERVATIONS & THE VIRGO SAMPLE

§1. The Telescope System

CO observations of galaxies in the Virgo sample were performed with the 13.7-meter radome-enclosed telescope of the Five College Radio Astronomy Observatory. The antenna is of Cassegrain design, with a single feed horn, sensitive to linear polarization, mounted at the antenna focus. A quasi-optical system, which lies in front of the feed horn, contains a chopper wheel for system calibration and a Fabrey-Perot interferometer for image sideband termination at cryogenic temperatures. At 115 GHz, the half-power beam width of the telescope is measured to be 45".

FCRAO's heterodyne receiver utilizes a cooled Schottky diode mixer with 1.4 GHz intermediate frequency GaAs FET amplifiers of 400 MHz bandwidth. Single sideband receiver temperatures at 115 GHz were measured to be 275 K in 1983-84, 250 K in 1984-85, and 215 K in 1985-86. Apart from this improvement in receiver sensitivity, the telescope underwent no significant changes during the period of observations, from December 1983 to June 1986. The beam efficiency (corrected to outside the atmosphere) remained constant at η_B = 0.53±0.04 during the 3 observing seasons.

The backend of the receiver utilizes two 256-channel, 1 MHz resolution filterbanks, providing 512 MHz of available bandwidth. At the

115.271203 GHz rest frequency of the CO J=1→0 transition, each 1 MHz channel corresponds to 2.60 km s^{-1} in Doppler velocity units, providing a total bandwidth of 1330 km s^{-1}. In practice, this total bandwidth was not usable, particularly during 1984-85 when bad baselines occasionally dominated one of the filterbanks. The lack of the full bandwidth is a problem only for the centers of the most luminous edge-on galaxies, as these systems can have line widths of 600-800 km s^{-1} (Rubin et al. 1985). These luminous galaxies were not observed when bad baselines were a problem. Normally, 1/2 to 3/4 of the full bandwidth provides adequate baseline on either side of the line.

Spectra were calibrated by the standard chopper wheel method (Penzias and Burrus 1973), which corrects for atmospheric (to first order) and ambient temperature losses to yield the corrected antenna temperature T_A^*. Second order corrections for atmospheric losses are important at 115 GHz, and require elevation-dependent correction factors to be applied to all the data. These corrections are fully described in Appendix A.

§2. Observational Methods

Spectra were obtained by position-switching between the main position and a reference position several arcminutes away from the galaxy. Position-switching has the advantage of cancelling the effects of receiver drift and atmospheric opacity variations on time scales longer than the switching rate. In principle, it is desirable to switch as fast as possible, in order to cancel variations on short as well as

long timescales. In practice, the position-switching rate is limited by the telescope slew rate and the need for efficient observing. The finite time required for the antenna to move from the main to the reference position and settle down is time spent not taking data, and should be kept to a minimum. For this reason, the reference positions were chosen to be as close as possible to the galaxies, while still far enough away to remain free of emission. Experience shows that CO emission is usually undetectable (with 1987 technology) where the optical emission falls to 26 mag arcsec^{-2}, so offsets equal to twice the optical radius were deemed safe. This policy resulted in reference position offsets of 5'-10' depending on the optical size of the galaxy listed in the UGC (Nilson 1973). It is also worth pointing out that small reference position offsets are desirable in view of the observation that large offsets have associated baseline problems.

The offsets were chosen to be in Right Ascension rather than azimuth so that the reference position was a specific location relative to the galaxy, and any contaminating galactic or extragalactic emission could be properly removed from the spectrum. Since the main and reference positions were therefore at different elevations, the reference time was split between positons east and west (in R.A.) of the galaxy. This technique, called double position-switching, compensates (to first order) for the difference in atmospheric opacity between the main and reference positions. As it turned out, contamination by galactic CO emission was not a problem for any of the Virgo galaxies observed, since the systemic velocities of most Virgo galaxies are

higher than velocities encountered in the Milky Way. Contamination is not a problem even for those galaxies with velocities near zero (as it is with HI observations) since the cluster is located at high galactic latitudes ($b \sim 75°$), and galactic CO emission in the solar neighborhood (Sanders, Solomon, and Scoville 1984) is confined primarily to a thin disk layer with a scale height of 60 parsecs. Palomar Sky Survey prints were examined to ensure that none of the reference positions were coincident with optically bright galaxies.

The size of the reference position offsets helps determine a practical switching rate. It takes the antenna roughly a second to move and settle at a new position 5'-10' away. Efficient observing therefore requires a switching rate much slower than once per second. Switching at a rate of once every 30 seconds was normally done, although switching at twice this rate in poor weather sometimes improved the baselines. Since the observational part of this thesis was completed, a beam chopping spectral line capability has been implemented at FCRAO. The 15 Hz switching rate in the beam chopping mode results in better baselines, but at the expense of increased overhead time lost while the edge of the chopper blade is in the beam path.

Spectra were taken every 45" along the major axis of each galaxy, out to where no emission was detected in ~2 hours of integration time. More precisely, enough data was taken to achieve an rms noise of ≤ 10 millikelvins (T_A^*), after smoothing the data to a resolution of 12 km s^{-1}. The weakest line which can be detected depends upon the width of the line, hence on the rotation curve and inclination of the galaxy,

and the velocity field of the galaxy within the main beam. In general, the weakest line feature which can be detected (3σ) in this amount of integration time has an integrated intensity of 1 K(T_A*) km s^{-1}.

§3. Pointing

The pointing, focus, and gain (calibration) of the telescope were measured normally at the beginning of each observing run, and occasionally during the middle of the run. The high velocity gas in Orion (OrionHV), and the carbon star IRC+10216 were the main standard sources used throughout the 3-year period, although the variable quasar 3C 273 was used to determine the pointing and focus during 1984. 3C 273 is preferable as a pointing source to OrionHV or IRC+10216, since it is located only 10° to the south of M87, which is at the center of the Virgo cluster. However, the flux of 3C 273 decreased from ~45 Jy in April 1983 to ~20 Jy by 1985, so that it became too weak to use as a pointing source at 115 GHz. No significant systematic pointing offsets were detected between 3C 273 and either OrionHV or IRC+10216, so that the lack of a pointing source near the Virgo cluster during 1985-86 provided no difficulties.

We have measured an rms pointing error of 4" in both azimuth and elevation, or 6" in total, from all 126 pointing measurements made during the Virgo galaxy observing runs, over the 3 observing seasons. This pointing rms of 6" on 3C273, Orion, and IRC+10216 is less than the 9" rms found from 365 pointing measurements taken over the entire sky, and over a large temperature range during 1984-85 (Lord, Young, and

Kinzel 1985). Presumably, this is due to the fact that the pointing model does not fit all parts of the sky equally well, so additional scatter is introduced when data from the entire sky are considered.

An error of 6" in pointing results in a reduction of 5% in intensity for a point source measured with a Gaussian beam with a half-power beam width of 45". However, the molecular gas in Virgo galaxies is generally extended over a region of 1-5 arcminutes. Consequently, for most of the positions observed, pointing errors do not result in significant errors in the integrated line intensities. For a galaxy whose molecular gas distribution is distributed exponentially (e.g. Young and Scoville 1982a), the largest intensity error resulting from a pointing error occurs at the center of the galaxy. A 6" offset from the center of a galaxy with an exponential CO disk of scale length 0.3' results in an intensity error of only 3%.

Small pointing errors can affect lineshapes more than intensities, particularly in the central regions of galaxies. Our spectrum from the center of NGC 4254 has an asymmetric double-horned profile. Either the molecular gas distribution in the center of this galaxy is truly asymmetric, or the telescope was not pointed at the true nucleus. On the basis of the model fitting which is described in Chapter IV, we estimate that the observed asymmetric profile could be due to a pointing offset of ~6". The symmetric profiles for most of central spectra with high signal-to-noise ratios indicates that pointing errors are generally smaller than ~10".

§4. The Virgo Sample

A great variety of galaxies exist in the Virgo cluster. In order to separate the effects of environment from those of morphological type and luminosity, it is necessary to observe a large sample of objects. The need for a large sample, and the 2-3 hours of observing time required for each spectrum, dictate the choice of major axis mapping. While it would of course be preferable to obtain complete maps of the galaxies, major axis mapping allows both the total CO luminosity and the extent of CO emission to be determined with reasonably small uncertainties in a significant number of galaxies.

In choosing any sample for scientific study, it is desirable to avoid selection effects which may bias the results. The CO sample was chosen to be a complete, blue magnitude-limited sample of spiral galaxies. Because of their availability, blue magnitudes have been used to select the sample galaxies. In adopting an apparent magnitude limit, we are in essence adopting an absolute magnitude limit, since all Virgo galaxies are at approximately the same distance. Given that a limited number of galaxies are to be observed, the brightest galaxies are preferred since these are the easiest to detect, are large enough to map, and are well-studied. With an apparent blue magnitude cutoff of $B_T^o = 12.0$, the galaxies in this sample span a range of a factor of 10 in luminosity. The particular value of $B_T^o = 12.0$ was chosen because the resulting sample includes enough galaxies to begin to allow the sorting of environmental effects from those of type and luminosity.

The motivation for having a complete magnitude-limited sample is to include all galaxies above a certain mass. Tully and Fisher (1977) first demonstrated that the total mass of a galaxy is correlated with its blue luminosity. Due to the presence of scatter in the Tully-Fisher relationship, there is a range in blue luminosities for galaxies of a given mass. The presence of this scatter introduces a bias in any magnitude-limited sample. The lower luminosity galaxies in the sample include actively star-forming low mass galaxies with blue colors, yet no galaxies of comparable mass which are forming stars less actively. The impact of this bias, which affects only the lower luminosity sample galaxies, will be discussed where relevent.

In selecting the sample, we have followed the work of Helou et al. (1984), who have mapped the 21 cm HI emission line along the major axis of all Virgo spirals in a complete, magnitude-limited sample with the sensitive Arecibo telescope. By choosing a subset of the Helou et al. sample, we ensure that the CO data can be compared with a homogenous set of HI data. Galaxies which are classified as type Sa or later, according to Binggeli, Sandage, and Tammann (1985, hereafter BST) within the rectangle defined by $4° \leq \delta \leq 20°30'$, $12^h \leq \alpha \leq 13^h$, and with magnitude $B_T{}^o \leq 12.0$, define the CO sample. The rectangle on the sky is roughly centered on M87, and extends somewhat beyond the region of 4.5° radius within which most of the HI-deficient galaxies are found (Haynes and Giovanelli 1986). The region is therefore large enough to include numerous systems with normal HI content, which is important for comparison purposes. In addition to the 38 galaxies in the complete,

magnitude-limited sample described above, 4 additional Virgo galaxies were included in the survey for their scientific interest: 2 SO's with large far-infrared fluxes, and 2 luminous spirals slightly south of $\delta=4°$. Two galaxies (NGC 4235 and NGC 4378) which meet the sample criteria have been excluded from the survey, since they are likely to be background galaxies. Table 2.1 lists the galaxies in the sample, along with their morphological types (columns 2 and 3), coordinates (columns 4 and 5), angular distance from M87 (column 6), cluster membership status (column 7), apparent blue magnitude (column 8), and heliocentric velocity (column 9).

The classifications of BST are used instead of those by deVaucouleurs and Pence (1979, hereafter dVP) because of the higher quality plate material of the former. A sample based on dVP classifications would contain the same galaxies except for NGC 4293, which BST classify as Sa pec, and dVP classify as SO/a. Only disk systems classified Sa or later were included as part of the complete sample, since few lenticulars and even fewer ellipticals have HI emission which has been detected (e.g. Wardle and Knapp 1986), and until recently, no elliptical or lenticular galaxy had been detected in the CO line (Verter 1985). We have, however, included 2 Virgo SO's in the survey (NGC 4526 and NGC 4710), which are remarkable in having significant far-infrared emission, but only upper limits on their HI emission.

Care must be taken with the different morphological types in the analysis of Virgo cluster data, to avoid problems due to the well-known "morphological segregation" in the cluster. Early-type spirals are

Explanation of columns in Table 2.1:

(1) NGC number.
(2) Morphological type from Binggeli, Sandage, and Tammann (1985), if available; otherwise from RSA.
(3) Morphological type from RC2.
(4) Right Ascension (1950) from Dressel and Condon (1976).
(5) Declination (1950) from Dressel and Condon (1976).
(6) Angular distance from M87.
(7) Cluster membership status, after deVaucouleurs and Corwin (1986):
    S = S cloud member; Virgo cluster proper.
    S'= S' cloud member; galaxies in the Declination range $5° < \delta < 10°$ may be ~20% more distant than the average galaxy in the S cloud.
    X = X 'cloud'; galaxies below $\delta = 5°$ are at a range of distances, some are more foreground than galaxies in the S cloud.
(8) Blue optical magnitude, corrected for inclination and extinction; B_T from deVaucouleurs and Pence (1979), $B_T - B_T^o$ from RC2.
(9) Systemic galaxy redshift $v_{sun} = cz$, generally from HI line (Helou et al. 1981, 1984; Giovanelli and Haynes 1983); although for 2 galaxies which are undetected in HI (NGC 4293 and NGC 4710), we list mean CO velocities; for NGC 4526, which remains undetected in both CO and HI, the velocity listed is from an optical spectrum (Huchra, private communication).

Table 2.1

Virgo Galaxy Sample Properties

NGC	RSA Type	RC2 Type	R.A. (h m s)	Dec. (° ' ")	R_{M87} (°)	Mem	B_T^o	v_{sun} (km s^{-1})
(1)	(2)	(3)	(4)	(5)	(6)	(7)	(8)	(9)
4064	SBc(s):	SB(s)a:P	12 01 37.3	+18 43 16	7.8	S	11.74	913
4178	SBc(s)II	SB(rs)dm	12 10 13.1	+11 08 30	4.7	S	11.35	377
4192	SbII:	SAB(s)ab	12 11 15.4	+15 10 23	4.8	S	10.31	-135
4212	Sc(s)II-III	SAbc?	12 13 06.4	+14 10 45	4.0	S	11.52	-83
4216	Sb(s)	SABb:	12 13 20.3	+13 25 38	3.7	S	10.29	138
4254	Sc(s)I.3	SA(s)c	12 16 16.9	+14 14 46	3.3	S	10.13	2405
4293	Sa pec	(R)SB(s)0/a	12 18 41.1	+18 39 36	6.4	S	10.80	930
4298	Sc(s)III	SA(rs)c	12 19 00.4	+14 53 03	3.2	S	11.75	1136
4302	Sc(on edge)	Sc:sp	12 19 10.2	+14 52 43	3.1	S	11.86	1150
4303	Sc(s)I.2	SAB(rs)bc	12 19 21.4	+04 44 58	8.2	X	9.95	1568
4312	Sab	SA(rs)ab:sp	12 19 59.4	+15 48 58	3.7	S	11.97	153
4321	Sc(s)I	SAB(s)bc	12 20 23.2	+16 06 00	3.9	S	9.89	1575
4380	Sab(s)	SA(rs)b:?	12 22 49.6	+10 17 33	2.7	S	11.98	971
4388	Sab	SA(s)b:sp	12 23 14.8	+12 56 18	1.3	S	11.20	2515
4394	SBb(sr)I-II	(R)SB(r)b	12 23 24.7	+18 29 30	5.9	S	11.47	914
4402	Sc(on edge)	Sbsp	12 23 35.8	+13 23 22	1.4	S	12.01	234
4419	Sa	SB(s)a,sp	12 24 25.1	+15 19 28	2.8	S	11.73	-243
4424	Sa pec	SB(s)a:	12 24 39.0	+09 41 51	3.1	S'	11.87	439
4438	Sb(tides)	SA(s)0/a:P	12 25 13.5	+13 17 11	1.0	S	10.43	69
4450	Sab pec	SA(s)ab	12 25 58.0	+17 21 40	4.7	S	10.63	1954
4501	Sbc(s)II	SA(rs)b	12 29 28.1	+14 41 50	2.1	S	9.85	2284
4526	SO_3(6)	SAB(s)0:	12 31 30.4	+07 58 33	4.8	S'	10.15	602
4527	Sb(s)II	SAB(s)bc	12 31 35.5	+02 55 45	9.8	X	10.92	1733
4532	SmIII	IBm	12 31 46.7	+06 44 43	6.0	S'	11.69	2021
4535	SBc(s)I.3	SAB(s)c	12 31 47.9	+08 28 25	4.3	S'	10.22	1962
4536	Sc(s)I	SAB(rs)bc	12 31 53.5	+02 27 50	10.2	X	10.52	1805
4548	SBb(rs)I-II	SB(rs)b	12 32 55.1	+14 46 20	2.4	S	10.72	484
4567	Sc(s)II-III	SA(rs)bc	12 34 01.1	+11 32 01	1.8	S	11.78	2277
4568	Sc(s)III	SA(rs)bc	12 34 03.0	+11 30 45	1.8	S	11.27	2255
4569	Sab(s)I-II	SAB(rs)ab	12 34 18.7	+13 26 18	1.7	S	9.86	-236
4571	Sc(s)II-III	SA(r)d	12 34 25.5	+14 29 33	2.4	S	11.63	342
4579	Sab(s)II	SAB(rs)b	12 35 12.6	+12 05 40	1.8	S	10.31	1520
4639	SBb(r)II	SAB(rs)bc	12 40 21.7	+13 31 56	3.1	S	11.88	1048
4647	Sc(rs)III	SAB(rs)c	12 41 01.1	+11 51 21	3.2	S	11.82	1422
4651	Sc(r)I-II	SA(rs)c	12 41 12.5	+16 40 05	5.1	S	10.99	797
4654	SBc(rs)II	SAB(rs)cd	12 41 25.7	+13 23 58	3.3	S	10.82	1039
4689	Sc(s)II.3	SA(rs)bc	12 45 15.3	+14 02 13	4.3	S	11.34	1620
4698	Sa	SA(s)ab	12 45 51.8	+08 45 37	6.3	S'	11.15	1008
4710	SO_3(9)	SA(r)0^+:sp	12 47 09.0	+15 26 15	5.3	S	11.30	1121
4713	SBc(s)II-III	SAB(rs)d	12 47 25.6	+05 34 58	8.5	S'	11.83	653
4808	Sc(s)III	SA(rs)cd:	12 53 17.0	+04 34 28	10.2	X	11.93	760
4866	Sa	SA0^+(r):sp	12 56 57.9	+14 26 25	7.2	S	11.12	1986

more tightly concentrated toward the center of the cluster than the late-type spirals. While this becomes readily apparent when a large number of Virgo galaxies are examined, its presence can be seen in the CO sample. Table 2.2 lists the sample galaxies as a function of morphological type, apparent magnitude, cluster position, and HI deficiency. (HI deficiency is explained in §V.2). Note that there are comparable numbers of S0-Sbc sample galaxies 0°-3° and 3°-6° from M87, while there are nearly 3 times as many Sc-Sm galaxies in the 3°-6° range compared to the 0°-3° range. This is also apparent in Figures 2.1 and 2.2, which display the locations of the sample galaxies on R.A.-Dec. maps of the cluster. Dressler (1986) has presented evidence that the early-type spirals have significantly different orbits than the late-type spirals: the early-type spirals tend to have predominantly radial orbits, while the late type spirals tend to have more isotropic orbits. It is undoubtedly more than just a coincidence that the early-type spirals are also more HI-deficient, as a class, than the late type spirals. Because of these significant differences between the early and late-type spirals, they will be analyzed separately.

§5. Foreground and Background Galaxies and the Structure of the Virgo Cluster

The Virgo cluster covers nearly 1% of the sky, so the question of contamination by foreground and background galaxies becomes relevant. Furthermore, given that the cluster is still in the process of formation, and that the universe is inhomogenous on scales smaller than

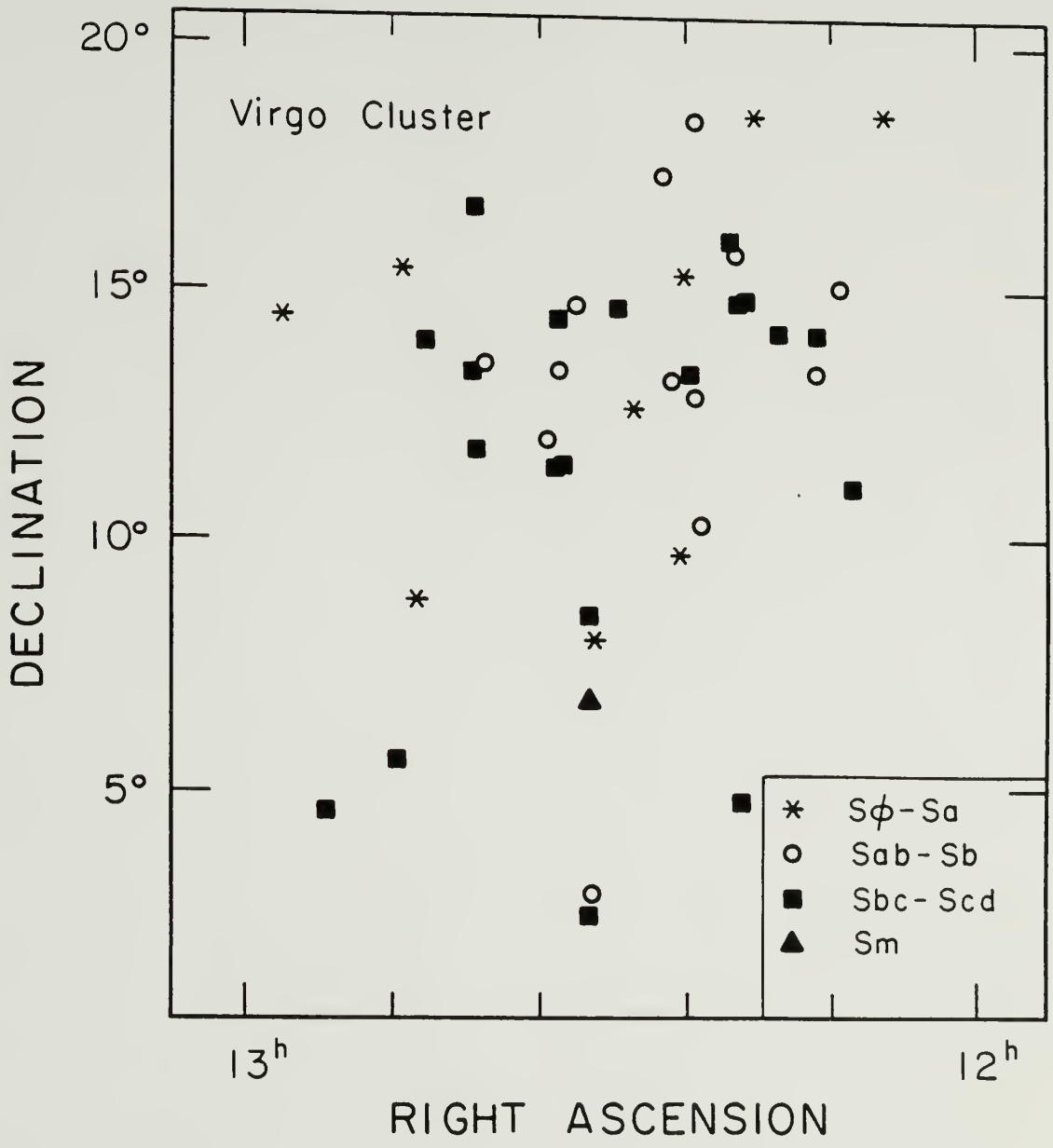

Figure 2.1 Location of sample galaxies on Right Ascension vs. Declination map of Virgo cluster.

Table 2.2

Virgo Sample Galaxies as a Function of
Type, Magnitude, Cluster Position & HI Deficiency

		NGC number of galaxy (HI deficiency)		
Type	B_T^o	0°-3° from M87	3°-6° from M87	6°-11° from M87
	10.0	4569 (0.99)		
		4579 (1.00)	4526 (--)	
			4450 (1.31)	
				4293 (--)
SO-Sab	11.0			4866 (0.24)
		4388 (1.06)		4698 (0.25)
			4710 (--)	
				4064 (0.99)
		4419 (1.06)	4424 (1.09)	
	12.0	4380 (1.05)	4312 (1.27)	
	10.0	4501 (0.47)		
			4216 (0.35)	
			4192 (0.09)	
		4438 (1.28)		
Sb-Sbc	10.8	4548 (0.86)		4527 (-0.35)
			4394 (0.85)	
	11.8		4639 (0.16)	
	10.0		4321 (0.52)	4303 (0.17)
			4254 (0.02)	
			4535 (0.17)	
				4536 (0.03)
			4654 (0.00)	
Sc-Sm	11.0		4651 (-0.16)	
		4568 (0.64)	4689 (1.06)	
			4178 (-0.13)	
			4212 (0.44)	
		4571 (0.44)	4298 (0.54)	4532 (-0.30)
		4567 (0.64)	4647 (0.51)	
			4302 (0.15)	4713 (-0.13)
	12.0	4402 (0.61)		4808 (-0.68)

Figure 2.2 Location of the sample galaxies on R.A. vs. Dec. maps of the Virgo cluster. The X marks the location of M87 at (or near) the center of the cluster. Circles of 4.5° radius, within which most of the HI-deficient galaxies are found, have been drawn on each map. (a) All 42 survey galaxies. (b) The 8 S0-Sa survey galaxies. (c) The 13 Sab-Sb survey galaxies. (d) The 21 Sbc-Sm survey galaxies.

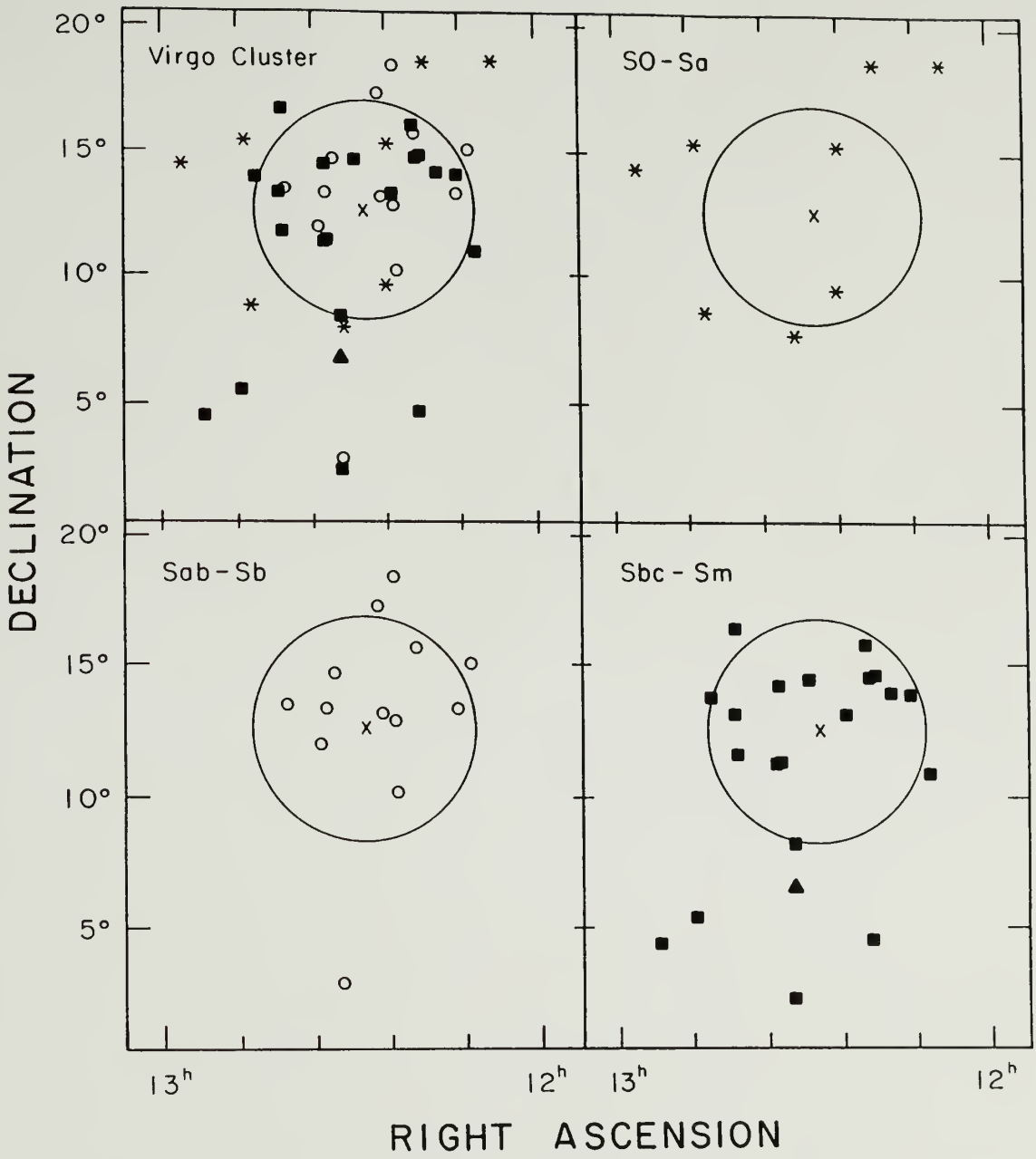
Virgo Cluster
S0 - Sa
Sab - Sb
Sbc - Sm
20°
15°
10°
5°
DECLINATION
13h
12h
RIGHT ASCENSION

100 Mpc, it is not surprising that the distribution of galaxies in the Virgo region is clumpy. Given the existence of spatially and kinematically distinguishable entities within the Virgo region, it is necessary to decide which of these are to be considered part of the "Virgo cluster". For the purposes of this work, it is desirable to include galaxies which are at roughly the same distance as the M87 clump, in order to avoid any distance-dependent biases. Galaxies which are at the same distance as the M87 clump, but which may not be physically associated with the M87 clump, are worth including in this study as comparison galaxies. It is those galaxies which are either much nearer or much further than the M87 clump which are to be excluded from this study.

The first crude step in estimating a galaxy's distance is to use its velocity and the Hubble velocity-distance law. This does not work well for individual galaxies in the Virgo cluster, since the spiral galaxy velocity dispersion within the cluster of 800 km s^{-1} is a significant fraction of Virgo's mean "Local Groupocentric" velocity of 1050 km s^{-1} (Huchra 1985). Nevertheless, it allows the exclusion of galaxies which are significantly background to Virgo.

An extensive redshift survey of all galaxies brighter than $m_{pg}=15.5$ in the Virgo region indicates that galaxies with $v_o > 3000$ km s^{-1} are obviously background objects, and those with smaller velocities must have their distances estimated by other methods (Huchra 1985). None of the galaxies in our sample, with a magnitude cutoff of $B_T^o < 12.0$, have velocities greater than 3000 km s^{-1}. However, there are

several galaxies with $2000 < v_o < 3000$ km s^{-1}, which must be considered as suspected background objects. For these galaxies--NGC 4254, NGC 4388, NGC 4501, NGC 4567, and NGC 4568--a distance has been estimated from the Tully-Fisher relation, using blue magnitudes and either the HI line velocity width (Helou et al. 1984) or an optical rotation curve (Chincarini and deSouza 1985). The Tully-Fisher distance estimates are consistent with Virgo membership in all 5 cases.

There are at least 3 regions in the Virgo area in which there are relatively nearby background or foreground groups with radial velocities less than 3000 km s^{-1}, and for which it is difficult to assign cluster membership. The first is an area between $\alpha = 12^h15^m$ and 12^h25^m, $\delta = 5°5'$ and 8°, where the so-called "W cloud" exists. The W cloud is a group of about 100 galaxies at twice the M87 distance, and only 1.5 magnitudes fainter than Virgo core galaxies (deVaucouleurs 1961). Two galaxies in this region of the sky, which are within our magnitude cutoff, have been excluded from the survey because of their likely membership in the background W cloud. NGC 4378 (B_T^o=11.94, v_o=2554 km s^{-1}) has a Tully-Fisher distance estimate which places it roughly twice as far as Virgo (Rubin et al. 1978), and therefore is a certain member of the W cloud. The other galaxy, NGC 4235 (B_T^o=11.93, v_o=2527 km s^{-1}) remains undetected in HI (Helou et al. 1984) and has no published optical rotation curve, so it is not possible to estimate a Tully-Fisher distance for this galaxy. However, its velocity and location on the sky make NGC 4235 a likely member of the W cloud. Even if it turns out to be a member of the Virgo cluster, the absence of HI,

far-infrared (IRAS Point Source Catalog), and radio continuum emission (Dressel and Condon 1978; Kotanyi 1980) make it unlikely that NGC 4235 has much molecular gas. A second background clump centered at $\alpha = 12^h12^m$, $\delta = 13°45'$, and about 1° in radius, called the "M cloud" (Ftaclas, Fanelli, and Struble 1984), is also at twice the M87 distance, but is smaller and less of a problem than the "W cloud". There are no galaxies brighter than $B_T^o = 12.5$ in this group.

A controversial question has been whether or not any of the negative velocity galaxies within 6° of M87 are foreground objects. Sulentic (1977) found that several of the negative velocity Virgo galaxies have larger angular diameters than most of the other Virgo galaxies, and claimed this as evidence that these are foreground galaxies. However, when an inclination correction is made to the angular diameters, the 4 spirals in Sulentic's group no longer stand out in the velocity-diameter plane, since they are all large inclination ($i > 60°$) systems. Furthermore, the negative velocities are likely to be an indication that these galaxies are indeed associated with the Virgo cluster, since only in the direction of Virgo are a significant number of negative velocity galaxies seen. These galaxies form the expected low velocity tail in the cluster velocity distribution (Sandage and Tammann 1976). Tully-Fisher distance estimates for at least 3 of these 4 spirals place them safely near the nominal Virgo distance (Helou, Hoffman, and Salpeter 1979).

One of the galaxies in Sulentic's suspected foreground group, NGC 4569, has been claimed to be at roughly half the Virgo distance on the

basis of the HI line width-absolute magnitude version of the Tully-Fisher relationship (e.g. Mould, Aaronson, and Huchra 1980; Tully and Shaya 1984). Further investigation reveals that the HI line width is not a reliable luminosity indicator for NGC 4569, since the atomic gas does not sample the full gravitational potential well of the galaxy. NGC 4569 is severely HI-deficient, with no HI in the outer disk (van Gorkom and Kotanyi 1985; Warmels 1986) as is typical for isolated galaxies. Using optical rotation curve data to derive a more meaningful Tully-Fisher distance, Stauffer, Kenney, and Young (1986) find that NGC 4569 lies within 2σ of the mean Virgo distance. Their results are also consistent with NGC 4569 being ~2-4 Mpc closer than M87, but still within the range of distances expected for the Virgo cluster.

The spiral galaxies within the traditional Virgo cluster, even with the M and W clouds removed, do not form a relaxed dynamical system. The velocity distribution of Virgo spirals indicates that spirals are still falling into the cluster (e.g. Tully and Shaya 1984; Huchra 1985). It is therefore not surprising that there are distinguishable regions within the traditional Virgo cluster where the spiral galaxies are either closer to or further from us than the M87 clump. deVaucouleurs (1961; see also deVaucouleurs and Corwin 1986) has identified 3 regions within the Virgo cluster sample area which contain galaxies that may be at different mean distances. deVaucouleurs uses, as one of his distance indicators, the "luminosity index", which is well correlated with absolute magnitude. All Virgo spirals north of δ

f 10° with velocities less than $v_o \sim 2600$ km s^{-1} (and which are not in the M cloud) are assigned to the Virgo cluster "proper", or S cloud, in deVaucouleurs' terminology. Spirals in the declination range $5° < \delta < 10°$ (and which are not in the W cloud) appear ~0.4 blue magnitudes fainter for their luminosity index, on average, than galaxies in the S cloud. deVaucouleurs assigns these galaxies to the S' cloud; galaxies within this region may be ~20% more distant than the S cloud galaxies. Below $\delta \sim 5°$ is the region called the "southern extension" or X cloud, which BST describe as a "huge prolate structure of the Virgo supercluster complex pointing toward the Virgo cluster". Apparently, galaxies in this region are at a range of distances (deVaucouleurs and Corwin 1986). Column 7 of Table 2.1 lists the cloud which deVaucouleurs assigns to each sample galaxy.

In order to assess the range of distances to the galaxies in our sample, we employ the infrared Tully-Fisher relationship, which is more objective than the "luminosity index" method of deVaucouleurs (although not necessarily more reliable). Plotted in Figure 2.3 is the corrected H (1.6 μm) magnitude $H^c_{-0.5}$ vs. the logarithm of the HI velocity width, corrected for inclination and non-circular velocities. Both quantities have been taken from Mould, Aaronson, and Huchra (1980) or Aaronson et al. (1982). Seventeen of the 42 sample galaxies are included in Figure 2.3. Galaxies in the S, S', and X clouds, which are denoted by different symbols, are all well described by the same slope and intercept. Part of the scatter in the Virgo cluster Tully-Fisher diagram is associated with the HI content of the galaxies. S cloud galaxies which are

Figure 2.3 Infrared Tully-Fisher relationship for Virgo cluster spirals. Galaxies are coded by the deVaucouleurs cloud to which they belong. Seventeen of the twenty-eight galaxies plotted here are in the CO survey; all of these are brighter than $H^c_{-0.5}=10.5$. The S cloud survey galaxies are: N4178, N4192, N4216, N4380, N4388, N4438, N4450, N4501, N4569, N4651, and N4654. The S' cloud survey galaxies are: N4532, N4535, N4698, and N4713. The X cloud survey galaxies are: N4536 and N4808. The four S cloud galaxies with HI def > 0.9 are indicated by open circles. These are: N4388, N4438, N4450, and N4569.

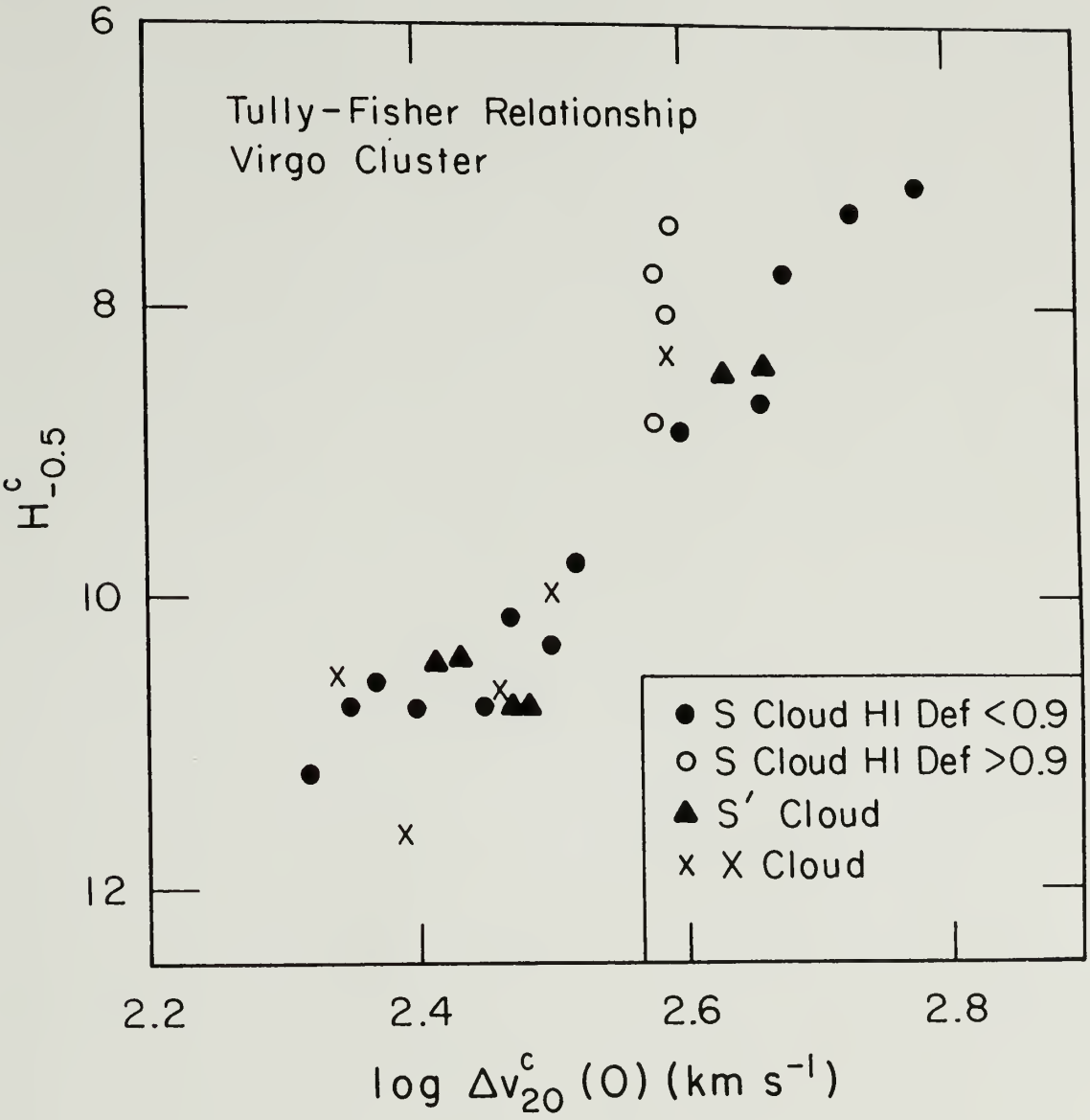
Tully-Fisher Relationship
Virgo Cluster
S Cloud HI Def <0.9
S Cloud HI Def >0.9
S′ Cloud
X Cloud
6
8
10
12
2.2
2.4
2.6
2.8
$H^c_{-0.5}$
log Δv^c_{20} (0) (km s^{-1})

severely HI-deficient (those galaxies with HI def > 0.9 are indicated by open circles in Figure 2.2), have HI line widths which are small for their H magnitudes (Stauffer, Kenney, and Young 1986). As we have already described for the case of NGC 4569, a reduced line width is explained by the lack of atomic gas in the outer disk (which is the highest velocity gas) in these severely HI-deficient systems. Removing these 4 galaxies from consideration reduces the scatter in this relation to ~0.4 magnitudes. If this scatter is the result of different distances to the individual galaxies, then the 1 σ distance variation among these galaxies is ~20%. This result is consistent with the results of deVaucouleurs and Corwin.

The luminous spiral galaxies NGC 4527 and NGC 4536 have been observed as part of the CO survey, even though they are not in the complete sample, in order to increase the number of luminous sample spirals with near-normal amounts of HI. These galaxies are in the X cloud, and therefore may not be at the same distance as the other Virgo spirals. The location of NGC 4536 in the Tully-Fisher diagram places it ~0.4 magnitudes above the best-fit line, suggesting that it may be as much as 20% closer to us than M87. This is within the acceptable range of distances for the purposes of this study. Although an H magnitude for NGC 4527 does not appear in the literature, the proximity of NGC 4536 and NGC 4527 on the sky, and their similar radial velocities suggest that the 2 galaxies are at approximately the same distance.

CHAPTER III

CO DATA & DERIVED PROPERTIES

§1. Introduction

As with all scientific measurements, it is desirable to relate the quantity actually measured to a physically meaningful quantity which is independent of the instrument. The amount of molecular gas is the quantity of astrophysical interest, and there are two steps involved in relating it to the observed CO line intensities. In this chapter, the observed CO integrated intensities ($=\int T_A^* dv$) are related to the CO line flux (in Janskys km s^{-1}) for the entire galaxy. In Chapter IV, the global CO line flux is related to the mass of molecular gas.

The extraction of the CO flux is not entirely straightforward, since it requires knowledge of the beam pattern and assumptions about the intrinsic distribution of CO emission. These complications have prevented observers of Milky Way molecular clouds from converting their antenna temperatures into brightness temperature units. However, the coupling calculation is more tractable in the case of CO emission from other galaxies for 2 reasons. First, the CO emission in all but the nearest extragalactic objects extends over less than a few arcminutes, where the beam pattern is relatively well-known. Second, the large-scale distribution of CO emission in most distant galaxies is fairly regular and symmetric on size scales of several kiloparsecs, contrasting with the irregular structure of individual Milky Way molecular

clouds on size scales of parsecs.

A likely reason many extragalactic CO observers have not quoted their results in flux units is that the critical relation between CO flux and molecular gas surface density is derived from Milky Way molecular clouds for which, because of their large size and irregular shape it is difficult to determine accurate fluxes. This is a separate issue which is discussed in Chapter IV, and is not a problem if large numbers of molecular clouds are used to calibrate the CO-H_2 surface density relation.

Although this chapter explains some aspects of the calibration, more thorough discussions are included in two appendices. Appendix A describes in detail the point source calibration at 115 GHz, including an elevation dependence to the calibration produced by a gain variation and atmospheric effects. Appendix B describes a method for calibrating extended sources which are undersampled.

§2. Summary of CO Data

A summary of all the CO line data is presented in Table 3.1. Data for all those galaxies which have been detected in 2 or more positions are presented in Figures 3.1 - 3.29. Each of these figures contains spectra for all observed positions in that galaxy, a plot of the radial distribution of CO intensities, and in most cases a spatial-velocity diagram. Central spectra for all galaxies detected in only 1 position are displayed in Figure 3.30. The central spectra for all undetected galaxies are shown in Figure 3.31.

Table 3.1

Record of Observations

NGC	i	PA	#obs	Δα (arcmin)	Δδ	$\int T_A^* dv$ (K km s^{-1})	T_A^*(peak) (mK)	rms (mK)	v_{mean} (km s^{-1})	Δv
(1)	(2)	(3)	(4)	(5)	(6)	(7)	(8)	(9)	(10)	(11)
4064	67°	150°	3	0.00	0.00	1.6 ± 0.4	21	5	927	150
				0.38	-0.65	0.2 ± 0.4	≤10	7	---	--
				-0.38	0.65	0.0 ± 0.4	≤14	7	---	--
4178	69°	30°	5	0.00	0.00	0.9 ± 0.3	18	8	415	95
				0.38	0.65	0.6 ± 0.4	≤16	9	---	--
				0.75	1.30	-0.4 ± 0.5	≤16	12	---	--
				-0.38	-0.65	-0.4 ± 0.4	≤11	10	---	--
				-0.75	-1.30	-0.3 ± 0.4	≤17	11	---	--
4192	74°	155°	8	0.00	0.00	4.9 ± 1.5	21	7	-105	330
				0.32	-0.68	2.5 ± 0.8	23	9	-17	150
				0.63	-1.36	1.9 ± 0.6	30	8	19	100
				0.95	-2.04	0.3 ± 0.4	≤12	10	---	--
				-0.32	0.68	3.1 ± 1.0	30	8	-205	160
				-0.63	1.36	1.2 ± 0.4	27	8	-309	90
				-0.95	2.04	1.6 ± 0.5	29	9	-345	50
				-1.27	2.72	0.6 ± 0.4	≤16	9	---	--
4212	47°	75°	5	0.00	0.00	4.1 ± 1.3	29	8	-60	130
				0.73	0.19	2.1 ± 0.6	53	10	-175	50
				1.45	0.39	0.3 ± 0.5	≤19	14	---	--
				-0.73	-0.19	1.2 ± 0.3	37	10	20	60
				-1.45	-0.39	0.3 ± 0.4	≤13	10	---	--
4216	80°	19°	9	0.00	0.00	0.3 ± 1.0	≤15	8	---	--
				0.24	0.71	1.2 ± 0.7	≤14	7	---	--
				0.49	1.42	2.3 ± 0.4	23	8	-68	160
				0.73	2.13	2.4 ± 0.4	26	7	-76	150
				0.98	2.84	0.4 ± 0.3	≤11	7	---	--
				-0.24	-0.71	0.8 ± 0.5	≤16	6	---	--
				-0.49	-1.42	1.8 ± 0.5	24	8	354	180
				-0.73	-2.13	1.3 ± 0.4	31	8	350	100
				-0.98	-2.84	0.3 ± 0.4	≤14	9	---	--

Table 3.1 (cont.)

NGC	i	PA	#obs	Δα (arcmin)	Δδ	$\int T_A^* dv$ (K km s^{-1})	T_A^*(peak) (mK)	rms (mK)	v_{mean} (km s^{-1})	Δv
(1)	(2)	(3)	(4)	(5)	(6)	(7)	(8)	(9)	(10)	(11)
4254	28°	45°	7	0.00	0.00	10.6 ± 2.0	89	10	2407	200
				0.53	0.53	3.5 ± 0.6	64	9	2468	95
				1.06	1.06	2.1 ± 0.5	51	8	2467	60
				1.59	1.59	1.3 ± 0.4	37	9	2507	30
				-0.53	-0.53	5.1 ± 0.9	88	11	2313	100
				-1.06	-1.06	3.2 ± 0.6	53	8	2315	60
				-1.59	-1.59	1.0 ± 0.3	19	7	2293	60
4293	76°	72°	3	0.00	0.00	6.3 ± 0.9	44	6	929	200
				0.71	0.23	0.6 ± 0.4	≤13	6	---	--
				-0.71	-0.23	0.3 ± 0.4	≤13	6	---	--
4298	67°	140°	5	0.00	0.00	6.0 ± 0.9	40	8	1100	220
				0.48	-0.57	4.0 ± 0.6	63	9	1060	100
				0.96	-1.15	0.7 ± 0.4	≤16	7	---	--
				-0.48	0.57	2.8 ± 0.6	41	10	1220	140
				-0.96	1.15	0.3 ± 0.3	≤10	7	---	--
4302	90°	178°	6	0.00	0.00	4.9 ± 0.9	38	7	1090	260
				0.03	-0.75	6.8 ± 1.0	55	8	1249	270
				0.05	-1.50	2.0 ± 0.5	36	9	1298	90
				0.08	-2.25	-0.3 ± 0.4	≤10	7	---	--
				-0.03	0.75	1.4 ± 0.4	18	7	1100	—
				-0.05	1.50	0.3 ± 0.4	≤10	7	---	--
4303	25°	0°	7	0.00	0.00	11.9 ± 2.1	92	8	1555	160
				0.00	0.75	5.3 ± 1.1	82	8	1590	80
				0.00	1.50	1.2 ± 0.3	20	7	1586	--
				0.00	2.25	0.4 ± 0.3	≤13	7	---	--
				0.00	-0.75	6.9 ± 1.4	137	7	1513	90
				0.00	-1.50	1.4 ± 0.4	24	8	1506	50
				0.00	-2.25	0.4 ± 0.3	≤16	8	---	--
4312	78°	170°	3	0.00	0.00	3.0 ± 0.7	33	8	161	100
				0.13	-0.74	-0.6 ± 0.4	≤11	7	---	--
				-0.13	0.74	0.4 ± 0.4	≤13	7	---	--

Table 3.1 (cont.)

NGC	i	PA	#obs	Δα (arcmin)	Δδ (arcmin)	$\int T_A^* dv$ (K km s^{-1})	T_A^*(peak) (mK)	rms (mK)	v_{mean} (km s^{-1})	Δv (km s^{-1})
(1)	(2)	(3)	(4)	(5)	(6)	(7)	(8)	(9)	(10)	(11)
4321	28°	120°	8	0.00	0.00	15.0 ± 2.6	99	7	1580	200
				0.65	-0.37	5.3 ± 1.1	66	8	1633	100
				1.30	-0.75	2.6 ± 0.7	39	10	1643	80
				1.95	-1.12	0.3 ± 0.4	<14	9	---	--
				-0.65	0.37	4.0 ± 0.8	76	9	1485	100
				-1.30	0.75	2.7 ± 0.7	57	9	1487	80
				-1.95	1.12	1.4 ± 0.4	31	8	1456	70
				-2.60	1.50	-0.1 ± 0.4	<14	9	---	--
4380	55°	63°	3	0.00	0.00	0.1 ± 0.5	<13	8	---	--
				0.67	0.34	-0.5 ± 0.4	<13	7	---	--
				-0.67	-0.34	-0.3 ± 0.4	<15	8	---	--
4388	79°	90°	5	0.00	0.00	2.7 ± 0.8	19	5	2500	350
				0.75	0.00	1.8 ± 0.4	31	7	2665	90
				1.50	0.00	-0.2 ± 0.4	<13	9	---	-
				-0.75	0.00	-0.5 ± 0.4	<11	5	---	-
				-1.50	0.00	0.2 ± 0.4	<16	7	---	-
4394	25°	138°	3	0.00	0.00	1.8 ± 0.6	18	5	891	200
				0.50	-0.56	-0.1 ± 0.5	<15	11	---	-
				-0.50	0.56	1.8 ± 0.5	19	9	870	140
4402	75°	90°	4	0.00	0.00	6.8 ± 1.6	53	8	244	200
				0.75	0.00	2.0 ± 0.5	39	8	338	70
				-0.75	0.00	5.7 ± 1.5	65	9	184	160
				-1.50	0.00	0.0 ± 0.5	<14	12	---	--
4419	67°	133°	5	0.00	0.00	10.2 ± 1.7	44	7	-203	300
				0.55	-0.51	1.8 ± 0.4	19	7	-323	100
				1.10	-1.02	0.2 ± 0.4	<13	9	---	--
				-0.55	0.51	7.5 ± 1.5	53	9	-91	180
				-1.10	1.02	0.1 ± 0.3	<13	7	---	--
4424	61°	95°	3	0.00	0.00	0.8 ± 0.3	15	5	449	70
				0.75	-0.07	0.4 ± 0.4	<13	8	---	--
				-0.75	0.07	0.1 ± 0.3	<13	7	---	--

Table 3.1 (cont.)

NGC	i	PA	#obs	Δα (arcmin)	Δδ (arcmin)	$\int T_A^* dv$ (K km s^{-1})	T_A^*(peak) (mK)	rms (mK)	v_{mean} (km s^{-1})	Δv (km s^{-1})
(1)	(2)	(3)	(4)	(5)	(6)	(7)	(8)	(9)	(10)	(11)
4438	68°	20°	3	0.00	0.00	2.9 ± 0.9	28	7	204	250
				0.26	0.70	1.4 ± 0.4	21	7	-7	110
				-0.26	-0.70	0.3 ± 0.4	≤15	7	---	--
4450	45°	0°	4	0.00	0.00	2.5 ± 0.9	21	9	1980	200
				0.00	0.75	1.5 ± 0.4	23	7	2018	100
				0.00	1.50	-0.4 ± 0.4	≤15	9	1844	120
				0.00	-0.75	1.5 ± 0.5	29	9	---	--
4501	58°	140°	7	0.00	0.00	12.0 ± 2.4	40	9	2263	450
				0.48	-0.57	5.7 ± 1.2	53	7	2437	250
				0.96	-1.15	2.9 ± 0.7	66	9	2495	100
				1.45	-1.73	0.9 ± 0.3	22	7	2493	60
				-0.48	0.57	6.8 ± 1.4	64	9	2082	220
				-0.96	1.15	2.7 ± 0.6	59	8	2048	100
				-1.45	1.73	0.5 ± 0.3	≤13	8	---	--
4526	90°	113°	3	0.00	0.00	0.0 ± 0.9	≤15	10	---	-
				0.35	-0.15	0.8 ± 0.6	≤18	10	---	-
				-0.69	0.29	-0.6 ± 0.5	≤15	8	---	-
4527	72°	67°	6	0.00	0.00	15.6 ± 2.5	72	10	1770	200
				0.69	0.29	8.7 ± 1.5	79	13	1833	160
				1.38	0.58	0.0 ± 0.4	≤14	8	---	--
				-0.69	-0.29	11.9 ± 2.0	68	12	1636	200
				-1.38	-0.58	2.8 ± 0.7	50	11	1550	120
				-2.07	-0.87	0.1 ± 0.5	≤16	9	---	--
4532	?	160°	3	0.00	0.00	0.2 ± 0.4	≤14	8	---	--
				0.26	-0.70	0.4 ± 0.4	≤14	7	---	--
				-0.26	0.70	0.5 ± 0.3	≤14	7	---	--
4535	43°	0°	7	0.00	0.00	4.7 ± 1.1	33	8	1949	250
				0.00	0.75	2.7 ± 0.7	45	8	1876	50
				0.00	1.50	1.4 ± 0.4	20	8	1864	50
				0.00	2.25	0.3 ± 0.3	≤13	7	---	--
				0.00	-0.75	2.1 ± 0.6	37	7	2041	90
				0.00	-1.50	2.1 ± 0.6	60	7	2064	50
				0.00	-2.25	1.0 ± 0.3	27	7	---	--

Table 3.1 (cont.)

NGC	i	PA	#obs	Δα (arcmin)	Δδ		$\int T_A^* dv$ (K km s^{-1})	T_A^*(peak) (mK)	rms (mK)	v_{mean} (km s^{-1})	Δv
(1)	(2)	(3)	(4)	(5)	(6)		(7)	(8)	(9)	(10)	(11)
4536	67°	116°	6	0.00	0.00		10.1 ± 1.8	44	10	1793	310
				0.67	-0.33		2.5 ± 0.6	22	8	1713	160
				1.35	-0.66		-0.1 ± 0.6	≤17	10	---	--
				-0.67	0.33		3.3 ± 0.6	23	8	1873	200
				-1.35	0.66		-0.5 ± 0.6	≤17	10	---	--
				-2.02	0.99		-0.3 ± 0.5	≤17	9	---	--
4548	37°	150°	7	0.00	0.00		3.7 ± 0.9	24	5	450	210
				0.38	-0.65		0.3 ± 0.3	≤10	6	---	--
				0.75	-1.30		1.1 ± 0.3	29	7	571	40
				1.13	-1.95		-0.6 ± 0.4	≤11	8	---	--
				-0.38	0.65		1.0 ± 0.3	19	7	369	70
				-0.75	1.30		1.1 ± 0.3	31	8	392	40
				-1.13	1.95		-0.4 ± 0.4	≤12	9	---	--
4567	46°	80°	4	0.00	0.00		4.7 ± 1.0	51	7	2284	180
				0.74	0.13	*	1.5 ± 0.5	36	5	2339	130
				-0.74	-0.13		1.7 ± 0.5	42	7	2192	80
				-1.48	-0.26		0.3 ± 0.3	≤10	8	---	--
4568	64°	23°	5	0.00	0.00		10.5 ± 2.3	61	10	2222	260
				0.29	0.69		5.2 ± 1.1	67	10	2345	110
				0.59	1.38	*	1.0 ± 0.3	36	5	2339	130
				-0.29	-0.69		4.5 ± 1.1	74	8	2112	110
				-0.59	-1.38		-0.7 ± 0.4	≤10	8	---	-
4569	63°	23°	5	0.00	0.00		14.6 ± 3.0	68	10	-203	320
				0.29	0.69		4.9 ± 1.1	67	9	-96	110
				0.58	1.38		0.6 ± 0.5	≤16	9	---	--
				-0.29	-0.69		7.2 ± 1.5	64	8	-326	160
				-0.58	-1.38		2.1 ± 0.7	35	8	-408	70
4571	38°	55°	5	0.00	0.00		1.8 ± 0.6	23	6	346	130
				0.61	0.43		1.1 ± 0.3	40	8	290	50
				1.22	0.86		-0.2 ± 0.4	≤16	11	---	--
				-0.61	-0.43		1.1 ± 0.3	30	8	379	40
				-1.22	-0.86		0.4 ± 0.4	≤17	11	---	--

Table 3.1 (cont.)

NGC	i	PA	#obs	Δα (arcmin)	Δδ	$\int T_A^* dv$ (K km s^{-1})	T_A^*(peak) (mK)	rms (mK)	v_{mean} (km s^{-1})	Δv
(1)	(2)	(3)	(4)	(5)	(6)	(7)	(8)	(9)	(10)	(11)
4579	37°	60°	6	0.00	0.00	4.1 ± 0.9	32	6	1465	380
				0.65	0.37	1.5 ± 0.4	30	7	1612	80
				1.30	0.75	-0.1 ± 0.3	<15	7	---	--
				-0.65	-0.37	2.6 ± 0.6	41	7	1403	130
				-1.30	-0.75	1.2 ± 0.4	27	7	1390	70
				-1.95	-1.13	0.7 ± 0.4	<18	9	---	--
4639	45°	123°	3	0.00	0.00	-0.3 ± 0.5	<12	5	---	--
				0.63	-0.41	0.7 ± 0.3	<13	7	---	--
				-0.63	0.41	0.4 ± 0.3	<11	7	---	--
4647	36°	125°	5	0.00	0.00	5.0 ± 0.8	51	9	1422	170
				0.61	-0.43	1.4 ± 0.4	32	6	1466	60
				1.23	-0.86	-0.1 ± 0.4	<10	7	---	--
				-0.61	0.43	2.2 ± 0.5	39	8	1362	80
				-1.23	0.86	0.6 ± 0.4	<10	7	---	--
4651	46°	80°	4	0.00	0.00	4.2 ± 1.2	18	7	741	360
				0.74	0.13	-0.1 ± 0.4	<15	7	---	--
				-0.74	-0.13	1.8 ± 0.6	17	7	912	170
				-1.48	-0.26	-0.5 ± 0.4	<16	8	---	--
4654	52°	125°	5	0.00	0.00	3.3 ± 0.8	36	8	1075	180
				0.61	-0.43	2.5 ± 0.6	36	6	1139	130
				1.22	-0.86	-0.3 ± 0.3	<10	7	---	-
				-0.61	0.43	3.7 ± 0.8	63	8	971	150
				-1.22	0.86	1.1 ± 0.4	<19	9	---	-
4689	30°	160°	5	0.00	0.00	3.6 ± 0.9	28	5	1614	210
				0.26	-0.70	2.0 ± 0.7	57	10	1685	60
				0.51	-1.41	0.0 ± 0.5	<19	12	---	--
				-0.26	0.70	2.1 ± 0.6	47	11	1545	70
				-0.51	1.41	-0.2 ± 0.4	<16	10	---	--
4698	57°	170°	3	0.00	0.00	0.4 ± 0.7	<13	8	---	--
				0.13	-0.74	-0.8 ± 0.6	<18	9	---	--
				-0.13	0.74	0.3 ± 0.5	<16	9	---	--

Table 3.1 (cont.)

NGC	i	PA	#obs	Δα (arcmin)	Δδ	$\int T_A^* dv$ (K km s^{-1})	T_A^*(peak) (mK)	rms (mK)	v_{mean} (km s^{-1})	Δv
(1)	(2)	(3)	(4)	(5)	(6)	(7)	(8)	(9)	(10)	(11)
4710	90°	27°	5	0.00	0.00	4.3 ± 1.0	31	5	1121	300
				0.17	0.33	2.4 ± 0.6	31	8	1090	200
				0.34	0.67	0.7 ± 0.5	≤13	8	---	--
				-0.17	-0.33	2.2 ± 0.7	26	9	1181	210
				-0.34	-0.67	0.3 ± 0.4	≤16	8	---	--
4713	49°	80°	3	0.00	0.00	-0.4 ± 0.5	≤16	9	---	--
				0.74	0.13	0.2 ± 0.5	≤16	11	---	--
				-0.74	-0.13	0.2 ± 0.5	≤16	10	---	--
4808	67°	127°	3	0.00	0.00	1.2 ± 0.6	≤17	9	---	--
				0.60	-0.45	0.7 ± 0.4	≤13	8	---	--
				-0.60	0.45	0.3 ± 0.4	≤12	8	---	--
4866	90°	87°	3	0.00	0.00	-0.2 ± 0.9	≤10	6	---	--
				0.75	0.04	-0.3 ± 0.5	≤11	7	---	--
				-0.75	-0.04	-0.7 ± 0.5	≤12	7	---	--

Explanation of Columns for Table 3.1:

(1) NGC number of galaxy.
(2) Inclination, from Helou et al. (1981, 1984) or computed as stated therein.
(3) Position angle of kinematic major axis, from Helou et al. (1981, 1984).
(4) Number of CO spectra obtained in survey.
(5-6) Observed position, in units of Right Ascension and Declination offsets from central position listed by Dressel and Condon (1976).
(7) CO integrated intensities $\int T_A^* dv$ and associated 1σ uncertainties, corrected to outside the atmosphere, as described in Appendix A.
(8) Peak antenna temperature of CO line, at a resolution of 12 km s^{-1}.
(9) rms noise of CO spectrum, in 4.2 MHz (12 km s^{-1}) channels.
(10) Intensity-weighted mean velocity of CO line; velocity units are cz; typical uncertainties are 10-20 km s^{-1}.
(11) Full width at 0% intensity of CO line; typical uncertainties are 20-30 km s^{-1}. The starred entries for NGC 4567 and NGC 4568 represent one spectrum from a position where the 2 galaxies overlap. The velocity information, peak antenna temperature, and rms of this spectrum is entered under both galaxies. For the CO integrated intensities, however, we have assigned a fraction of the total intensity to each galaxy. The total CO intensity for this position is 2.5 ± 0.5 K km s^{-1}. For more details, see the notes to Table 3.3.

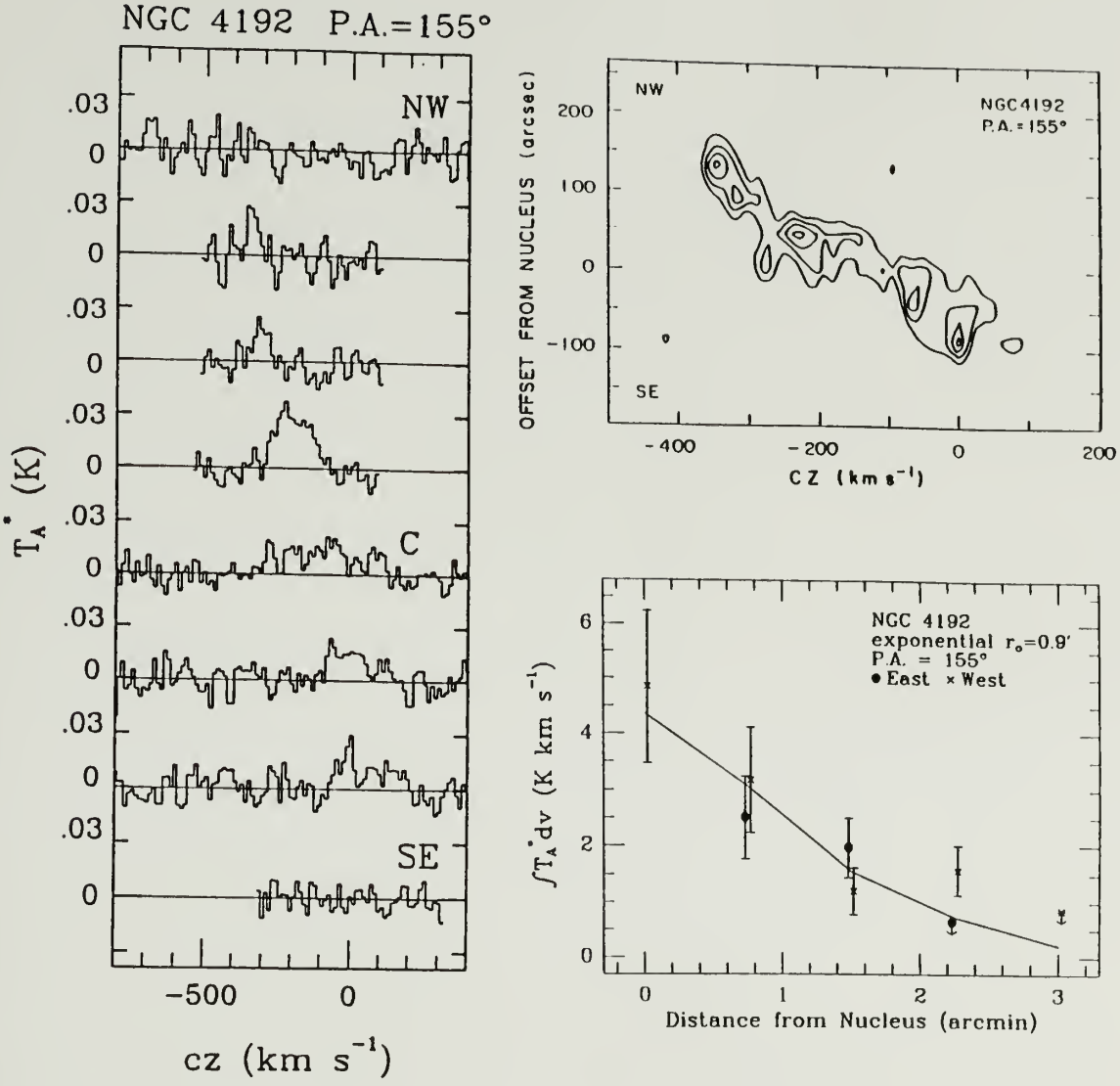

Figure 3.1 (a) CO spectra along major axis of NGC 4192, at intervals of 45". C denotes the spectrum obtained from the central position. (b) Spatial-velocity diagram for NGC 4192. Contour intervals are 10, 15, 20, and 25 mK(T_A^*). (c) Radial distribution of observed CO integrated intensities for NGC 4192. The line through the data points represents the Gaussian-weighted model source which best fits the observations.

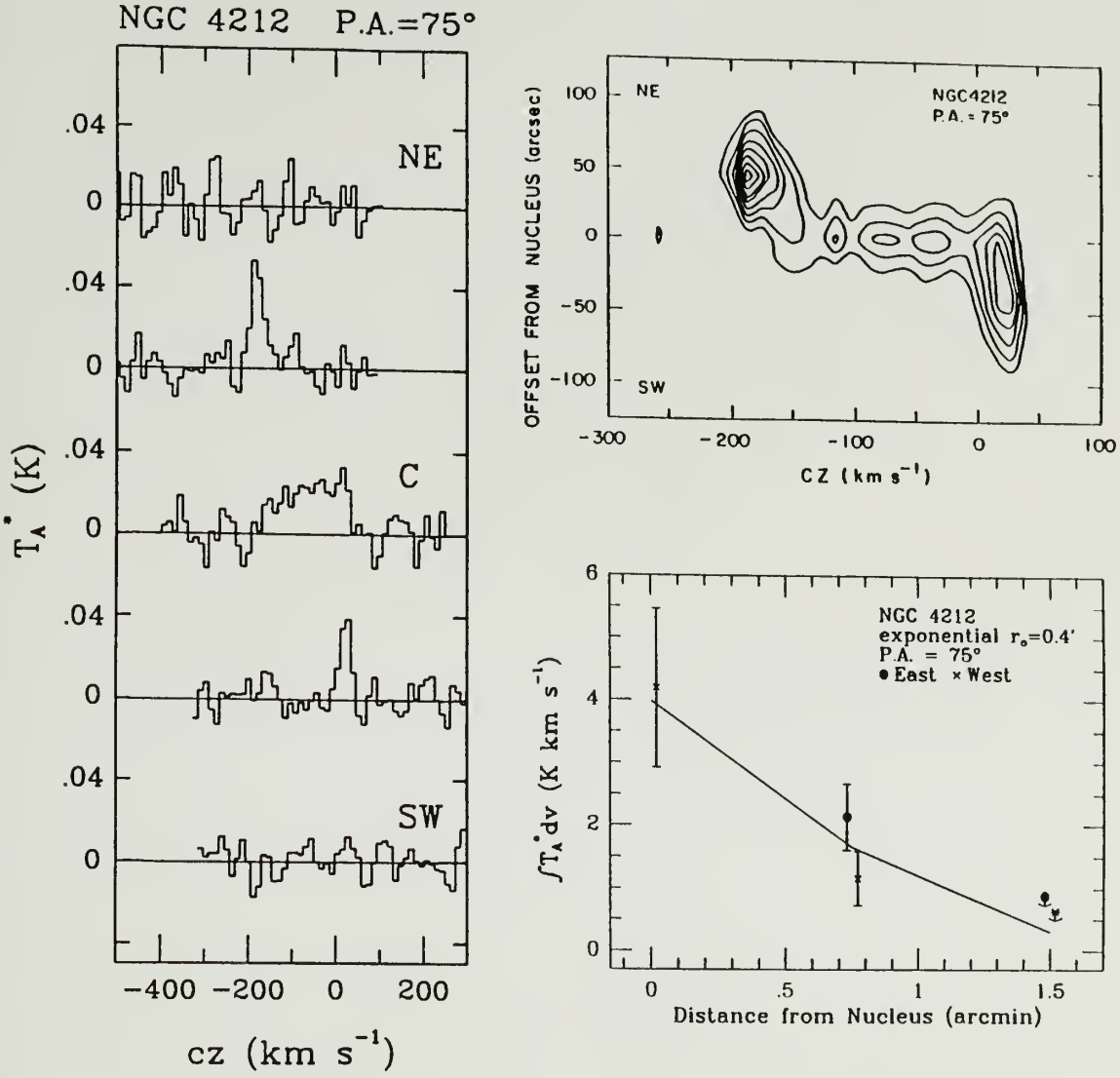

Figure 3.2 (a) CO spectra along major axis of NGC 4212, at intervals of 45". C denotes the spectrum obtained from the central position. (b) Spatial-velocity diagram for NGC 4212. Contour intervals are 10, 15, 20, 25, 30, 35, 40 and 45 mK(T_A^*). (c) Radial distribution of observed CO integrated intensities for NGC 4212. The line through the data points represents the Gaussian-weighted model source which best fits the observations.

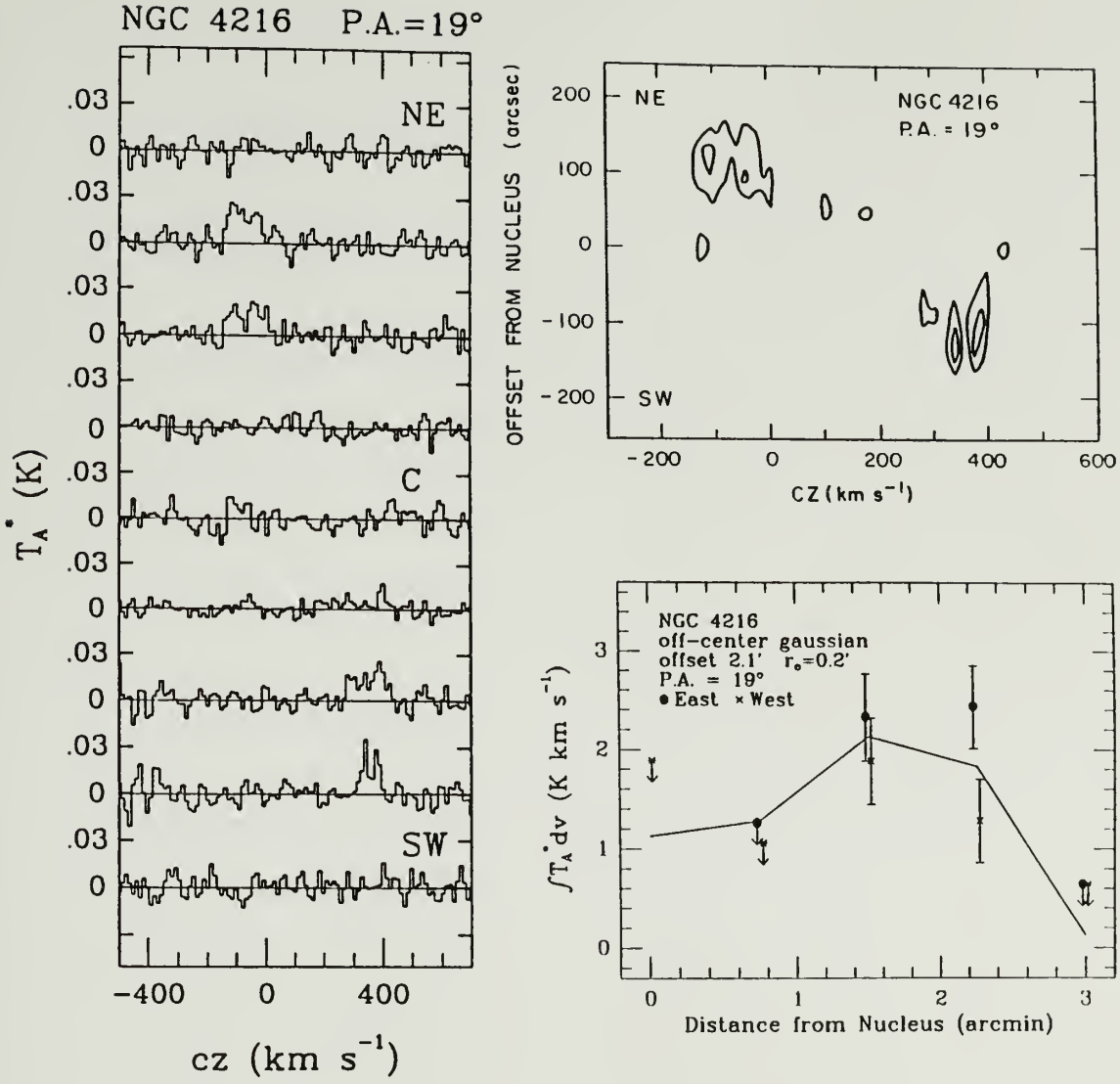

Figure 3.3 (a) CO spectra along major axis of NGC 4216, at intervals of 45". C denotes the spectrum obtained from the central position. (b) Spatial-velocity diagram for NGC 4216. Contour intervals are 10 and 20 mK(T_A^*). (c) Radial distribution of observed CO integrated intensities for NGC 4216. The line through the data points represents the Gaussian-weighted model source which best fits the observations.

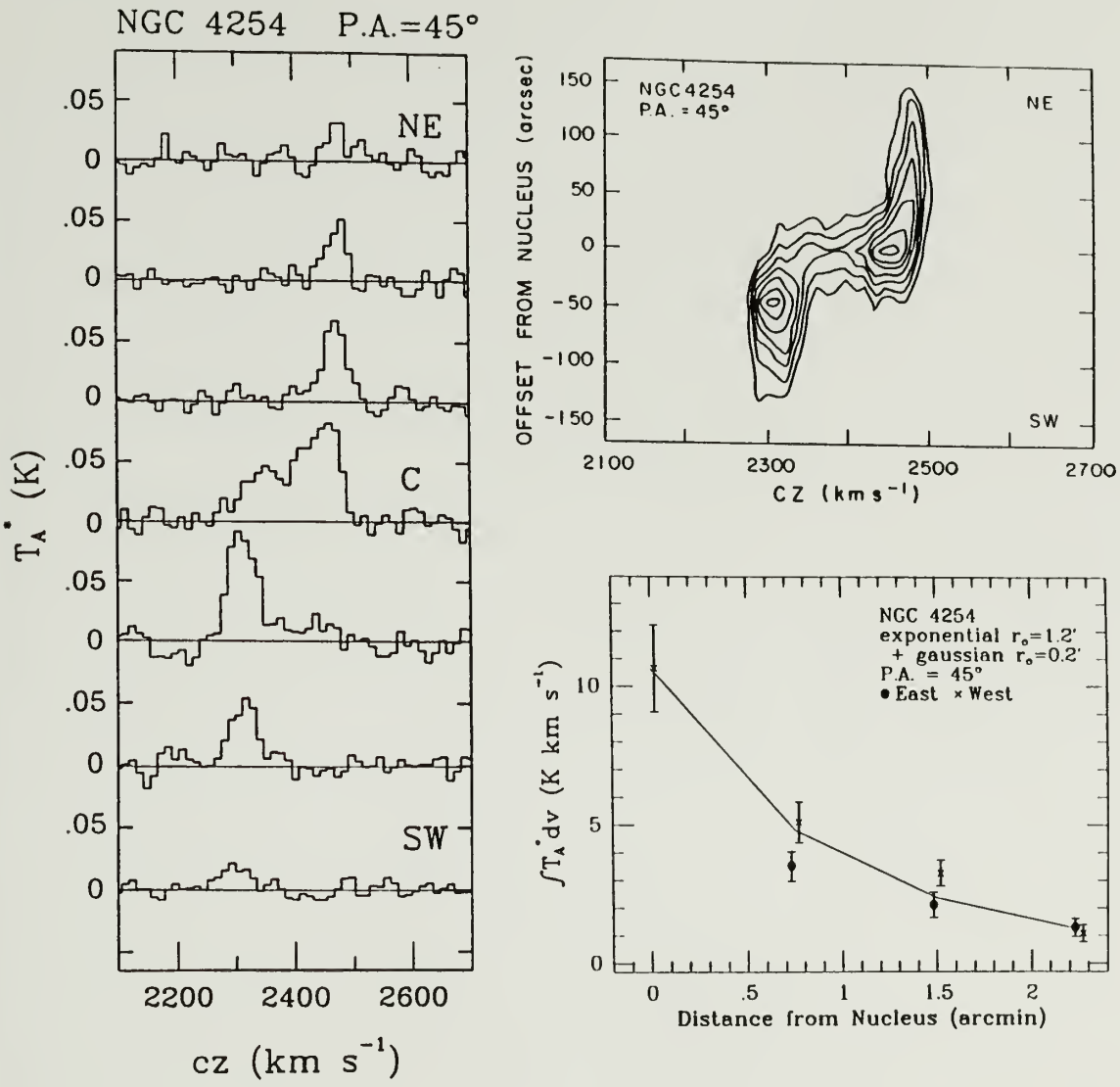

Figure 3.4 (a) CO spectra along major axis of NGC 4254, at intervals of 45". C denotes the spectrum obtained from the central position. (b) Spatial-velocity diagram for NGC 4254. Contour intervals are 20, 30, 40, 50, 60, 70 and 80 mK(T_A^*). (c) Radial distribution of observed CO integrated intensities for NGC 4254. The line through the data points represents the Gaussian-weighted model source which best fits the observations.

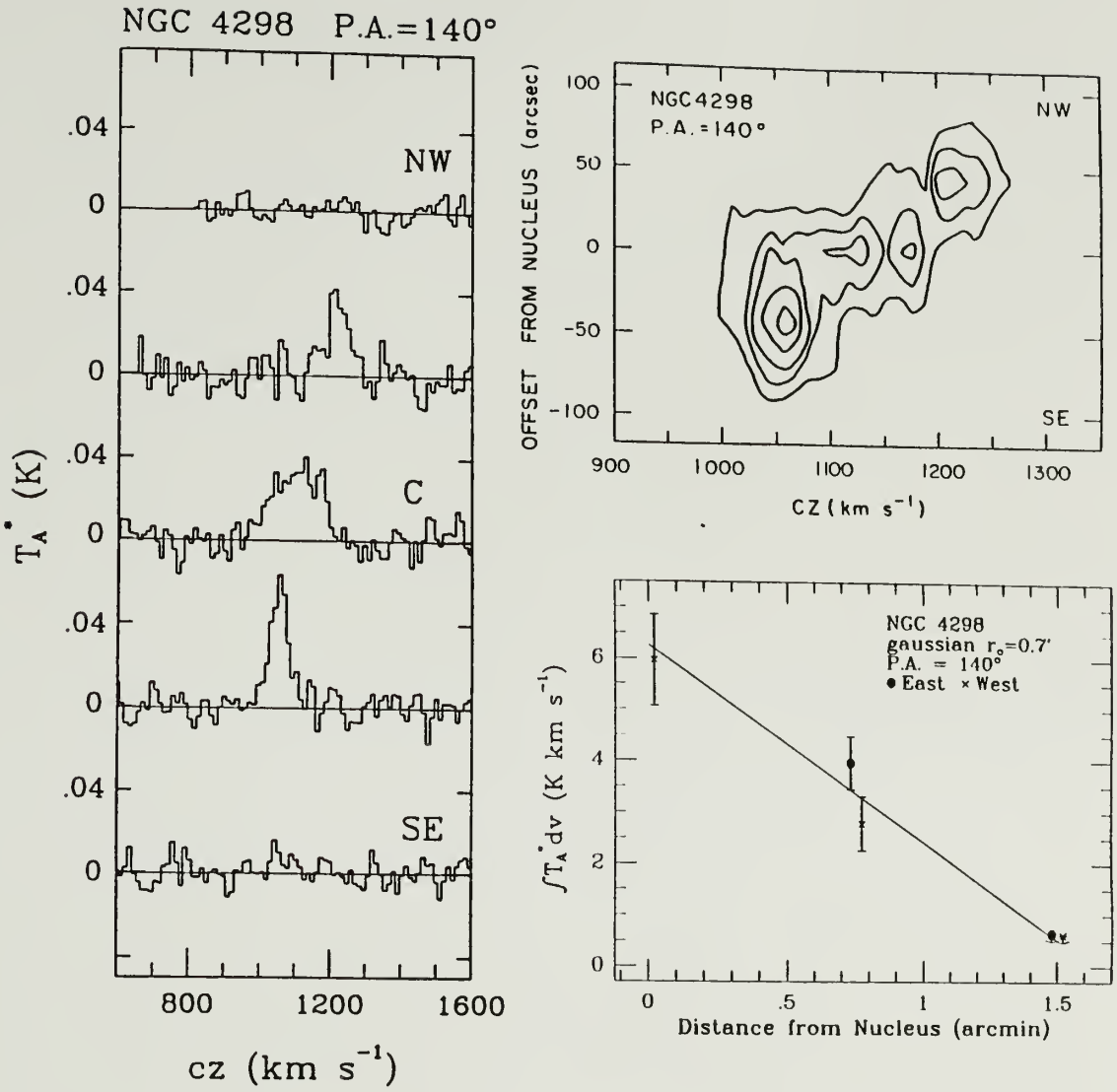

Figure 3.5 (a) CO spectra along major axis of NGC 4298, at intervals of 45". C denotes the spectrum obtained from the central position. (b) Spatial-velocity diagram for NGC 4298. Contour intervals are 10, 20, 30, 40 and 50 mK(T_A^*). (c) Radial distribution of observed CO integrated intensities for NGC 4298. The line through the data points represents the Gaussian-weighted model source which best fits the observations.

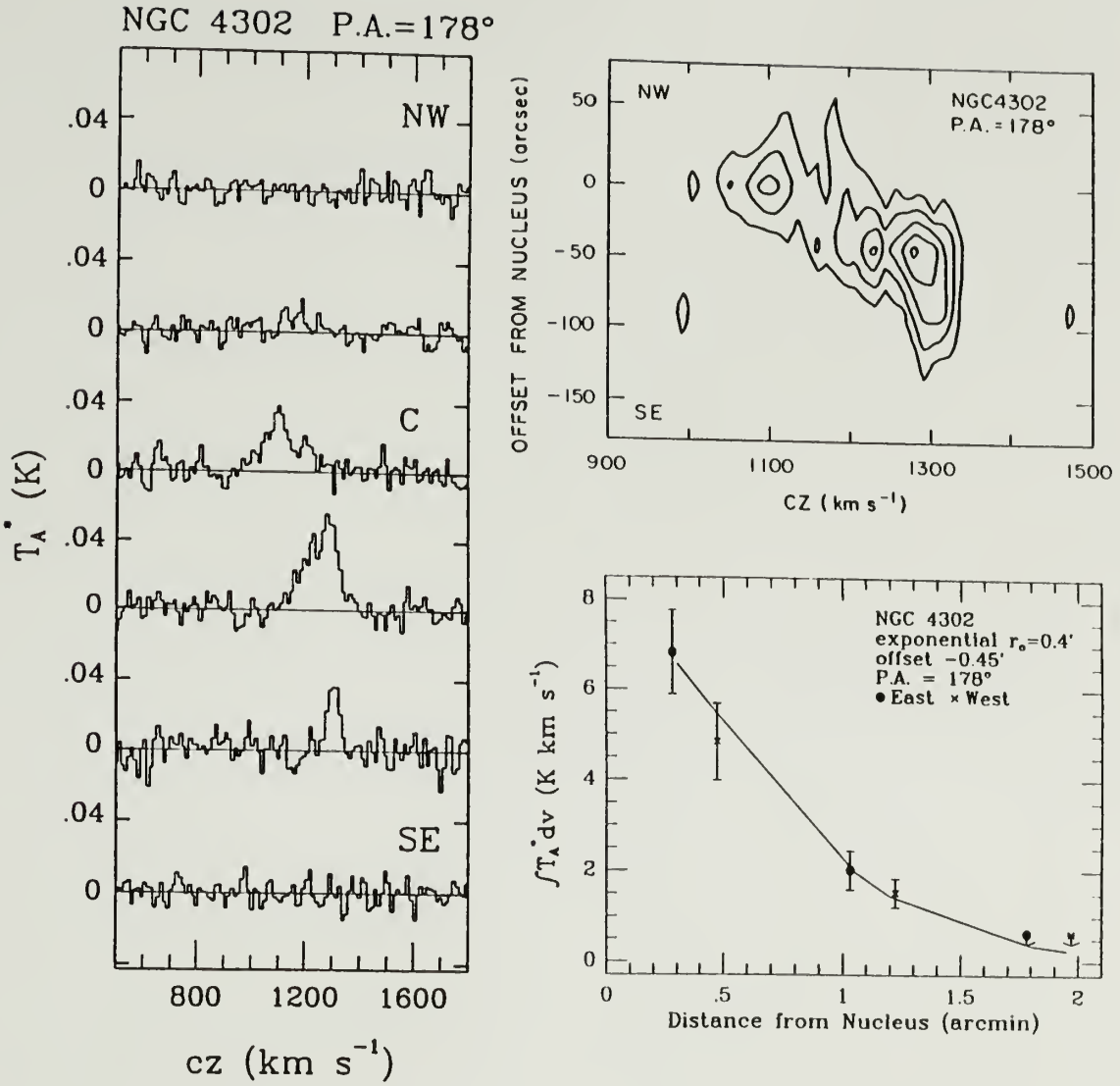

Figure 3.6 (a) CO spectra along major axis of NGC 4302, at intervals of 45". C denotes the spectrum obtained from the central position. (b) Spatial-velocity diagram for NGC 4302. Contour intervals are 10, 20, 30, 40 and 50 mK(T_A^*). (c) Radial distribution of observed CO integrated intensities for NGC 4302. The line through the data points represents the Gaussian-weighted model source which best fits the observations.

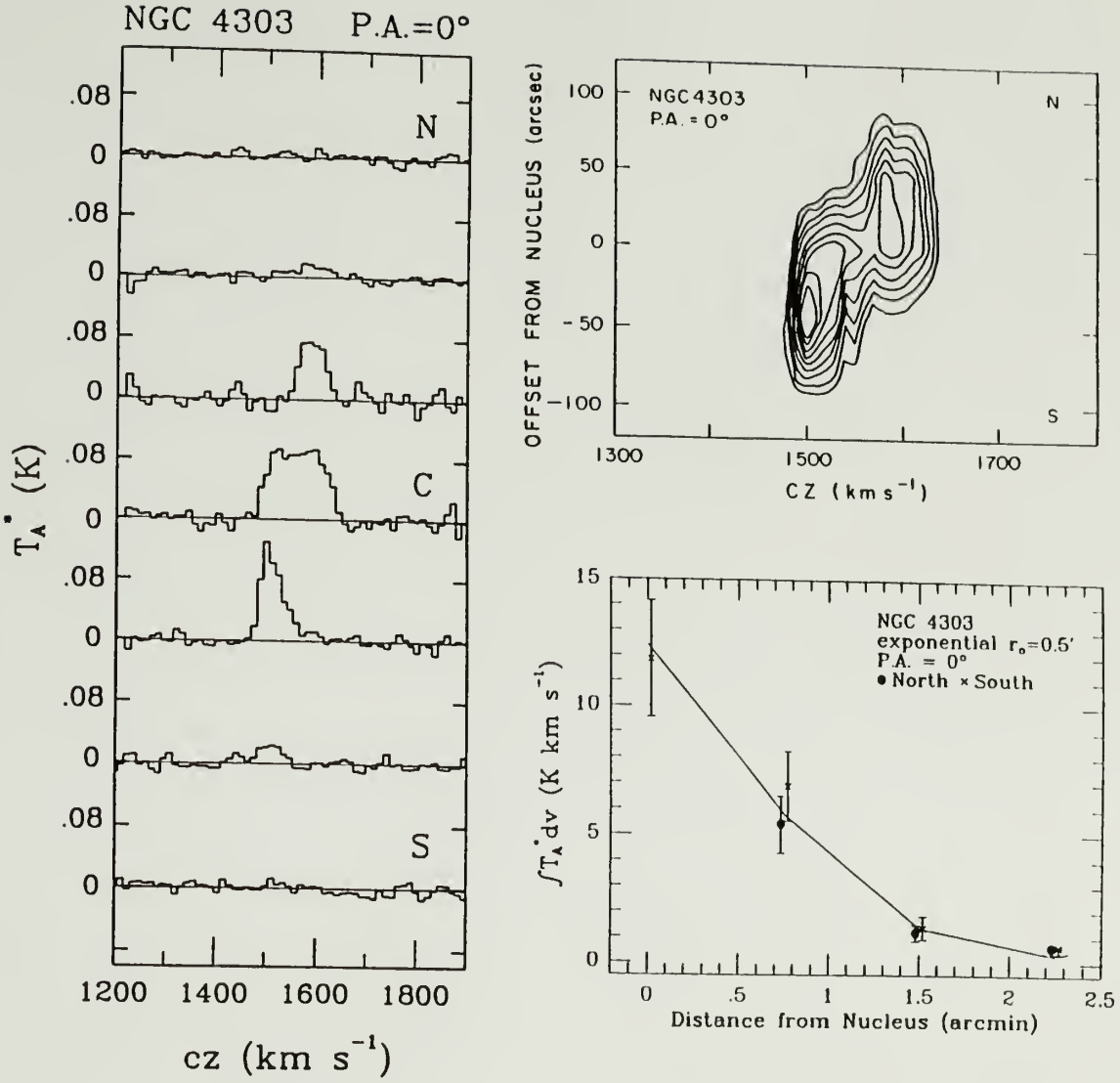

Figure 3.7 (a) CO spectra along major axis of NGC 4303, at intervals of 45". C denotes the spectrum obtained from the central position. (b) Spatial-velocity diagram for NGC 4303. Contour intervals are 20, 30, 40, 50, 60, 70, 80, 90 and 100 mK(T_A^*). (c) Radial distribution of observed CO integrated intensities for NGC 4303. The line through the data points represents the Gaussian-weighted model source which best fits the observations.

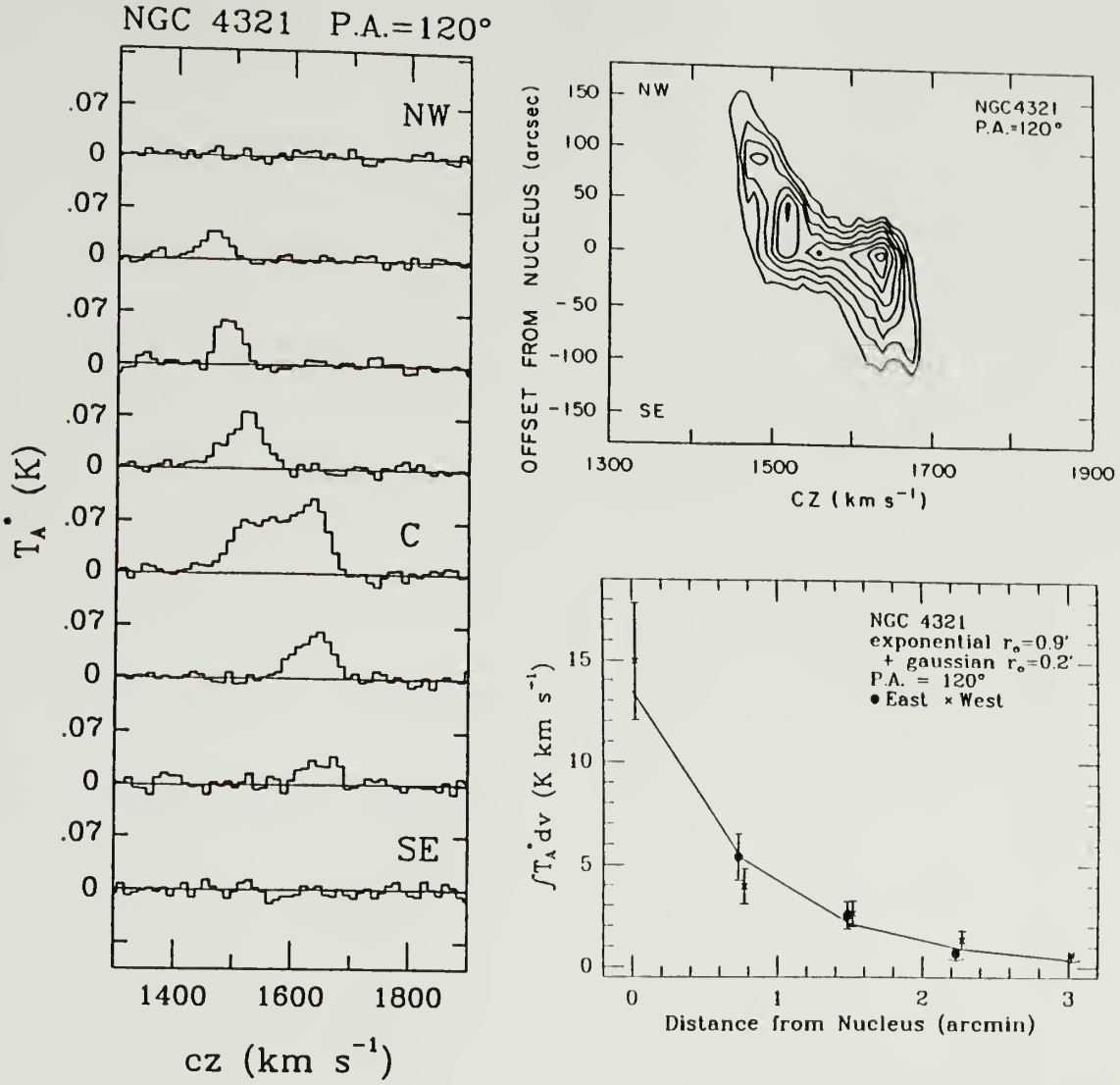

Figure 3.8 (a) CO spectra along major axis of NGC 4321, at intervals of 45". C denotes the spectrum obtained from the central position. (b) Spatial-velocity diagram for NGC 4321. Contour intervals are 20, 30, 40, 50, 60, 70, 80 and 90 mK(T_A^*). (c) Radial distribution of observed CO integrated intensities for NGC 4321. The line through the data points represents the Gaussian-weighted model source which best fits the observations.

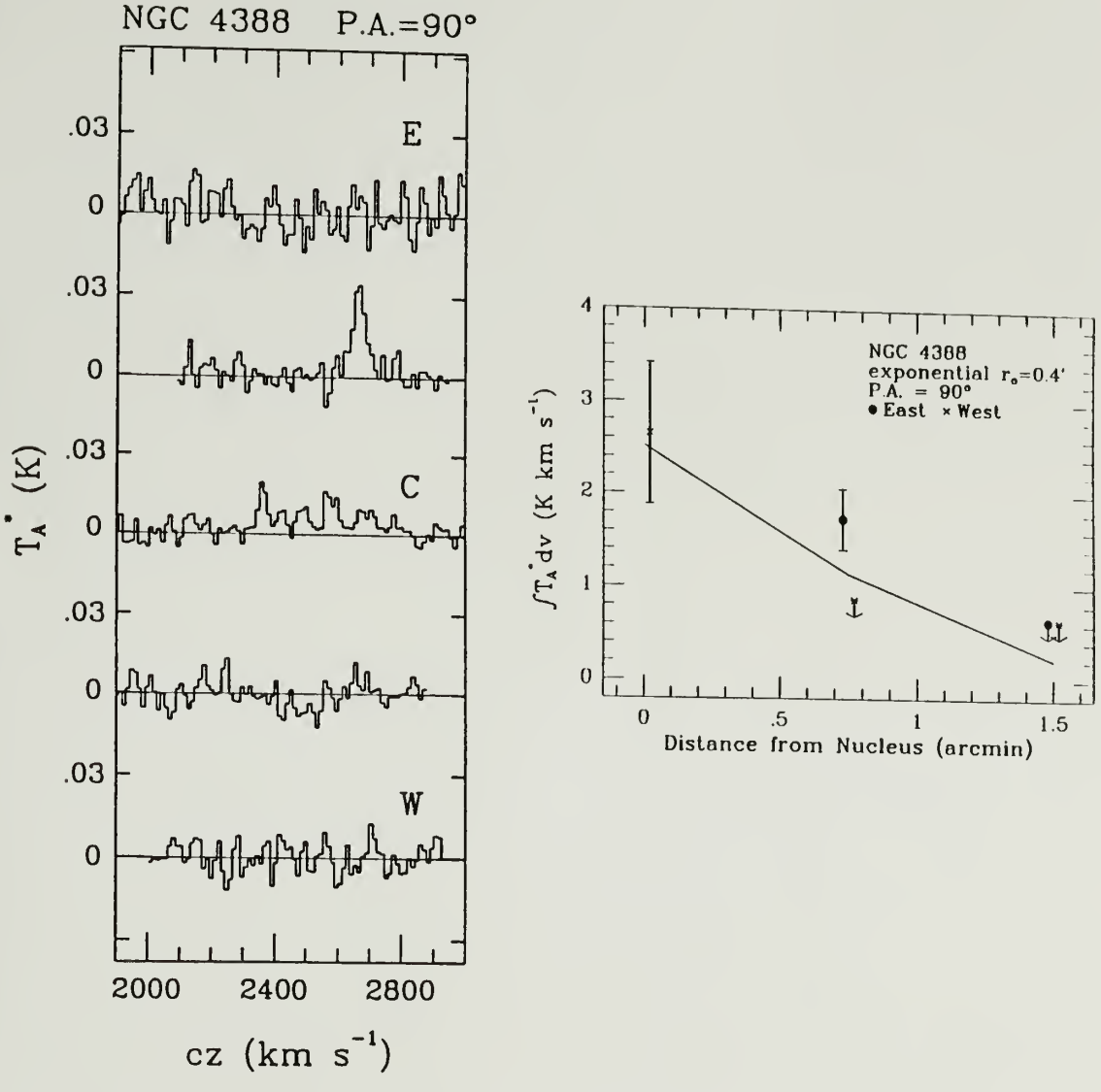

Figure 3.9 (a) CO spectra along major axis of NGC 4388 at intervals of 45". C denotes the spectrum obtained from the central position. (b) Radial distribution of observed CO integrated intensities for NGC 4388. The line through the data points represents the Gaussian-weighted model source which best fits the observations.

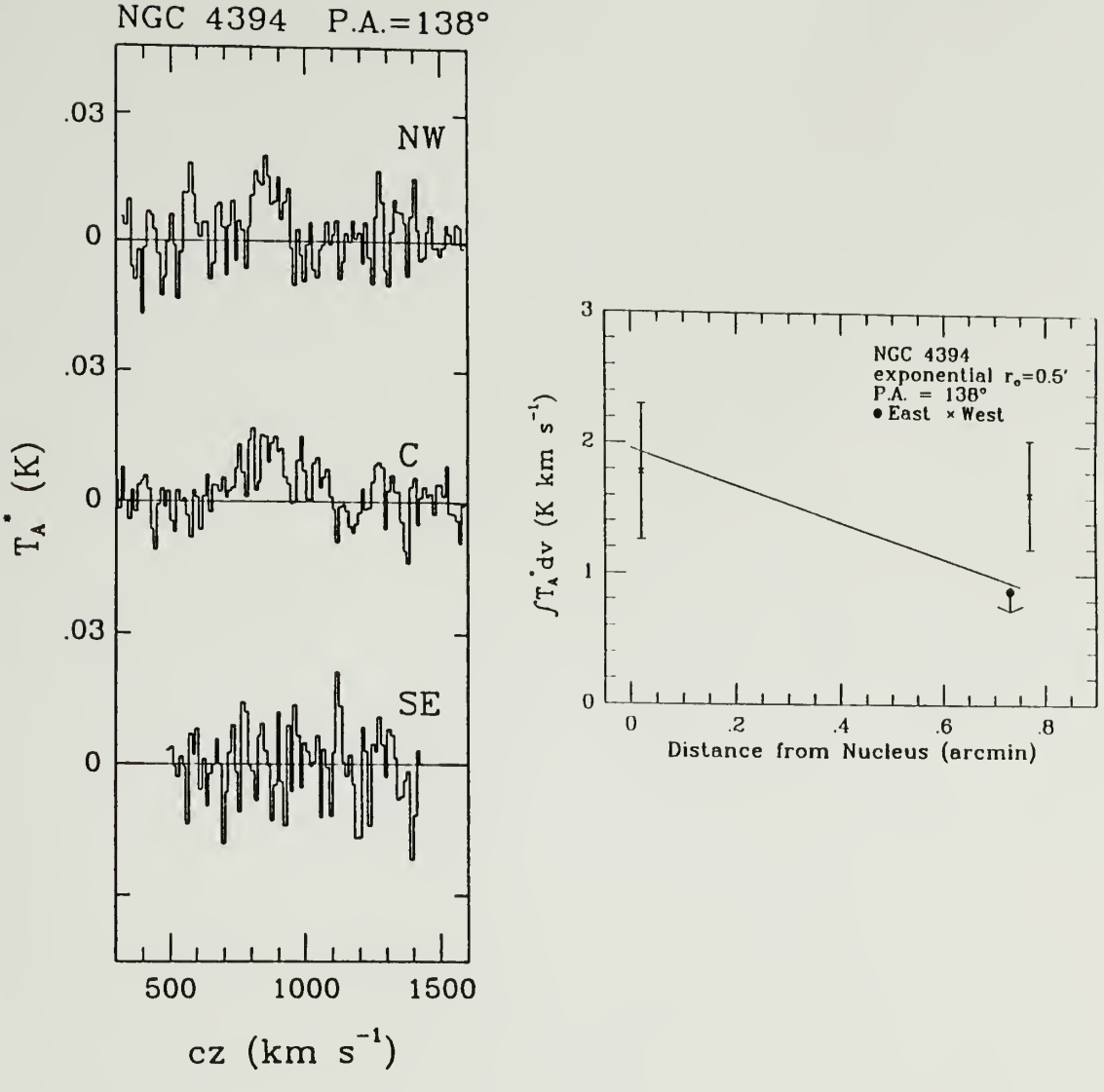

Figure 3.10 (a) CO spectra along major axis of NGC 4394, at intervals of 45". C denotes the spectrum obtained from the central position. (b) Radial distribution of observed CO integrated intensities for NGC 4394. The line through the data points represents the Gaussian-weighted model source which best fits the observations.

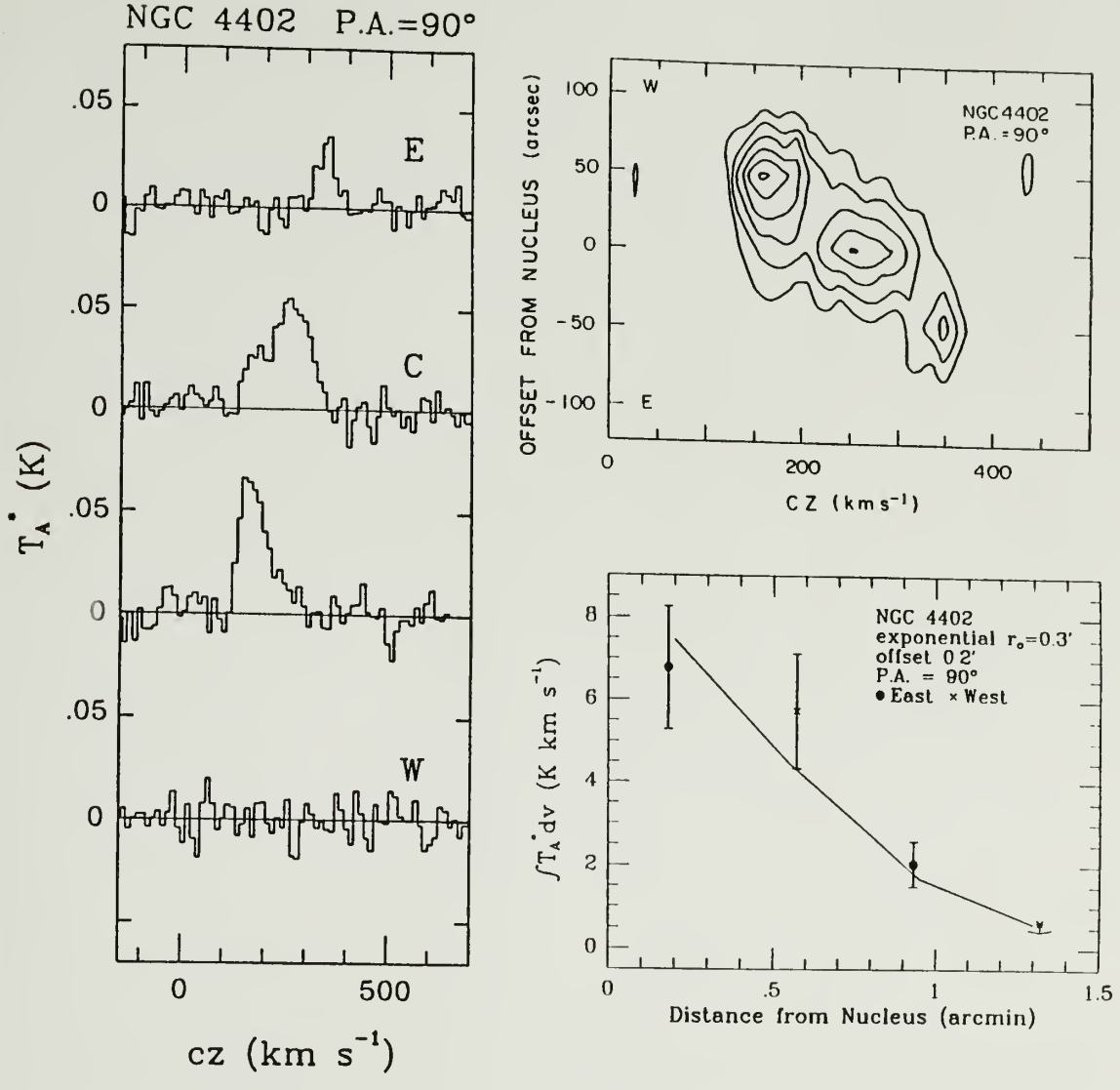

Figure 3.11 (a) CO spectra along major axis of NGC 4402, at intervals of 45". C denotes the spectrum obtained from the central position. (b) Spatial-velocity diagram for NGC 4402. Contour intervals are 10, 20, 30, 40, 50 and 60 mK(T_A^*). (c) Radial distribution of observed CO integrated intensities for NGC 4402. The line through the data points represents the Gaussian-weighted model source which best fits the observations.

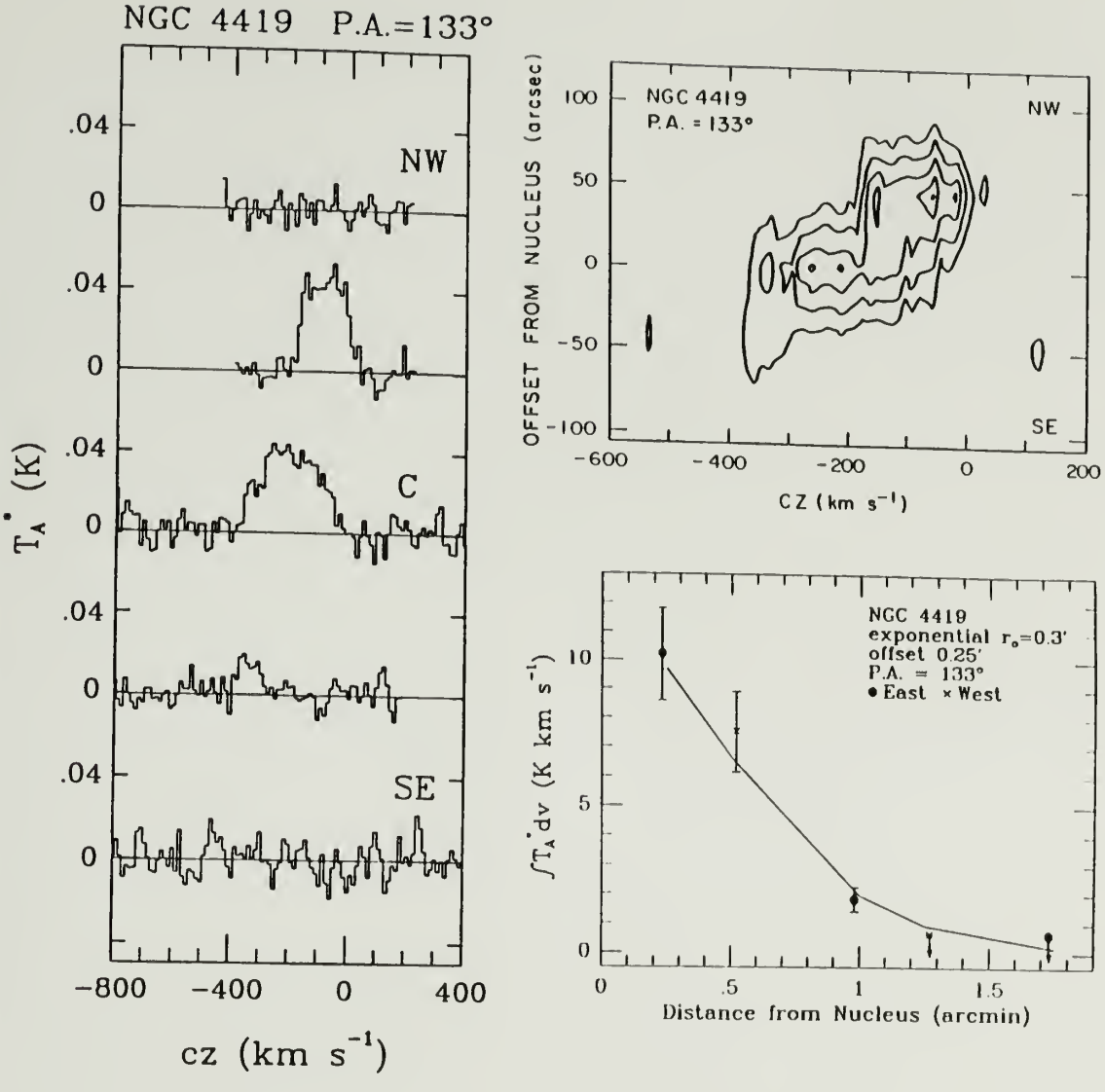

Figure 3.12 (a) CO spectra along major axis of NGC 4419, at intervals of 45". C denotes the spectrum obtained from the central position. (b) Spatial-velocity diagram for NGC 4419. Contour intervals are 10, 20, 30, 40 and 50 mK(T_A^*). (c) Radial distribution of observed CO integrated intensities for NGC 4419. The line through the data points represents the Gaussian-weighted model source which best fits the observations.

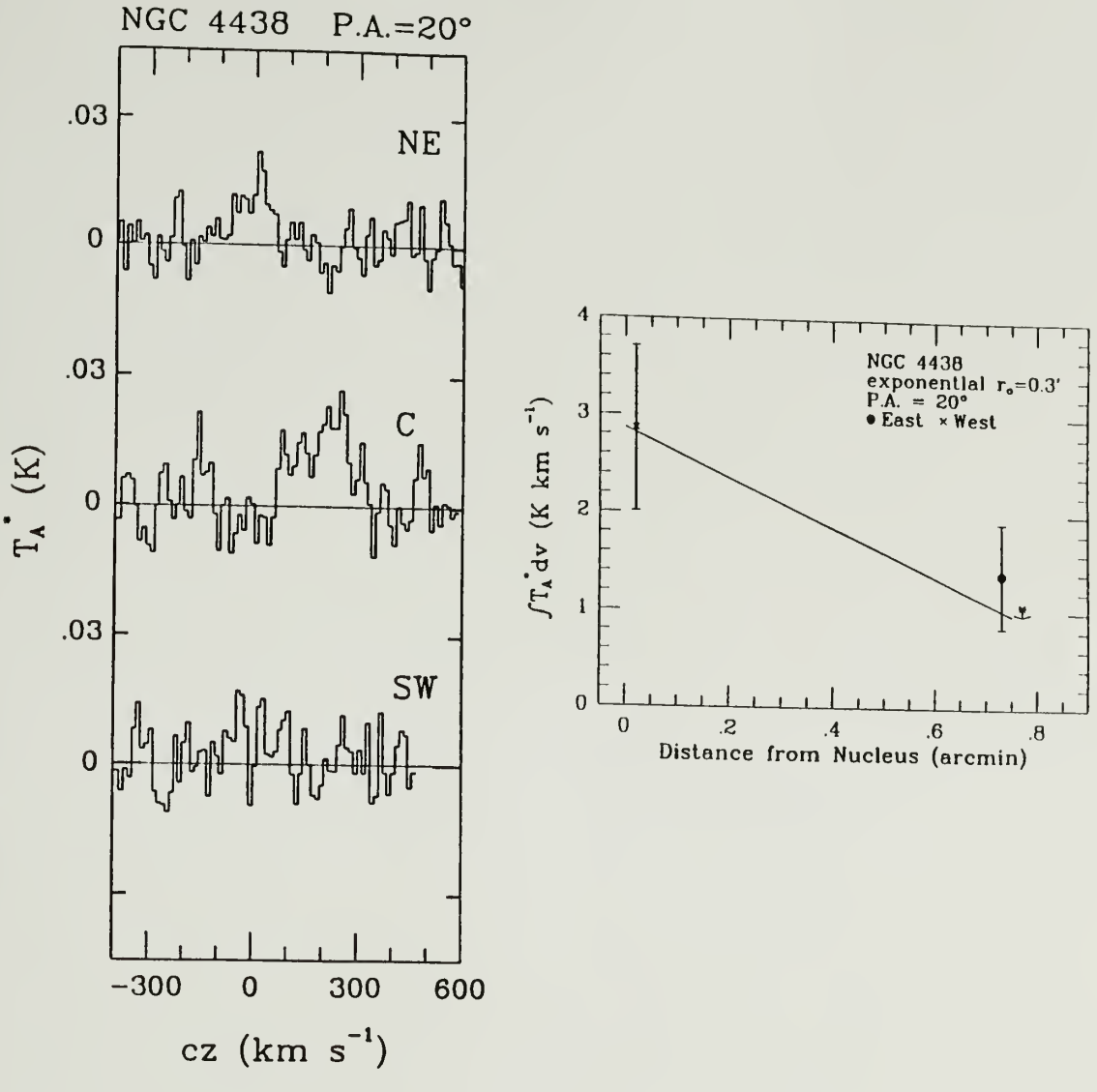

Figure 3.13 (a) CO spectra along major axis of NGC 4438, at intervals of 45". C denotes the spectrum obtained from the central position. (b) Radial distribution of observed CO integrated intensities for NGC 4438. The line through the data points represents the Gaussian-weighted model source which best fits the observations.

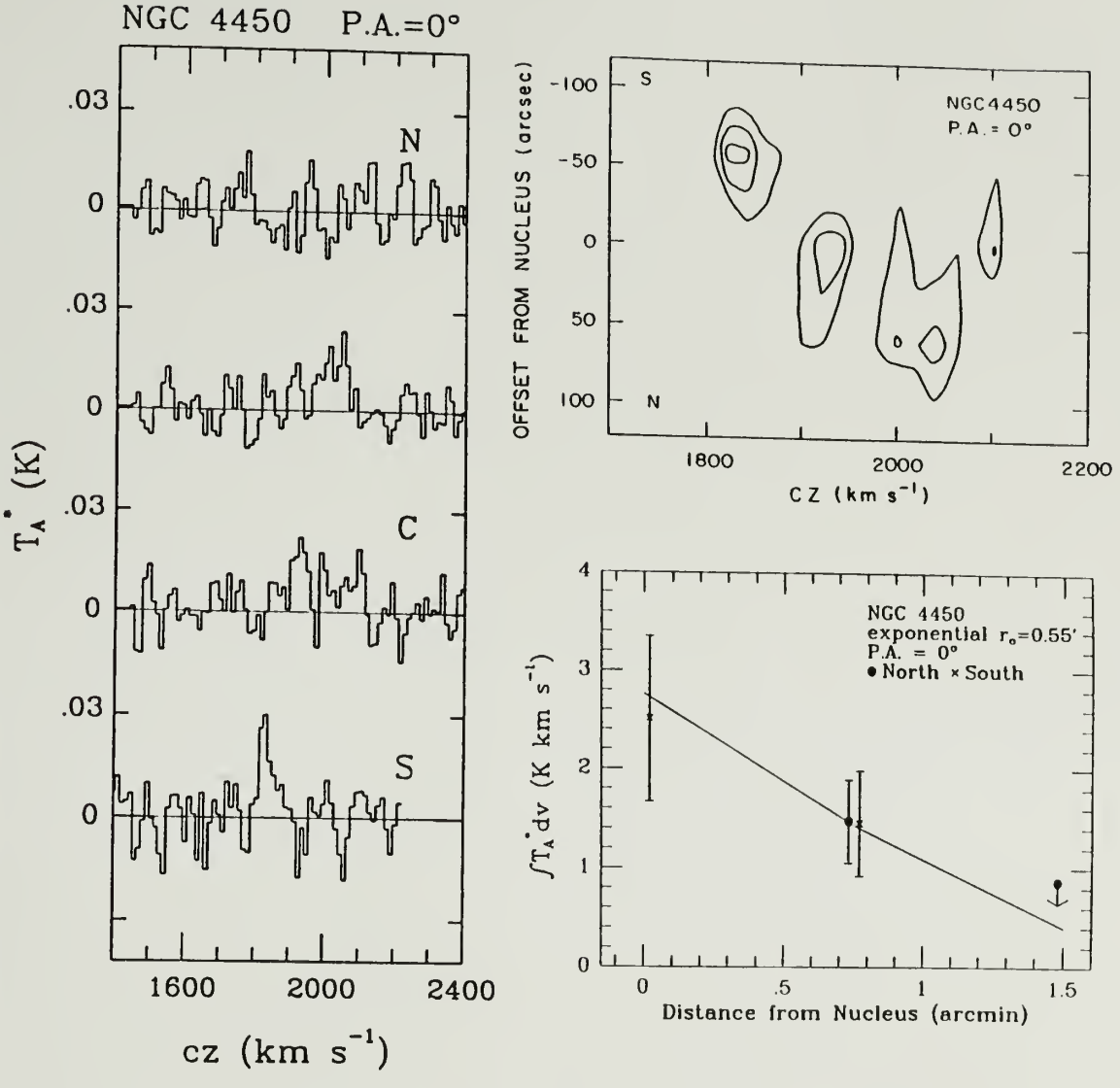

Figure 3.14 (a) CO spectra along major axis of NGC 4450, at intervals of 45". C denotes the spectrum obtained from the central position. (b) Spatial-velocity diagram for NGC 4450. Contour intervals are 8, 13 and 18 mK(T_A^*). (c) Radial distribution of observed CO integrated intensities for NGC 4450. The line through the data points represents the Gaussian-weighted model source which best fits the observations.

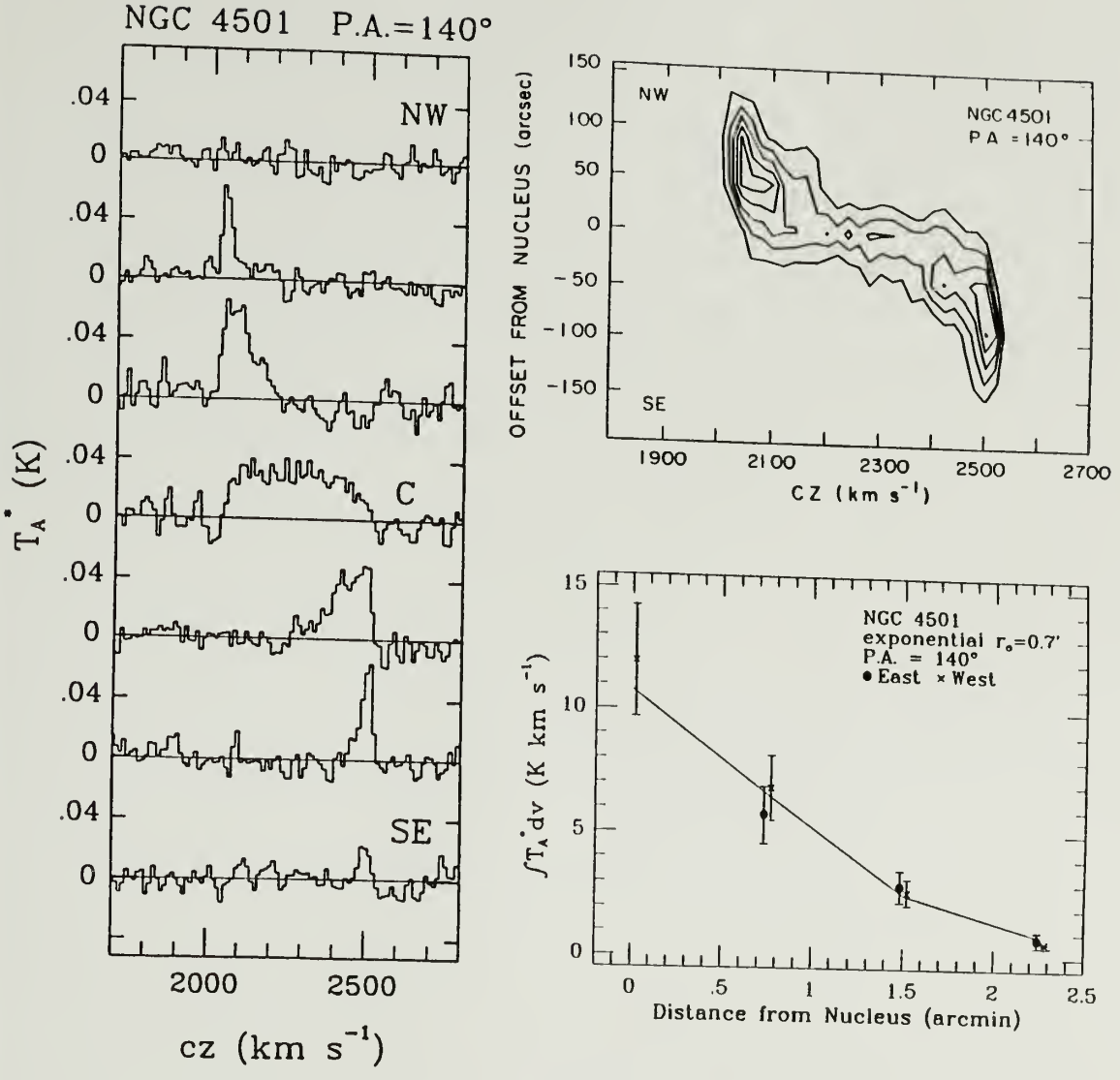

Figure 3.15 (a) CO spectra along major axis of NGC 4501, at intervals of 45". C denotes the spectrum obtained from the central position. (b) Spatial-velocity diagram for NGC 4501. Contour intervals are 10, 20, 30, 40 and 50 mK(T_A^*). (c) Radial distribution of observed CO integrated intensities for NGC 4501. The line through the data points represents the Gaussian-weighted model source which best fits the observations.

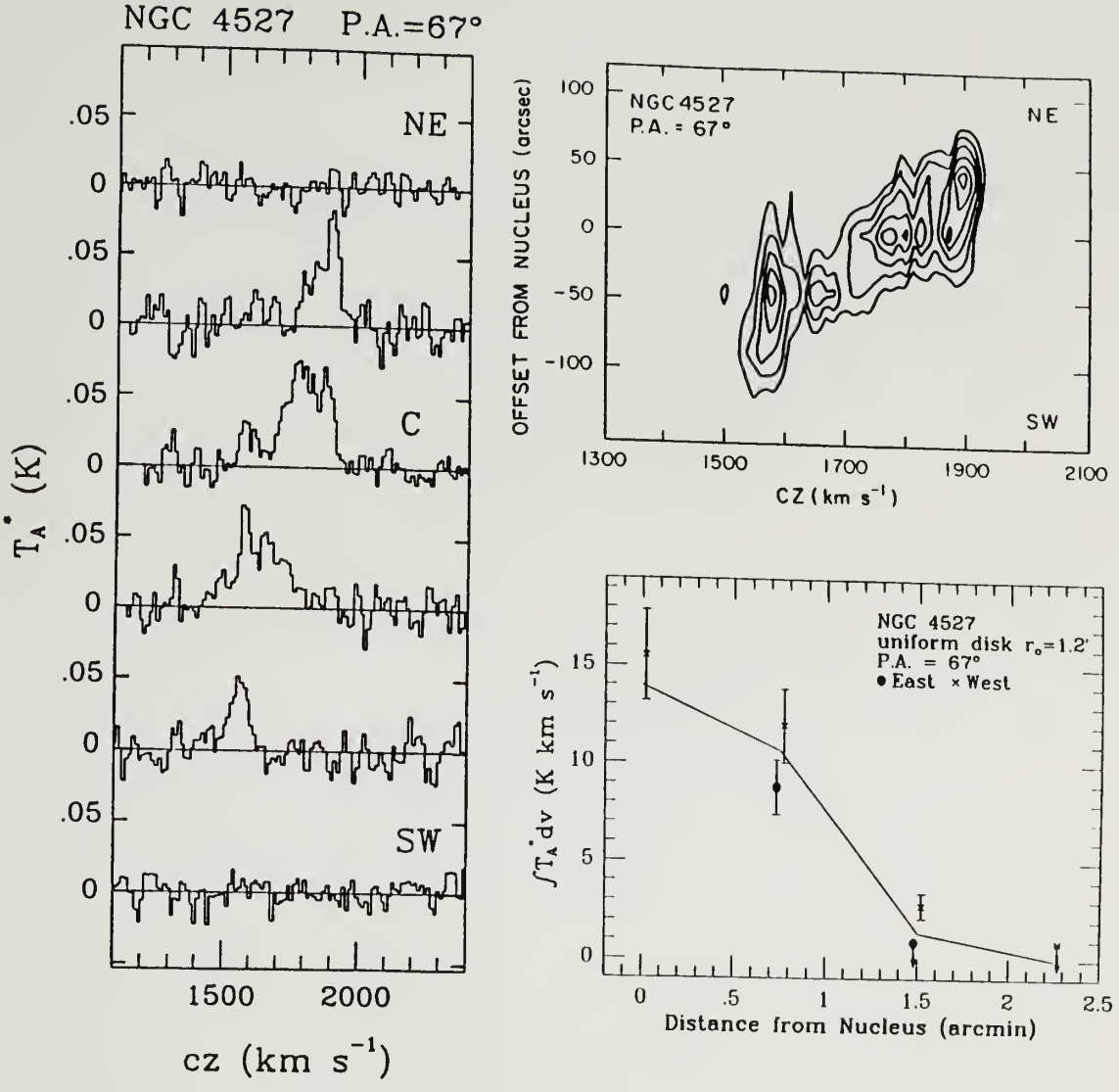

Figure 3.16 (a) CO spectra along major axis of NGC 4527, at intervals of 45". C denotes the spectrum obtained from the central position. (b) Spatial-velocity diagram for NGC 4527. Contour intervals are 20, 30, 40, 50 and 60 mK(T_A^*). (c) Radial distribution of observed CO integrated intensities for NGC 4527. The line through the data points represents the Gaussian-weighted model source which best fits the observations.

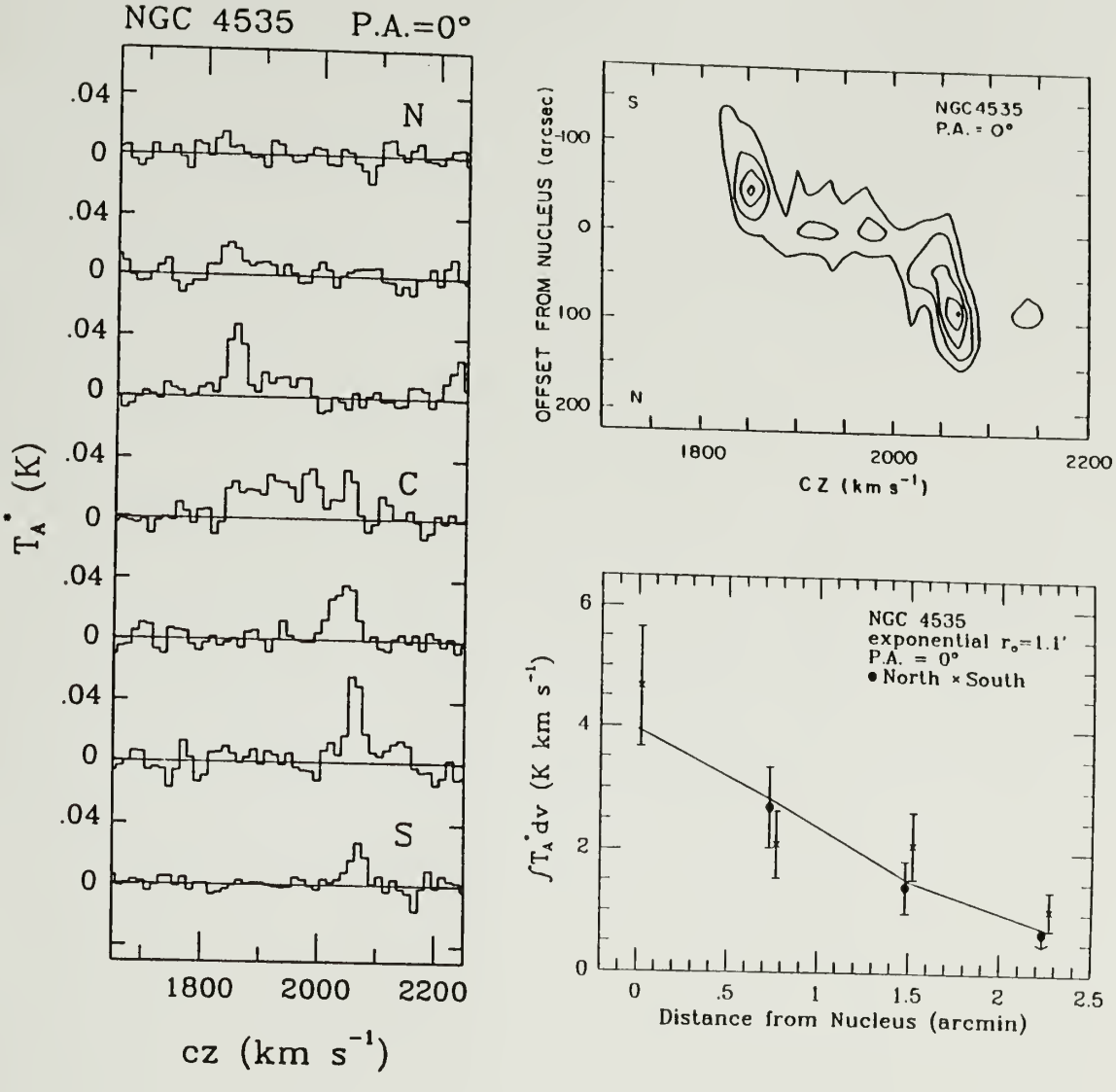

Figure 3.17 (a) CO spectra along major axis of NGC 4535, at intervals of 45". C denotes the spectrum obtained from the central position. (b) Spatial-velocity diagram for NGC 4535. Contour intervals are 10, 20, 30, 40 and 50 mK(T_A^*). (c) Radial distribution of observed CO integrated intensities for NGC 4535. The line through the data points represents the Gaussian-weighted model source which best fits the observations.

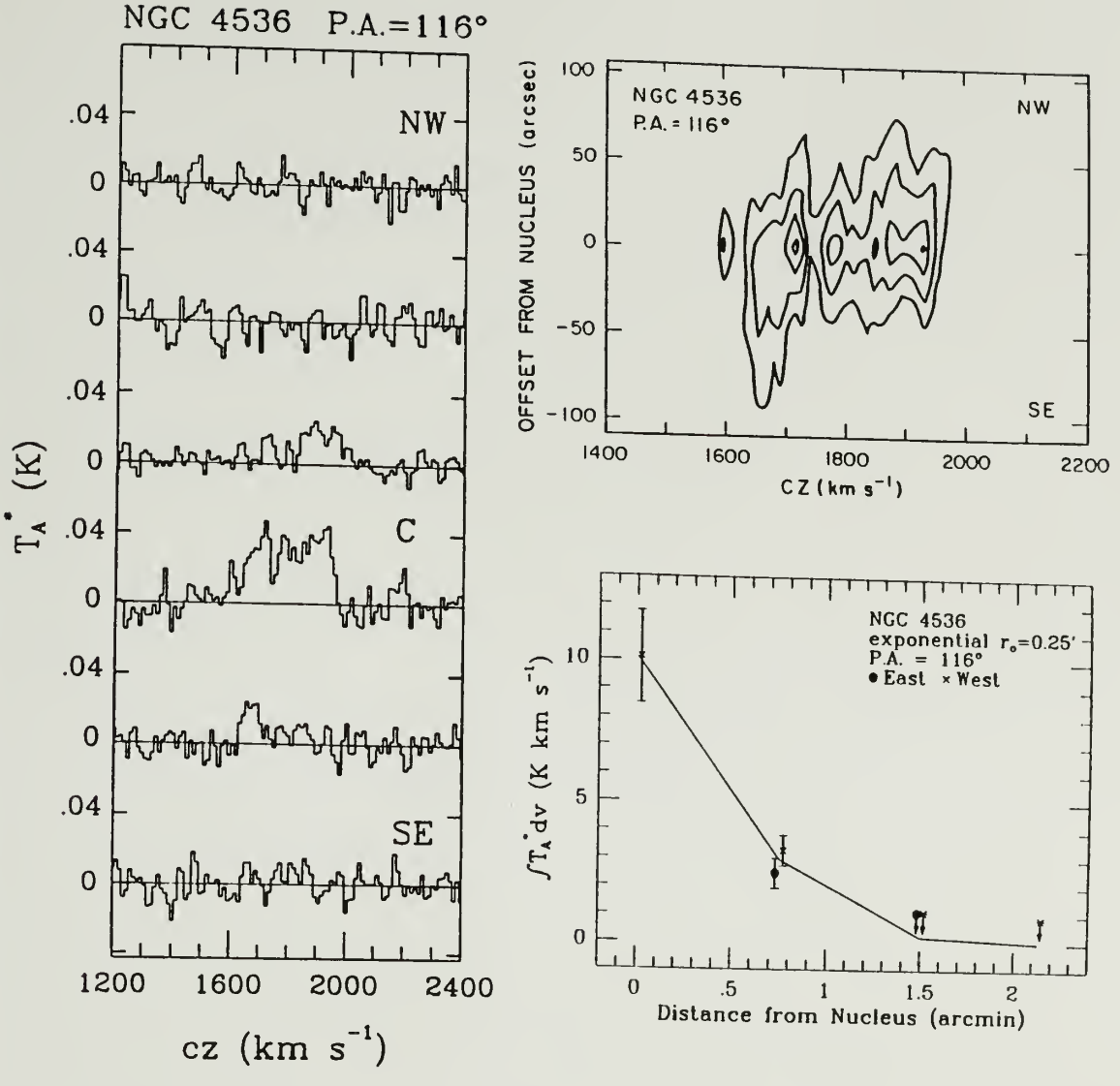

Figure 3.18 (a) CO spectra along major axis of NGC 4536, at intervals of 45". C denotes the spectrum obtained from the central position. (b) Spatial-velocity diagram for NGC 4536. Contour intervals are 10, 20, 30 and 40 mK(T_A^*). (c) Radial distribution of observed CO integrated intensities for NGC 4536. The line through the data points represents the Gaussian-weighted model source which best fits the observations.

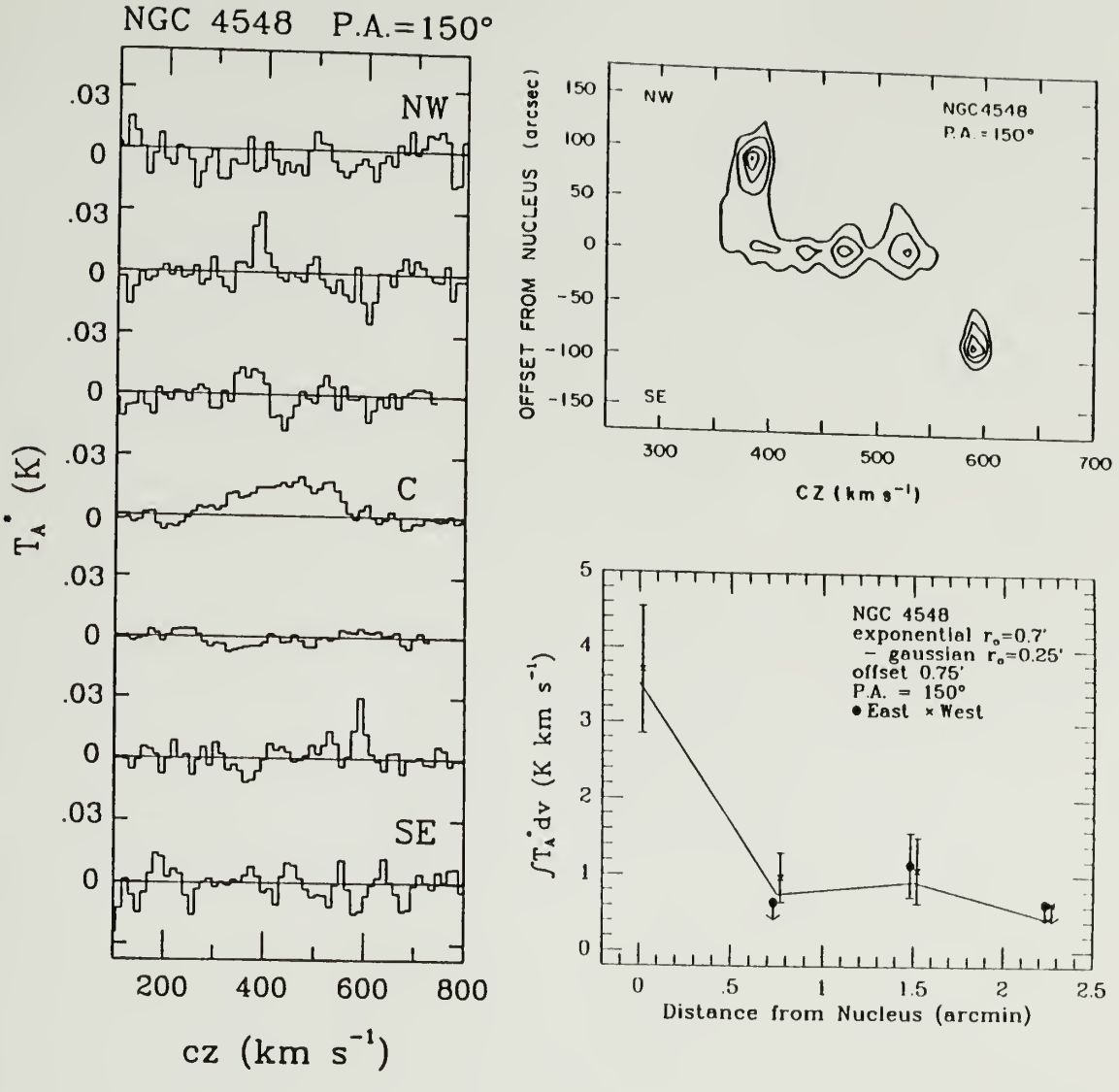

Figure 3.19 (a) CO spectra along major axis of NGC 4548, at intervals of 45". C denotes the spectrum obtained from the central position. (b) Spatial-velocity diagram for NGC 4548. Contour intervals are 10, 15, 20, 25 and 30 mK(T_A^*). (c) Radial distribution of observed CO integrated intensities for NGC 4548. The line through the data points represents the Gaussian-weighted model source which best fits the observations.

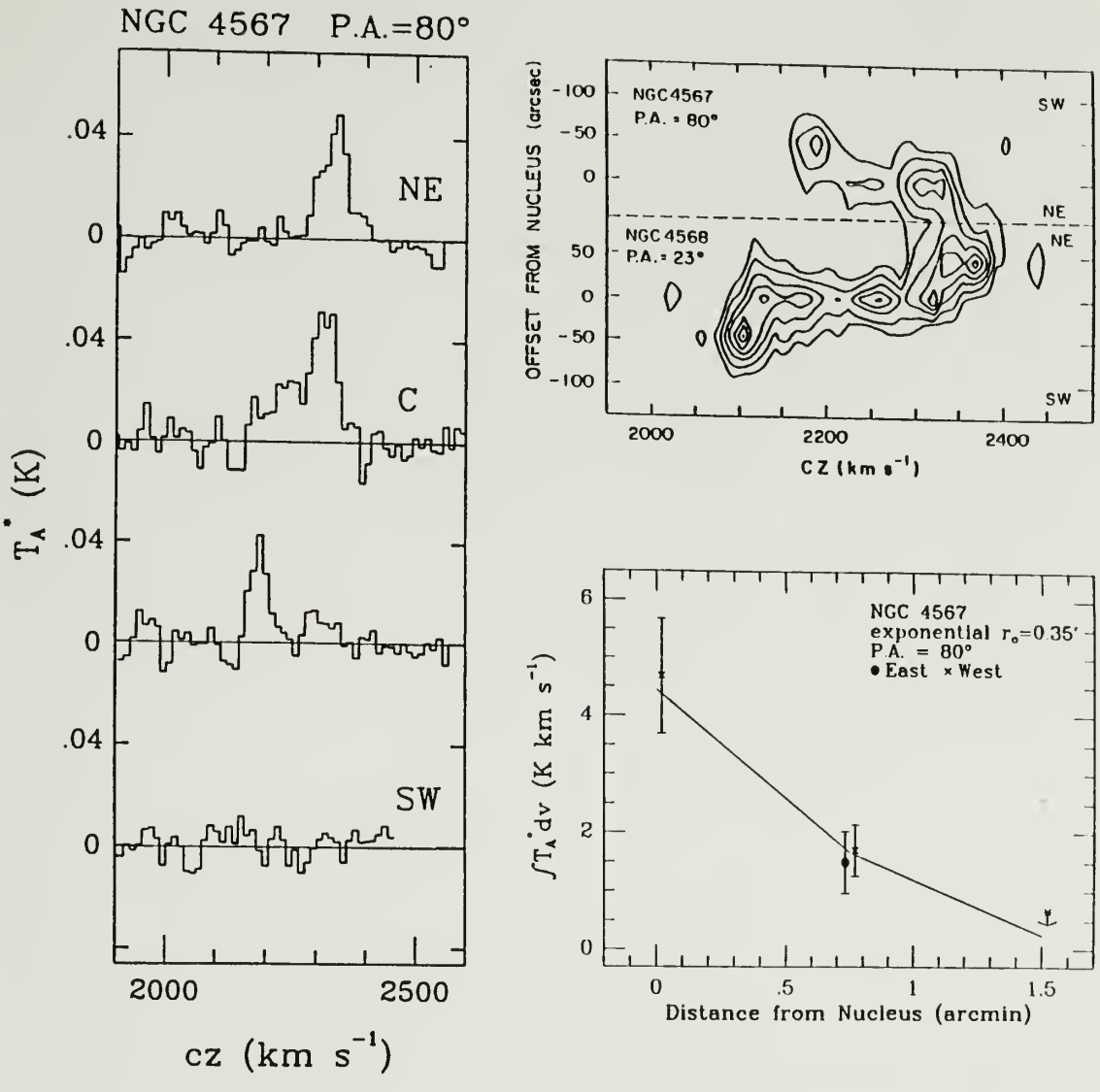

Figure 3.20 (a) CO spectra along major axis of NGC 4567, at intervals of 45". C denotes the spectrum obtained from the central position. The spectrum from the NE region is confused with emission from NGC 4568. (b) Spatial-velocity diagram for NGC 4567 and NGC 4568. Contour intervals are 10, 20, 30, 40, 50, 60 and 70 mK(T_A^*). (c) Radial distribution of observed CO integrated intensities for NGC 4567. The line through the data points represents the Gaussian-weighted model source which best fits the observations.

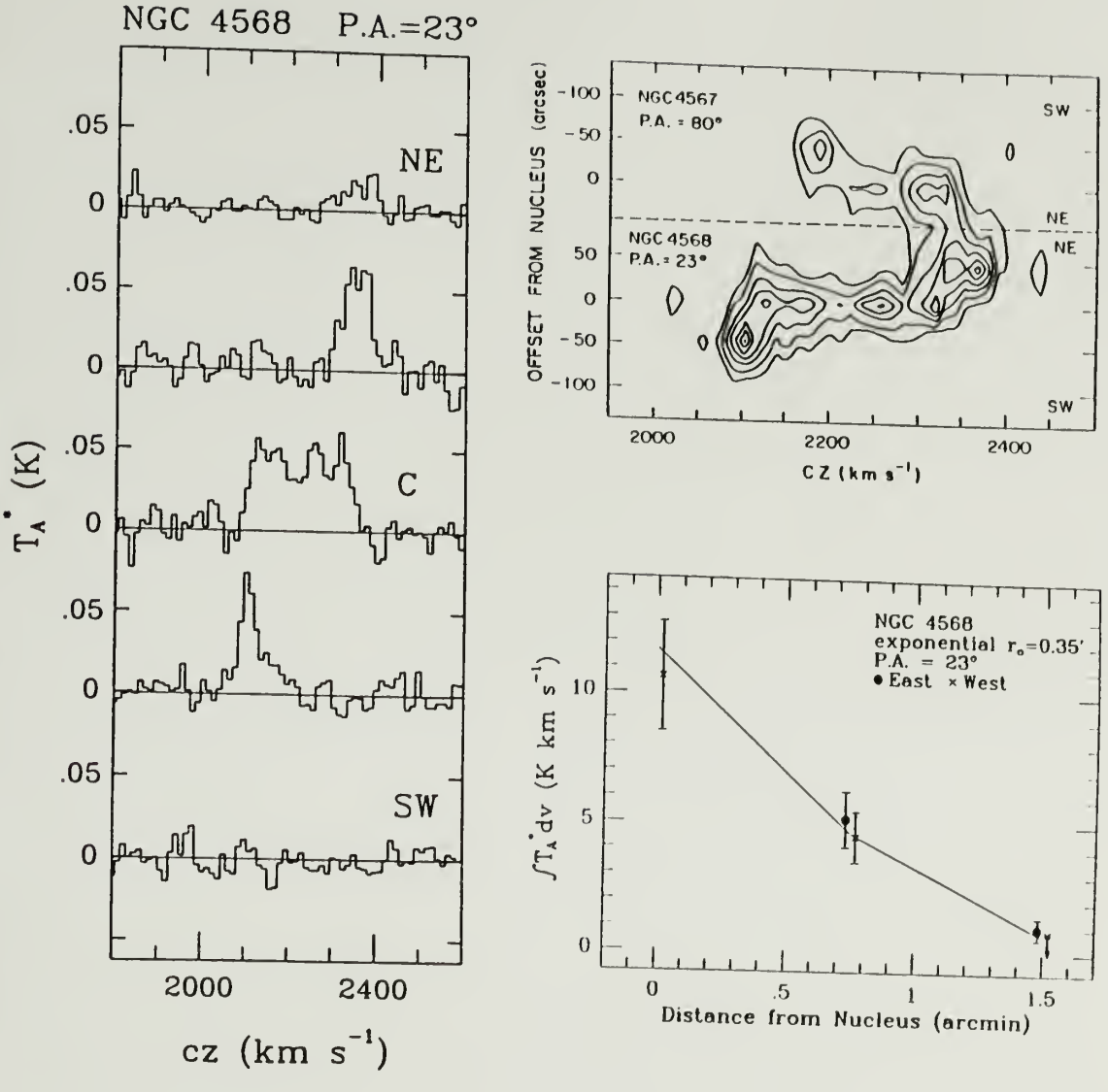

Figure 3.21 (a) CO spectra along major axis of NGC 4568, at intervals of 45". C denotes the spectrum obtained from the central position. The spectrum from the NE region is confused with emission from NGC 4567. (b) Spatial-velocity diagram for NGC 4567 and NGC 4568. Contour intervals are 10, 20, 30, 40, 50, 60 and 70 mK(T_A^*). (c) Radial distribution of observed CO integrated intensities for NGC 4568. The line through the data points represents the Gaussian-weighted model source which best fits the observations.

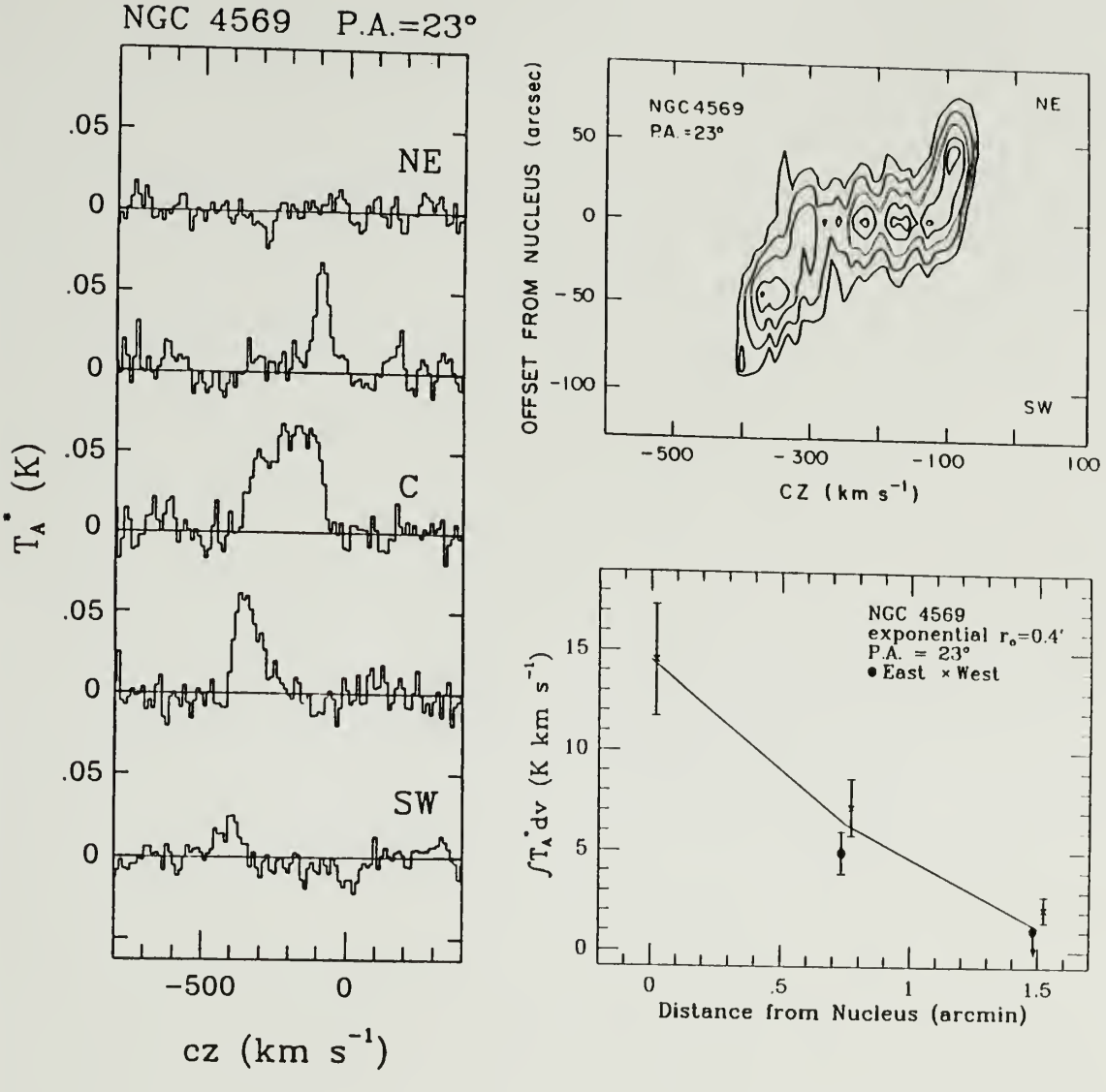

Figure 3.22 (a) CO spectra along major axis of NGC 4569, at intervals of 45". C denotes the spectrum obtained from the central position. (b) Spatial-velocity diagram for NGC 4569. Contour intervals are 20, 30, 40, 50 and 60 mK(T_A^*). (c) Radial distribution of observed CO integrated intensities for NGC 4569. The line through the data points represents the Gaussian-weighted model source which best fits the observations.

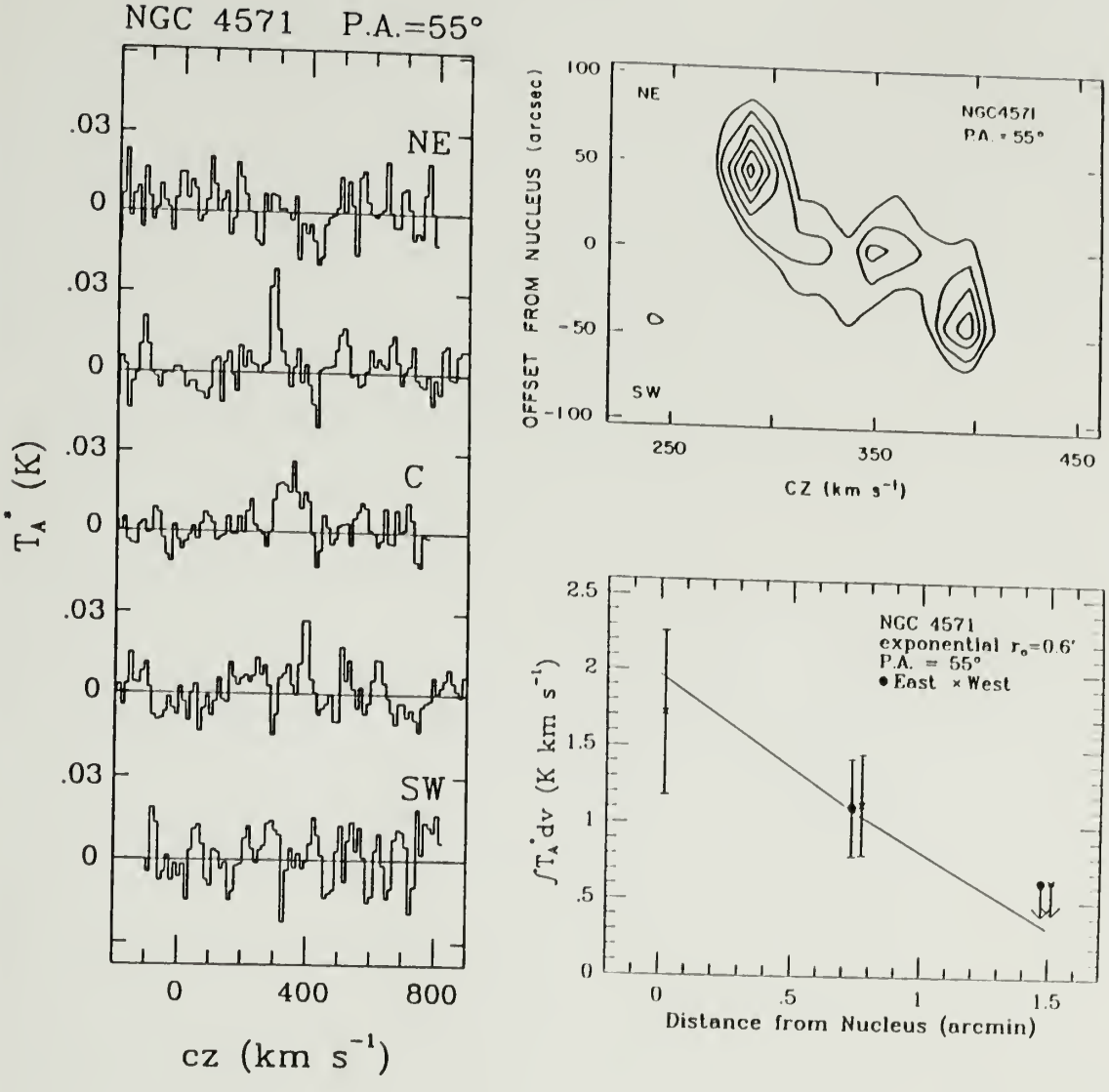

Figure 3.23 (a) CO spectra along major axis of NGC 4571, at intervals of 45". C denotes the spectrum obtained from the central position. (b) Spatial-velocity diagram for NGC 4571. Contour intervals are 10, 15, 20, 25, 30 and 35 mK(T_A^*). (c) Radial distribution of observed CO integrated intensities for NGC 4571. The line through the data points represents the Gaussian-weighted model source which best fits the observations.

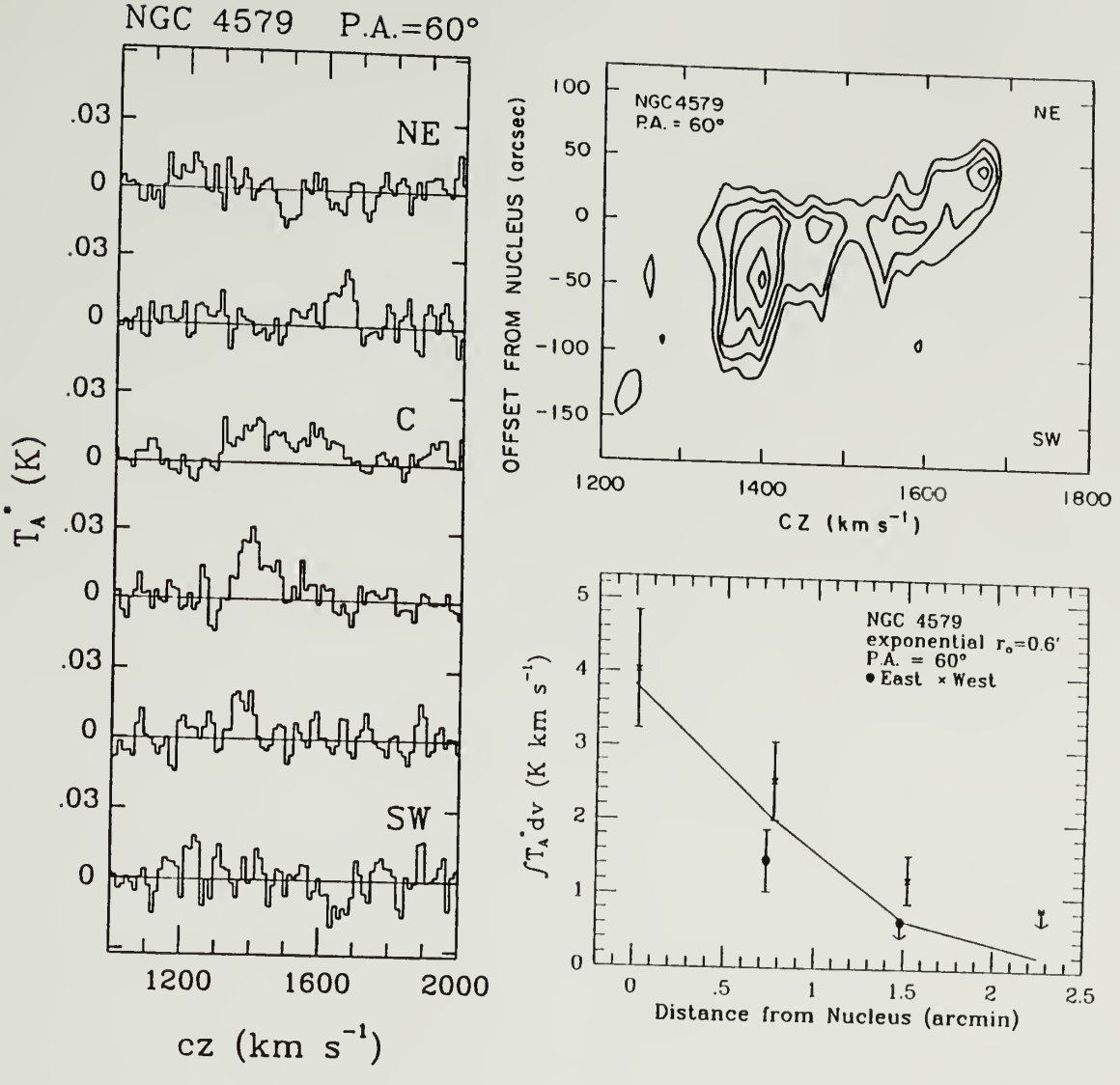

Figure 3.24 (a) CO spectra along major axis of NGC 4579, at intervals of 45". C denotes the spectrum obtained from the central position. (b) Spatial-velocity diagram for NGC 4579. Contour intervals are 10, 15, 20, 25, 30 and 35 mK(T_A^*). (c) Radial distribution of observed CO integrated intensities for NGC 4579. The line through the data points represents the Gaussian-weighted model source which best fits the observations.

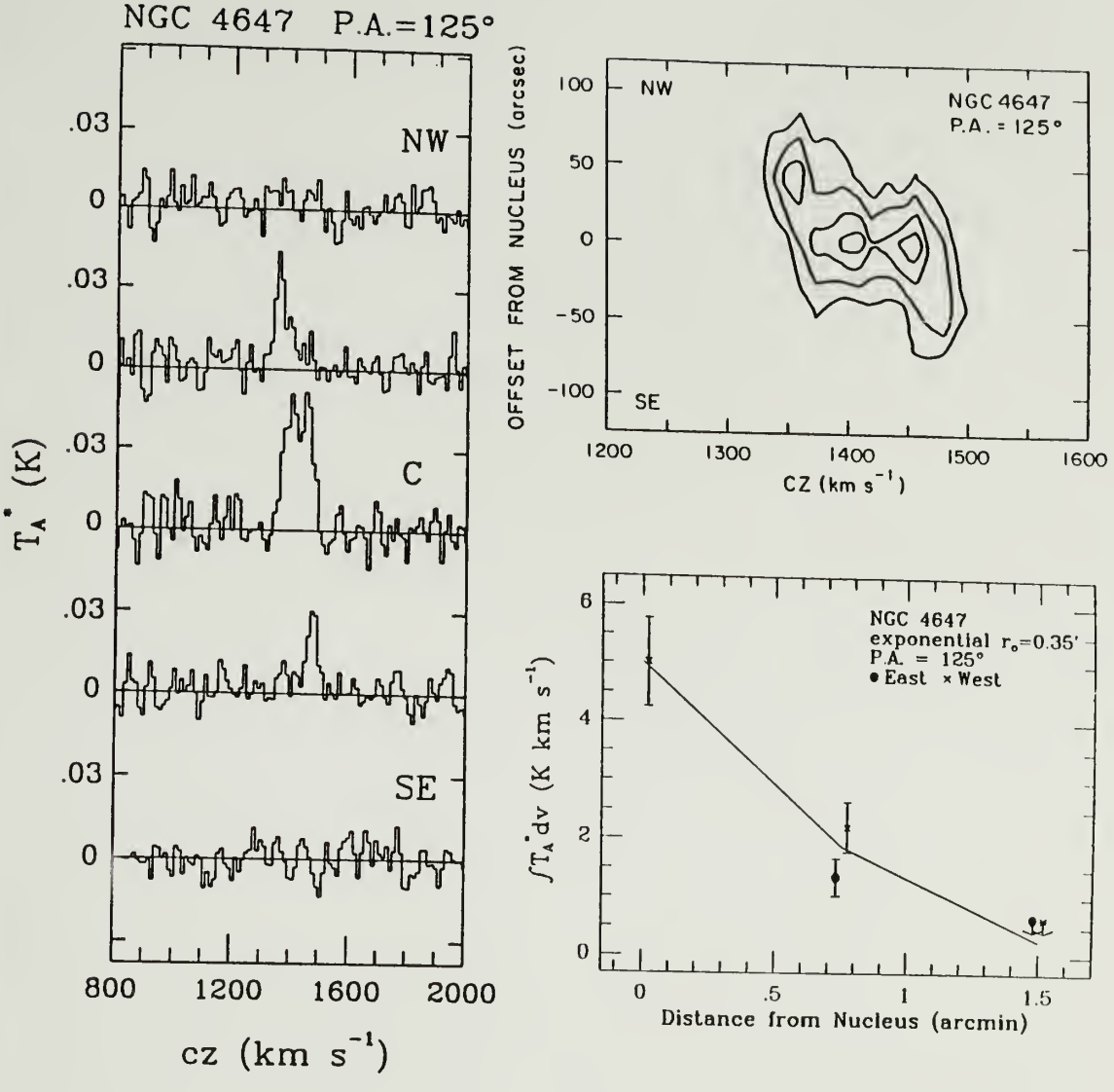

Figure 3.25 (a) CO spectra along major axis of NGC 4647, at intervals of 45". C denotes the spectrum obtained from the central position. (b) Spatial-velocity diagram for NGC 4647. Contour intervals are 10, 20, 30 and 40 mK(T_A^*). (c) Radial distribution of observed CO integrated intensities for NGC 4647. The line through the data points represents the Gaussian-weighted model source which best fits the observations.

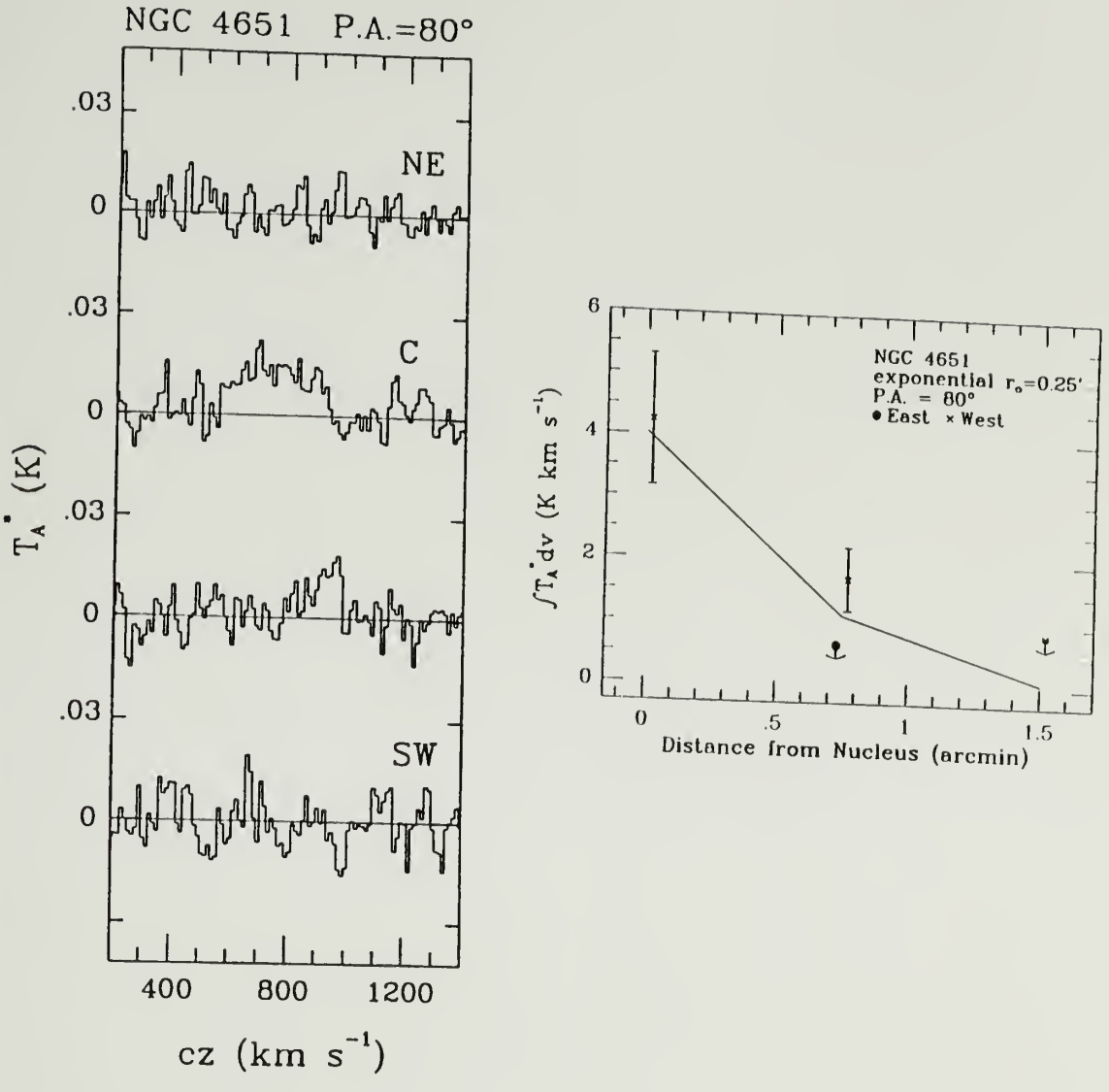

Figure 3.26 (a) CO spectra along major axis of NGC 4651, at intervals of 45". C denotes the spectrum obtained from the central position. (b) Radial distribution of observed CO integrated intensities for NGC 4651. The line through the data points represents the Gaussian-weighted model source which best fits the observations.

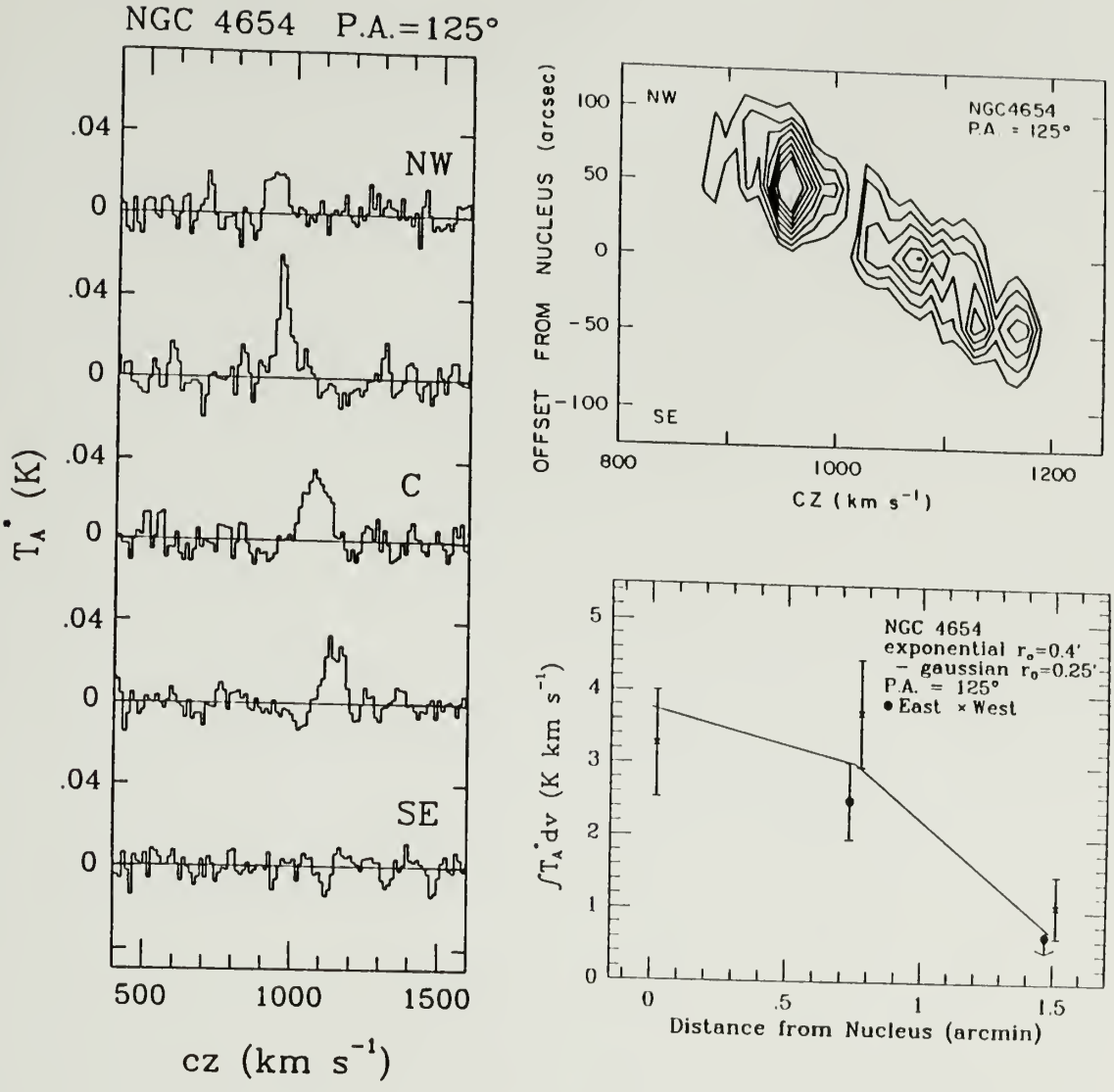

Figure 3.27 (a) CO spectra along major axis of NGC 4654, at intervals of 45". C denotes the spectrum obtained from the central position. (b) Spatial-velocity diagram for NGC 4654. Contour intervals are 10, 15, 20, 25, 30, 35, 40 and 45 mK(T_A^*). (c) Radial distribution of observed CO integrated intensities for NGC 4654. The line through the data points represents the Gaussian-weighted model source which best fits the observations.

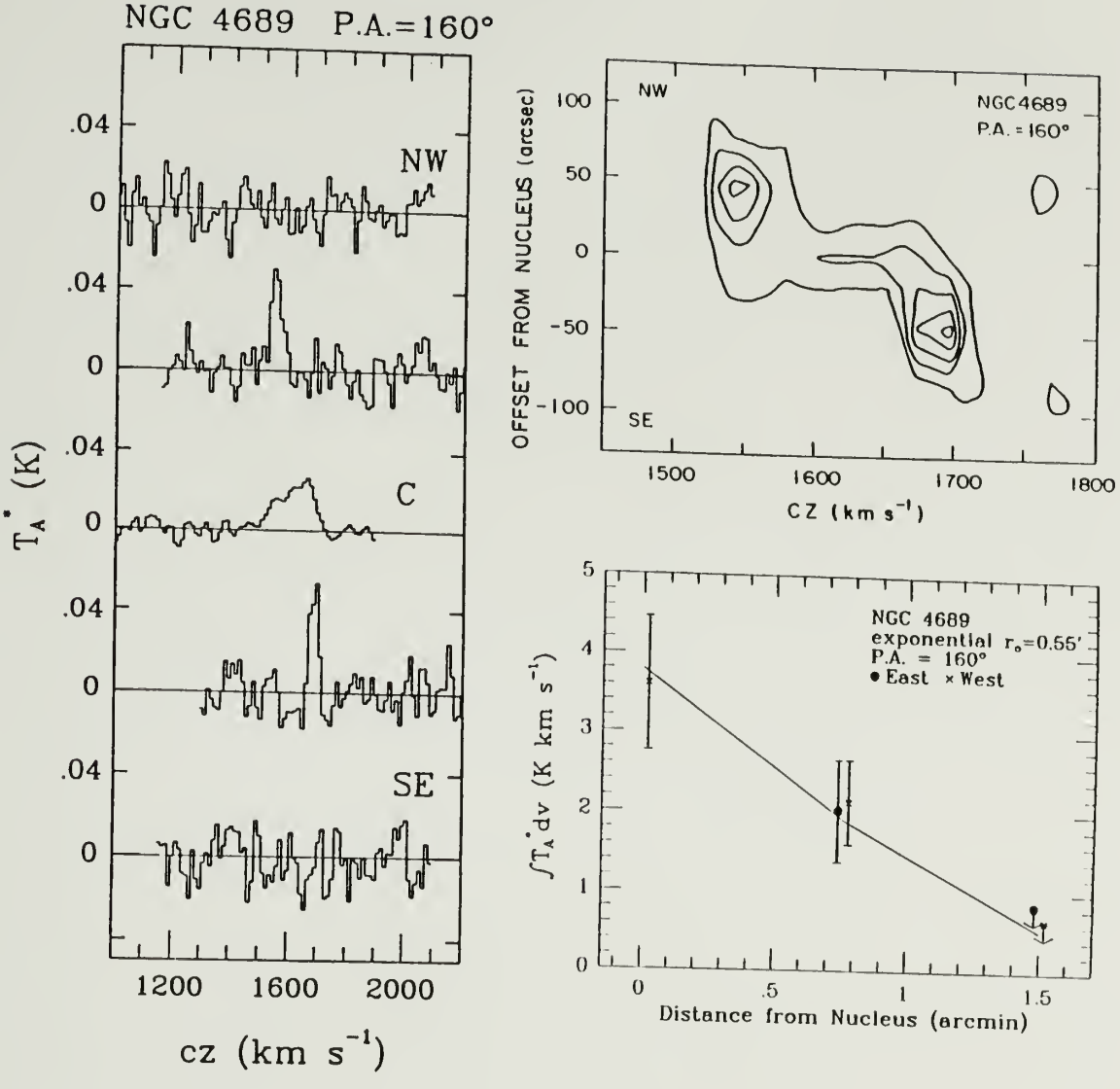

Figure 3.28 (a) CO spectra along major axis of NGC 4689, at intervals of 45". C denotes the spectrum obtained from the central position. (b) Spatial-velocity diagram for NGC 4689. Contour intervals are 10, 20, 30, 40 and 50 mK(T_A^*). (c) Radial distribution of observed CO integrated intensities for NGC 4689. The line through the data points represents the Gaussian-weighted model source which best fits the observations.

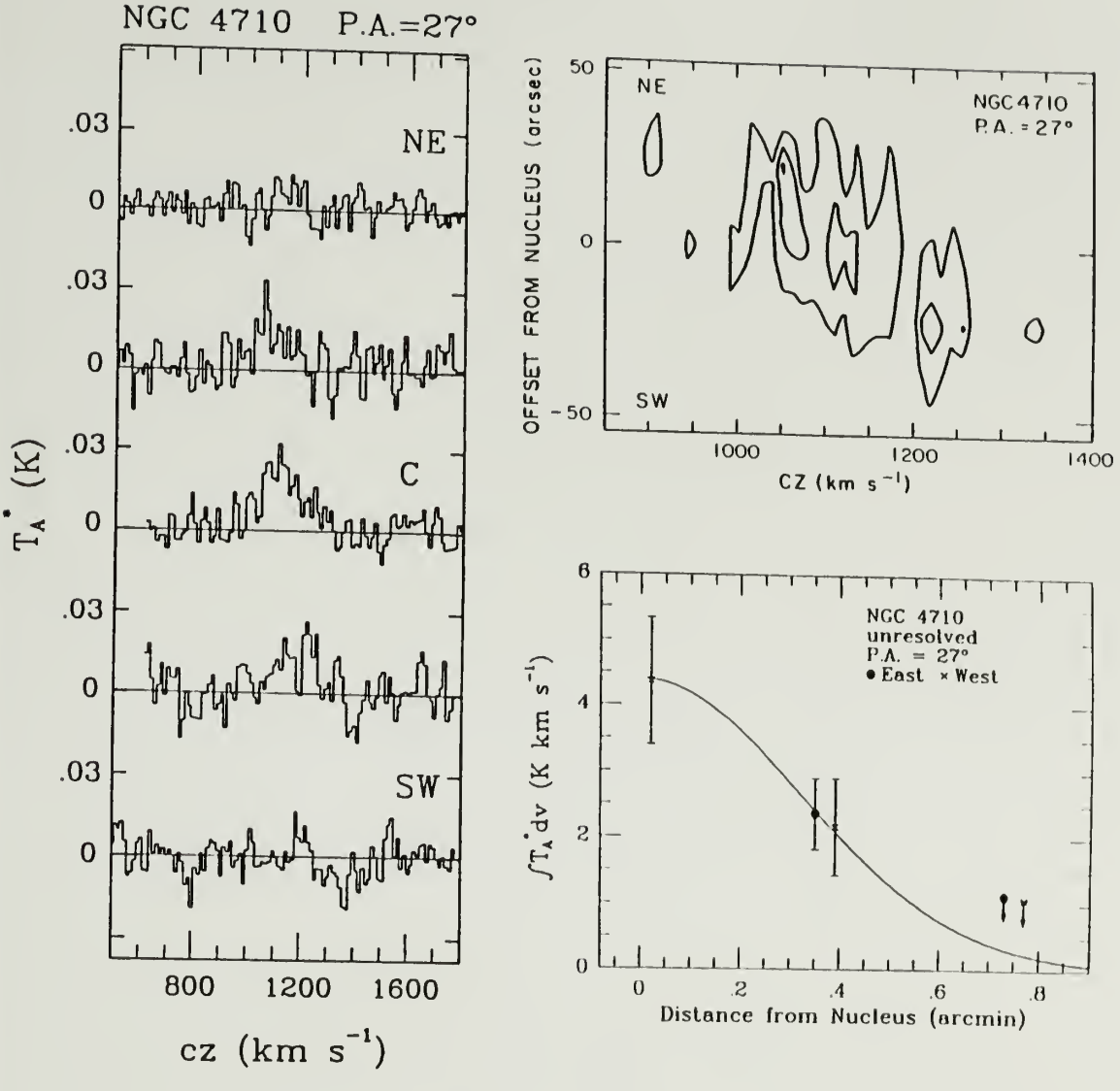

Figure 3.29 (a) CO spectra along major axis of NGC 4710, at intervals of 22.5". C denotes the spectrum obtained from the central position. (b) Spatial-velocity diagram for NGC 4710. Contour intervals are 10, 20 and 30 mK(T_A^*). (c) Radial distribution of observed CO integrated intensities for NGC 4710. The line through the data points represents a Gaussian with a half power, full width of 45".

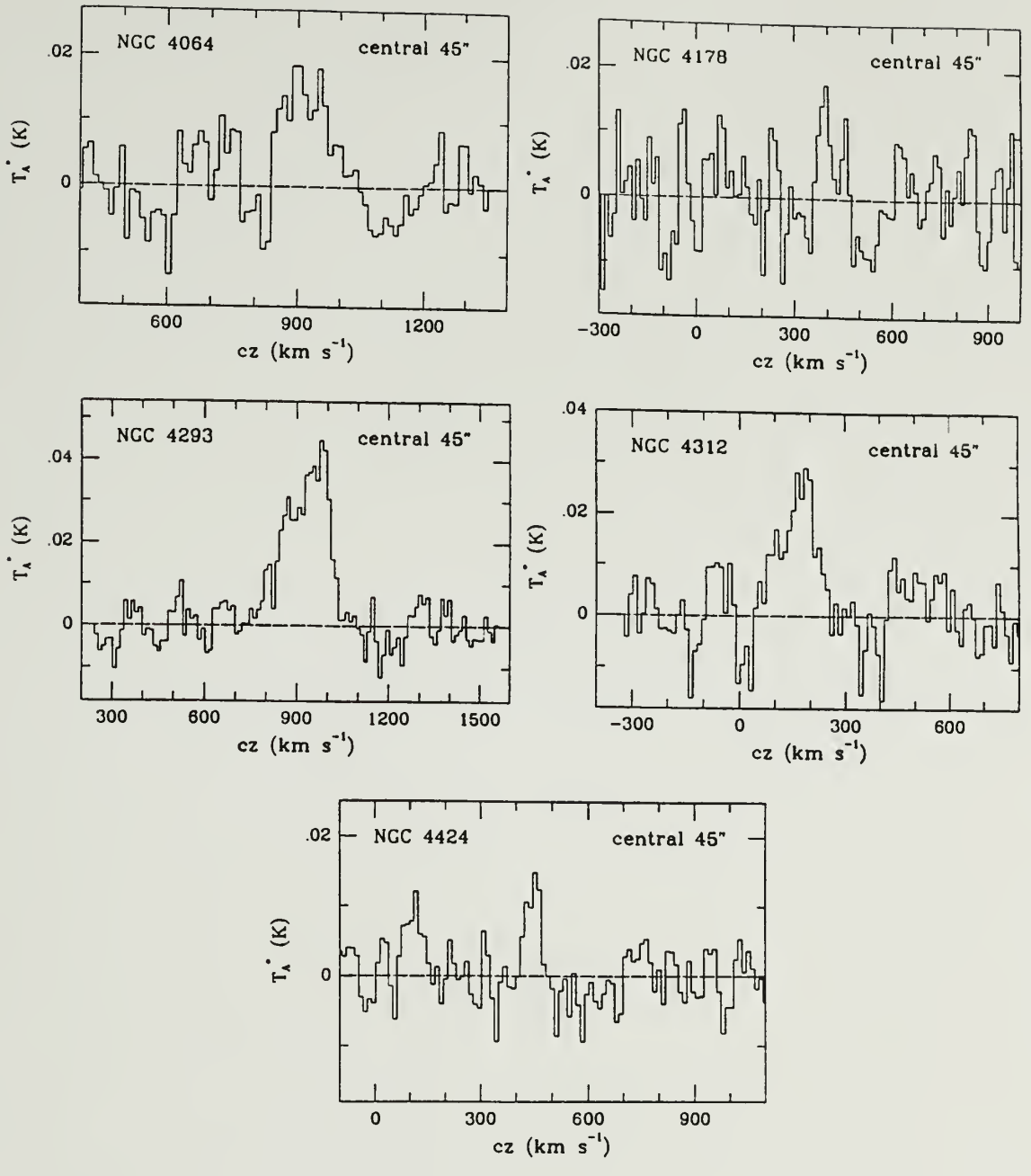

Figure 3.30 CO spectra from the central 45" of galaxies which were detected (≥3σ) in only the centers.

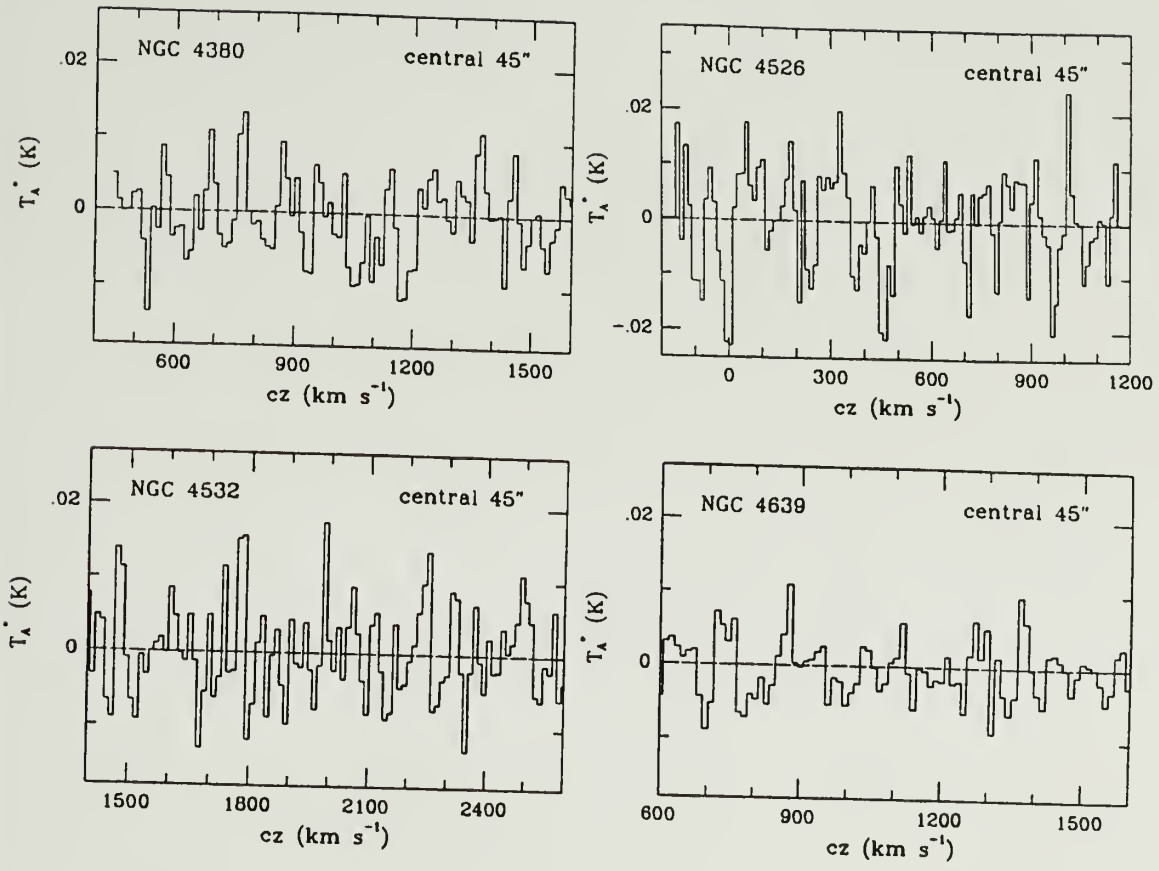

Figure 3.31 CO spectra from the central 45" of galaxies which were not detected at any position.

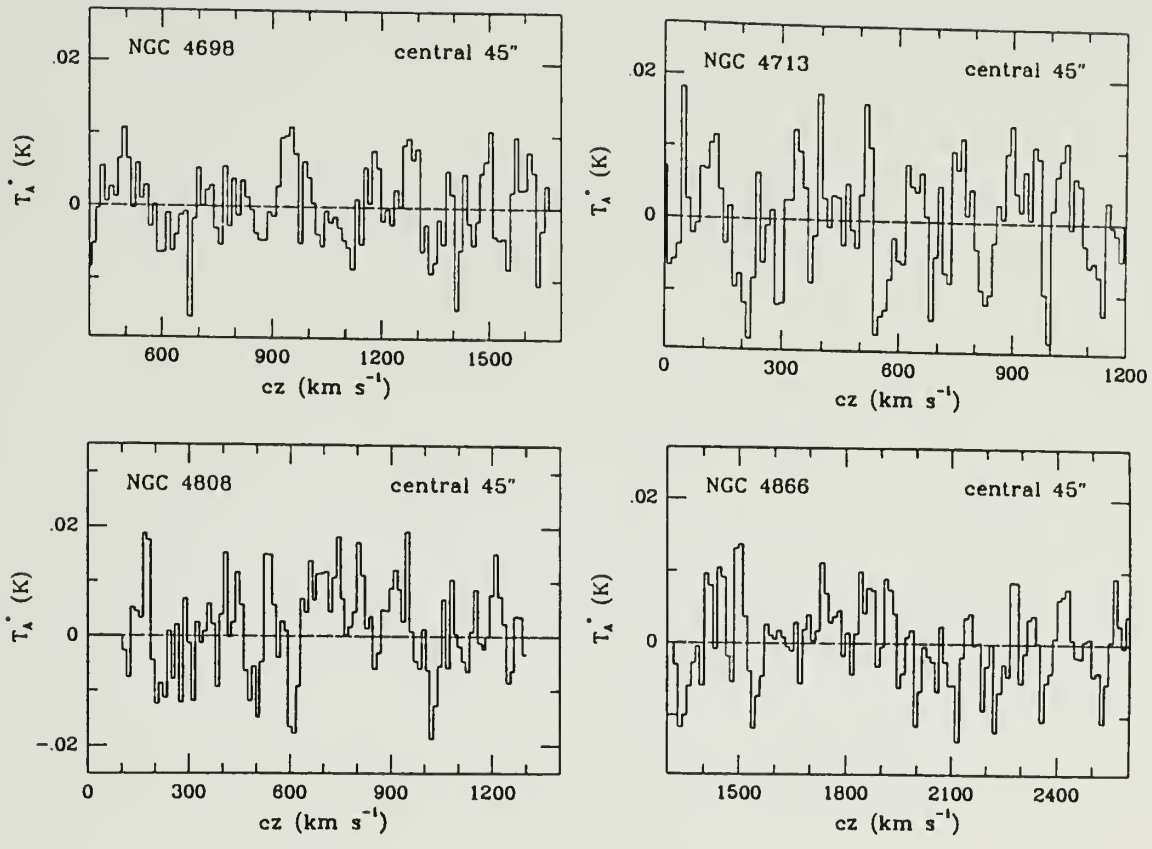

Figure 3.31, cont.

A total of 202 spectra have been obtained in the 42 galaxies. Thirty-four of the 42 galaxies have been detected in at least one position (>3σ); these 34 galaxies contain 113 detections. For each of the survey spectra, Table 3.1 lists the position of the observation, the integrated intensity $\int T_A^* dv$ and its uncertainty, the peak antenna temperature T_A^*(peak), the rms noise level, the mean velocity, and the velocity width.

The integrated CO line intensities and their associated uncertainties, the peak antenna temperatures, and the rms noise level (see columns 7-9 of Table 3.1) have been fully corrected for gain variation and atmospheric effects. This correction is described in detail in Appendix A, and amounts to multiplying the raw telescope intensities by elevation-dependent correction factors, which range from 1.05 at 65° to 1.22 at 30°.

The uncertainties in the individual line intensities listed in column 7 are the quadrature sums of 3 uncertainty components: a calibration component, a noise component, and a baseline component. In Appendix A a formal 1σ uncertainty of 8% is derived for the calibration component, from the analysis of nearly 200 calibrator source observations. We adopt the more conservative value of 10% for the calibration uncertainty in all spectra. The noise components of the line uncertainties depend upon the rms noise T_{rms} and linewidth Δv (see columns 9 and 11 in Table 3.1), such that

$$\Delta I_{CO}(\text{noise}) = T_{rms}\ (12\Delta v)^{1/2} \quad . \qquad \text{(III-1)}$$

In equation III-1, T_{rms} represents the noise level acheived in a 4.2-MHz (12 km s^{-1}) (channel in units of Kelvins) and Δv (in units of Km s^{-1}) represents the velocity width of the line at 0% intensity.

Many of the line features in galaxies observed are wide enough to occupy a significant fraction of the total 512 MHz bandwidth. Consequently, baseline removal is a potential source of significant error for broad, weak, spectral lines. First-order baselines have been removed from most of the spectra to derive the final values of integrated intensity. Second- or third-order baselines were removed from a few spectra whose visual appearance was greatly improved by the higher order fit. Uncertainties from baseline removal have been estimated by removing polynomials of various orders (1,2,3) over different parts of the usable baseline to determine the range in possible values for the line intensities. The uncertainties from the different order fits are normally ~5-10%, but as high as 25% for some of the broad, weak features.

For weak lines in galaxies with unknown velocity fields, a potential source of error can be the velocity range over which a line feature is integrated. This is not a significant source of error in the present study, since the velocity fields are known from the relatively high signal-to-noise Arecibo HI position-velocity maps of Virgo spirals (Giovanelli and Haynes 1983; Helou et al. 1981; Helou et al. 1984).

The detection of broad, weak lines is notoriously difficult in millimeter spectroscopy because of baseline problems of various character and origin. In order to avoid mistaking a baseline feature for a spectral line, the following procedure was used to verify the reality of all weak lines. 1) The first and second halves of the data were averaged separately, and any line feature was required to look the same in each half. 2) Each individual 5-minute scan was examined for baseline excursions. If one or more individual scans was found to contain a feature which significantly influenced the appearance of the average, it was thrown away. 3) The line's velocity and width had to agree with the known HI velocity field. In 2 cases in the present study, a feature originally thought to be a line was subsequently found not to be, by rigorous application of the above procedures.

§3. Derivation of Global CO Fluxes

In order to calculate the global flux of the CO line in galaxies, it is necessary to account for the extended nature and the undersampling of the emission. In Appendix B, it is shown that the total CO line flux S_{CO} can be related to the observed integrated intensity $\int T_A^* dv$ by the following expression:

$$S_{CO} = CC \; (\Sigma \int T_A^* dv) \; (\Sigma f)^{-1} \qquad \text{(III-2)}$$

where CC is the calibration factor for converting antenna temperature (T_A^*) to Janskys for point sources, or the calibration constant (CC). The summations in this expression are over all observed positions.

Both the $\int T_A^* dv$ and CC terms which appear in equation III-2 are fully corrected for gain variation and atmospheric effects, as described in Appendix A. The quantity f, which we call 'the fraction of emission observed', describes how undersampled the flux is, and is given by:

$$f = \frac{\int_0^{2\pi} T_R(\Omega)\, B(\Omega)\, d\Omega}{\int_0^{2\pi} T_R(\Omega)\, d\Omega} \qquad \text{(III-3)}$$

where $B(\Omega)$ is the beam pattern, as defined in equation B-5, and $T_R(\Omega)$ is the source brightness distribution. Note that for a source smaller than the beam, $f \sim 1.0$, while for larger sources, $f < 1.0$.

We have chosen, by use of equation III-2, to weight all of the observed $\int T_A^* dv$ equally. In the Bell Labs 7-meter telescope Virgo CO survey, Stark et al. (1986), using a similar procedure to estimate CO fluxes, chose to weight each observation by the inverse square of the noise and in proportion to the line strength. This scheme has the property of weighting the inner galaxy lines more heavily than those in the outer disk, since the inner galaxy lines tend to have higher signal-to-noise ratios. However, for major axis mapping this is somewhat undesirable since each outer point represents a large area of the galaxy which is unobserved. As a compromise, we deem it optimal to weight all lines equally. The weighting scheme of Stark et al. may be appropriate for their 5-point maps, but is inappropriate for major axis maps.

In order to find a model brightness distribution $T_R(\Omega)$ which

represents the galaxy for the flux calculation, we have chosen to fit the azimuthally-averaged data with a convolution of the beam and trial sources. This is justified because we are using the modelling results only to infer fluxes and diameters, and not to claim anything about the detailed distribution. The uncertainty in the CO flux which arises from the assumption of azimuthal symmetry is discussed below in this section. Quantitative measures of the CO asymmetry are derived in §III.7.

The galactic brightness temperature distribution $T_R(\Omega)$ which appears in equation III-3 is estimated by least-squares fitting the observed $\int T_A^* dv$ with various model brightness distributions $T_R(\Omega)$ weighted by the beam pattern $B(\Omega)$. For more details, see Appendix B. In an attempt to find the best-fit model for the CO distribution, simple, azimuthally-symmetric exponential, gaussian, and uniform disk components were fit to the major axis observations of each galaxy. In several cases, the simple, centered, one-component model could not adequately fit the observations. In these cases, an off-center or two-component model was also tried.

Twenty-eight of the forty-two galaxies in the sample were detected in 3 positions or less. For these galaxies, it is generally not possible to distinguish between exponential, gaussian, r^{-1}, or other distributions in which intensity decreases with increasing galactic radius. In order to decide what distribution to assume for these 28 galaxies, we examine the distributions in the 14 galaxies which have been detected in 4 or more positions. Table 3.2 summarizes the best-

Table 3.2

Radial Distributions in Galaxies with More than 3 Detections

Galaxy	# Det	Description of best fit model[a]	Comments
NGC 4192	6	exponential	
NGC 4216	4	off-center gaussian	molecular ring
NGC 4254	7	exponential + central component	hotter gas in center?
NGC 4302	4	exponential offset from center	
NGC 4303	5	exponential	
NGC 4321	6	exponential + central component	hotter gas in center?
NGC 4501	6	exponential	
NGC 4527	4	uniform disk	
NGC 4535	6	exponential	
NGC 4548	4	exponential - off-center component	molecular bar ?
NGC 4568	4	exponential, slightly asymmetric	interacting w/N4567
NGC 4569	4	exponential, slightly asymmetric	
NGC 4579	4	exponential, slightly asymmetric	
NGC 4654	4	asymmetric, exponential - central component	peak NW of nucleus

Notes to Table 3.2:

a) For more detailed description, see Table 3.3.

fit CO distributions for these 14 galaxies. In 11 out of the 14 cases, the distribution is dominated by an exponential-like component. In 2 of the 11 exponential-like cases, there is an additional central component (NGC 4254 and NGC 4321); in 4 of the 11 cases, the distribution is somewhat asymmetric (NGC 4568, NGC 4569, NGC 4579, NGC 4654); and in 1 case the exponential is not centered at the position given by Dressel and Condon (1976) (NGC 4302). Despite these complications, it is apparent that an exponential-like distributions is the best one parameter approximation of the azimuthally-averaged CO distributions in most Virgo spiral galaxies. Exponential-like CO distributions have been found previously in many Sc galaxies (e.g. Young and Scoville 1982a). For these reasons, and the fact that most spiral galaxies have exponential-like blue light distributions, we have chosen to model the 28 galaxies with less than 4 detections as exponentials. In any case, the error resulting from making this assumption mistakenly is not large. In those galaxies which can be reasonably fit by either a gaussian, an exponential, or a uniform disk, the maximum uncertainty in inferred CO fluxes is ~10%.

In all galaxies fit by an exponential or gaussian, the distribution was truncated 1.3' beyond the outermost detection. The effect of this cutoff on the total CO flux is generally less than a few percent, but in the cases of the large face-on galaxies (NGC 4254, NGC 4303, NGC 4321, NGC 4535), it amounts to ~10%.

The final results of the model fitting are presented in Table 3.3. The best fitting models, together with the observed CO intensities, are

Explanation of Columns in Table 3.3:

(1) NGC number of galaxy.
(2) Inclination of galaxy, from Helou et al. (1981, 1984) or calculated as described therein.
(3) Number of CO observations in present survey.
(4) Number of CO detections ($\geq 3\sigma$) in present survey.
(5) Form of primary component of CO radial distribution in best fitting model:
    exp = exponential
    gauss = gaussian
    unif = uniform source
    unres = unresolved
(6) Reference to description of more elaborate model if a one-component model could not adequately fit the data; if this column is blank, then the best fitting model is centered and consists of the one component referred to in columns 5 & 7.
(7) Scale length of primary component in column 5; see text for definitions.
(8) Fraction of emission observed for the best fitting model.
(9) Global CO line flux and associated 1σ uncertainty for best fitting model; upper limits are 2σ.
(10) Diameter of best fitting model which contains 70% of the total CO flux.
(11) Diameter where face-on main beam CO brightness temperature falls to 1.5 K km s^{-1}.
(12) CO flux asymmetry parameter; see text for definition; values in parentheses indicate that the asymmetry is probably not intrinsic, but may be the result of not using the correct coordinates for the true dynamical center.
(13) CO diameter asymmetry parameter; see text for definition.

Table 3.3

Modeling Results

NGC	i	No. obs	No. det	Dist	2nd comp	Scale length	Σf	S_{CO} (Jy km s^{-1})	D_{COeff} (arcmin)	D_{COiso} (arcmin)	A_{COF}	A_{COD}
(1)	(2)	(3)	(4)	(5)	(6)	(7)	(8)	(9)	(10)	(11)	(12)	(13)
4064	67°	3	1	exp		0.18'	1.00	93 ± 40	≤0.8'	≤0.9'	–	–
4178	69°	5	1	exp		0.30'	0.94	60 ± 30	≤0.8'	≤0.9'	–	–
4192	74°	8	6	exp		0.90'	0.72	940 ± 170	3.7'	2.2'	−0.14	−0.02
4212	47°	5	3	exp		0.40'	0.67	510 ± 90	1.8'	1.9'	+0.28	+0.22
4216	80°	9	4	gauss	a	0.20'	0.78	620 ± 120	4.4'	4.5'	+0.19	+0.02
4254	28°	7	7	exp	b	1.20'	0.37	3000 ± 850	3.4'	5.3'	−0.15	+0.02
4293	76°	3	1	exp		0.08'	1.05	270 ± 45	≤0.4'	≤0.9	–	–
4298	67°	5	3	gauss		0.70'	0.86	660 > 110	1.8'	2.4'	+0.18	+0.05
4302	90°	6	4	exp	c	0.40'	1.05	620 ± 100	1.8'	2.0'	(+0.61	+0.41)
4303	25°	7	5	exp		0.48'	0.50	2280 ± 470	2.2'	3.4'	−0.12	−0.02
4312	78°	3	1	exp		0.15'	1.05	160 ± 40	≤0.7'	≤1.0'	–	–
4321	28°	8	6	exp	d	0.90'	0.39	3340 ± 920	3.4'	4.5'	+0.04	−0.10
4380	55°	3	0	exp		0.40'	0.78	< 60	–	–	–	–
4388	79°	5	2	exp		0.40'	1.00	230 ± 40	1.8'	1.2'	≥+0.41	+0.22
4394	25°	3	2	exp		0.50'	0.57	280 ± 60	1.6'	1.7'	≥−0.27	−0.23
4402	75°	4	3	exp	e	0.30'	0.98	630 ± 120	1.4'	2.4'	(−0.48	−0.23)
4419	67°	5	3	exp	f	0.30'	0.91	920 ± 190	1.4'	2.2'	−0.61	−0.27
4424	61°	3	1	exp		0.30'	0.87	56 ± 30	≤1.0'	≤0.9'	–	–
4438	68°	3	2	exp		0.30'	0.94	210 ± 40	1.2'	1.3'	≥−0.30	−0.13
4450	45°	4	3	exp		0.55'	0.54	450 ± 90	2.2'	2.1'	0.00	0.00
4501	58°	7	6	exp		0.70'	0.59	2220 ± 480	2.9'	3.8'	−0.04	+0.02
4526	90°	3	0	exp		0.30'	1.34	< 90	–	–	–	–
4527	72°	6	4	unif		1.20'	0.92	1810 ± 320	2.0'	3.0'	−0.21	−0.08
4532	60°?	3	0	unif		1.00'	0.79	< 60	–	–	–	–
4535	43°	7	6	exp		1.10'	0.38	1570 ± 410	3.5'	3.9'	−0.07	−0.13
4536	67°	6	3	exp		0.25'	0.96	740 ± 130	1.2'	2.3'	+0.14	+0.06
4548	37°	7	4	exp	g	0.70'	0.60	540 ± 140	3.0'	3.3'	−0.12	+0.02
4567	46°	4	3	exp	h	0.35'	0.69	500 ± 90	1.6'	2.2'	–	–
4568	64°	5	4	exp	h	0.40'	0.86	1050 ± 190	1.8'	2.7'	–	–
4569	63°	5	4	exp		0.40'	0.82	1500 ± 260	1.8'	3.2'	+0.23	+0.11
4571	38°	5	3	exp		0.60'	0.52	380 ± 80	2.3'	1.6'	0.00	+0.01
4579	37°	6	4	exp		0.60'	0.47	910 ± 200	2.6'	2.7'	+0.30	+0.24
4639	45°	3	0	unif		1.00'	0.65	< 70	–	–	–	–
4647	36°	5	3	exp		0.35'	0.66	600 ± 120	1.6'	2.2'	+0.23	+0.15
4651	46°	4	2	exp		0.25'	0.81	350 ± 60	1.2'	1.6'	+0.41	+0.21
4654	52°	5	4	exp	i	0.40'	0.62	730 ± 150	2.4'	2.6'	+0.22	+0.09
4689	30°	5	3	exp		0.55'	0.50	710 ± 150	2.2'	2.4'	+0.02	0.00
4698	57°	3	0	exp		0.50'	0.76	< 90	–	–	–	–
4710	90°	5	3	unres		–	2.10	200 ± 30	≤0.5'	≤1.3'	–	–
4713	49°	3	0	exp		0.50'	0.68	< 70	–	–	–	–
4808	67°	3	0	exp		0.40'	0.87	<100	–	–	–	–
4866	90°	3	0	exp		1.00'	1.00	< 90	–	–	–	–

Notes to Table 3.3:

a) NGC 4216: best fitting model is a gaussian doughnut, offset from the center by 2.1', with a scale length of 0.2'.

b) NGC4 254: best fitting model is an exponential with a second gaussian component added to the center; scale length of 0.2'; central amplitude of gaussian component is 3 times that of the exponential component; similar to NGC 4321.

c) NGC 4302: this dusty edge-on spiral has a best fit model which is an exponential offset by -0.45' along the major axis from the central position given by Dressel and Condon (1976). The CO line profiles in the central region of this galaxy indicate that the dynamical center is probably closer to $\alpha = 12^h19^m11.2^s \pm 1.5^s$ $\delta = +14°52'16" \pm 6"$ (1950).

d) NGC 4321: best fitting model is an exponential with a second gaussian component added to the center; scale length of gaussian 0.2'; central amplitude of gaussian component is 3 times that of the exponential component; similar to NGC 4254.

e) NGC 4402: best fitting model offset from center by +0.20' along major axis from central position given by Dressel and Condon (1976). The CO line profiles in the central region of this galaxy suggest that the dynamical center is probably closer to $\alpha = 12^h23^m23.8^s \pm 1.5^s$ $\delta = +13°23'22" \pm 6"$ (1950).

f) NGC 4419: best fitting model is exponential offset by 0.25' along the major axis from central position given by Dressel and Condon (1976); CO line profiles suggest that distribution is intrinsically asymmetric.

g) NGC 4548: the kinematic major axis of this barred (SBb) galaxy is nearly perpendicular to the bar; consequently, the observed positions 45" from the nucleus did not cover the bar, but did cover the off-bar positions at the same radius. These 2 positions do not have much emission; the best fit model is an exponential with an off-center gaussian component removed; offset 0.7'; amplitude 0.8, scale length 0.25'. Several barred galaxies (e.g. M83, Lord 1987) have greater CO emission along the bar, so the CO flux for NGC 4548 listed here may be too low.

Notes to Table 3.3 (cont.):

h) NGC 4567 and NGC 4568: these two inclined Sc's form an interacting pair which overlap in postion and velocity space in the northeast regions of both galaxies. The position 90" to the northeast of NGC 4568's nucleus is separated by only 7" from the position 45" to the northeast of NGC4567's nucleus. Since there is only one velocity component in this region, it is not possible to decide how much of the CO emission 'belongs' to either galaxy. Since the separation of these 2 observed positions is roughly the same as the pointing uncertainty of the telescope, the 2 spectra have been averaged, and are found to have $\int T_A^* dv = 2.5$ K km s^{-1}. 1.5 K km s^{-1} of this has been assigned to NGC4567, in order to make its distribution roughly symmetric about the nucleus. The remainder has been assigned to NGC 4568. This assignment, although somewhat arbitrary, is justified because the position closer to NGC4567 was found to have a stronger line.

i) NGC 4654 has an asymmetric CO distribution. The position 45" NW of the nucleus has a stronger line than the central 45". This region also displays a peak in HI, radio continuum, and Hα emission. Best fitting model is an exponential with a central gaussian component subtracted; scale length 0.25; amplitude 1.0.

plotted as a function of radius for each galaxy in Figure 3.1. If the data could not distinguish between exponential, gaussian, or uniform disk models, an exponential distribution was chosen for galaxies with detections. For undetected galaxies, the model which yielded the largest upper limit is listed in Table 3.3. Second components were included only for those galaxies which could not be well-fitted by a single component. Listed in column 5 of Table 3.3 is the type of distribution used for the final galaxy model. If the data were well-fit by a single component model centered at the position given by Dressel and Condon (1976), column 6 appears blank. If the galaxy was fit by a more complex model, the entry in column 5 indicates the primary component, while the letter in column 6 refers to a detailed description of the model. Column 7 lists the scale length, r_o, of the primary component, defined in the case of exponential distributions by:

$$T_R(r) = T_R(0)\, e^{-r/r_o} \qquad \text{(III-4)}$$

while for gaussian models r_o is given by:

$$T_R(r) = T_R(0)\, e^{-\ln 2 (r/r_o)^2} \qquad \text{(III-5)}$$

and for uniform disk models by:

$$T_R(r) = T_R(0) \quad \text{for } r \leq r_o \qquad \text{(III-6)}$$
$$= 0 \quad \text{for } r \leq r_o$$

Column 8 lists the fraction of emission observed, Σf, which is used in equation III-2 to compute the global CO line flux. This frac-

tion ranges from ~0.4 for the large face-on Sc's NGC 4254, NGC 4303, and NGC 4321, to ~1.0 for the edge-on systems like NGC 4302. The 2 S0 galaxies observed (NGC 4526 and NGC 4710) were oversampled with half-beam spacing, resulting in a value of f significantly greater than 1.0.

The global CO line flux and 1σ uncertainty appear in column 9. The quoted uncertainty is the quadrature sum of 3 components, which are discussed below. The first component of the CO flux uncertainty is that due to the uncertainty in the individual line intensities, which are listed in Table 3.1. This component includes all calibration, baseline, and signal-to-noise uncertainties. For each galaxy, an intensity-weighted mean uncertainty has been calculated from the individual line unertainties. Since the individual line uncertainties are uncorrelated, the intensity-weighted mean uncertainty has been divided by $\sqrt{N_{det}}$, where N_{det} is the number of detections ($\geq 3\sigma$), to yield this component of the CO flux uncertainty. For most of the Virgo galaxies, this component is ~15%.

Galaxies which are significantly undersampled obviously have larger uncertainties in their derived CO fluxes than those galaxies which are more fully sampled. In order to estimate this second component of the uncertainty, fully sampled CO maps at 45" resolution of the face-on galaxies M51 (Lord 1987) and NGC 6946 (Tacconi 1987) have been analyzed. The 45" beam subtends ~2.2 kpc in each of these galaxies, since each is located at a distance of ~10 Mpc. At any given radius in these 2 galaxies, with 2.2 kpc resolution, the 1σ scatter in CO intensities is ~36%.

Since the Virgo cluster is roughly twice as distant as M51 and NGC 6946, the 45" beam in Virgo galaxies subtends 4 times the area. The 1σ scatter in CO intensities at a given azimuth in Virgo galaxies might therefore be expected to be somewhat less than 36%. If the distribution of intensities were completely random, the 1σ azimuth scatter in Virgo galaxies would be expected to be $36/\sqrt{4}\%=18\%$. However, since molecular features are correlated on various length scales, we have selected the more conservative value of 30% for the 1σ scatter in CO intensities at a given azimuth for Virgo galaxies. This roughly agrees with the difference in CO intensities observed on opposite sides of the Virgo nuclei.

Using this 1σ value of 30%, we have estimated the typical uncertainty in the total flux due to undersampling the emission. The procedure for doing this consisted of simulating "observations" of an artificial galaxy with a 1σ azimuth scatter of 30%. At each position the computer would randomly select one of the possible intensity values appropriate for that radius. An estimate of the total flux can be made, using these random "observations". By randomly "observing" the same galaxy many times, a statistical estimate has been made of the difference between the true and inferred total fluxes. For models with a 1σ azimuth scatter of 30%, and which have 40% of their emission observed (i.e. f=0.40) along the major axis, the 1σ difference between true and inferred total CO fluxes is found to be ~20%. From testing a variety of models, we have found that the following simple relation estimates the undersampling component (ΔS_u) of the total flux

uncertainty:

$$\Delta S_u(\%) = 33(1-\Sigma f) \quad . \qquad \text{(III-7)}$$

When all of the emission is observed (i.e. $\Sigma f=1.0$), $\Delta S_u=0$, since there is no uncertainty due to undersampling. This simple relation does not work for $\Sigma f \leq 0.30$, but is adequate for the Virgo observations described in this thesis, since the minimum value of Σf in the Virgo sample is 0.37.

The third and final component of the CO flux uncertainty relates to how well the adopted model matches the observations. We have measured the quality of fit for each galaxy with the reduced χ^2 statistic (e.g. Bevington 1969). As can be seen in the radial distribution plots in Figures 3.1 - 3.29, each model distribution generally agrees with the observed CO intensities to within the 1σ uncertainty in $\int T_A^* dv$. Thus, the reduced χ^2 of the best fitting model is typically less than 1.0, and always less than 2.0. For each of the galaxies, we have estimated the range in flux values permitted by considering all the models which fit the data reasonably well. The galaxies with $\chi^2=1.0$ generally have a flux range of ~10% for acceptable models, while those with $\chi^2=2.0$ have a flux range of ~20%. Thus we have adopted an uncertainty component due to the fit which is proportional to the reduced χ^2 of the best fitting model; this uncertainty component has a maximum value of 20%.

§4. A Comparison of FCRAO and Bell Labs Virgo CO Surveys

A CO survey of 47 Virgo spirals made with the Bell Telephone Labs (BTL) 7-meter telescope has recently been reported by Stark et al. (1986). In Figure 3.32, we compare the CO fluxes and upper limits derived in the last section with those of Stark et al. for the 28 galaxies in common. There is a large amount of scatter in this figure, which requires explanation.

First, we point out several differences in the way that fluxes and uncertainties are determined in the 2 surveys. Although the manner of estimating global fluxes is similar, Stark et al. employ a different weighting scheme (described in §III.4), and assume model distributions with no outer galaxy cutoffs. While these differences undoubtedly cause some of the scatter, we believe that most of the truly discrepant cases have other explanations. Furthermore, the 1 σ uncertainties quoted by the 2 groups cannot be directly compared. While the uncertainties we list in Table 3.3 include contributions from the rms noise, baseline fitting, calibration variation, undersampling, and quality of fit determinations, Stark et al. have considered only the rms noise and quality of fit determinations. Thus it may be that some of their quoted uncertainties are underestimates.

Some illuminating statistics of the two Virgo surveys are compared in Table 3.4. Note that while the BTL sample includes a larger number of galaxies, we have detected a larger number of galaxies, collected a larger number of spectra, and obtained nearly twice the number of

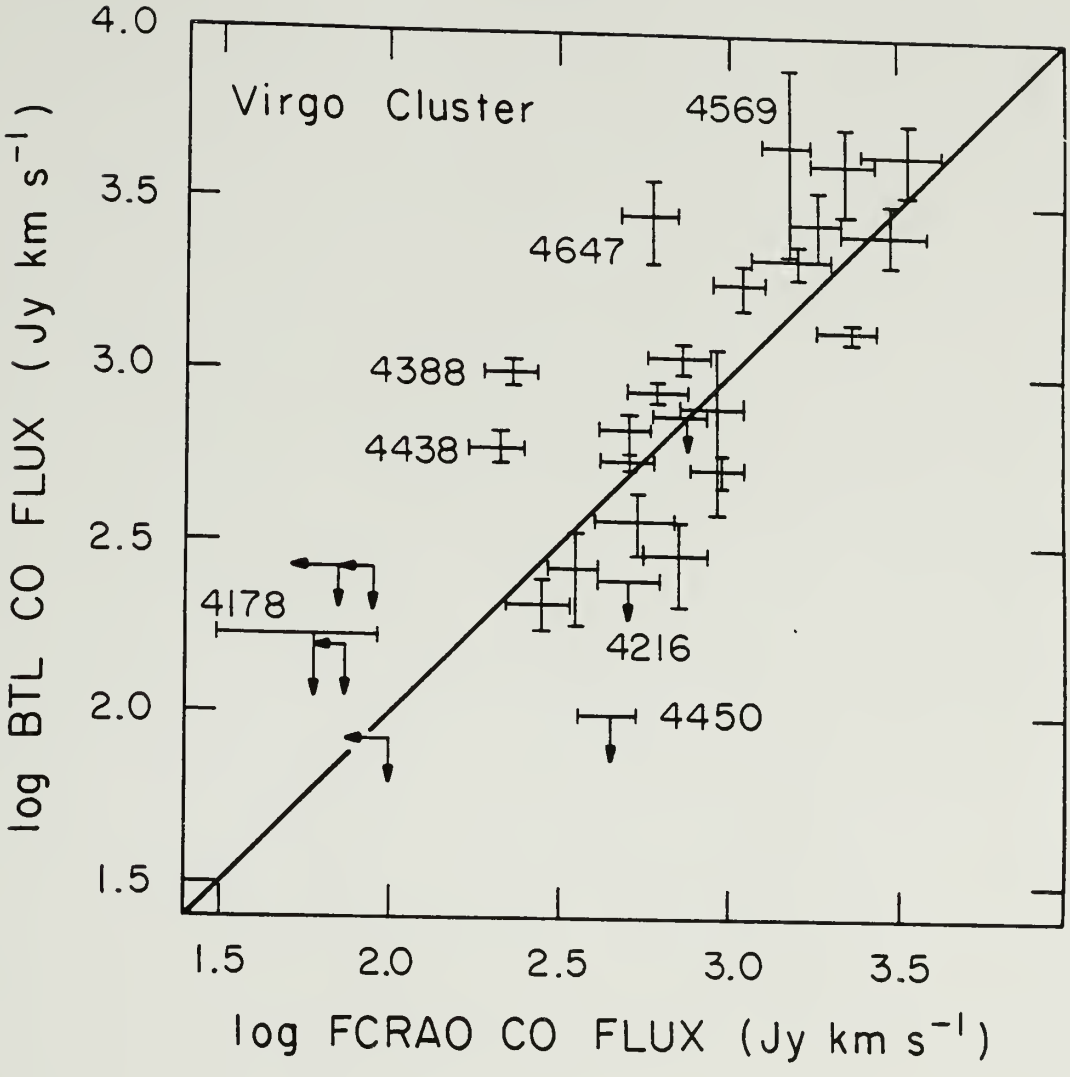

Figure 3.32 A comparison of the global CO line fluxes derived at FCRAO (this work) and Bell Labs (Stark et al. 1986) for the 28 Virgo cluster galaxies in common. The upper limits shown are 2 σ. The line through the figure represents equal fluxes.

Table 3.4

Comparison of FCRAO and Bell Labs Virgo CO Surveys

Quantity being compared[1]	FCRAO[2]	Bell Labs[3]
# of galaxies observed	42	47
# of galaxies detected	34 (81%)	25 (53%)
# of galaxies detected in 3 or more positions	25 (59%)	11 (23%)
# of positions observed	202	145
# of positions detected	113 (56%)	60 (41%)
average # of positions observed in observed galaxies	4.8	3.1
average # of detections in detected galaxies	3.4	2.4

Notes to Table 3.4:

1) Detections refer to signal-to-noise ratios greater than 3 σ.
2) FCRAO refers to this thesis.
3) Bell Labs refers to Stark et al. (1986).

detected positions. Twenty-two of their 47 galaxies were observed in only 1 position, and the remainder were mapped in a criss-cross 5-point pattern with the observations spaced 90" from the nucleus in either Right Ascension or Declination (the HPBW of the BTL telescope at 115 GHz is 100"). Our observing strategy of mapping along the major axis until no emission was detected results in a much better estimate of the brightness distribution $T_R(\Omega)$, which is needed to reliably estimate the total flux. Thus, although the larger beam area of the BTL telescope implies that more of each galaxy's surface area can be covered per observation, our observing procedure resulted in a larger number of positions observed per galaxy, and a higher number of detections per galaxy (see Table 3.4), which serve to more reliably constrain the distribution of emission.

Although the 45" half-power beamsize of the FCRAO telescope is small compared to the angular sizes of Virgo galaxies, so that each galaxy's surface area will be undersampled relative to the maps made at BTL, the emission is not seriously undersampled in the FCRAO maps. From the modeling results presented in Table 3.3, we find that on average 70±20% of the total CO flux is contained within our major axis maps.

Here, we try to account for the fluxes which are most discrepant between the two surveys. Four of the galaxies undetected in the BTL survey have been detected in the FCRAO survey (NGC 4178, NGC 4216, NGC 4450, NGC 4536). A weak (3σ), narrow line was detected in the center of NGC 4178 in the FCRAO survey, at a level consistent with the BTL

upper limit. Lower luminosity Sc galaxies, like NGC 4178, generally have slowly rising rotation curves (Rubin et al. 1985), which result in narrow central line profiles. The fact that a narrow line is observed despite the high inclination (i=69°) suggests that the molecular gas is confined to an area smaller than the beam. NGC 4216 was observed in 9 positions in our survey, and detected in 4 outer disk positions, making it the only Virgo cluster galaxy with a confirmed molecular ring or central molecular depression. Stark et al. observed only the nucleus, which we also failed to detect. In NGC 4450, we have detected 3 weak (3-4σ) lines in the central 3 positions. Since these lines are weak, the greater beam dilution with the Bell Labs 7-meter telescope may account for Stark et al.'s non-detections in this galaxy. In NGC 4536, we have detected CO emission in 3 positions, including a strong line (44 mK) in the center of the galaxy. Stark et al. report a non-detection in the central region.

There are 3 galaxies for which the fluxes derived by Stark et al. are a factor of $\geq$3 higher than the fluxes we have derived (NGC 4388, NGC 4438, NGC 4647). Both groups detected 2 or more positions in each of these 3 galaxies. In NGC 4388, both groups observed positions centered at ($\Delta\alpha$, $\Delta\delta$) = (+1.5,0) and (-1.5,0). While the BTL data indicate detections at both positions, we find no emission at either position. Thus it may be that the molecular gas is spread out in this galaxy, and is easier to detect with a larger beam. However, our major axis map includes sensitive observations of the entire bright optical disk region of NGC 4388, as seen on the Palomar Sky Survey Plate. If the

BTL detections can be confirmed, it would imply that this galaxy has a very unusual molecular gas distribution. The second galaxy, NGC 4438, is the closest survey galaxy to M87, and has distorted spiral arms and a disturbed central bulge. We surveyed only 3 positions along the apparent major axis of NGC 4438's bulge, and did not search for any emission along any of the distorted arms or filaments. Since the 5 observations of the Bell Labs survey cover a larger area of this disturbed galaxy, we cannot justifiably claim to have a more accurate estimate of its flux. The third galaxy is NGC 4647, which is a close companion of the elliptical galaxy NGC 4649, but shows no obvious signs of disturbance. The discrepancy in fluxes arises from the fact that Stark et al. report 4 fairly strong detections 1.5' from the nucleus (in R.A. and Dec.), while we detect no emission 1.5' from the nucleus (along the major axis). The line strengths they observe are inconsistent with the distribution of emission we infer. We note that 1.5' is beyond the optically bright disk region of this galaxy, as seen on the POSS plate.

There are 5 galaxies (NGC 4192, NGC 4303, NGC 4548, NGC 4569, NGC 4689) that Stark et al. have detected in only 1 position, and that we have detected in 3-6 positions, yielding us much better estimates of the brightness distributions. Finally, the 2 groups disagree by nearly 3σ on the flux of NGC 4568, which is an inclined Sc galaxy interacting with NGC 4567. Because the nuclei of NGC 4567 and NGC 4568 are separated by less than 1.5', and they overlap in velocity space, observations with a 1.6' beam suffer from confusion. Stark et al. apparently

have not corrected for this confusion. There is one position which is confused in the FCRAO maps of this galaxy pair: an attempt to correct for it is described in the notes to Table 3.3.

§5. CO Diameters

It is of great interest to compare the radial distribution of molecular gas in the HI-deficient Virgo spirals with non-HI-deficient galaxies. In order to make such a comparison, it is desirable to derive a measure of the extents of CO emission in galaxies which accounts for the galactic inclinations, and the range of source sizes relative to the beam. We have established two measures of a galaxy's CO extent: an effective diameter, and an isophotal diameter. Each of these diameters is described below, along with its advantages and disadvantages.

The concept of an effective diameter in astronomy is simple: it is that diameter which contains a certain fraction (e.g. 70%) of the total emission. Effective CO diameters for the Virgo galaxies have been calculated analytically, using the azimuthally-symmetric model distributions which best fit the observations. We have chosen to define our effective CO diameters at the 70% level: 70% is large enough to contain the majority of a galaxy's flux, yet it is not so large that it is highly dependent on low signal-to-noise spectra in the outer regions of a galaxy. It also enables a convenient comparison between CO and HI diameters, since 70% is the same level used by Giovanelli and Haynes (1983) to define their effective HI diameters.

The advantages of effective diameters are that they are easy to calculate, and they account easily for the inclination of a galaxy. Unlike isophotal diameters, effective diameters depend on the entire CO distribution, and so provide a convenient one-parameter description of the radial distribution of a galaxy. In this respect, they are similar to the scale lengths used to describe the exponential, gaussian, and uniform disk fits to the data in §III.4. The difference is that the effective diameters of gaussian and exponential distributions can be meaningfully intercompared, whereas the scale lengths of gaussian and exponential distributions cannot.

A characteristic of effective diameters which is a disadvantage for our purposes is that they are not very sensitive to differences in outer disk distributions. Since gas removal occurs more readily in the outer disk, it is important to have a measure of CO extent which can distinguish between galaxies with identical central gas distributions but different outer disk distributions. Hence we also employ an isophotal CO diameter: a diameter where the CO intensity falls to a certain, conveniently defined level.

We have defined an isophotal diameter which is suitably corrected for inclination and resolution, and which can be directly related to the mass surface density of molecular gas. As will be discussed in Chapter IV, the mass surface density of molecular gas is directly related to the integrated main beam CO brightness temperature $\int T_R dv$. In order to calculate a diameter which is corrected for inclination, we first calculate what $\int T_A^* dv$ would be at each position if the galaxy

were face-on. This requires several steps, which we outline briefly here. 1) Find the azimuthally-symmetric model brightness distibution $T_R(\Omega)$ for the inclined galaxy which best fits the observed integrated intensity $\int T_A^* dv$(obser-ved). 2) Calculate f(inclined), the fraction of emission observed, for each position in the inclined, best-fit model. 3) Create an image of a face-on galaxy using the parameters (scale length, etc.) which describe the best-fit models of the inclined galaxy. 4) "Observe" each position in the face-on galaxy with a 45" gaussian beam, and calculate the fraction of emission observed, f(face-on), and the coupling efficiency η_c(face-on), for each position. (The coupling efficiency ηc is defined in Appendix B.) Given these quantities, $\int T_R dv$(face-on) can be computed as follows. From equation B-2,

$$\int T_R dv(\text{face-on}) = \frac{\int T_A^* dv(\text{face-on})}{\eta_{fss}\ \eta_c(\text{face-on})} \quad . \qquad \text{(III-8)}$$

The face-on value of integrated intensity $\int T_A^* dv$(face-on) can be related to the actual observed integrated intensity $\int T_A^* dv$(observed) by the use of equation B-13 (which is the same as equation III-2), once it is realized that inclining the galaxy does not change its total flux (assuming that there is no cloud shadowing). This leads to the relation:

$$\frac{\int T_A^* dv(\text{face-on})}{f(\text{face-on})} = \frac{\int T_A^* dv(\text{observed})}{f(\text{actual})} \quad . \qquad \text{(III-9)}$$

Since the actual fraction of emission observed is unknown, we substitute our best estimate of it, which is f(inclined), the fraction of emission observed in the inclined, azimuthally-symmetric best-fit model. Combining equations III-8 and III-9, with this substitution in III-9, yields:

$$\int T_R dv(\text{face-on}) = \frac{f(\text{face-on})}{f(\text{inclined})} \quad \frac{\int T_A^* dv(\text{observed})}{\eta_{fss}\ \eta_c(\text{face-on})} \quad . \qquad \text{(III-10)}$$

By linear interpolation, the diameter where $\int T_R dv$(face-on) falls to 1.5 K km s^{-1} has been calculated. In considering what value of $\int T_R dv$(face-on) to employ, it was deemed appropriate to use as small a value as possible, so as to be most sensitive to possible environmental changes in the outer disk. The value of $\int T_R dv$(face-on)=1.5 K km s^{-1} roughly corresponds to a 3σ $\int T_A^* dv$ detection in face-on galaxies like NGC 4321, and a 5-6σ detection in highly inclined galaxies like NGC 4192. For a CO-H_2 proportionality factor of $\chi=2.8\times10^{20}$ H_2 cm^{-2} $K(T_R)^{-1}$ km^{-1} s, (see Chapter IV), $\int T_R dv$ = 1.5 K km s^{-1} corresponds to 4.2×10^{20} H_2 cm^{-2}, or 6.75 M_o pc^{-2}.

We note here that equation III-10 has also been used to estimate the face-on, azimuthally-averaged, radial distributions of CO brightness in all of the detected Virgo sample galaxies. These inclination-corrected distributions of $\int T_R dv$(face-on) have been used to estimate the inclination-correction radial distributions of H_2 which appear in

Chapters V and VI.

A desirable characteristic of isophotal diameters is that they are less model dependent than the effective diameters. While the isophotal diameters do make use of the best-fit model to make the inclination and resolution corrections, their model dependence is slight. The assumption of azimuthal symmetry is used in the calculation of f(inclined), f(face-on) and η_c(face-on), but the fact that f(face-on) appears in the numerator of equation III-10, while η_c(face-on) appears in the denominator reduces the overall model dependence of $\int T_R dv$(face-on).

The 2 types of diameters are compared in Figure 3.33. It is evident that the 2 quantities are well-correlated, and that the isophotal diameters are generally larger than the effective diameters. A least squares fit yields

$$D_{CO\,iso} = 1.20 \pm 0.15\ D_{CO\,eff} \qquad \text{(III-11)}$$

The isophotal diameters are generally greater than the effective diameters since the isophotal cutoff level was deliberately chosen to be near the outermost detection, at a level which contains roughly 90% of the total emission. A certain amount of scatter is expected in Figure 3.33, since galaxies with different kinds of distributions or different surface brightnesses will have different relations between their effective and isophotal diameters. A discussion on 2 of the galaxies which deviate significantly from the mean relation will serve to illustrate why we believe that isophotal diameters are a more reliable diagnostic tracer of environmental effects than effective diameters.

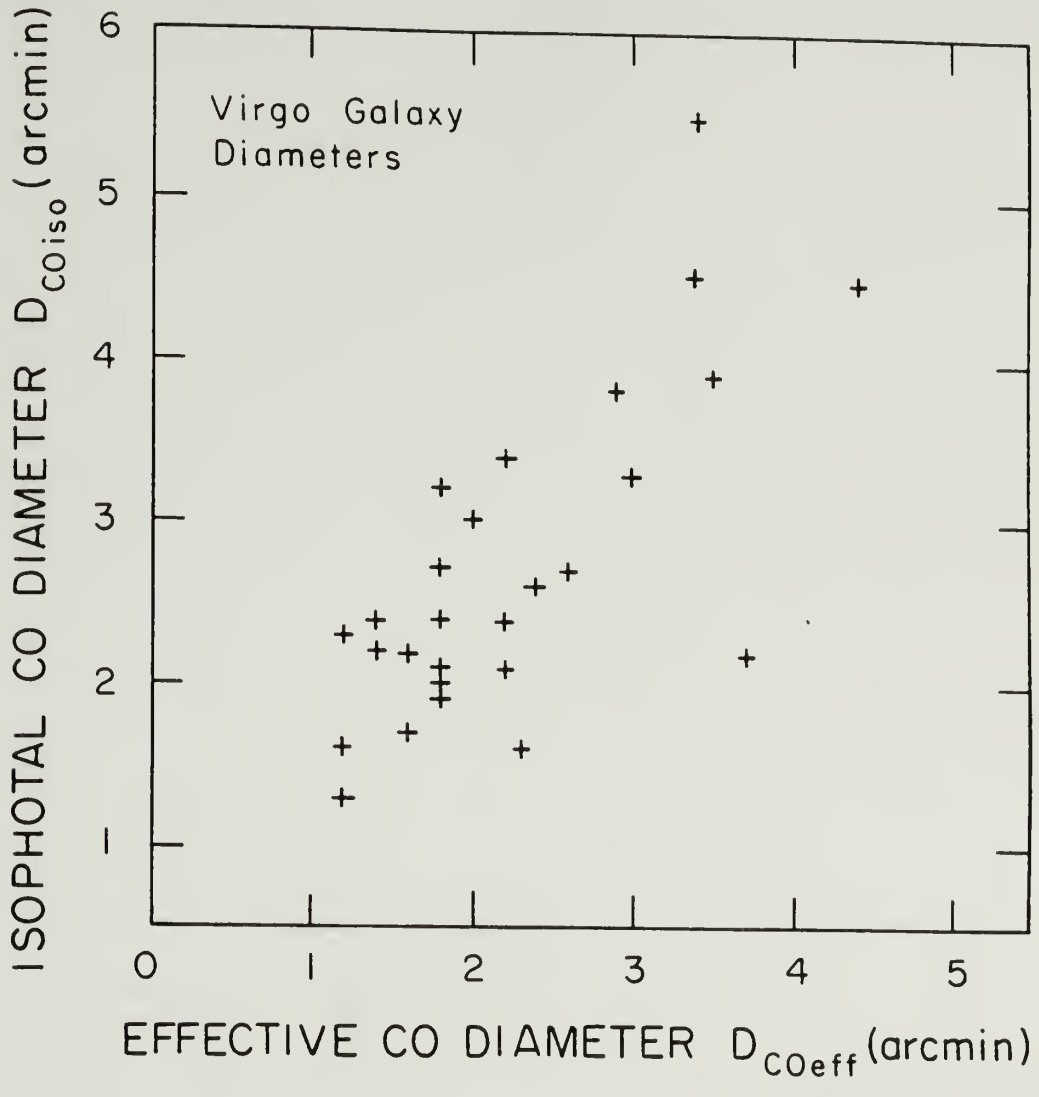

Figure 3.33 Relation between isophotal and effective CO diameters for Virgo cluster galaxies. Isophotal diameters are defined at an intensity level of $\int T_R dv(\text{face-on}) = 1.5$ K km s^{-1}. Effective diameters are defined as the diameters which contain 70% of the total flux. Upper limits are not shown.

The most deviant galaxy in Figure 3.33 is NGC 4192, with an effective CO diameter of 3.7', and an isophotal CO diameter of 2.2'. NGC 4192 is a highly inclined Sb, with relatively weak emission throughout the disk, implying that the face-on CO surface brightness is low. This, together with a large extent of CO emission, gives NGC 4192 a small isophotal diameter and a large effective diameter. NGC 4254 (D_{COeff}=3.4', D_{COiso}=5.3') has roughly the same effective diameter as NGC 4192, but a much larger isophotal diameter. NGC 4254 is a face-on Sc galaxy whose radial distribution is best fitted by exponential with an additional strong central component. The presence of this centrally concentrated flux reduces the effective diameter without affecting the isophotal diameter.

Most of the external gas removal mechanisms which are considered to be occurring in Virgo cluster galaxies are more effective far out in the disk, where the total mass surface density binding the gas to the galaxy is relatively low. Since we are interested in determining whether molecular gas has been removed from the disk, we will rely primarily on isophotal diameters as a probe of possible environmental effects, because they are not affected by the amount of gas in the galactic nuclei. However, to avoid being overly reliant on one derived quantity, we will employ both types of diameters in our analysis.

§6. CO Asymmetries

Many of the galaxies in the Virgo cluster core are found to have asymmetric HI distributions (Warmels 1986), raising the issue of

whether the molecular gas distributions are also asymmetric. In this section, we describe two quantitative measures of asymmetries in the CO distributions which will be used in Chapter V. The CO asymmetry parameters derived here serve not only as a probe of environmental effects, but also indicate uncertainties in the total CO fluxes which are caused by our assumption of azimuthal symmetry. These asymmetry-related uncertainties are fully reflected in the χ^2 component of the CO flux uncertainties, which are described in §III.4 and will not be discussed further here.

The CO asymmetry parameters we employ are similar to the HI asymmetry parameters defined by Helou et al. (1981) and Warmels (1986). The CO diameter asymmetry parameter is defined by:

$$A_{COD} = \frac{R_+ - R_-}{R_+ + R_-} \qquad \text{(III-12)}$$

where R_+ (R_-) refers to the radius where the CO emission falls to $\int T_R dv(\text{face-on}) = 1.5$ K km s^{-1} along the major axis on the side of the nucleus closest to (furthest from) M87. The maximum possible value of A_{COD} is +1.0, corresponding to all the emission existing on the M87 side; while $A_{COD} = -1.0$ indicates that all the emission is on the side away from M87. The intracluster gas thought to be responsible for the stripping of HI appears to be concentrated near M87. If the galaxy-ICM interactions cause asymmetries in the molecular gas distributions, one might expect the asymmetries to exhibit preferential alignments either

toward or away from M87.

This CO diameter asymmetry parameter and Warmels' HI diameter asymmetry parameter are both based on the radius where the emission falls to some isophotal level. However, 4 important differences must be mentioned: 1) Warmels' HI asymmetries are measured strictly east and west, whereas our asymmetry parameters are measured along the major axis. 2) The HI diameter asymmetry parameters are measured further out in the disk, and at a lower mass surface density, than the CO diameter asymmetry parameter. 3) Warmels' Westerbork HI synthesis observations sample nearly all of each galaxies' HI emission, whereas our CO observations generally undersample the CO emission. 4) The signal-to-noise ratio of the HI data is generally higher than that of the CO data. As a consequence of these last two reasons, the CO diameter asymmetry parameter is a crude estimate of the intrinsic CO asymmetry, with respect to the HI asymmetry parameter of Warmels.

Due to these problems, we have also employed a CO flux asymmetry parameter, similar to the HI flux asymmetry parameter defined by Helou et al. (1981). The CO flux asymmetry parameter is defined by:

$$A_{COF} = \frac{F_+ - F_-}{F_+ + F_-} \qquad \text{(III-13)}$$

where F_+ and F_- refer to the CO fluxes along the major axes on the sides closest and furthest from M87. These are obtained simply by summing the observed CO intensities $\int T_A^* dv$ on the appropriate side of

the nucleus, excluding the central position. Key differences between A_{COD} and A_{COF} are that A_{COF} makes use of more data (A_{COD} depends almost entirely on only the outermost two positions), and A_{COF} is not model-dependent (as is A_{COD}). Thus A_{COF} should be a more reliable estimate of the intrinsic CO asymmetry.

We are interested in determining whether the observed asymmetries in the CO distributions of any of the Virgo galaxies are significantly higher than the CO asymmetries observed in well-studied, reasonably symmetric galaxies. The CO asymmetries of the Virgo galaxies have been compared with the CO asymmetries in M51 and NGC 6946, since these two face-on galaxies have fully sampled CO maps (Lord 1987; Tacconi 1987). If these galaxies were at the distance of the Virgo cluster, the 1 σ variation in CO intensities at a given radius with 45" resolution would be ~30% (see §3). Given a 1 σ scatter of 30%, the expected 1 σ variation in A_{COF} ranges from 0.15 for a source with 2 or 3 detections, to 0.09 for a source with over 5 detections. Similarly, the expected 1 σ variation in A_{COD} ranges from 0.05-0.08. There are uncertainties in the asymmetry parameters due to uncertainties in the integrated CO intensities. It is found that the formal 1 σ uncertainties in A_{COF}, from the propogation of CO intensity errors, range from 0.06-0.16 with a typical value of 0.11. Similarly, the formal 1 σ uncertainties in A_{COD} range from 0.04-0.10 with a typical value of 0.07. Thus the asymmetries which exist in reasonably symmetric galaxies (like M51 and NGC 6946) are comparable to the formal uncertainties in the asymmetry parameters. Figure 3.34 displays the 2 CO asymmetry parameters, normalized

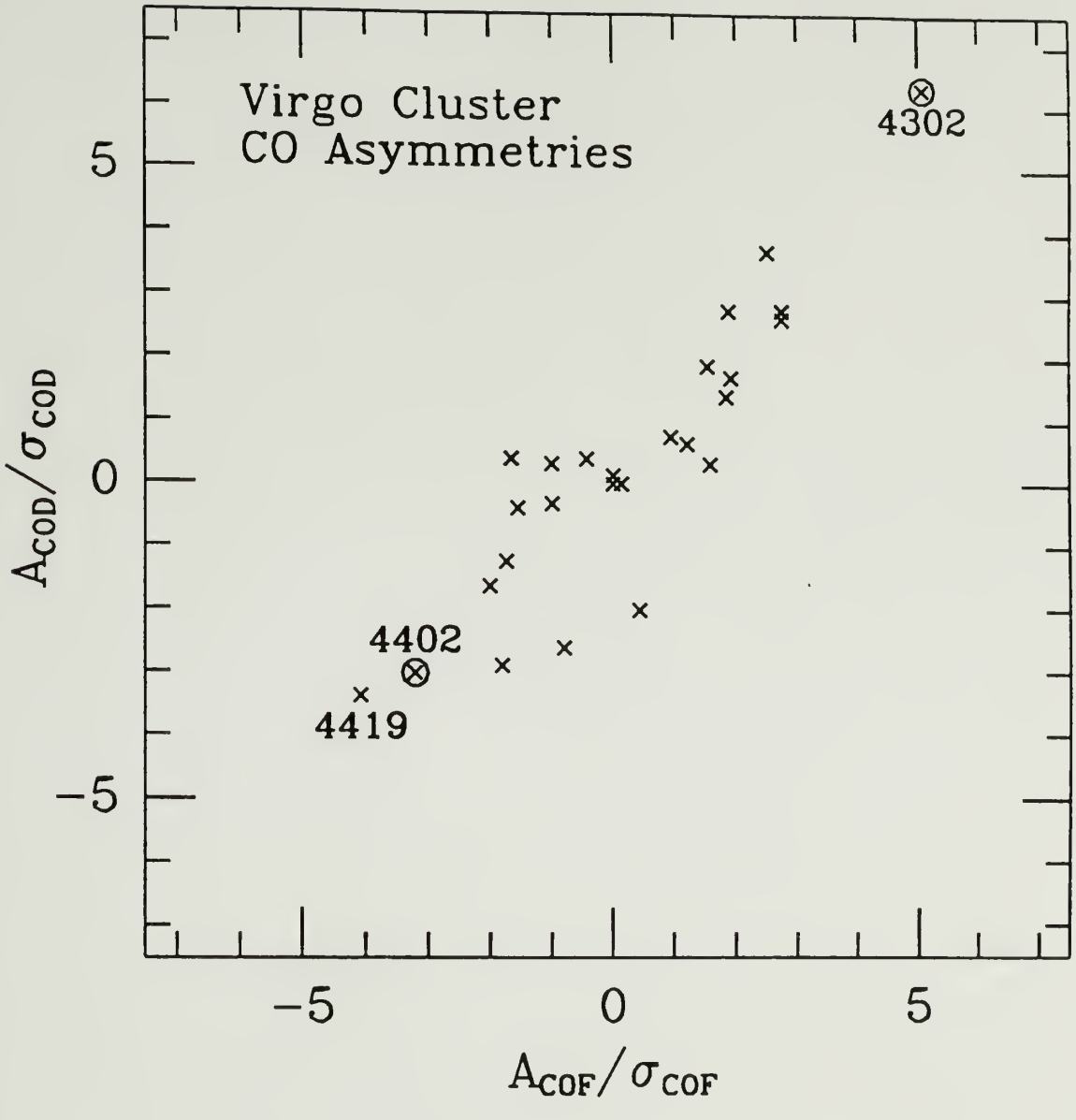

Figure 3.34 CO diameter asymmetry parameter vs. CO flux asymmetry parameter for Virgo spirals, each normalized by the 1 σ uncertainty. Both asymmetry parameters and the 1 σ uncertainties are defined in the text. The 2 galaxies whose crosses are circled may have artificially high asymmetry parameters.

by the 1σ uncertainties, for all the Virgo galaxies which have been detected in at least 2 positions. The 1σ values used in Figure 3.34 are the observed asymmetries in galaxies like M51 and NGC 6946, although these observed asymmetries are nearly equal to the 1σ formal uncertainties. There is a good correlation between the 2 asymmetry parameters, since they are not independent measures of asymmetry.

Only 3 Virgo galaxies have values of A_{COD} and A_{COF} which are both greater than 3σ. We believe that 2 out of the 3 galaxies with the largest values of CO asymmetries are not intrinsically very asymmetric, but have these large values because the central positions listed by Dressel and Condon (1976) do not refer to the true dynamical centers. NGC 4302 and NGC 4402 are both dusty, highly inclined galaxies with no obvious nuclear bulge. It is therefore difficult to determine the coordinates of their dynamical centers by inspection of an optical photograph, which was the method employed by Dressel and Condon. The CO line profiles of both NGC 4302 and NGC 4402, which are shown in Figures 3.6 and 3.11, are indicative of such an offset from the true nucleus. The central line profiles are asymmetric, and of the two spectra obtained on either side of the nucleus, the stronger line is asymmetric with a sharp cutoff on one side and a tail on the other. If the velocity fields and CO radial distributions in these galaxies are actually reasonably symmetric (as we suspect), then we find that the true dynamical center of NGC 4302 is ~27" south and ~1" east of the position listed by Dressel and Condon, while NGC 4402's center is ~12" west (estimates of the central coordinates are given in the notes to Table

3.3). For the galaxy modeling in §III.4, we have adopted these coordinates in the determination of the total CO fluxes of NGC 4302 and NGC 4402.

The third galaxy with large asymmetry parameters appears to be truly asymmetric. NGC 4419 is an inclined Sa galaxy with some dust near the center, but not enough to obscure the location of the nucleus. The bright nucleus is easy to identify on an optical photograph, unlike the nuclei of NGC 4302 and NGC 4402. The CO line profiles of NGC 4419 (shown in Figure 3.12) are reasonably symmetric, unlike NGC 4302 and NGC 4402. Inspection of a color photograph of NGC 4419 taken by R. Schild reveals that dust lanes are more prominent to the northwest side of the nucleus, where strong CO emission is detected. In view of this galaxy's large CO asymmetry, large HI deficiency, and large S_{CO}/S_{HI} ratio, we believe that this galaxy's ISM has been significantly modified by the Virgo environment. A discussion of NGC 4419's properties in the context of other Virgo galaxies is presented in §VI.8.

CHAPTER IV

THE RELATION BETWEEN CO EMISSION AND MOLECULAR GAS MASS

§1. Introduction

The utility of the CO emission line is that it is thought to be a reasonably good tracer of the mass within molecular clouds. It is perhaps a fluke of nature that this is so. Since ^{12}CO emission is generally optically thick, it is not a priori obvious that the ^{12}CO line is a measure of the mass within a molecular cloud. However, a dynamical property of molecular clouds apparently gives validity to the use of ^{12}CO line emission as a mass tracer; CO surveys of the Milky Way reveal a correlation between the size of a molecular cloud and its linewidth (e.g. Sanders, Solomon, and Scoville 1984). In other words, molecular clouds are virialized--larger clouds have larger linewidths, allowing ^{12}CO photons over a range of velocities, and therefore deep within the cloud to escape.

Three techniques have been used to estimate the mass of galactic molecular clouds. Hence, there are three forms of empirical evidence linking the total ^{12}CO emission line luminosity from a galactic molecular cloud with its total mass. Dickman (1978) demonstrated a linear correlation between (relatively optically thin) ^{13}CO column densities and visual extinction in dark clouds for extinctions up to $A_V = 5$ magnitudes. More recently, Dickman (1986) has extended this correlation up to extinctions of $A_V = 15$ magnitudes. A conversion factor bet-

ween ^{13}CO and H_2 column densities follows from this correlation, if the gas-to-dust ratio is known. Since ^{12}CO emission is more optically thick, it does not correlate as well with visual extinction along a given line of sight. However, it is an empirical fact that the cloud-averaged ^{12}CO to ^{13}CO line intensity ratios are remarkably similar from cloud to cloud (Solomon et al. 1979; Stark 1983). Young and Scoville (1982a) have used this fact to derive the $^{12}CO/N(H_2)$ ratio from A_v's and ^{12}CO line intensities for a given gas-to-dust ratio. This relationship constitutes the first part of the empirical evidence that ^{12}CO is a good tracer of molecular mass.

The observation that larger diameter molecular clouds have larger line widths is probably the physical basis for the similarity in cloud-averaged $^{12}CO/^{13}CO$ intensity ratios, and in itself leads to a second piece of evidence for a CO luminosity-mass correlation. While it cannot be demonstrated that clouds are in true virial equilibrium, the cloud diameter-linewidth relation indicates that a fixed proportion of the gravitational energy released in cloud formation is somehow converted to kinetic energy. Such clouds are said to be 'virialized', and their total mass can be crudely estimated by the virial theorem. CO can be used as a fairly reliable mass tracer since the CO line luminosities of galactic clouds correlate with their virial mass estimates.

A third method for estimating cloud masses involves a comparison of thelongitude distribution of gamma-rays with CO and HI emission. This is appealing since it is independent of excitation and metallicity effects, and free of assumptions about the virial theorem or gas-to-

dust ratios, although it depends upon the galactic distribution of cosmic rays. Most of the high-energy gamma-rays in the galaxy are the by-product of cosmic ray collisions with interstellar nucleons. In a study of the radial distribution and energy dependence of the galactic 70 MeV-5 GeV gamma-ray emissivity, Bloemen et al. (1986) have simultaneously solved for the radial distribution of cosmic rays and the large-scale distributions of interstellar nucleons. Their comparison of gamma-ray emissivity with HI and CO surveys reveals that the CO emission line luminosity is an excellent large-scale tracer of nucleons within molecular clouds between radii of 2 and ~15 kpc. In particular, this study found that the CO-H_2 ratio is independent of galactocentric radius between 2-15 kpc, within the uncertainties, despite the known metallicity gradient in the galaxy. The central few hundred parsecs of the galaxy does exhibit a strong CO peak without a correspondingly large gamma-ray peak (Blitz et al. 1985), yet it is presently unclear whether this is the result of an anomolous CO-H_2 proportionality factor, or the exclusion of cosmic rays from clouds near the nucleus of the galaxy.

The fact that all three of these methods yield CO-H_2 ratios which are similar to within a factor of 2 indicates that CO is a reliable large-scale tracer of molecular mass within the Milky Way. Unfortunately, none of these tests can currently be carried out in other galaxies, meaning that the galactic value must be applied cautiously. In the next section we discuss a theoretical prescription of the calibration factor, based on a virial theorem analysis. In

§IV.5, we discuss evidence for possible variations in the $CO-H_2$ proportionality factor.

§2. A Virial Theorem Analysis

Since the relation between CO integrated intensities and H_2 surface density cannot be directly measured in Virgo galaxies, we must instead analyze measurable quantities which may be related to the $CO-H_2$ proportionality factor. As a guide to help us determine which physical quantities are important, we summarize the virial theorem analysis of Dickman, Snell, and Schloerb (1986, hereafter DSS).

The relationship between CO line luminosities of clouds and their masses has been placed on firmer theoretical ground by the analysis of DSS. Making only two basic assumptions--that molecular clouds are virialized, and that the global CO emission profile of a galaxy can be treated as a simple superposition of independent, spatially-averaged molecular cloud profiles--DSS show that a linear correlation is expected between ^{12}CO integrated intensities and cloud mass surface density. This relation can be written as:

$$\sigma_o = b \int T_R(CO)dv \qquad \text{(IV-1)}$$

where σ_o represents the average mass surface density of clouds within the main beam (the mass of all the gas and stars within molecular clouds), and $\int T_R(CO)dv$ is the average main beam brightness (or radiation) temperature, which is corrected for atmospheric and coupling effects. In the case of a galaxy filled with identical clouds, the

constant of proportionality b is:

$$b = \frac{1}{T_o} \left\{\frac{4\rho}{3\pi\alpha G}\right\}^{1/2} \qquad \text{(IV-2)}$$

where T_o is the area-averaged cloud brightness temperature, ρ is the mean cloud density, and $\alpha \sim 2$ is a dimensionless parameter which corrects for geometry and density variations, and saturation broadening. In the more realistic case of a power law distribution of cloud sizes, a useful expression for b can be obtained if a cloud size-linewidth relation is assumed. The size-linewidth relation can be expressed as:

$$\Delta v(l_i) = \delta v_o \, (l_i/l_o)^{\beta} \qquad \text{(IV-3)}$$

where $\Delta v(l_i)$ is the observed half-intensity line width in a cloud of diameter l_i, and δv_o is the line width in a cloud of diameter l_o. With equation IV-3, the proportionality factor b becomes approximately:

$$b \sim \frac{1}{T_o} \frac{2\delta v_o}{\pi\alpha G} \frac{l_{max}^{\beta-1}}{l_o^{\beta}} \qquad \text{(IV-4)}$$

where l_{max} represents the diameter of the largest clouds in the galaxy. DSS give a more general expression for b, which includes explicit dependences on the lower size cutoff (l_{min}) and the cloud power law exponent. However, the value of b is not strongly dependent on either of these quantities in most cases, particularly as $l_{min} \to 0$.

Current estimates for β in the Milky Way range from $\beta \sim 0.38$ (Larson

1981) to $\beta \sim 0.55$ (Scoville et al. 1987), implying that $b \sim l_{max}^{-0.5}$. Thus the CO-H_2 proportionality factor is most sensitive to the mean gas temperature T_o, and less sensitive to either the mean cloud density ρ or the maximum cloud size l_{max}.

§3. The Relation Between CO Intensity and Molecular Gas Surface Density

One of the primary aims of this work is the comparison of the HI and H_2 masses within galaxies. As such, we wish to include only the H_2 component of the mass within molecular clouds. Estimates of a cloud's total mass by the virial theorem need to be corrected for the non-H_2 mass within the cloud. The only non-negligible mass 'contaminant' is probably helium, which is thought to comprise 27% of the gas mass of Milky Way interstellar clouds (e.g. Trimble 1975). Therefore the virial cloud mass estimates need to be divided by a factor of 1.36 to yield the H_2 mass within clouds.

The relationship between CO emission and H_2 mass is most conveniently expressed in terms of the area-averaged H_2 surface density within the main beam, σ_{H_2}, and the integrated-over-velocity main beam brightness temperature $\int T_R(CO)dv$, or:

$$\sigma_{H_2} = \chi \int T_R(CO)dv \qquad \text{(IV-5)}$$

The CO-H_2 proportionality factor in equation IV-5 has been denoted χ to distinguish it from both the quantity X defined by Bloemen et al. (1986), which is not in units of T_R, and the quantity b defined by DSS,

which includes the total mass of molecular clouds (and not just H_2). The T_R which appears in equation IV-5 is the average main beam brightness temperature, which is fully corrected for atmospheric and coupling effects, and is given by equations B-2 through B-4. It is related to the observable T_A^* by:

$$T_R = \frac{T_R^*}{\eta_c} = \frac{T_A^*}{\eta_c \eta_{fss}} \qquad \text{(IV-6)}$$

where the coupling efficiency η_c is estimated by model fitting, as described in Appendix B. For galaxy-to-galaxy comparisons, it is useful to estimate the face-on molecular mass surface density. This has been done by using the best-fitting model to estimate what $\int T_R(CO)dv$ would be if the galaxy were face-on, using equation III-10.

We adopt in this thesis a CO-H_2 proportionality factor of:

$$X = 2.8 \times 10^{20} \ H_2 \ cm^{-2}/K(T_R) \ km \ s^{-1} \ . \qquad \text{(IV-7)}$$

This is the value found by Bloemen et al. (1986) in their analysis of the galactic gamma-ray emissivity. The same factor is also found by comparing virial mass estimates and CO luminosities of over 1000 Milky Way molecular clouds (Scoville et al. 1987), if the value given in that paper is multiplied by a correction factor of $(1.7)^{-1/2} = 0.77$ to account for saturation broadening (DSS). While there are other studies of the CO-H_2 proportionality factor, some of which are based on a virial theorem analysis (see Bloemen et al. for summary), we have chosen these

two studies since they are completely independent, and are both based on large numbers of molecular clouds distributed throughout the galaxy. The good agreement for the two methods is perhaps fortuitous. Systematic uncertainties in the CO-H_2 calibration undoubtedly dominate the ~10% formal statistical uncertainties derived by Bloemen et al. and Scoville et al. The magnitude of the systematic uncertainty is probably a factor of ~2, as estimated by the range of proportionality factors derived by different groups (Bloemen et al. 1986).

One systematic uncertainty in the Bloemen et al. study is the unkown contribution to the gamma-ray emissivity from collisions of cosmic rays with ionized gas nucleons. Bloemen et al. have attributed all the gamma-rays to collisions of cosmic rays with neutral atomic (HI) and neutral molecular (H_2) gas nucleons. Therefore their CO-H_2 proportionality factor is strictly an upper limit. If the mass of gas in so-called 'warm ionized medium' is as great as Kulkarni and Heiles (1987) suggest, then the Bloemen et al. CO-H_2 proportionality factor should be revised downward by ~10-30%.

It is important to clarify which temperature is referred to in equation IV-5. Since the existence of a CO-H_2 proportionality is based upon a physical relationship between the mass of a molecular cloud and the number of CO($J=1\rightarrow0$) photons escaping from it, it is desirable to express the proportionality factor in terms of the telescope-independent radiation (or brightness) temperature T_R. Most authors of galactic CO studies have expressed their intensities in units of T_R^* (Kutner and Ulich 1981), which is equivalent to the radiation tem-

perature of a uniform source which fills a certain specified solid angle (for convenience often taken to be the size of the moon). T_R^* does not correct for the coupling between the beam and the source, and is therefore a telescope-dependent quantity. The telescope-independent T_R, which is corrected for source-beam coupling, is obtained if T_R^* is divided by the coupling efficiency η_c (equation IV-6). Calculations of coupling efficiencies have not, in general, been made by observers of galactic CO emission, in large part because the large angular size and irregular shape of galactic CO emission regions, combined with the poorly-known telescope error patterns, make this calculation difficult.

We point out that the intensities in the Columbia telescope galactic plane CO survey, on which the Bloemen et al. study is based, are expressed in units of the radiation temperature of uniform source which just fills the main beam (HPBW=8'). However for the Columbia telescope this differs from T_R^* by only 2% (Cohen, Dame, and Thaddeus 1986). The intensities in the Massachusetts-Stony Brook galactic plane CO survey, on which the Scoville et al. study is based, are expressed in units of T_R^*. However, since a galactic molecular cloud is typically ~30' in diameter, on average η_c ~1.0, and $T_R \sim T_R^*$. Thus while the coupling calculation on a cloud-by-cloud basis has not been attempted in either of the aforementioned galactic plane surveys, $T_R \sim T_R^*$ for both surveys in a statistical sense. We are therefore justified in expressing equation IV-7 in units of T_R without changing the numerical value of the proportionality factor.

Although $T_R \sim T_R^*$ for typical Milky Way clouds, there is a significant difference between T_R and T_R^* for external galaxies, whose angular size is typically less than a few arcminutes. From the calculations described in Appendix B, we find that η_c ranges from 0.4-0.8 for positions observed in Virgo galaxies, implying that $T_R \sim 1.2\text{-}2.5 T_R^*$.

As emphasized by DSS, equation IV-5 is not valid for individual lines-of-sight, but is valid if a number of independently-emitting molecular clouds are subtended by the telescope beam. This is the case for all the extragalactic CO observations reported in this work. It should be remembered that since clouds are not always distributed throughout the main beam, it is not always possible to reliably estimate σ_{H_2}. For galaxies which have unresolved CO emission, the use of equations B-2 through B-4 and IV-5 result in a lower limit estimate of the molecular mass surface density. For edge-on galaxies which have unresolved emission in only one direction (the minor axis), a face-on mass surface density can be estimated by galaxy modeling, if azimuthal symmetry is assumed.

§4. The Relation Between CO Flux and Molecular Gas Mass

For extragalactic studies, it is convenient to have an expression relating the total CO flux to the total molecular mass. From a combination of equation IV-5 with

$$S_{CO} = \frac{2k}{\lambda^2} \int\int T_R(\Omega, v) d\Omega dv \qquad \text{(IV-8)}$$

and

$$M_{H_2} = D^2 \int \sigma_{H_2}(\Omega) d\Omega \qquad \text{(IV-9)}$$

it is easily shown that

$$M_{H_2} = \chi \frac{\lambda^2}{2k} D^2 S_{CO} \qquad \text{(IV-10)}$$

or,

$$M_{H_2} = 3.93 \times 10^{-17} \chi D^2 S_{CO} \qquad \text{(IV-11)}$$

where, in equation IV-11, M_{H_2} has units of M_o, χ has units of solar masses H_2 cm^{-2} $K(T_R)^{-1}$ km^{-1} s, D is distance in megaparsecs, and S_{CO} is in Jy km s^{-1}. The critical quantity χ has been measured only within the Milky Way, and is not necessarily a universal constant. For χ = 2.8×10^{20} H_2 cm^{-2} $K(T_R)^{-1}$ km^{-1} s, which is adopted in this work from studies of Milky Way molecular clouds,

$$M_{H_2} = 1.1 \times 10^4 D^2 S_{CO} \qquad \text{(IV-12)}$$

where M_{H_2} is in M_o, D is in megaparsecs, and S_{CO} is in Janskys km s^{-1}. Since this value does not necessarily apply to all the Virgo galaxies, we discuss possible variations in §IV.5.

It is often useful to express the luminosity in the CO line. The relation between CO flux and CO luminosity in erg s^{-1} is given by:

$$L_{CO} = 4.65 \times 10^{32} D^2 S_{CO} \qquad \text{(IV-13)}$$

and in L_o by:

$$L_{CO} = 0.119\ D^2\ S_{CO} \qquad \text{(IV-14)}$$

where we have used 1 $L_o = 3.9 \times 10^{33}$ erg s^{-1}. For the value of χ adopted in this thesis, the relationship between M_{H_2} (in solar masses) and L_{CO} (in solar luminosities) is given, in solar units by:

$$M_{H_2} = 9.2 \times 10^4\ L_{CO} \quad . \qquad \text{(IV-15)}$$

§5. Possible Variations in the CO-H_2 Proportionality Factor

None of the three observational methods described in §IV.1 for measuring the CO-H_2 proportionality factor in the Milky Way have yet been fully carried out in another galaxy. However, there are both galactic and extragalactic observations which suggest that the CO-H_2 proportionality factor is not a universal constant. There is evidence that χ may be dependent upon temperature, density, metallicity and galaxy luminosity. These will be discussed in turn.

The $^{12}CO/^{13}CO$ line intensity ratios in other galaxies indirectly probe the CO-H_2 proportionality factor. Being more optically thin than ^{12}CO, ^{13}CO might naively be considered a more reliable tracer of H_2. However, the global $^{12}CO/^{13}CO$ ratios are difficult to interpret, since the emission from the two isotopic species may arise from different physical regions of a cloud corresponding to different temperatures, as a result of optical depth effects or chemical fractionation. Furthermore, the ^{13}C isotope may be enhanced relative to ^{12}C as the result of nucleosynthesis. While the $^{12}CO/^{13}CO$ ratio interpretation is not straightforward, the observed range of global values (e.g. Rickard

and Blitz 1985; Young and Sanders 1986) indicates that there is a range in the mean molecular cloud properties of galaxies. Although the variations in this ratio cannot easily be ascribed exclusively to variations in the CO-H_2 proportionality factor, it is possible that this is at least partially the case.

Evidence for this interpretation is presented in Young and Sanders (1986), who find a linear correlation between global $^{12}CO/^{13}CO$ intensity ratios and 60 μm/100 μm flux density ratios ($=S_{60\,\mu m}/S_{100\,\mu m}$) in a sample of 9 galaxies. The $S_{60\,\mu m}/S_{100\,\mu m}$ ratios, which are a probe of global dust temperatures, are highest in the galaxies with the largest $^{12}CO/^{13}CO$ intensity ratios. If the bulk of the 40-120 μm far-infrared radiation from most galaxies is associated with dust in molecular clouds (Young et al. 1986a), the large $^{12}CO/^{13}CO$ line intensity ratios in galaxies like M82 and NGC 1068 are probably due to higher gas temperatures. Although the physical regions probed by the CO emission (10K gas) and the 60-100 μm emission (25-40K dust) are different, the $^{12}CO/^{13}CO$ vs. $S_{60\,\mu m}/S_{100\,\mu m}$ correlation of Young and Sanders is strongly suggestive of a temperature dependence to the CO-H_2 calibration. (It should be pointed out that Young and Sanders do not interpret the correlation in this way.)

Although the observed $^{12}CO/^{13}CO$ vs. $S_{60\,\mu m}/S_{100\,\mu m}$ correlation suggests a temperature dependence to the CO-H_2 proportionality factor and a linear temperature dependence is theoretically expected, no temperature dependence has yet been observed among Milky Way clouds. Scoville et al. (1987) find no significant difference in the ratio of

cloud CO luminosity to virial cloud masses for cloud samples with mean peak CO temperatures of 11 K and 7 K. This surprising result needs to be confirmed and/or explained. It may be that gas temperature is correlated with some other cloud property which affects the virial mass determination. In fact, Scoville et al. find that for clouds of a given size, clouds with HII regions, which are systematically hotter, have larger linewidths than non-HII region clouds (at least for clouds with diameters $\leq$25 parsecs). This suggests that part of the turbulent kinetic energy of hot clouds is not derived from gravitational energy, and as a result the virial theorem overestimates the mass of these clouds.

Since the question of a temperature dependence is currently unsettled, we have adopted a constant CO-H_2 proportionality factor for all Virgo galaxies. If there is a linear temperature dependence then the actual CO-H_2 proportionality factor in the Virgo sample may span a factor of ~3, judging from the results of Young and Sanders (1986) and the range in global dust temperatures deduced from the 60 μm/100 μm flux density ratios of Virgo galaxies. In order to ensure that the assumption of a temperature-independent CO-H_2 proportionality factor does not influence any of our results, we will test relevant correlations in Chapters V and VI for a dependence on the $S_{60\,\mu m}/S_{100\,\mu m}$ ratios.

The study of Scoville et al. (1987) does find tentative evidence for a cloud size dependence on the Milky Way CO-H_2 calibration (or equivalently, a cloud density dependence, since cloud sizes are well correlated with mean cloud densities). The magnitude of this possible

dependence, which is a factor of ~2 in the CO-H_2 proportionality factor for a variation of a factor of ~4 in either the cloud diameter or mean cloud density, agrees well with the theoretical predictions of DSS (equations IV-2 and IV-4). Since there is no measurable parameter for Virgo galaxies which is obviously correlated with the cloud size distribution, it will be necessary to rely on theoretical arguments to assess the importance of this effect on the results presented in Chapters V and VI.

One physical parameter which does not explicitly appear in the DSS analysis, yet must be considered, is the abundance of metals. In one respect, variations in the metallicity have little effect on the CO-H_2 calibration, since ^{12}CO is so optically thick. If it were possible to remove 90% of the ^{12}CO molecules from a Milky Way molecular cloud without otherwise altering it, the cloud-averaged ^{12}CO line would appear much the same, since neither the CO brightness temperature nor the cloud velocity dispersion would change. The only difference would be that the cloud would have a smaller apparent surface area in CO, because the CO emission in the parts of the cloud with a small H_2 column density would become optically thin. However, since most of the CO-emitting surface of Milky Way molecular clouds is very optically thick, this effect would be small.

On the other hand, the low CO intensities observed in irregular galaxies (e.g. Elmegreen, Elmegreen, and Morris 1980; Tacconi and Young 1985; Israel et al. 1986) may be at least partly due to a higher value of the CO-H_2 proportionality factor, which may in turn be related to

their low metallicities. In a recent discussion on the weak CO emission in the Magellanic Clouds, Israel et al. (1986) observe out that the optical surface areas of giant dark clouds in both the LMC and the SMC are similar to the surface areas of Milky Way molecular clouds, yet the LMC and SMC molecular cloud complexes have CO brightness temperatures ~4 times lower than typical Milky Way clouds. Israel et al. suggest that the stronger ultraviolet radiation field of the Magellanic Clouds, together with their low metallicities and associated low dust-to-gas ratios produce a CO-H_2 proportionality factor which is a few times higher than that in the Milky Way. However, we point out that the abundance of H_2 in the Clouds is still unknown. Thus, an alternative explanation for the CO emission in the Clouds is a dearth of molecular gas.

Dust is generally believed to shield CO molecules from the destructive dissociating power of the UV radiation (although see Glassgold, Huggins, and Langer (1985) on the possibility that CO might be self-shielding). Thus the lower dust-to-gas ratio, lower metallicity, and stronger UV field in the Magellanic Clouds all result in a decrease in the apparent size of a CO-emitting region. (These effects may therefore all be incorporated into the DSS formulation through the cloud size parameter (l or l_{max}) if the cloud size is suitably defined.) While their individual effects on the CO-H_2 proportionality factor may not be large, their combined effect can be large. It is important to note that these three effects are not completely independent, and that all may result in part from a lower metallicity. Dust

is formed from metals, so that a lower dust-to-gas ratio is expected in a low metallicity galaxy. Dust absorbs UV radiation and reradiates energy in the infrared, so that in a galaxy with a lower dust content, a higher fraction of the UV radiation avoids absorption. These effects influence the abundances of both CO and H_2, but might be expected to affect the abundance of CO more severely than that of H_2. Molecular hydrogen is self-shielding, so that a lower dust-to-gas ratio does not strongly affect the H_2 destruction rate. However, H_2 forms on the surface of dust grains so that a lower dust-to-gas ratio reduces the H_2 formation rate. Thus, the characteristic of a lower dust-to-gas ratio which affects the abundances of CO and H_2 most differently is the increased destruction rate of CO molecules. The physical properties of the ISM in the Magellanic Clouds (i.e. lower dust-to-gas ratio, higher UV radiation density) suggest that both CO and H_2 abundances will be reduced in the Clouds, but that the CO abundances may be more significantly reduced. Consequently, the CO-H_2 proportionality factor may be systematically higher in galaxies like the Magellanic Clouds.

It is likely that the possibly higher CO-H_2 proportionality factor in the Magellanic Clouds is associated with low metallicity, low galactic mass, and low galactic luminosity. Bothun et al. (1984) interpret a relation between (J-K) color and H magnitude for late-type cluster galaxies as a relationship between metallicity and luminosity. If their interpretation is correct, then the metallicity varies by 1 or 2 orders of magnitude over a range of 5 magnitudes in absolute luminosity. In view of this result and the low ratio of CO luminosity to

blue luminosity in low mass galaxies (Tacconi and Young 1985), we must consider a possible luminosity-dependence to the CO-H_2 calibration.

In one respect, a luminosity-dependent CO-H_2 proportionality factor should not greatly affect results in this thesis, since the Virgo galaxy sample was selected to have a range of only 2 magnitudes in blue luminosity. The LMC is ~1.5 magnitudes fainter than the faintest Virgo galaxy in our sample, so that if the adopted constant CO-H_2 proportionality factor becomes invalid below a certain threshhold luminosity (or mass), then the effect on our results will be minimal. There is reason to be cautious, however, since the difference in absolute magnitude between the Milky Way and the LMC is only ~2 magnitudes (deVaucouleurs and Corwin 1986). In order to ensure that the presence of a luminosity-dependent CO-H_2 proportionality factor does not affect the results in Chapters V and VI, we will test all of the relevant correlations for a luminosity dependence.

CHAPTER V

MOLECULAR AND ATOMIC GAS PROPERTIES OF VIRGO SPIRALS

§1. Introduction

The aim of this chapter is to determine how the CO properties of the Virgo spirals have been altered by the cluster environment. An effective way to assess this would be to compare the Virgo galaxies with a suitable control sample of isolated galaxies. However, the CO data for such a control sample does not yet exist. Because of the large amount of observing time required, it was not possible to collect data for both a Virgo and an isolated galaxy sample. Instead, the analysis will be based on intercomparisons within the cluster. While it is clearly preferable to have both intracluster and cluster vs. non-cluster comparisons, the intracluster comparisons do have several advantages. 1.) Since the Virgo sample is a complete, magnitude-limited sample of galaxies at the same distance, all Virgo spirals above some optical luminosity have been observed. The resulting lack of strong selection effects contrasts with any isolated galaxy comparison sample, which would contain galaxies at different distances and therefore be subject to the Malmquist bias and other selection effects. 2.) All the galaxies are at the same distance (±20% due to the 3-dimensional nature of the cluster, see Chapter II), so that the scatter which is introduced in correlations because of distance uncertainties is not a large factor here. 3.) Part of the analysis will be

based on HI observations of a control sample of isolated galaxies, but not CO observations. We will utilize the HI deficiency parameter, which is a measure of a galaxy's HI content with respect to a typical isolated galaxy. It is the comparison of the HI contents of Virgo and isolated galaxies that lead to the conclusion that many Virgo spirals are deficient in atomic gas (Davies and Lewis 1973; Chamaraux et al. 1980; Giovanelli and Haynes 1983). The "normal" HI content of a spiral galaxy is now based on HI observations of over 300 isolated galaxies (Haynes and Giovanelli 1984), a much larger sample than will be attainable through CO measurements anytime in the near future. While there are still some selection effects present in this HI isolated galaxy sample, the large number of objects minimizes their impact on our conclusions. In this chapter, comparisons are made between the CO properties of the HI-normal and HI-deficient Virgo galaxies. Under the assumption that the HI-normal Virgo spirals are "normal" in their CO properties (i.e. typical of isolated galaxies), using the HI deficiency parameter is tantamount to having a large body of CO data on isolated galaxies.

§2. Optical and HI Data Used in Analysis

A compendium of the observed optical and HI data which will be compared with the CO data is presented in Table 5.1. The morphological types (column 2) used in this chapter's analyses are taken, where possible, from Binggeli, Sandage, and Tammann (1985, hereafter BST), who used high quality plate material for the galaxy classification.

Explanation of Columns in Table 5.1:

(1) NGC number of galaxy.

(2) Morphological type, based mostly on Binggeli, Sandage, and Tammann (1986), and coded according to:

1=S0	6=Sbc
2=S0/a	7=Sc
3=Sa	8=Scd
4=Sab	9=Sd-Sm
5=Sb	p=peculiar

(3) Blue optical magnitude B_T^o, corrected for inclination and galactic extinction. B_T from deVaucouleurs and Pence (1979), $B_T - B_T^o$ from RC2, or computed according to RC2.

(4) Blue isophotal diameter D_o, at 25 mag arcsec^{-2}, corrected for inclination and galactic extinction, from RC2.

(5) 21 cm HI line flux, all from Arecibo observations. Source of data is indicated by first entry in column 11. Upper limits are 3σ. Galaxies with velocities near zero are confused with galactic HI emission, and have been corrected for this by the authors. NGC4567 and NGC4568 cannot be resolved by the Arecibo beam; the flux is given for the pair as a whole (see text).

(6) HI line width at 20% of peak intensity; data source indicated by first entry in Column 11; values in parentheses are lower limits based on CO line width in central 45" aperture.

(7) Effective HI diameter, as defined in §5.2; data source indicated by first entry in column 11.

(8) Isophotal HI diameter, as defined in §5.2; data source indicated by second entry in column 11.

(9) HI flux asymmetry parameter, as defined in §5.2; data source indicated by first entry in column 11.

(10) HI diameter asymmetry parameter, as defined in §5.2; data source indicated by second entry in column 11.

(11) Reference key for HI data. The first entry indicates the source of data for HI flux (column 5), HI line width (column 6), effective HI diameter (column 7), and HI flux asymmetry parameter (column 9). The second entry indicates the source of data for isophotal HI diameters (column 8), and HI diameter asymmetry parameters (column 10).

a=Giovanelli and Haynes 1983
b=Helou, Hoffman, and Salpeter 1984
c=Giovanardi, Krumm, and Salpeter 1983
d=Helou et al. 1981
e=Warmels 1986
f=van Gorkom and Kotanyi 1986

Table 5.1

Observed Optical & HI Properties of Virgo Galaxies

Galaxy NGC	Type	B_T^o	Optical Diameter (arcmin)	HI Flux (Jy km s^{-1})	HI Line Width (km s^{-1})	HI Diameters D_{eff} (arcmin)	HI Diameters D_{iso} (arcmin)	HI Asymmetries A_{HIF}	HI Asymmetries A_{HID}	HI Ref
(1)	(2)	(3)	(4)	(5)	(6)	(7)	(8)	(9)	(10)	(11)
4064	3	11.74	3.9	1.2	207	<2.2				b,
4178	7	11.35	4.2	66.6	277	4.8	7.6	-0.04	0.00	a,e
4192	5	10.31	7.8	83.7	477	8.8	11.0	+0.18	+0.09	a,e
4212	7	11.52	2.9	12.0	282					b
4216	5	10.29	6.3	33.7	546	6.4	7.8	0.00	+0.09	a,e
4254	7	10.13	5.5	72.0	268	4.2	8.0	+0.05	+0.14	a,e
4293	3p	10.80	5.4	<1.0	(>200)					c
4298	7	11.75	2.9	12.9	273	<2.2				b
4302	7	11.86	3.8	25.7	383	5.1				b
4303	7	9.95	6.2	99.1	175	6.6	8.0	+0.02	0.00	a,e
4312	4	11.97	3.6	1.8	227	<2.2				b
4321	7	9.89	7.1	38.0	266	5.2	7.2	+0.10	+0.06	a,e
4380	4	11.98	3.4	3.0	303	3.2				b
4388	4	11.20	4.0	5.3	360	<2.6	>2.4	+0.15	-0.09	a,e
4394	5	11.47	4.1	4.7	171		4.6		-0.02	d,e
4402	7	12.01	3.2	7.2	289	<2.6	>2.6	(-0.38	+0.10)	a,e
4419	3	11.73	2.8	1.7	397					c
4424	3	11.87	3.4	2.8	(>120)	2.3				b
4438	5p	10.43	7.9	6.1	350					c
4450	4	10.63	4.7	4.4	317	<2.6	3.7	+0.19		a,f
4501	6	9.85	6.3	30.4	541	3.8	6.6	+0.26	-0.11	a,e
4526	1	10.15	5.9	<0.7	-					c
4527	5	10.92	5.2	116.0	381	9.0		-0.04		a
4532	9	11.69	3.0	42.3	208	3.2				b
4535	7	10.22	6.6	85.3	290	7.6	8.6	-0.15	-0.04	a,e
4536	7	10.52	6.5	69.1	304	6.2		-0.12		a
4548	5	10.72	5.4	10.7	264	3.8	5.2	+0.09	-0.02	a,e
4567	7	11.78	2.8	21.4	211		2.0			b,f
4568	7	11.27	4.0		338		4.0			b,f
4569	4	9.86	8.3	12.4	399	3.2	4.0	-0.04	-0.25	a,e
4571	7	11.63	3.8	15.1	163	5.4	4.6	-0.13	-0.03	a,e
4579	4	10.31	5.4	11.2	366	3.8	4.8	-0.09	+0.21	a,e
4639	5	11.88	2.8	15.8	292		4.6	-0.10	+0.07	d,e
4647	7	11.82	3.0	8.2	209	<2.2	>3.0		+0.02	b,f
4651	7	10.99	3.6	57.2	390		8.1	+0.12	+0.07	d,e
4654	7	10.82	4.4	56.3	309	4.6	7.2	-0.23	-0.25	a,e
4689	7	11.34	4.1	9.1	206	2.8	3.6		+0.10	b,e
4698	3	11.15	3.9	50.3	445		9.8		-0.02	b,e
4710	1	11.30	3.9	<1.7	(>300)					c
4713	7	11.83	2.6	58.2	186	4.9	>8.0		-0.05	b,e
4808	7	11.93	2.3	85.3	280	6.3				b
4866	3	11.12	4.8	28.2	557	10.6		-0.15		a

For the galaxies outside the range of the BST survey, RSA classifications are used, with one exception. Although the RSA classifies NGC 4064 as an SBc galaxy, we use the RC2 and UGC SBa classification. An examination of the galaxy image on the Palomar Plates reveals that the low surface brightness outer disk is featureless, with no suggestion of spiral structure. The inner region of the galaxy has a high surface brightness area which appears to be bulge-dominated. With a medium value of the bulge-to-disk ratio (B/D) and very weak spiral structure, NGC 4064 is more properly considered an early type galaxy. An Sa classification is also consistent with the observation of Dressler (1986) that early type cluster galaxies tend to have radial orbits in the cluster, while late type cluster galaxies tend to have isotropic orbits. NGC 4064 has a radial velocity which is only ~200 km s^{-1} different from the mean cluster velocity (compared to a line-of-sight velocity dispersion of 817 km s^{-1} for spirals; Huchra 1985), and is located a distant 8.5° from M87, consistent with a predominantly radial orbit.

Blue optical magnitudes, B_T^o (column 3), are taken from the carefully calibrated catalog of deVaucouleurs and Pence (1979), while the corrections for inclination and galactic extinction, $B_T^o - B_T$, are taken from the RC2 (deVaucouleurs, deVaucouleurs, and Corwin 1976). Isophotal optical diameters, D_o (column 4), which are measured in blue light at an isophote of 25 mag $arcsec^{-2}$ and are corrected for inclination and galactic extinction, are also taken from the RC2.

The HI flux data (column 5) are taken from several sources,

although most of the data comes from the work of two groups, and all were obtained with the sensitive Arecibo telescope. Since our Virgo sample was chosen to be a subset of the Helou et al. (1981, 1984) sample, HI fluxes for most of the galaxies can be found in their papers. However, we have used the fluxes from Giovanelli and Haynes (1983, hereafter GH83) where available, rather than those in Helou et al. (1981), since GH83 sampled more positions along the major axis of each galaxy, and calibrated the spectra more accurately, according to GH83. For five of the S0-Sa galaxies, we have used the sensitive measurements of Giovanardi, Krumm, and Salpeter (1983). For galaxies observed by more than one group, agreement is generally very good, except for those cases discussed by GH83. A comparison of the fluxes for galaxies in common suggests that the typical 1σ uncertainty is ~20%.

There are several galaxies in the sample which are members of binary systems (NGC 4298, NGC 4302, NGC 4394, NGC 4567, NGC 4568, and NGC 4647). Of these, there is one system which appears to be in close contact. The interacting binary Sc pair NGC 4567/4568 is unresolved by the Arecibo beam (HPBW=3.2'); consequently the HI flux in column 5 is given for the pair as a whole (Helou et al. 1984, hereafter HHS). On the basis of the VLA map of this pair (van Gorkom and Kotanyi 1986), which partially resolves the galaxies, it appears that 78±10% of the emission is associated with NGC 4568 and 22±10% with NGC 4567. However, since we wish to avoid complications due to the possible transfer of loosely bound HI gas from one galaxy to the other, we will

treat the pair as a single entity in comparisons of the global properties.

Global HI linewidths, which can be used to estimate total galactic masses, are listed in column 6. These linewidths are measured at 20% of the peak intensity. For galaxies which remain undetected in HI, a lower limit to the global linewidth is provided by the CO linewidth in the central 45". NGC 4424 is also listed as a lower limit, even though HI has been detected in it, since its line profile is suspiciously small (Helou et al. 1984). It may be that HI is confined to the very central region of this galaxy, so the HI line does not sample the higher velocity outer disk regions.

Two types of HI diameters are used in the analysis, corresponding to the CO isophotal and effective diameters. The effective HI diameters (column 7) are obtained from 2 sources. GH83 have computed D_{70}, the diameter which contains 70% of the total HI flux, which is defined in exactly the same way as the effective CO diameters in Chapter 3. For galaxies not observed by GH83, but included in HHS, we have used 1.09D(1/e) as the effective HI diameter. D(1/e) is the diameter where the HI flux falls to 1/e of the central position. This is a fundamentally different quantity than D_{70}, but HHS find that $D_{70}/D(1/e) = 1.09 \pm 0.14$ for the galaxies in common with GH83.

Isophotal HI diameters (column 8) are measured where the face-on HI surface density falls to 1 M_o pc^{-2}, and are taken from Warmels (1986), if available, or van Gorkom and Kotanyi (1986). The values from the Westerbork observations of Warmels have been corrected for

inclination by the author. The values for the VLA observations of van Gorkom and Kotanyi have been corrected by cos(inclination). With two exceptions, there is excellent agreement between the Westerbork and VLA isophotal diameters. The Westerbork diameters are significantly larger for both NGC 4569 (D_W/D_{VLA}=1.45) and NGC 4579 (D_W/D_{VLA}=1.60). For the other 10 galaxies in common, D_W/D_{VLA}=1.09±0.09. Since the synthesized beams for the VLA observations of NGC 4569 and NGC 4579 are smaller than the beams for the Westerbork observations and most of the other VLA observations, it may be that the VLA maps of NGC 4569 and NGC 4579 have missed some extended emission in these galaxies.

Two types of asymmetry parameters are listed in Table 5.1: HI flux and HI diameter asymmetry parameters. The HI flux asymmetry parameter (column 9) is based on Arecibo observations (GH83 and HHS), and is defined in the same way as the CO flux asymmetry parameter (see equation III-12). Both CO and HI flux asymmetry parameters are measured along the major axes of the galaxies, yet the large difference in resolution (45" for CO vs. 3.2' for HI) and radial distributions means that the same regions are not being compared.

The HI diameter asymmetry parameter (column 10) is taken from Warmels (1986), but with a different sign convention. Warmels defined a positive asymmetry in the case of a galaxy with a larger HI extent on the eastern side; we define a positive asymmetry if the HI extent is greater on the side closest to M87. Thus, for galaxies west of M87, the sign of A_{HID} in column 10 is the same as Warmels, while for galaxies east of M87, the signs are reversed. There are important dif-

ferences between the Westerbork A_{HID} and A_{COD} defined in III.7. The Westerbork observations sampled the entire galaxy and measured asymmetries along east-west axes, while the CO observations undersampled the emission and measured asymmetries along the major axes. Furthermore, the HI diameters are measured further out in the disk and at a lower surface density than the CO diameters (1.0 M_o pc^{-2} for HI vs. 6.8 M_o pc^{-2} for CO). Apart from these differences, A_{HID} is defined in the same way as A_{COD} (equation III-11).

A summary of derived galaxy properties, using the observed quantities from Table 5.1, is presented in Table 5.2. The distance to every galaxy is assumed to be 20 Mpc. Columns 2 and 3 give the blue optical luminosities and linear diameters. Columns 4 and 5 list quantities which are related to the galactic mass. The mass of a galaxy within a given radius can be determined from its rotation curve. Under the assumption of a spherical mass distribution, the mass contained within a radius R, M(R), is given in M_o by:

$$M(R) = 6.7 \times 10^4 \; R \; D \; V(R)^2 \qquad \text{(V-1)}$$

where R is in arcminutes, the distance D is in megaparsecs, and the rotational velocity V(R) in the plane of the galaxy at a galactocentric distance R is in km s^{-1}. Most galaxies have rotation curves which are flat, or which rise slowly in the outer disk (Rubin et al. 1985), allowing V(R) to be approximated as a constant in the outer disk. Widely available HI linewidths, W_{HI}, can be used to estimate the maximum rotational velocity, V_{max}, by the relation:

Explanation of Columns in Table 5.2:

(1) NGC number of galaxy.

(2) Blue optical luminosity, from B_T^o, assuming 0.00 magnitudes equals 4440 Jy (Johnson 1966), $L_o = 3.9 \times 10^{33}$ erg s^{-1}, D = 20 Mpc.

(3) Linear blue optical diameter, from D_o (RC2).

(4) Maximum rotation velocity in disk, computed from $W_{HI} = 2(V_{max} \sin(i) + V_t)$; values in quotes are lower limits from central 45" CO linewidths.

(5) Total (indicative) mass within the 25.0 mag arcsec^{-2} isophote; computed from $M(R) = 6.7 \times 10^4 R D V_{max}^2$, with M(R) in M_o, R in kpc, D in Mpc, and V_{max} in km s^{-1}; values in quotes are lower limits from central 45" CO linewidths.

(6) HI mass, computed from $M_{HI} = 2.36 \times 10^5 D^2 S_{HI}$, with M_{HI} in M_o, D in Mpc, and S_{HI} in Jy km s^{-1}, upper limits are 3 σ.

(7) HI deficiency parameter, as defined in §5.2.

(8) Luminosity in CO(J=1→0) emission line, upper limits are 2 σ.

(9) H_2 mass, computed from $M_{H_2} = 1.1 \times 10^4 D^2 S_{CO}$, with M_{H_2} in M_o, D in Mpc, S_{CO} in Jy km s^{-1}, upper limits are 2 σ.

Table 5.2

Derived Optical, HI, CO, and Mass Properties of Virgo Galaxies

Galaxy NGC (1)	L_B (10^9 L_o) (2)	D_{opt} (kpc) (3)	V_{max} (km s^{-1}) (4)	M_{tot} (10^9 M_o) (5)	M_{HI} (10^8 M_o) (6)	HI Def (7)	L_{CO} (10^3 L_o) (8)	M_{H_2} (10^8 M_o) (9)
4064	12.6	23	99	26	1.1	0.99	4.4	4.1
4178	18.0	24	135	52	62.9	-0.13	2.9	2.6
4192	46.9	45	236	290	79.0	0.09	44.7	41.4
4212	15.4	17	176	61	11.3	0.44	24.3	22.4
4216	47.8	37	265	296	31.8	0.35	29.5	27.3
4254	55.4	32	260	249	68.0	0.02	143.0	132.0
4293	29.9	31	(>91)	(>30)	<0.9	-	12.9	11.9
4298	12.5	17	135	36	12.2	0.54	31.4	29.0
4302	11.3	22	180	82	24.3	0.15	29.5	27.3
4303	65.3	36	179	133	93.6	0.17	109.0	100.0
4312	10.2	21	104	26	1.7	1.27	7.6	7.0
4321	69.1	41	258	316	35.9	0.52	159.0	147.0
4380	10.1	20	170	66	2.8	1.05	<2.9	<2.6
4388	20.7	23	171	79	5.0	1.06	10.9	10.1
4394	16.1	24	174	83	4.4	0.85	13.3	12.3
4402	9.8	19	137	40	6.8	0.61	30.0	27.7
4419	12.7	16	203	77	1.6	1.06	43.8	40.5
4424	11.1	20	(>55)	(>7)	2.6	1.09	2.7	2.4
4438	42.0	46	176	164	5.8	1.28	10.0	9.2
4450	34.9	27	207	135	4.2	1.31	21.4	19.8
4501	71.6	37	305	392	28.7	0.47	105.0	96.8
4526	54.3	34	-	-	<0.7	-	<4.3	<4.0
4527	26.7	30	188	123	110.0	-0.35	86.2	79.6
4532	13.2	17	106	23	40.0	-0.30	<2.9	<2.6
4535	51.0	38	195	168	80.5	0.17	74.7	69.1
4536	37.6	38	152	101	65.2	0.03	35.2	32.6
4548	32.2	31	199	144	10.1	0.86	25.7	23.8
4567	12.1	16	130	32	20.2	0.64	23.8	22.0
4568	19.4	23	175	82			51.9	48.0
4569	71.0	48	210	246	11.7	0.99	71.4	66.0
4571	13.9	22	113	32	14.3	0.44	18.1	16.7
4579	46.9	31	284	292	10.6	1.00	43.3	40.0
4639	11.0	16	190	67	14.9	0.16	<3.3	<3.0
4647	11.7	17	157	50	7.7	0.51	28.6	26.4
4651	25.1	21	254	156	54.0	-0.16	16.7	15.4
4654	29.3	26	181	96	53.1	0.00	34.7	32.1
4689	18.2	24	182	91	8.6	1.06	33.8	31.2
4698	21.6	23	251	165	47.5	0.25	<4.3	<4.0
4710	18.8	23	(>138)	(>50)	<1.6	-	9.5	8.8
4713	11.6	15	107	20	54.9	-0.30	<3.3	<3.1
4808	10.5	13	141	31	80.5	-0.68	<4.8	<4.4
4866	22.2	28	267	23	26.6	0.24	<4.3	<4.0

$$W_{HI} = 2(V_{max}\sin(i) + V_t) \qquad (V\text{-}2)$$

where i is the galaxy inclination, and V_t is the non-rotational (turbulent) velocity component. Values for V_{max} are listed in column 4, using the HI linewidths from Table 5.1, and assuming that V_t = 10 km s^{-1}. In column 5, we list M_{tot}, the total (indicative) mass within the 25 mag $arcsec^{-2}$ blue isophote ($D_o/2$), under the assumption that V_{max} = $V(D_o/2)$.

The total HI mass, in column 6, is computed from the standard relation:

$$M_{HI} = 2.36x10^5 \, D^2 \, S_{HI} \qquad (V\text{-}3)$$

where M_{HI} is in M_o, D is the distance in Mpc, and S_{HI} is in Jy km s^{-1}.

As a measure of the 'normalcy' of the HI content of the Virgo galaxies, we employ the HI deficiency parameter of GH83, which is similar to the original measure of HI deficiency by Chamaraux et al. (1980). In a study of the HI content of 324 isolated galaxies, Haynes and Giovanelli (1984, hereafter HG84) demonstrated that the HI mass of an isolated galaxy depends mainly on its optical diameter, and only slightly on its morphological type. Their detailed study confirms the original suggestion by Shostak (1978) that the HI surface density averaged over the optical disk is nearly constant among (isolated) galaxies. Since the type dependence for types Sa-Sm is slight, we follow GH83 in adopting an HI deficiency parameter which is independent of morphological type. The formula we use for the 'expected' HI mass

is (GH83):

$$\log M_{HI}(\text{isolated}) = 7.01 + 0.88 \log D_{opt}{}^2 \qquad (V\text{-}4)$$

where M_{HI} is measured in solar units, and the optical diameter D_{opt} in this relation is the Holmberg diameter, measured in kiloparsecs to a surface brightness of 26.5 mag arcsec^{-2}. The good correlation of HI mass and optical diameter in isolated galaxies allows a useful parameterization of the normalcy of any galaxy's HI content to be defined as (GH83):

$$\text{HI def} = \log M_{HI}(\text{isolated}) - \log M_{HI}(\text{actual}) \; . \qquad (V\text{-}5)$$

HI deficiency values for the Virgo sample are listed in column 7 of Table 5.2. These have been taken from Giovanelli and Haynes (1985), or computed according to the precepts in GH83. Although we have adopted a type-independent HI deficiency parameter, there is evidence (e.g. HG84) that isolated Sa-Sab galaxies have, on average, ~0.1-0.2 dex less HI mass for their optical area than late type spirals. The magnitude of this effect is comparable to the 1σ scatter in HI masses for isolated galaxies of a given type and optical size, which is ~0.2 in the log (HG84). In order to be cautious about the possible type dependence, we will analyze early and late type spirals separately.

It is important to emphasize, as have Chamaraux et al. (1986), that the HI deficiency parameter only has meaning in a statistical sense. HI def does not represent the actual HI deficiency of a galaxy, but the deficiency it would have if its "initial" HI content were exactly the same as the average for its type and size. From the

scatter in the HI masses in isolated galaxies of a given type and optical diameter, we deduce that the HI deficiency parameter yields the actual HI deficiency to within a 1σ uncertainty of $\sim$0.2.

Finally, we point out that the "normal" HI content of S0 galaxies is not well established, due to the large fraction of S0's which remain undetected (e.g. Wardle and Knapp 1986; Chamaraux et al. 1986). Because of this, it is not possible to define an HI deficiency parameter for S0's. There are 2 Virgo S0 galaxies (NGC 4526 and NGC 4710) which are not part of the complete, magnitude-limited sample, yet were mapped in CO. These galaxies, which remain undetected in HI, will not be included in any analysis which utilizes the HI deficiency parameter. In addition, NGC 4293, which is classified as a Sa pec by BST and as SBO/a by RC2 and is part of the complete, magnitude-limited sample, will not be included in any HI deficiency plots. It too remains undetected in HI despite a sensitive search. From its 3σ upper limit on HI flux (Giovanardi, Krumm, and Salpeter 1983), equations V-1 and V-2 would yield HI def $>$ 1.80 for NGC 4293, an extremely large value. On the basis of its early type classification, its low HI content, and other similarities to NGC 4710, we will discuss NGC 4293 together with NGC 4526 and NGC 4710 separately in Chapter VI.

The total luminosity in the CO line, in solar units, is listed in column 8. The total mass of molecular hydrogen, given in column 9, is computed from:

$$M_{H_2} = 1.1 \times 10^4 \, D^2 \, S_{CO} \qquad \text{(V-6)}$$

where M_{H_2} is in M_o, D is in Mpc, and S_{CO} is in Jy km s^{-1}. This relation, which is derived in §IV.4, is based on a CO-H_2 proportionality factor $\chi = 2.8 \times 10^{20}$ H_2 cm^{-2} $K(T_R)^{-1}$ km^{-1} s.

§3. Comparison of CO Luminosities with Galaxian Mass and Optical Properties

In order to assess how 'normal' the CO emission is in Virgo cluster galaxies, it is necessary to find a parameter which compensates for the size, or mass, or number of stars within the galaxies. This is best done with CO observations of a large sample of isolated galaxies, which do not yet exist. Hence we examine the Virgo sample itself for a suitable normalization parameter. Cluster interaction-related phenomena add scatter to all the correlations which are presented, and may even introduce systematic trends, thereby reducing their reliability as predictors of 'normal' or 'average' behavior. For our purposes, however, the normalization relations derived from the Virgo sample will prove adequate.

One way to assess the normalcy of CO emission is to compare it with emission from starlight. For this purpose, it would be desirable to use light in a band which is dominated by old stars, such as H band (1.6 μm). Since H magnitudes are not available for the entire Virgo sample, readily available B magnitudes are used instead. B magnitudes are less than an ideal choice, since different stellar populations contribute to the blue light from galaxies. It has been estimated (e.g. Schweizer 1976) that as much as ~50-70% of the blue light in

'normal' galaxies with small B/D arises from stars which are less than 2×10^9 years old. Thus ~30-50% of the blue light from Sc galaxies comes from older stars, while for galaxies with larger B/D, the fraction coming from old stars is even larger. Since the contribution to the blue light from recent star formation varies significantly among galaxies, we must identify possible biases which may affect the conclusions. One important bias has been identified. Since the sample galaxies were chosen on the basis of their blue magnitudes, the lower luminosity end of the sample will contain low mass galaxies with blue B-H colors that are actively forming stars. Yet, spirals of comparable mass, but with redder B-H colors and less star formation, will fall below the magnitude cutoff, and not be included in the sample. The effects of this bias will be discussed where relevant.

Global CO fluxes are plotted vs. B_T^o in Figure 5.1a, where the different symbols represent different morphological types. The same data, but with error bars plotted, appear in Figure 5.1b. In order to enable the reader to more clearly identify the different morphological types, all subsequent figures will display only a mean error bar. Figures 5.2 and 5.3 display CO fluxes vs. the blue isophotal optical diameters and indicative masses. The relations exhibited in Figures 5.1 - 5.3 are all very similar. Although there are significant correlations in Figures 5.1 - 5.3, there is also a large amount of scatter. As a result of the analysis presented in this chapter, we have identified 2 parameters which contribute to this scatter--the HI content and the morphological type.

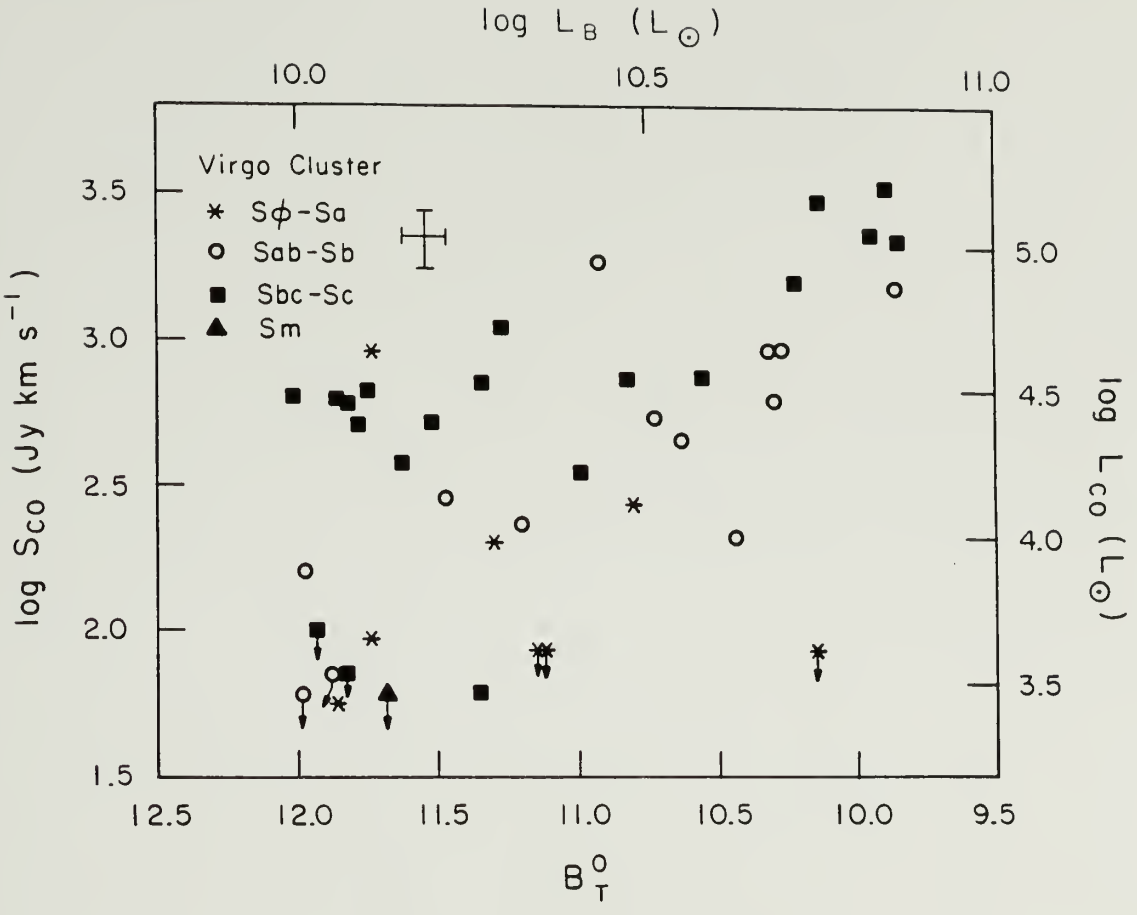

Figure 5.1a Logarithm of the CO flux vs. the blue optical magnitude B_T^o. Indicated on the other axes are the CO luminosity and the blue luminosity, both in solar units, assuming D = 20 Mpc. 2σ upper limits are plotted. The different symbols represent different morphological types, and are coded according to the legend. These same symbols will be used in subsequent figures, unless otherwise stated. The error bar symbol represents the mean ±1σ uncertainty in each coordinate.

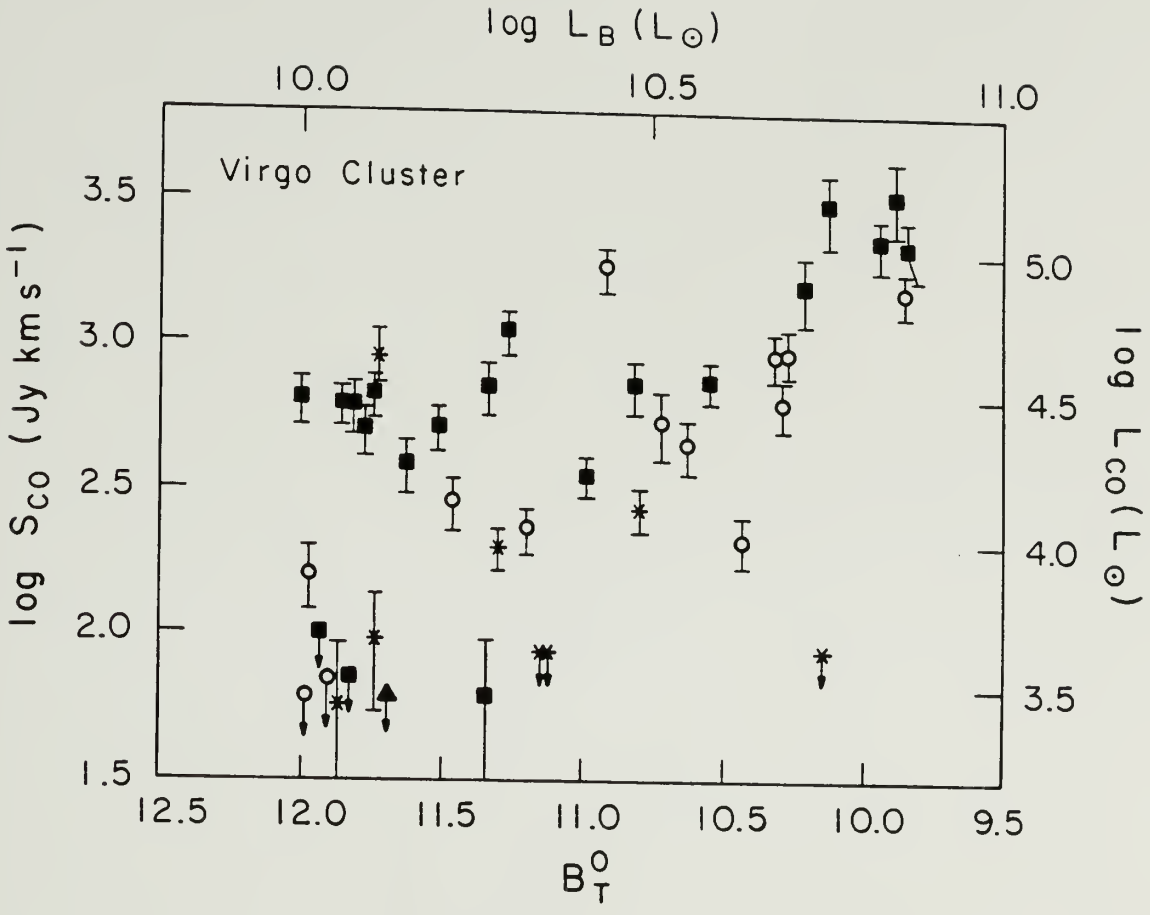

Figure 5.1b Same as Figure 5.1a, with individual error bars plotted.

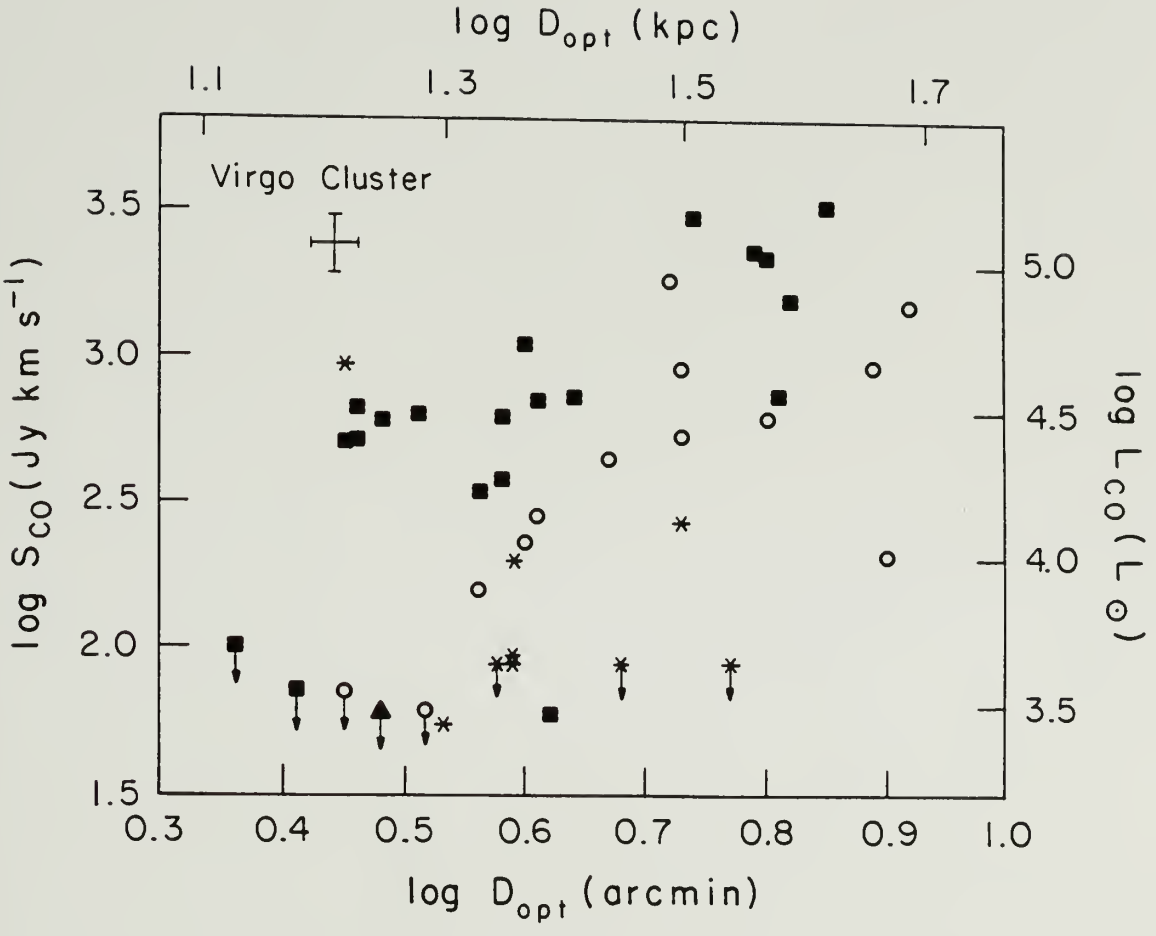

Figure 5.2 CO flux vs. apparent blue optical diameter (D_o from the RC2), both in log units. Indicated on the other axes are the CO luminosity and the linear blue optical diameter, in kiloparsecs. Symbols are the same as in Figure 5.1a.

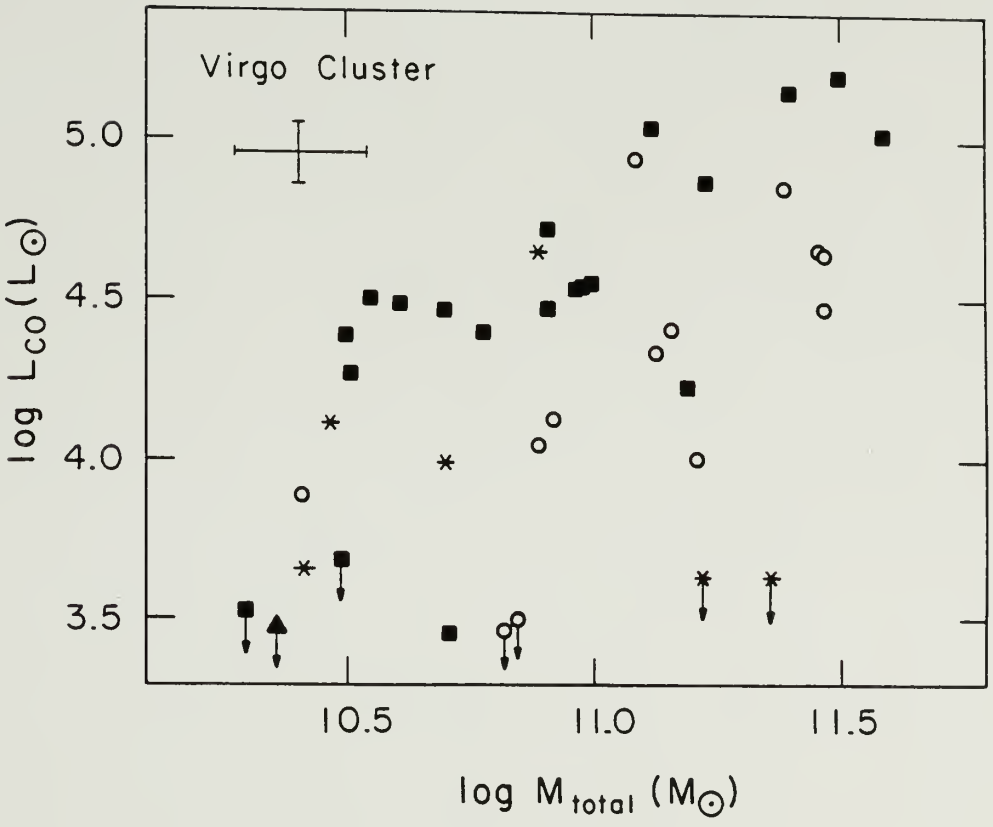

Figure 5.3 Log-log plot of CO luminosity vs. total (indicative) mass.

Stark et al. (1986) compared global CO fluxes with total blue fluxes in 47 Virgo galaxies, and also found a large amount of scatter, but did not discuss whether the scatter was correlated with morphological type or any other parameter. Reasonably good correlations for separate morphological types between the CO and blue emission for the central 50" of 25 Virgo spirals were shown by Young, Scoville, and Brady (1985). Although there is a tendency for the Sbc-Sm galaxies to lie above the Sa-Sb galaxies in Figures 5.1 - 5.3, the least squares fits summarized in Table 5.3 show that this is not a significant difference if all the Sbc-Sm galaxies are considered. Omitting all galaxies with HI def < 0 significantly reduces the scatter for the late type galaxies, but does not significantly alter the fits to the early type galaxies, since there is only one Sa-Sb galaxy with HI def < 0. Since the amount of scatter in the L_{CO} vs. L_B, $D_{opt}{}^2$, and M_{tot} planes for Sc galaxies alone are greater than the difference between morphological types, the dependence of CO emission on morphological type will be deferred until §V.10. The discussion in the remainder of this section will concentrate on the other causes of scatter.

Among the Sc galaxies, there is an order of magnitude variation in the L_{CO}/L_B, $L_{CO}/D_{opt}{}^2$, and L_{CO}/M_{tot} ratios. Examination of Figure 5.2 reveals that among the 14 Sc-Sm galaxies in the magnitude range $10.9 \leq B_T{}^o \leq 12.0$, there are 5 galaxies with a mean $L_{CO}/D_{opt}{}^2$ that is a factor of ~5 lower than the other 9 galaxies in this group. The large

scatter in L_{CO}/D_{opt}^2 for Sc-Sm galaxies is due almost entirely to these 5 galaxies. In Figures 5.4 and 5.5, we plot L_{CO}/D_{opt}^2 vs. the distance from M87, and vs. HI deficiency, and show that in every case these galaxies are HI-rich systems which are further than 4.5° from M87. There are no Sc galaxies brighter than B_T^o=10.9 which have L_{CO}/D_{opt}^2 this low. We note that the higher luminosity, HI-normal, Sc galaxies in the outer cluster (NGC 4303, NGC 4536) have L_{CO}/D_{opt}^2 values comparable to the Sc galaxies in the central part of the cluster.

The results of least squares fits to $\log(L_{CO}/D_{opt}^2)$ vs. HI deficiency for various galaxy samples are summarized in Table 5.3. For the Sab-Sb galaxies, there is no significant correlation between L_{CO}/D_{opt}^2 and HI deficiency (significant at less than the 90% confidence level). However, it is difficult to detect such an effect, since most of the early type galaxies are located in the cluster core, and most of them are HI deficient. Conversely, the fit to the Sbc-Sm galaxies yields a correlation coefficient of r=0.63, which is significant at the 99.5% level. Considering that all the Sc CO upper limits are for galaxies with HI def < 0, the true correlation is even more significant than this estimate implies.

In Figure 5.6, histograms of the L_{CO}/D_{opt}^2 ratios are plotted for 3 samples from the Virgo Sbc-Sm galaxies: those with $B_T^o<11.0$, those with $11.0<B_T^o<12.0$ and HI def<0, and those with $11.0<B_T^o<12.0$ and HI def>0. The distributions of L_{CO}/D_{opt}^2 are the same in the 2 samples described by $B_T^o<11.0$, and $11.0<B_T^o<12.0$ with HI def>0. The distribu-

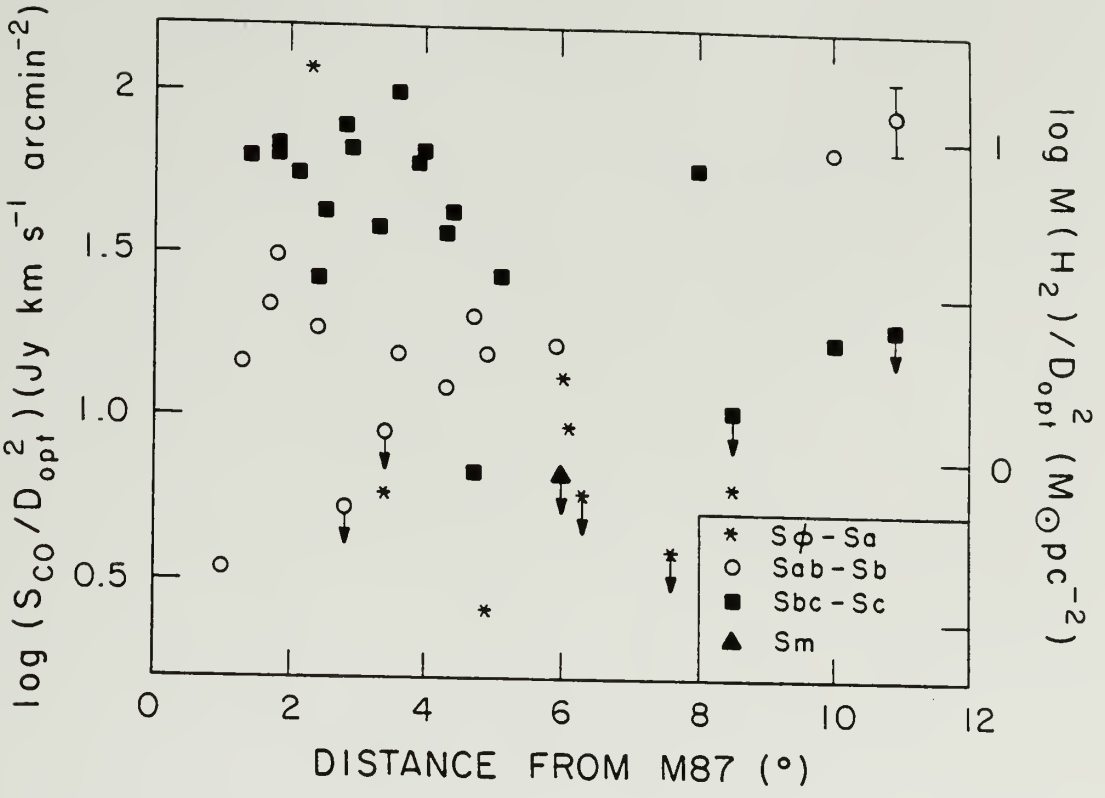

Figure 5.4 Logarithm of CO flux to optical area ratio vs. distance from M87. Along the left axis is the log of the H_2 mass to optical area ratio, assuming the CO-H_2 proportionality factor described in Chapter III. Note that among the Sc galaxies (squares), the only ones with $\log(M_{H_2}/D_{opt}^2) < 0.5$ are in the outer cluster ($R_{M87} > 4.5°$).

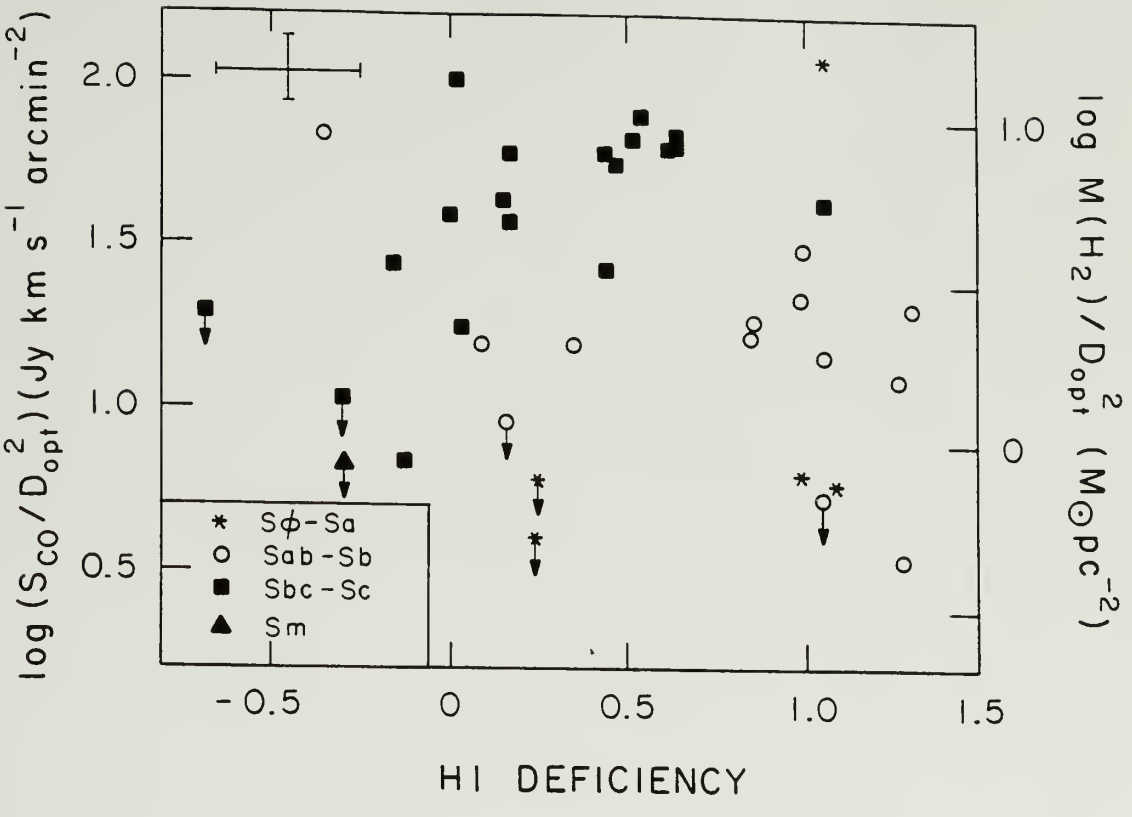

Figure 5.5 Logarithm of the CO flux to optical area ratio (and H_2 mass to optical area ratio) vs. HI deficiency. Note that the only Sc galaxies (squares) with $\log(M_{H_2}/D_{opt}{}^2) < 0.5$ are HI-rich (i.e. HI def < 0.0).

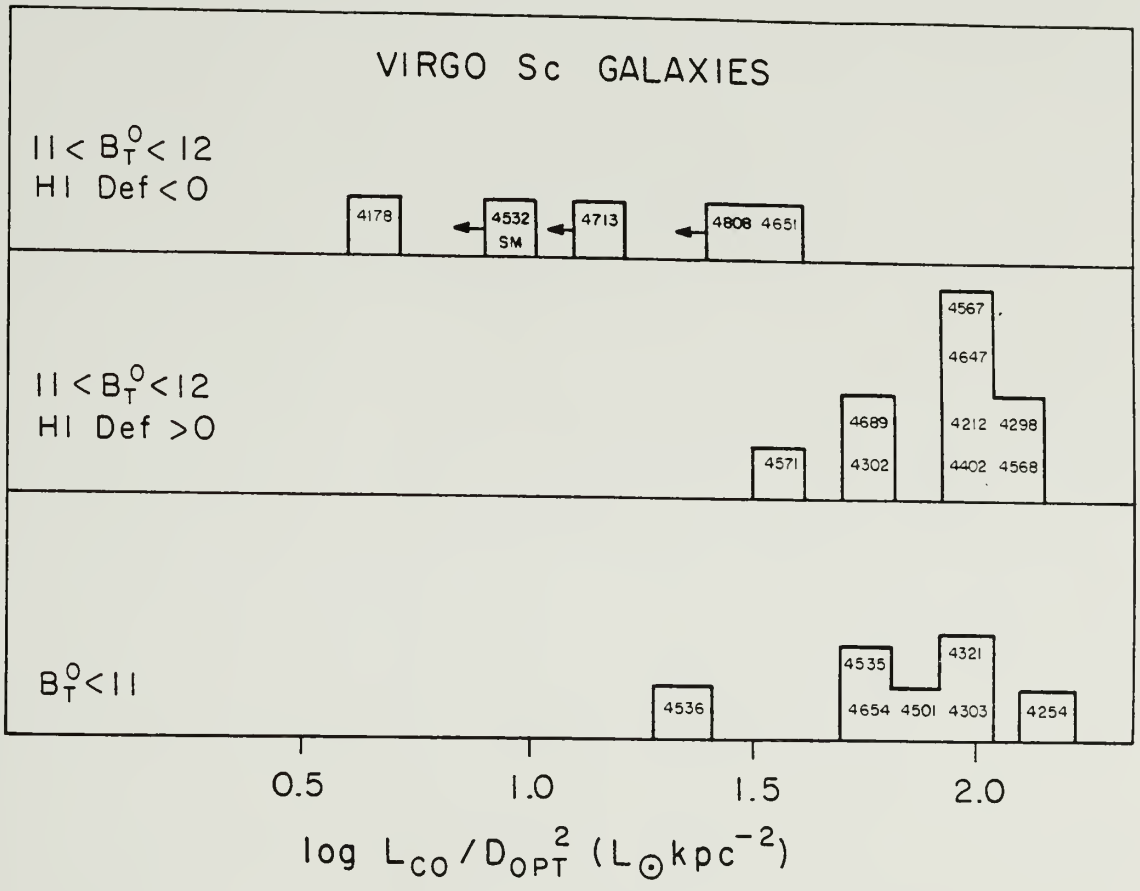

Figure 5.6 Histograms of $\log(L_{CO}/D_{opt}^2)$ for 3 subsets of the Virgo Sbc-Sm galaxies: those with $11.0<B_T^0<12.0$ and HI def<0.00; those with $11.0<B_T^0<12.0$ and HI def>0.00; and those with $B_T^0<11.0$. 2σ upper limits are indicated by shading. The fainter, HI-rich galaxies have the smallest values of L_{CO}/D_{opt}^2.

Table 5.3

Least Squares Fitting Results for Various Gas Quantities[a]

y[b]	x[b]	Galaxies Fit	Slope	x-intercept	r[c]	Notes
L_{CO}	L_B	39 Sa-Sm	1.20±0.22	-8.08±2.24	0.66	d
		18 Sa-Sb	1.25±0.30	-8.88±3.12	0.69	
		21 Sbc-Sm	1.21±0.25	-8.10±2.62	0.72	
		16 Sbc-Sm HI def>0	0.83±0.11	-3.95±1.12	0.89	
L_{CO}	D_{opt}	39 Sa-Sm	1.89±0.46	1.65±0.64	0.54	d
		18 Sa-Sb	1.93±0.64	1.36±0.93	0.57	
		21 Sbc-Sm	2.48±0.50	1.04±0.69	0.73	
		16 Sbc-Sm HI def>0	1.64±0.31	2.36±0.44	0.80	
L_{CO}	M_{ind}	38 Sa-Sm	0.78±0.16	-4.19±1.77	0.60	d
		17 Sa-Sb	0.61±0.21	-2.62±2.36	0.55	
		21 Sbc-Sm	1.11±0.17	-7.65±1.85	0.82	
		16 Sbc-Sm HI def>0	0.79±0.10	-3.96±1.06	0.90	
L_{CO}/D_{opt}^2	HI def	39 Sa-Sm	-0.09±0.13	-4.46±0.10	-0.11	d
		13 Sab-Sb	-0.28±0.17	-4.47±0.15	-0.45	
		21 Sbc-Sm	0.58±0.16	-4.44±0.08	0.63	
		16 Sbc-Sm HI def>0	0.17±0.17	-4.21±0.08	0.26	
$M(HI+H_2)/D_{opt}^2$	HI def	18 Sa-Sb	-0.54±0.13	0.95±0.11	-0.69	
		21 Sbc-Sm	-0.33±0.08	1.17±0.04	-0.70	
$M(H_2)/M(HI)$	HI def	18 Sa-Sb	0.93±0.20	-0.52±0.18	0.73	d
		21 Sbc-Sm	1.46±0.18	-0.39±0.08	0.90	
		16 Sbc-Sm HI def>0	0.85±0.16	0.06±0.08	0.80	

Table 5.3, (cont.)

y^b	x^b	Galaxies Fit	Slope	x-intercept	r^c	Notes
$\sigma_{HI}/\langle\sigma_{HI}(T,I)\rangle$ in inner galaxy	HI def	33 Sa-Sd	-0.27±0.11	-0.02±0.06	-0.41	e,f
		8 Sab-Sb	-0.04±0.23	-0.15±0.18	-0.05	
		24 Sbc-Sd	-0.38±0.09	0.03±0.04	-0.64	
		17 Sbc-Sd HI def>0	-0.35±0.14	0.02±0.07	-0.52	
$M(HI)/M(H_2)$ in inner galaxy	HI def	22 Sa-Sm	-0.67±0.16	-0.24±0.09	-0.67	d
		8 Sab-Sb	-0.68±0.23	-0.10±0.17	-0.69	
		13 Sbc-Sc	-0.98±0.26	-0.24±0.12	-0.78	
		10 Sbc-Sc HI def>0	-0.43±0.14	-0.54±0.07	-0.69	
$S_{60\mu m}/S_{100\mu m}$	HI def	39 Sa-Sm	-0.05±0.04	-0.41±0.03	-0.17	
		18 Sa-Sb	0.03±0.07	-0.48±0.07	0.10	
		21 Sbc-Sm	-0.12±0.06	-0.39±0.03	-0.40	

Notes to Table 5.3:

a) Tabulated quantities are the result of fits to the equation:

$$\log y = m \log x + b$$

where m is the slope, and b is the x-intercept. The logarithm of all quantities listed in columns 1 and 2 have been fit, with the exception of HI deficiency, which is already a logarithmic quantity.

b) Units are solar luminosities, solar masses, and kiloparsecs.

c) Correlation coefficient.

d) 2σ upper limits are treated as detections.

e) Some Virgo galaxies which are not part of the CO sample are included here.

f) The slope of -0.04±0.23 for the Sab-Sb galaxies includes the discrepant galaxy NGC 4388, whose HI map is noisy. The slope with NGC 4388 removed from the sample is -0.30±0.12.

tion for the fainter Sbc-Sm galaxies which are HI-rich (i.e. HI def<0) are completely different from the other two samples, with a much lower mean value of $L_{CO}/D_{opt}{}^2$, and almost no overlap. An examination of Figures 5.1-5.6 indicates that the CO properties do not vary smoothly with either HI deficiency or distance from M87, but are instead bimodal in nature. This is confirmed by the fits summarized in Table 5.3. In particular, although there is a significant correlation between $\log(L_{CO}/D_{opt}{}^2)$ and HI deficiency when all the Sbc-Sm galaxies are included, there is no significant correlation when only those Sbc-Sm galaxies with positive HI deficiencies are considered.

The properties of these 2 populations of CO-rich and CO-poor lower luminosity late type galaxies are summarized in Table 5.4. While the 2 samples have nearly identical distributions of blue luminosity, optical diameter, and total (indicative) mass, their L_{CO}/L_B, $L_{CO}/D_{opt}{}^2$, and L_{CO}/M_{tot} ratios differ by factors of >5-7. Lest we jump to any hasty conclusions, we must first evaluate whether the known systematic differences in the optical colors, optical diameters, and HI linewidths between the HI-deficient and non-HI-deficient galaxies are large enough to cause the 2 samples to differ in L_B, $D_{opt}{}^2$, and M_{tot} by a factor of 5.

Kennicutt (1983) showed that the B-V colors of Virgo Sc's are redder than those of typical field Sc's. In Chapter VI, we find a difference of 0.26 magnitudes in B-V between the CO-rich and CO-poor lower luminosity Sc's. H magnitudes, which are dominated by the light from older stars, are not available for the entire sample. However, Bothun

Table 5.4

Mean Properties of Virgo Sc-Sm Galaxies with $10.9 < B_T^o < 12.0$

Quantity[a]	Mean Value of Quantity[b] HI Def < 0	HI Def > 0	Difference
Number	5	9[c]	
log L_B	10.17±0.07	10.13±0.03	0.08 (1.1 σ)
log D_{opt}^2	2.49±0.10	2.57±0.05	0.08 (0.8 σ)
log M_{tot}	10.61±0.16	10.72±0.06	0.11 (0.7 σ)
log L_{CO}	≤3.67±0.14[d]	4.46±0.04	≥0.79 (≥5.6 σ)
log L_{CO}/L_B	≤-6.51±0.10[d]	-5.67±0.04	≥0.84 (≥8.4 σ)
log L_{CO}/D_{opt}^2	≤1.22±0.11[d]	1.88±0.05	≥0.72 (≥6.5 σ)
log L_{CO}/M_{tot}	≤-6.90±0.03[d]	-6.27±0.04	≥0.69 (≥17 σ)
HI Deficiency	-0.31±0.09	0.56±0.08	0.87 (9.7 σ)
Cluster Location	4.7°-10.2°	1.4°-4.2°	

Notes to Table 5.4:

a) Units are L_o, M_o, and kiloparsecs.

b) The quoted errors reflect the uncertainties in the means. In order to get the dispersions, multiply by $\sqrt{N}$.

c) Five of the nine galaxies are members of galaxy pairs; the means for the 4 non-pair galaxies are within 1 σ of the means for the 5 paired galaxies.

d) Computed using the 2 σ upper limits for NGC 4532, NGC 4713, and NGC 4808.

et al. (1984) find that $\Delta(B-V)_T^o = 0.26$ generally corresponds to $\Delta(B-H)_{-0.5} = 0.8$ for late-type galaxies in the Pegasus I and Pisces clusters. This translates into a factor of 2 enhancement (0.32 dex) of the B luminosity relative to that in the H band. This suggests that the mean $\log(L_{CO}/L_H)$ values differ for the 2 samples by $\geq$0.52 dex. Thus the CO luminosities in the HI-deficient sample are $\geq$3.3 times greater, in the mean, than their HI-rich counterparts, when H magnitudes are used to normalize the CO luminosities.

Peterson, Strom, and Strom (1979) have presented evidence that the blue optical diameters of Virgo cluster spirals of a given magnitude (at the 26.6 mag arsec^{-2} isophote) are ~30% smaller than those in the Hercules cluster (although see Bosma 1985 on a possible problem with the diameter and magnitude absorption corrections). If such a difference exists between the HI-deficient and non-HI-deficient lower luminosity late type Virgo spirals at the 25 mag arcsec^{-2} isophotal level, then the difference in optical surface areas between the 2 samples might be 70%. If present, this effect would reduce the difference in $\log(L_{CO}/D_{opt}{}^2)$ between the 2 samples, but only from 0.72 dex to 0.57 dex.

The method used to estimate total (indicative) masses is not free from systematic errors. Since the total mass $M(R) \sim RV_{max}{}^2$, the total mass determination is plagued by not only systematic uncertainties in the optical diameters, but by systematic uncertainties in the inclination-corrected linewidths. Since $V_{max} \sim W_{HI}/\sin(i)$, V_{max} is subject to uncertainties in both the measured linewidth and the incli-

nation correction, which is largest for low inclination galaxies. All 5 galaxies in the HI-rich sample have $i>45°$, so the uncertainty in their inclination corrections is small. Although 3 of the 9 HI-poor galaxies have $i<45°$, their omission does not significantly alter the mean L_{CO}/M_{tot} ratio of the HI-rich sample.

A much larger concern is that the HI linewidths used to infer V_{max} are systematically smaller in the HI-deficient systems due to the removal of HI from the outer disk. Stauffer, Kenney, and Young (1986) have shown that the global HI linewidth of the Virgo spiral NGC 4569 significantly underestimates its maximum rotational velocity. NGC 4569 has almost no HI in the outer disk, where the highest velocities are found, probably as the result of an interaction with the intracluster medium. Although NGC 4569 is an extreme example, Stauffer, Kenney, and Young find a difference of ~0.1 dex in velocity widths between non-HI-deficient Virgo spirals and those which are HI-deficient by more than a factor of 3. If a linewidth difference of this magnitude is appropriate between the HI-rich and HI-poor lower luminosity late type Virgo samples, then the systematic uncertainty in indicative mass estimates may be as large as a factor of 2, if a 30% difference in disk diameters is also included. Thus a liberal estimate of the systematic error in mass determination reduces the difference in $\log(L_{CO}/M_{tot})$ between the 2 samples from 0.69 to 0.39, but cannot completely account for the difference. We therefore conclude that the differences in the L_{CO}/L_B, $L_{CO}/D_{opt}{}^2$, and L_{CO}/M_{tot} ratios for the 2 samples are due predominantly to a difference of a factor of >2-4 in the CO luminosities.

Thus the magnitudes of these biases are not large enough to give all the Virgo Sc galaxies the same ratio of CO luminosity to total mass. However, the existence of these biases (particularly the definite bias in B-V colors) indicates that the HI-rich, CO-poor galaxies may have smaller masses, on average, than the HI-poor, CO-rich galaxies of the same blue magnitude. As such, it is possible that the ISM differences between the HI-rich, CO-poor and HI-poor, CO-rich lower luminosity late type Virgo galaxies are partly or entirely due to differences in galaxy mass. Alternatively, there are 2 other explanations for the observed anti-correlation in atomic and molecular gas masses in the lower luminosity late type galaxies. The first is that some process in the cluster core enhances the conversion of HI into H_2 in low-mass, small B/D galaxies. The second possibility is that the CO-poor, HI-rich galaxies in the outer cluster are younger than the galaxies in the central part of the cluster, and younger than the typical isolated galaxy. These hypotheses are discussed in §V.9.

Is a systematic difference in the CO-H_2 proportionality factor responsible for the difference in CO luminosities between the 2 samples? We believe not. The very fact that the CO-poor galaxies are HI-rich, while the CO-rich galaxies are HI-poor, suggests that CO is representing the molecular gas mass in both samples. The possibilities of a systematic difference in the CO-H_2 proportionality factors are more fully discussed in §V.11. We note here briefly that the mean $S_{60\mu m}/S_{100\mu m}$ ratios, which indicate dust temperatures, are the same for the 2 samples. While the relationship between gas and dust temperature

is unknown, it is unlikely that hotter molecular gas in the HI-poor sample enhances the CO luminosity.

§4. Comparison of Global CO & HI Fluxes

4.1 Introduction

If there were no interplay between the stars and ISM in a galaxy, then the atomic and molecular components of a galaxy's ISM could respond in 3 general ways to the event which causes a given Virgo galaxy to be HI-deficient. A) The HI is converted into H_2, so that the total gas mass ($HI+H_2$) remains constant. B) The HI is removed from the galaxy, but the H_2 is unaffected. C) Both the HI and H_2 components become deficient in equal proportion. B and C may be considered special cases of the more general case in which the H_2-deficiency is some fraction of the HI-deficiency.

Obviously, these three cases represent an oversimplification of reality. The true evolution of the HI and H_2 content of all galaxies depends upon the detailed interplay of HI, H_2, and stars. Normal evolution changes the HI and H_2 content of galaxies, as gas cycles between the atomic and molecular phases, as gas is used up to form stars, and as stellar mass loss returns gas to the ISM. In environmentally-altered Virgo galaxies, any of these processes may occur at rates which differ from those in unaltered galaxies. In the following, we explore the gas evolution history of Virgo spirals under the simplifying assumption that the interplay between gas and stars does not signifi-

cantly alter the relative amounts of HI and H_2 in the HI-deficient Virgo spirals. This assumption seems reasonable on 2 grounds. While the current star formation rates in HI-deficient Virgo spirals are reduced (Kennicutt 1983; Chapter VI), the magnitude of the SFR reduction is not as great as the magnitude of the HI deficiency. The analysis in Chapter VI shows that the galaxies which are globally deficient in HI by a factor of 10 have had their SFR reduced by no more than a factor of 2-3, in the mean. Second, since significant stellar mass loss occurs in the older stellar population (Faber and Gallagher 1976), the change in the stellar mass loss rate in HI-deficient galaxies will be even less than the change in the current SFR.

Even without the complicating effects of star formation and stellar mass loss, the evolution of the HI and H_2 phases over time may hide the original nature of the ISM-ICM interaction. For example, it is conceivable that the HI and H_2 phases are in equilibrium. Suppose that all of a galaxy's HI is swept away, but all the molecular gas remains. If disruptive events associated with star formation in molecular clouds return a significant fraction of gas to the atomic phase, then a galaxy may evolve to become equally deficient in both HI and H_2, even though only atomic gas was removed in the original event. If the time scale to acheive this hypothetical equilibrium were short enough, and Virgo galaxies were found to be deficient in CO, then it would not be possible to distinguish widescale molecular gas-stripping from rapid, post-HI-stripping conversion of HI into H_2.

Furthermore, all three possibilities outlined above may be mani-

fest among the galaxies in the Virgo cluster, or even within a single galaxy. The nature of the ICM-ISM interaction is likely to depend upon the galaxy's velocity with respect to the ICM, the inclination of the disk with respect to the galaxy's velocity vector, the density of the ICM (hence the orbit of the galaxy through the cluster), the local ISM surface density, and the total mass surface density of the galactic disk. Since these parameters vary among the Virgo galaxies, and some of them vary within a single galaxy, there are good reasons for expecting scatter in any comparison of the relative amounts of atomic and molecular gas.

A final complication arises from the different radial distributions of the atomic and molecular gas components in galaxies. It is possible that the inner and outer galaxy are affected differently by cluster processes, and that any differences in the HI and CO properties are merely a by-product of the tighter concentration of molecular gas in the inner regions of spiral galaxies. This important subject is discussed in §V.6.

4.2 Theoretical Gas Evolution Tracks

With these complications in mind, we present two comparisons of the relative amounts of atomic and molecular gas which will help discriminate between different gas-evolution scenarios. In Figures 5.7a and 5.8a, we present the S_{CO}/S_{HI} and $M(HI+H_2)/D_{opt}{}^2$ ratios as a function of HI deficiency. Since both L_{CO} and M_{HI} are proportional to $D_{opt}{}^{1.0\pm0.2}$, these quantities are corrected to first order for the size

Figure 5.7 a) Logarithm of CO to HI flux ratio (and H_2 to HI mass ratio) vs. HI deficiency for all sample Sa-Sm galaxies. b) Same as Figure 5.7a, but with only the Sa-Sb galaxies plotted. The curves represent 3 possible gas evolutionary tracks. Curve A represents the conversion of HI into H_2, with the total (HI+H_2) gas mass remaining constant. Curve B, with a slope of 1, represents an H_2 content which is independent of the HI content. (This might be called the 'H_2 = normal curve'). Curve C, with a slope of 0, represents an H_2 deficiency equal to the HI deficiency. All the curves are fixed to meet at HI def = 0.00. The vertical location of this junction is determined by the 'normal' $M(H_2)/M(HI)$ ratio of an isolated galaxy with HI def = 0.00, whose logarithm is defined to be r_o. For Sa-Sb galaxies, r_o is currently not well fixed by the observations. The curves drawn are based on $r_o = -0.6$, which is a reasonable fit to the Virgo Sa-Sb galaxies with HI def<0.4 in both Figures 5.7b and 5.8b. The value of r_o determines the intercepts of all curves, as well as the shape of curve A. As r_o becomes large, curve A becomes indistinguishable from curve B. As r_o becomes smaller, curve A approaches an infinite slope for HI def<0, and becomes further separated from from curve B for HI def>0. c) Same as Figure 5.7b, but for Sbc-Sm galaxies. Curves A, B, and C are the same as in Figure 5.7b, except that $r_o = -0.3$.

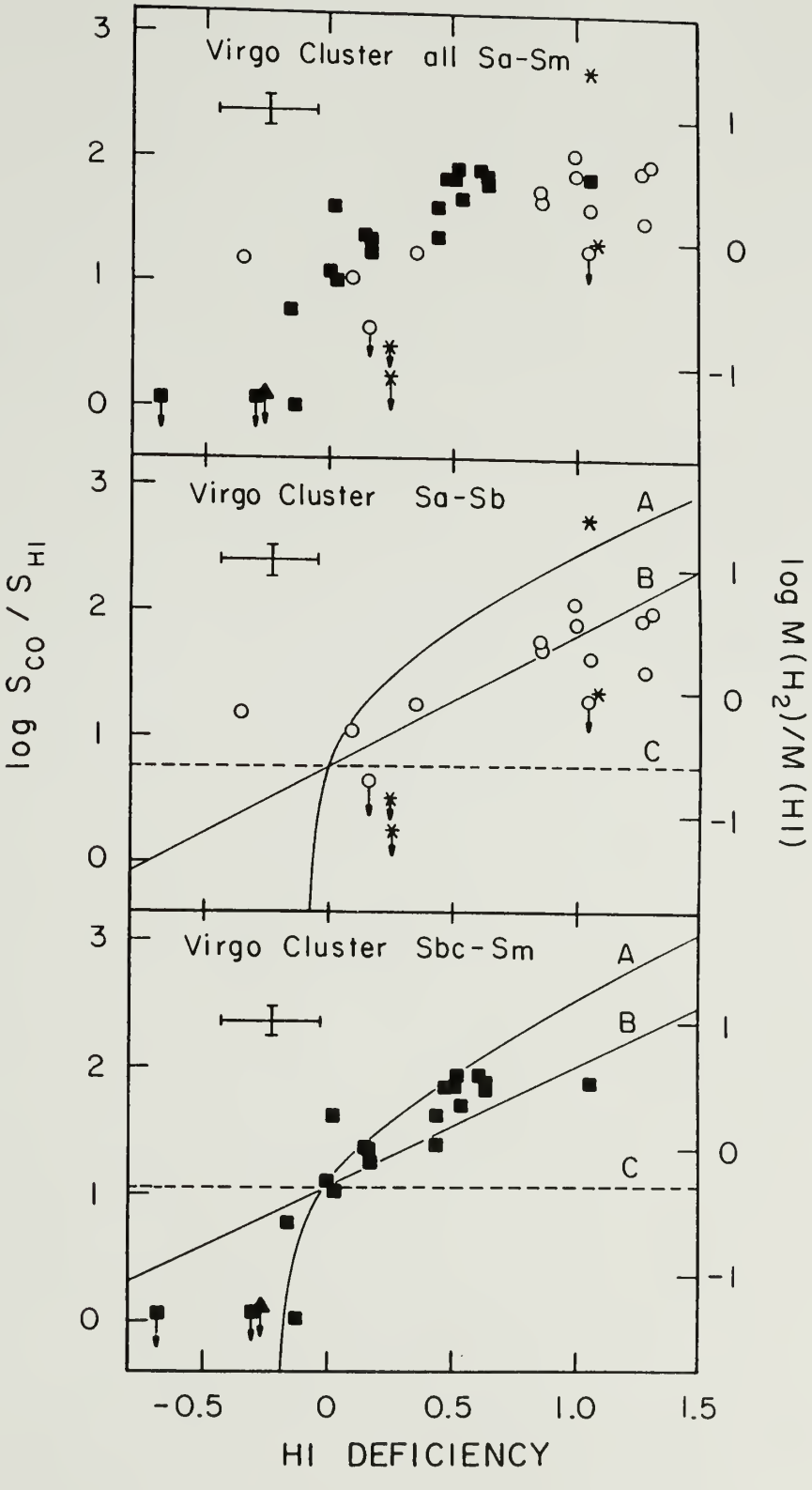
Virgo Cluster all Sa-Sm
Virgo Cluster Sa-Sb
Virgo Cluster Sbc-Sm
A
B
C
log S_{CO} / S_{HI}
log M(H_2)/M(HI)
HI DEFICIENCY
-0.5
0
0.5
1.0
1.5

Figure 5.8 Logarithm of $M(HI+H_2)/D_{opt}^2$ vs. HI deficiency for all sample Sa-Sm galaxies. The vertical axis represents the total hydrogen mass ($HI+H_2$), normalized by the optical area of the galaxy. b) Same as Figure 5.8a, but with only the Sa-Sb galaxies plotted. The curves A, B, and C represent the same 3 gas evolutionary tracks as in Figure 5.7b. The location of the curves are fixed by $r_o = -0.6$, with the additional assumption that Sa-Sb galaxies of a given optical diameter have 0.15 dex less gas ($HI+H_2$) than an Sbc-Sm galaxy of the same size. c) Same as Figure 5.8b, but for Sbc-Sm galaxies. Location of curves is determined by $r_o = -0.3$.

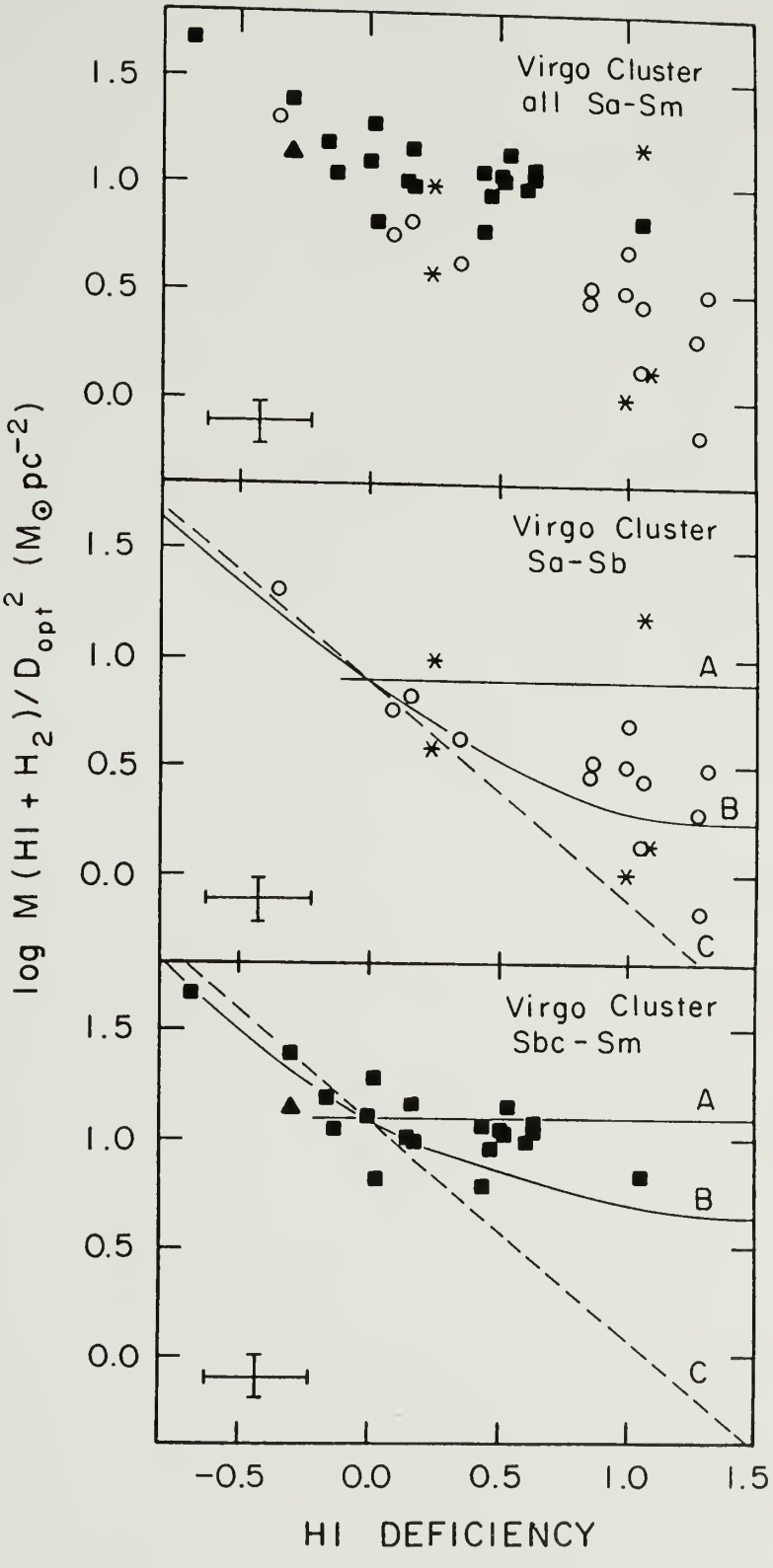
Virgo Cluster
all Sa-Sm
Virgo Cluster
Sa-Sb
Virgo Cluster
Sbc - Sm
A
B
C
log M (HI + H2) / Dopt2 (M⊙ pc-2)
HI DEFICIENCY
1.5
1.0
0.5
0.0
-0.5
0.0
0.5
1.0
1.5

dependence of the CO and HI luminosities. Under the assumption that the S_{CO}/S_{HI} (i.e. $M(H_2)/M(HI)$) ratio for an HI-normal galaxy of a given morphological type and diameter is a well-defined quantity with only a small amount of scatter, the behavior of the S_{CO}/S_{HI} and $M(HI+H_2)/D_{opt}^2$ ratios as the HI deficiency changes constrains how the HI and H_2 components of the ISM respond to the cluster environment. Since the CO/HI flux ratio may depend upon morphological type, we separate the galaxies into Sa-Sb and Sbc-Sm morphological classes in Figures 5.7b-c and 5.8b-c. There may also be a modest size (or luminosity) dependence to the S_{CO}/S_{HI} and $M(HI+H_2)/D_{opt}^2$ ratios, if $M(HI)$ and $M(H_2)$ have different dependences on D_{opt}. We note that the largest Sc galaxies lie above the smaller Sc galaxies in Figure 5.7a. This possible size effect is smaller than the effect of the type dependence, at least among the Virgo sample galaxies.

In the CO/HI flux ratio vs. HI deficiency plane, the locus of points which describe an H_2-deficiency equal to the HI-deficiency is a line with a slope of zero. This line is labelled 'C' in Figures 5.7b and 5.7c. The line which describes the case in which the H_2 content is unrelated to the HI content, or equivalently, a 'normal' H_2 content unaffected by the HI deficiency, has a slope of 1. This line is labelled 'B' in Figures 5.7b and 5.7c. The slope for each of these cases does not depend upon the mean CO-H_2 proportionality factor adopted, as long as there is no systematic variation with HI deficiency. For the case in which the molecular gas deficiency is some fraction of the atomic gas deficiency, the data in Figure 5.7 would

describe a slope between 0 and 1.

The curve describing the conversion of HI into H_2, with the total gas mass remaining constant, depends upon the H_2/HI mass ratio for a 'normal' galaxy (i.e. a galaxy with HI def = 0.00), and consequently on the CO-H_2 proportionality factor. If a galaxy begins with an HI deficiency of 0.00, and has an initial H_2/HI mass ratio given by:

$$r_o = \log \left(\frac{M_{H_2}}{M_{HI}} \right)_{HI\ def=0} \qquad (V-7)$$

it can easily be shown that if this galaxy acheives an HI deficiency = HI def by converting HI into H_2, it will change its H_2/HI mass ratio by an amount given by:

$$\Delta \log \frac{M_{H_2}}{M_{HI}} = \log \left(\frac{M_{H_2}}{M_{HI}} \right)_{HI\ def} - \log \left(\frac{M_{H_2}}{M_{HI}} \right)_{HI\ def=0} = \log Q \qquad (V-8)$$

where

$$Q = \frac{1 + 10^{-r_o} - 10^{-(r_o + HI\ def)}}{10^{-HI\ def}} \quad . \qquad (V-9)$$

Using the Virgo Sc galaxies with $-0.2 < HI\ def < 0.2$ to normalize the CO/HI relationship, we find $r_o = -0.3$, using equation IV-8 to relate CO flux and H_2 mass. As an example, a galaxy which acheives HI def = 1.00 by converting 90% of its HI into H_2 will increase its H_2/HI mass ratio

by 1.45 in the log, assuming r_o=-0.3. It is more difficult to normalize this curve for early type Virgo spirals, since there are so few with low HI deficiencies. The 'A' curve drawn in Figure 5.7b is based on r_o=-0.6, which is a reasonable fit to the non-HI-deficient Sa-Sb galaxies in both Figures 5.7b and 5.8b.

Additional clues to the gas evolution history of Virgo spirals can be gained by comparing the behavior of the total gas content as a function of HI deficiency. It is desirable to compare the location of the galaxies in Figures 5.7 and 5.8, since these plots have different advantages. A disadvantage to Figure 5.8 is that the relative location of the galaxies in the $\log((M_{HI}+M_{H_2})/D_{opt}{}^2)$ vs. HI deficiency plane depends upon the mean CO-H_2 proportionality factor, unlike the CO/HI flux ratio vs. HI deficiency plane. This is offset by several advantages. Since the HI deficiency is nearly proportional to $\log(M_{HI}/D_{opt}{}^2)$ (see section V.2), both the abscissa and ordinate in Figure 5.8 have been normalized by the optical area of the galaxies in order to reduce the scatter caused by including galaxies of different size. Upper limits to the CO flux are not a problem in Figure 5.7b, since the HI mass is larger than the H_2 mass upper limit for all the galaxies which are undetected in CO. The allowable range in total gas masses for the undetected galaxies is small--whether the undetected galaxies have no molecular gas or an amount equal to the 2σ upper limit does not significantly change the location of any of the galaxies in Figure 5.8. These galaxies have been assigned an H_2 mass of zero in Figure 5.8.

Two of the gas evolution tracks are simply straight lines in this plane. If the galaxy becomes equally deficient in both atomic and molecular gas, the galaxy moves along a straight line whose slope is -1 (labelled 'C' in Figure 5.8). If a galaxy converts its HI into H_2, so that the total gas mass remains constant, the galaxy will move along a line with a slope of zero (labelled 'A' in Figure 5.8). Since the total gas mass is constrained to be a constant in this case, there is a limit to how negative the HI deficiency can be. This limit is given by:

$$\text{HI def (min)} = -\log(1 + 10^{r_o}) \qquad \text{(V-10)}$$

for a constant total gas mass. For the Sc galaxies, which have r_o=-0.3, HI def (min) = -0.18. This limit is not a physical limit, but is merely an expression of the fact that if the galaxy was once more HI-rich than HI def (min), it must have lost gas mass (through star formation or stripping) to reach its present state.

The shape of the H_2 = constant curve depends upon the value of r_o. It can be shown that a galaxy which acheives a non-zero HI deficiency, while maintaining the same H_2 mass, will change its total gas content by an amount described by the following expression:

$$\Delta\log\left(\frac{M_{HI}+M_{H_2}}{D_{opt}^2}\right) = \log\left(M_{HI}+M_{H_2}\right)_{\text{HI def=0}} - \log\left(M_{HI}+M_{H_2}\right)_{\text{HI def}} = \log\kappa \qquad \text{(V-11)}$$

where

$$\kappa = \frac{1 + 10^{r_o}}{10^{-HIdef} + 10^{r_o}} \quad . \qquad (V\text{-}12)$$

For a galaxy which evolves to HI def=1.00 without changing its H_2 content, the total gas mass will be reduced by 0.40 in the log, assuming r_o=-0.3. In the limit as r_o becomes very negative (i.e. $M_{HI} \gg M_{H_2}$), log $\kappa \rightarrow$ HI def, and the slope approaches -1. Thus, if the molecular gas mass is insignificant with respect to the atomic gas mass, a galaxy will evolve along a slope of -1 in Figure 5.8, regardless of what is happening with the molecular component of the ISM. For negative HI deficiencies in the case of $r_o < 0.0$, this curve approaches a slope of -1, and is nearly indistinguishable from the H_2 deficiency = HI deficiency case. In other words, the location of galaxies with HI def < 0.00 in Figure 5.8 tells us nothing about the evolution of the H_2 phase, since the gas evolution tracks converge. For galaxies in the HI-rich regime, Figure 5.7 is more useful, since the gas evolution tracks diverge for HI def < 0.00. On the other hand, if the atomic gas mass is insignificant with respect to the molecular gas mass (i.e. $r_o \ll 0$, $M_{HI} \ll M_{H_2}$), a galaxy will evolve along a slope of 0 in Figure 5.8, since the total gas mass will be nearly independent of the HI deficiency.

For the H_2=constant curves in Figure 5.8 (labelled 'B'), we have assumed r_o=-0.3 for the late type spirals, and r_o=-0.6 for the early type spirals to remain consistent with Figure 5.7. In addition, in

order for the early type galaxies with low HI deficiencies to lie close to the intersection of curves at HI def=0.00 in Figure 5.8b, we have assumed that an Sa-Sb galaxy of a given D_{opt} has 0.15 dex less HI gas mass than an Sbc-Sm galaxy of the same size. The resulting sets of curves in Figures 5.7 and 5.8 are therefore consistent, but the early and late types should not be mixed. Finally, we again point out that if the H_2-deficiency is some fraction of the HI-deficiency, the galaxies in Figure 5.8 would lie between curves B and C.

4.3 Discussion

The evolution of the atomic and molecular phases of the interstellar media of Virgo cluster galaxies is constrained by the location of the galaxies in Figures 5.7 and 5.8. These figures clearly show that the data are inconsistent with an H_2 deficiency as severe as the HI deficiency. This result indicates that not only have molecular clouds avoided removal by some cluster process, but that the time scale for HI and H_2 to acheive equilibrium (if they ever do) is very long. This important result will be discussed further in Chapter VII.

One other general conclusion can be drawn from the data in Figure 5.8. The slopes of the data in Figures 5.8b and c can be used to estimate the <u>total gas deficiency</u> ($HI+H_2$) as a function of the HI deficiency. Separate least squares fits for the Sa-Sb and Sbc-Sm galaxies to $\log(M(HI+H_2)/D_{opt}^2)$ vs. HI deficiency have been performed, and are summarized in Table 5.3. From the slopes derived from these fits, we conclude that galaxies which are HI-deficient by a factor of 10 are

gas-deficient by only a factor 2-3, in the mean.

The overall data for the early type spirals are best described by the H_2 = constant curve in both Figures 5.7b and 5.8b, and poorly described by the HI→H_2 curve. This conclusion is supported by the slopes of the least squares fits to the data in Figures 5.7b and 5.8b, which are summarized in Table 5.3. The slope of -0.54 ± 0.13 for the Sa-Sb galaxies in Figure 5.8b (i.e. $\log(M(HI+H_2)/D_{opt}^2)$ vs. HI deficiency) reveals that the early type galaxies are gas-deficient, but that the magnitude of the gas deficiency is less than the magnitude of the HI deficiency. The slope of 0.93 ± 0.20 for the Sa-Sb galaxies in Figure 5.7b (i.e. $\log(M(H_2)/M(HI))$ vs. HI deficiency) is consistent with a slope of 1.0, which describes the situation if $M(H_2)$ is independent of the HI deficiency. This conclusion is weakened by the large amount of scatter for large HI deficiencies, and by the paucity of early type Virgo spirals with HI def < 0.50, which makes it difficult to normalize the gas evolution curves.

It is presently unclear whether the large scatter in Figure 5.8b for the early-type Virgo galaxies with HI def > 0.5 is merely an artifact of the paucity of early types with HI def < 0.5, or represents something significant about the evolution of stripped early-type spirals. If the latter is true, the HI-deficient early-type Virgo spirals may have followed different gas evolutionary paths, or may be at different stages in their evolution. For example, NGC 4419 is very gas rich ($\log M(HI+H_2)/D_{opt}^2 = 1.2$) for its large HI deficiency (HI def = 1.06), and thus may be considered a strong candidate for a galaxy

which has converted a significant amount of HI into H_2. On the other hand, there are a couple of early-type galaxies with HI def > 1.0 which lie close to curve C, which describes an H_2 deficiency equal in magnitude to the HI deficiency. These are candidates for galaxies which have either lost molecular gas by an ISM-ICM interaction, or have gradually lost molecular gas through normal evolution (i.e. star formation) after an HI removal event. We note that NGC 4064 is very HI deficient (HI def = 0.99) and relatively gas poor ($\log M(HI+H_2)/D_{opt}^2 = 0.0$). This galaxy is located 7.8° from M87, which is far outside the active "stripping zone". It therefore may have acheived its low H_2 mass through normal evolution over the $\sim 3 \times 10^9$ year interval it would take for a galaxy to travel from the cluster core to a projected location 7.8° away.

Examination of the Sc-Sm galaxies with HI def < 0.00 in Figure 5.7c reveals that these galaxies do not fall along the H_2 = constant curve, but are consistent with the HI→H_2 curve. The slope of 1.46±0.18 from the least squares fit to $\log(M(H_2)/M(HI))$ vs. HI deficiency for all the Sbc-Sm data (see Table 5.3) is 3σ greater than 1.0, which suggests that the HI→H_2 process may be occurring in some of the Virgo galaxies. It is premature, however, to conclude that the HI→H_2 process has definitely enhanced by an ISM-ICM interaction. It must be emphasized that each of the gas evolution curves drawn in Figures 5.7 and 5.8 may be appropriate for galaxies within a limited mass range. Due to the previously mentioned difference in B-V colors in the HI-rich, CO-poor and HI-poor, CO-rich lower luminosity late type galaxies, the HI-rich,

CO-poor galaxies are probably the least massive galaxies in the sample. Thus, the location of the HI-rich, CO-poor galaxies along curve A in Figure 5.7c may be an artifact of their being the least massive galaxies in the sample.

A fit to all the late type spirals with HI def > 0 in Figure 5.7c is consistent with a slope of 1.00. Curves A and B lie close to one another, and each has a slope of ~1.0 for HI def > 0. Because of the uncertainty in the actual HI deficiency of an individual galaxy, the possible existence of a size dependence to the $M(H_2)/M(HI)$ ratio, the existence of interacting binary galaxies among the Sc galaxies, uncertainties in the normalizations of the gas evolution curves and the $CO \rightarrow H_2$ proportionality factor, and the complicating effects of stars and evolution alluded to in §V.4.1, the data in Figures 5.7 and 5.8 cannot clearly distinguish between the H_2 = constant and $HI \rightarrow H_2$ cases for the Sc galaxies with HI def > 0.00. It is concluded that there is no molecular gas deficiency in the HI-deficient Virgo Sc galaxies. The conversion of HI into H_2 may be enhanced by an ISM-ICM interaction, but selection effects might also explain the observed anti-correlation in HI and CO luminosities in the lower luminosity Sc's.

§5. Comparison of CO, HI, and Optical Diameters

In order to understand the nature of the ISM-ICM interaction in the Virgo galaxies, the radial distribution of atomic and molecular gas in each galaxy must be examined. Ever since large amounts of molecular gas were detected in the central few kiloparsecs of our galaxy

(Scoville and Solomon 1975), it has been recognized that the HI and H_2 radial distributions in galaxies are dissimilar. Young and Scoville (1982a) showed that the CO distributions in a few luminous Sc galaxies are similar to their blue light distributions, while their HI distributions are broader and flatter, and in most cases exhibit central depressions (Rogstad and Shostak 1972). In roughly half of all spirals with a prominent bulge in which atomic and molecular gas distributions have been measured, both CO and HI exhibit central depressions (Stark 1979; Young and Scoville 1982c; Young 1986), yet the HI has a broader and flatter distribution than the CO. In view of the central confinement of molecular gas in a typical galaxy, and the large fraction of HI in the outer disk, it is important to determine whether large global CO/HI ratios are merely the result of the outer galaxy becoming HI-deficient while the inner galaxy remains unscathed.

Since the CO emission in most galaxies is peaked strongly toward the center, the total CO flux is dominated by emission from the very region of the galaxy with the highest gravitational binding energy--a region from which it is therefore difficult to remove interstellar gas. If molecular gas were deficient in only the outer disk, the total CO flux would not be the most sensitive tracer of a molecular gas deficiency. The outer disk is more susceptible to external gas removal processes, so here we examine whether the Virgo galaxy CO distributions are dependent upon their HI deficiencies.

First, we compare the CO diameters derived in Chapter III with the optical and HI diameters described in §V.2. Figure 5.9 displays

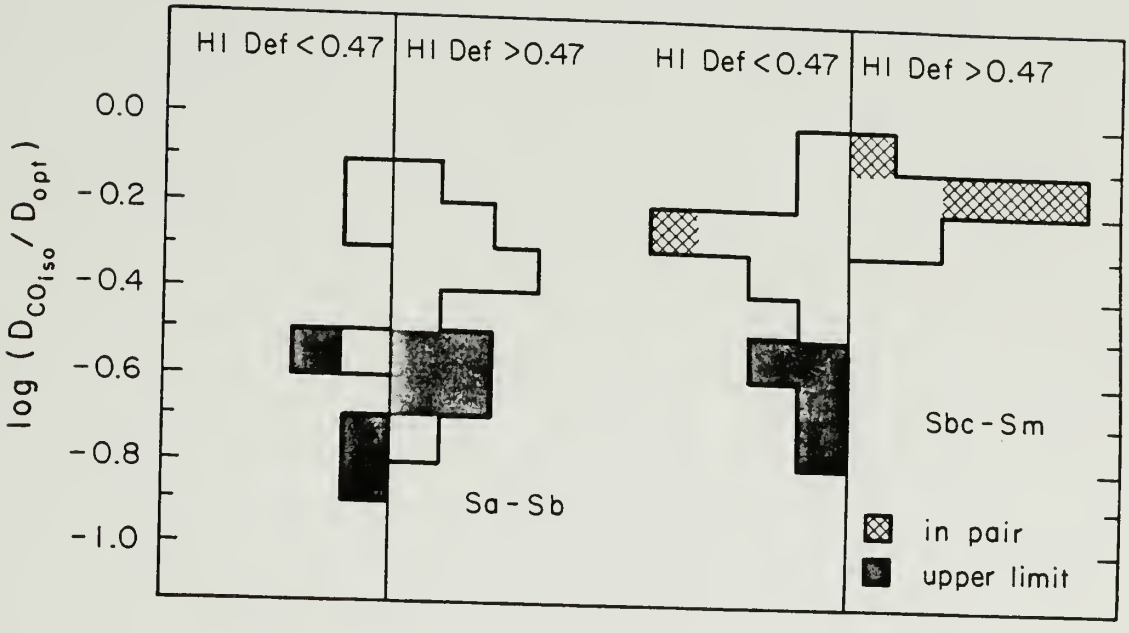

Figure 5.9 Logarithmic histograms of isophotal CO diamters, normalized by blue optical isophotal diameters for 39 Sa-Sm Virgo galaxies. The CO isophotal diameter is defined at the inclination-corrected 1.5 K(T_R) km s^{-1} level, while the optical diameter is defined at the inclination- and extinction-corrected 25 mag $arcsec^{-2}$ level. The galaxies are binned according to morphological type (Sa-Sb or Sbc-Sm) and HI deficiency (dividing point is HI def=0.47, i.e. HI deficient by a factor of 3). Galaxies which are members of pairs (as judged by position and velocity), and upper limits are appropriately shaded. For the Sa-Sb galaxies, the HI-deficient and non-HI-deficient galaxies have similar distributions. For the Sbc-Sm galaxies, there is a lack of HI-deficient galaxies with small CO diameters.

histograms of the isophotal CO diameters, normalized to isophotal optical diameters, both as a function of morphological type and HI deficiency. Isophotal diameters are used for this comparison rather than effective diameters since the isophotal diameters are more sensitive to the outer disk, and upper limits can be defined in the case of isophotal diameters. Histograms for the ratios of CO effective diameter to optical diameter (not shown) are very similar to those for D_{COiso}/D_{opt}, except that the undetected galaxies cannot be included. For the Sa-Sb galaxies, the distributions of D_{COiso}/D_{opt} appear to be independent of HI deficiency, although this comparison is plagued by a lack of HI-normal Sa-Sb Virgo systems. For the Sbc-Sm galaxies, the HI-deficient galaxies have a larger mean D_{COiso}/D_{opt} than the non-HI-deficient galaxies. The smallest CO diameters are found in the lower luminosity HI-rich systems which remain undetected in CO. Thus the process which has caused some galaxies to become HI-deficient has not appreciably reduced their molecular gas diameters. The fact that the smallest CO diameters among the Sbc-Sm galaxies are found in the non-HI-deficient systems may be the result of a selection effect (i.e. the HI-rich, CO-poor galaxies may have the lowest masses in the sample). Alternatively, it may be that some of the lower luminosity Sc galaxies may have had their molecular gas diameters increased by interactions within the cluster.

A comparison of CO and HI diameters confirms that the HI diameters in the HI-deficient galaxies are shrunken with respect to their CO diameters. The histograms in Figure 5.10 display the ratios of effec-

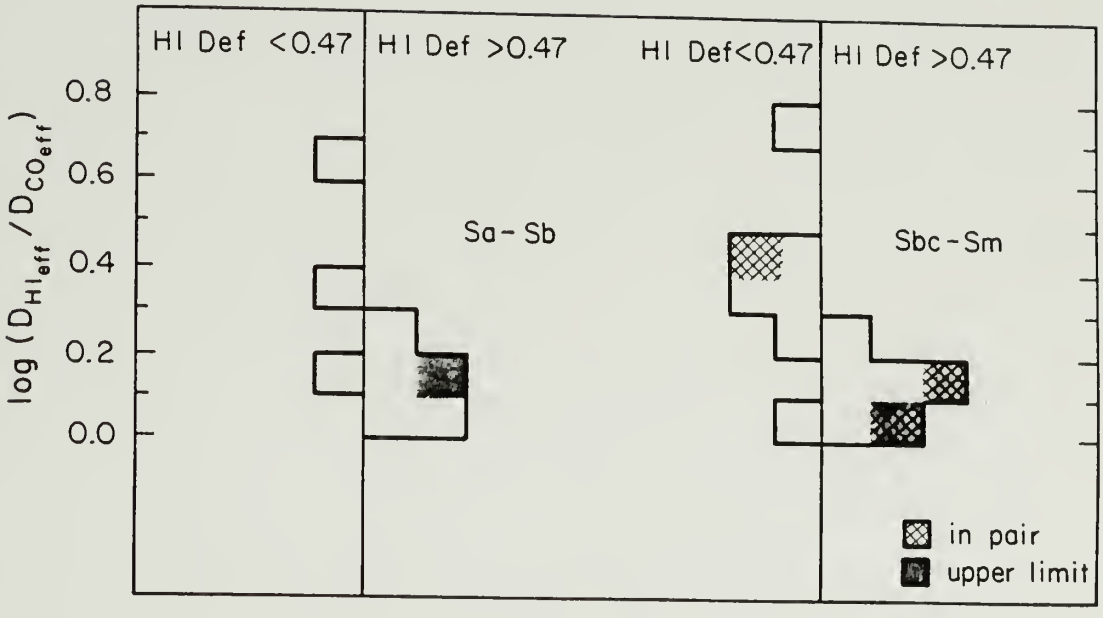

Figure 5.10 Logarithmic histograms of HI effective diameters, normalized by CO effective diameters. Effective diameters are the diameter which contains 70% of the total flux. For both early and late types, the HI deficient galaxies have systematically smaller HI effective diameters with respect to their CO effective diameters.

tive HI diameter to effective CO diameter, binned according to morphological type and HI deficiency. In both Sa-Sb and Sbc-Sm samples, the HI-deficient galaxies tend to have smaller effective HI diameters with respect to their effective CO diameters. A similar result is obtained for the HI and CO isophotal diameters, as shown in Figure 5.11. A drawback to both Figures 5.10 and 5.11 is that not all of the survey galaxies can be included, since HI distributions are not available for the entire sample. This problem is partially offset by the fact that Figures 5.10 and 5.11 include different subsets of galaxies. However, the incompleteness causes Figure 5.10, in particular, to be somewhat misleading. In this figure, the galaxies with the largest values of D_{HIeff}/D_{COeff} are due to CO non-detections, while the HI-deficient subsamples appear to contain no members of this class. This is misleading only in the case of the early-type galaxies, since there are 4 HI-deficient Sa-Sb galaxies in the sample which are unresolved or undetected in CO. These 4 galaxies probably have large D_{HIeff}/D_{COeff} ratios, yet there is no information on their HI diameters currently available. The situation for the late type spirals is accurately reflected in Figure 5.10: the only late type sample galaxies which have large HI extents relative to their CO extents are the low luminosity, HI-rich, CO-poor systems.

The comparison of the CO, HI, and optical diameters demonstrates that the Virgo galaxy CO extents are no smaller in the HI-deficient galaxies, and even greater in the HI-deficient lower luminosity late-type galaxies. Yet it is still unclear whether the HI deficiency

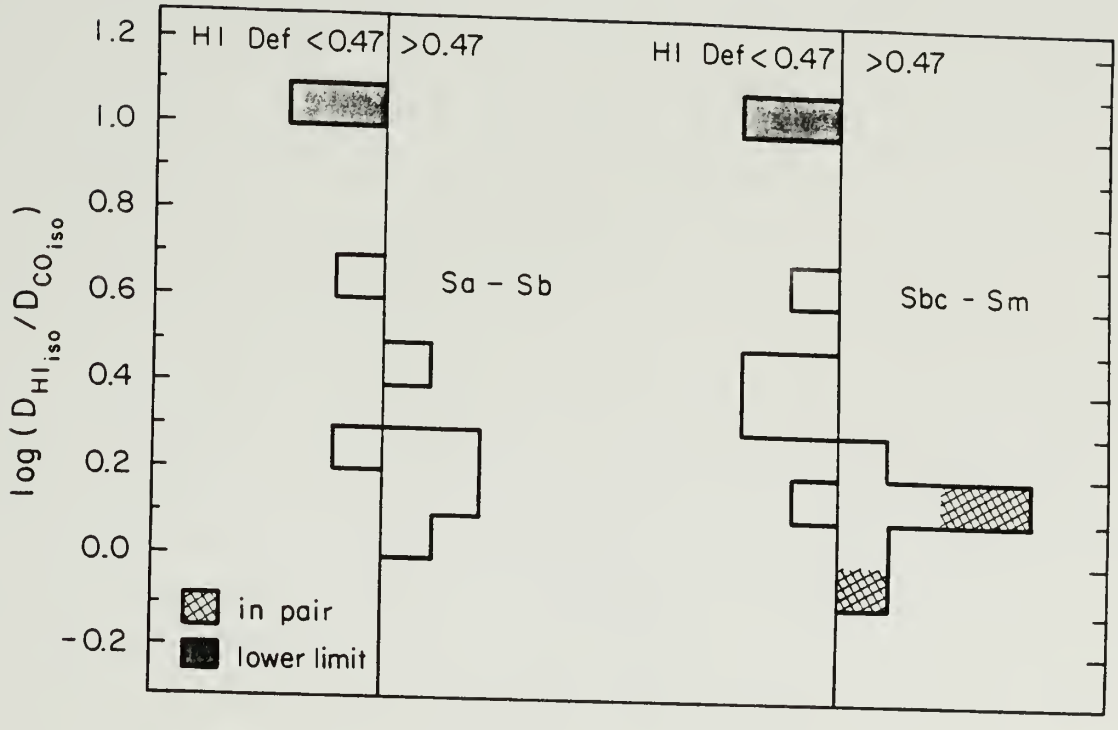

Figure 5.11 Logarithmic histograms of HI isophotal diameters, normalized by CO isophotal diameters. The HI isophotal diameter is defined at the 1 M_o pc^{-2} level. The CO isophotal diameter is defined at the 1.5 K(T_R) km s^{-1} level, which corresponds to an H_2 surface density of 6.8 M_o pc^{-2}, if the CO-H_2 proportionality factor described in Chapter III is used. The HI deficient galaxies of all types have smaller HI isophotal diameters with respect to their CO isophotal diameters.

extends all the way in to the inner galaxy where the CO is detected. The CO diameters are significantly smaller than the HI diameters (see the vertical scale in Figures 5.10 and 5.11), which in principal allows the galaxies to be HI-deficient exclusively in the outer disk, and completely normal in the inner disk. This issue is addressed next with an analysis of the gas distributions in the inner regions of each galaxy.

§6. Comparison of CO and HI Radial Distributions

Figure 5.12 displays the radial distributions of HI and CO in the 22 Virgo galaxies which our survey has in common with the HI mapping survey of Warmels (1986). The CO distributions are expressed in units of σ_{H_2}, the surface density of molecular hydrogen, and have been corrected for inclination and source-beam coupling as described in Chapter III. The HI distributions are corrected for inclination and projection effects, as described by Warmels. Among these 22 galaxies, 16 of the 19 galaxies which are detected in CO have CO distributions which increase monotonically toward the center. All 19 detected galaxies from this sample of 22 have their CO emission more centrally confined than their HI. And in 18 out of the 22 galaxies, the mass of molecular gas exceeds the mass of atomic gas in the inner galaxy.

An examination of the gas distributions in Figure 5.12 yields the qualitative impression that even the central regions of the galaxies with global HI deficiencies are HI-deficient. In most galaxies with $-0.10 < \text{HI def} < 0.60$, the surface densities of HI and H_2 are observed

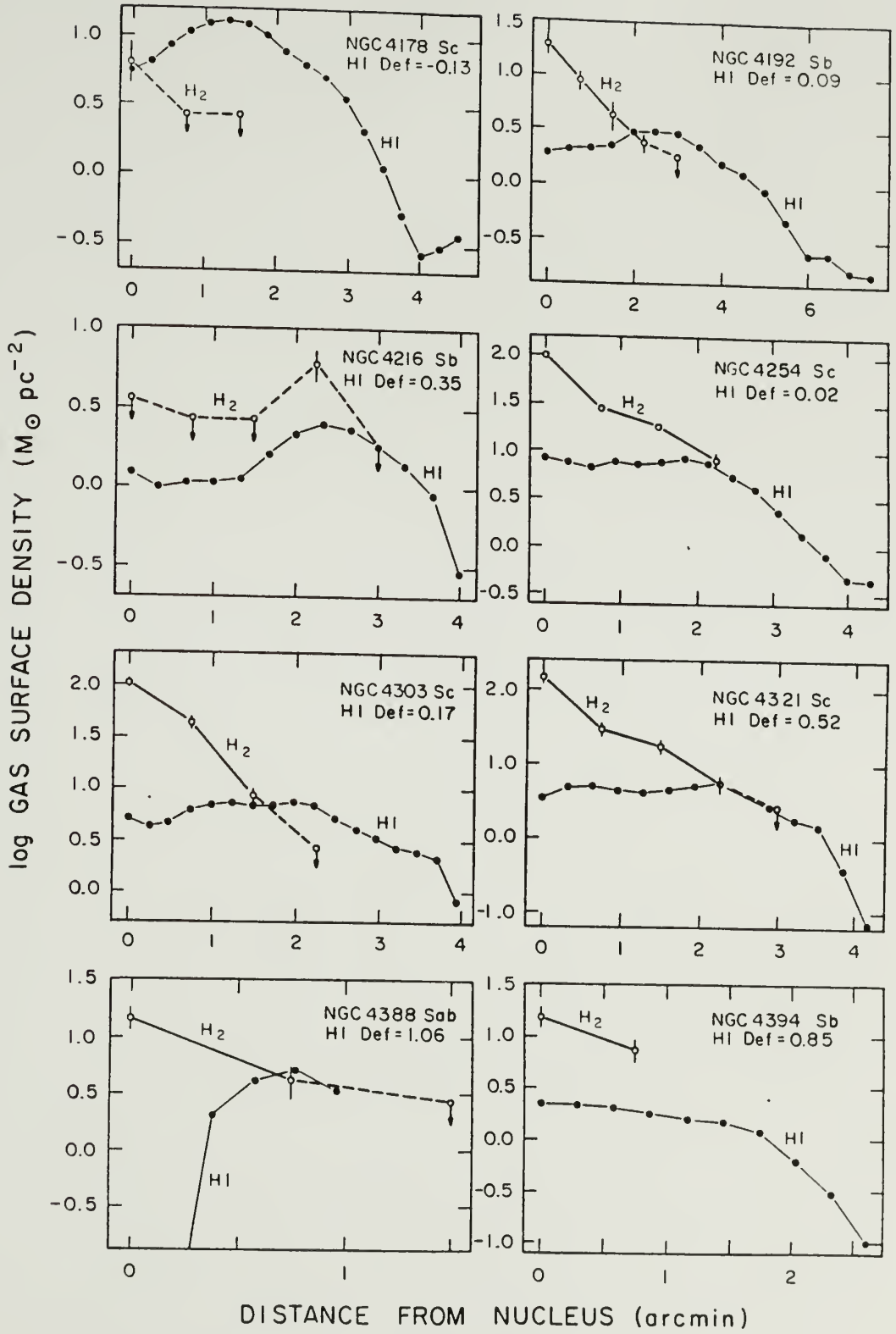
NGC 4178 Sc
HI Def = -0.13
NGC 4192 Sb
HI Def = 0.09
NGC 4216 Sb
HI Def = 0.35
NGC 4254 Sc
HI Def = 0.02
NGC 4303 Sc
HI Def = 0.17
NGC 4321 Sc
HI Def = 0.52
NGC 4388 Sab
HI Def = 1.06
NGC 4394 Sb
HI Def = 0.85
H2
HI
log GAS SURFACE DENSITY (M⊙ pc-2)
DISTANCE FROM NUCLEUS (arcmin)

Figure 5.12

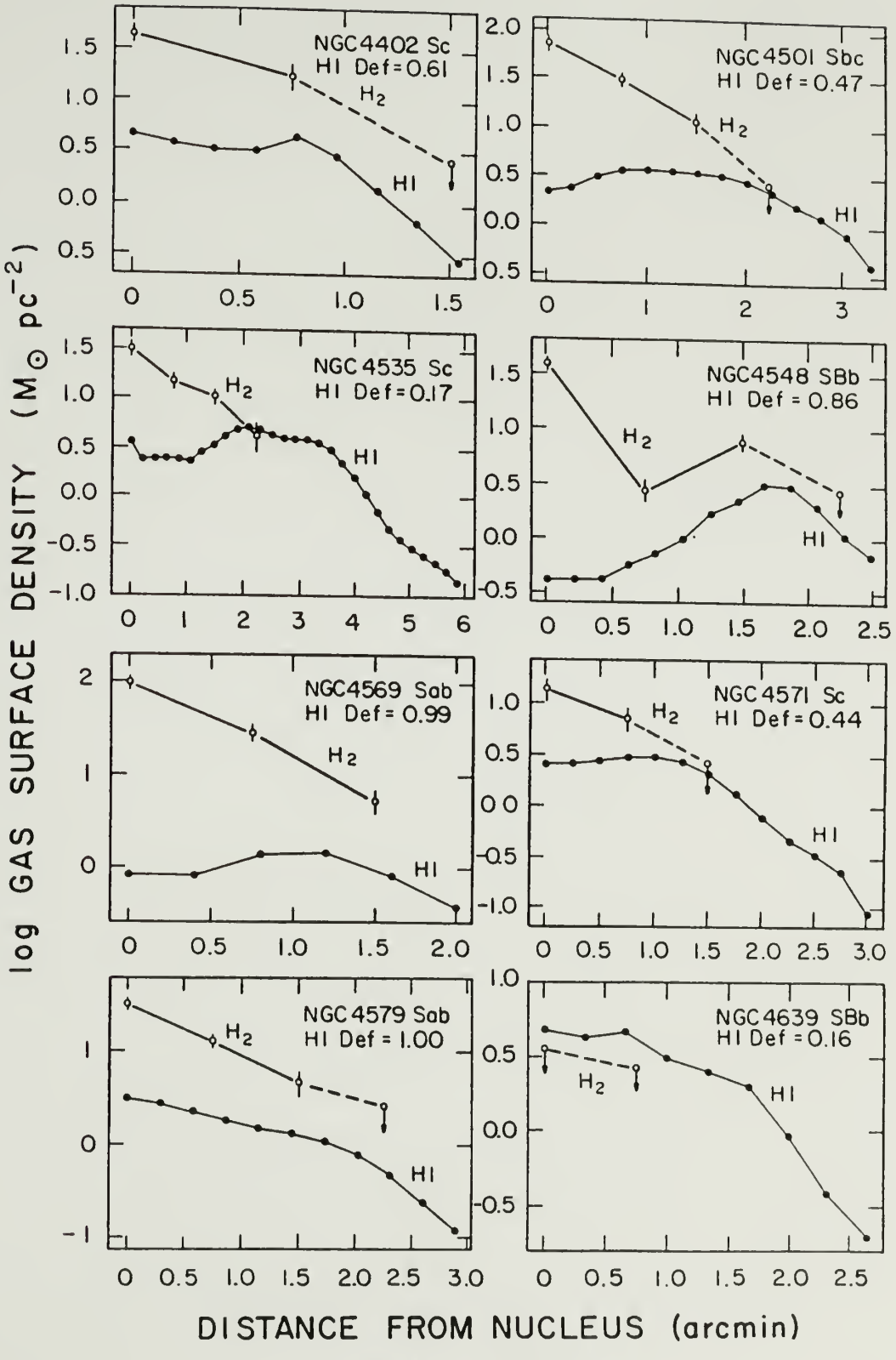

Figure 5.12 (cont.)

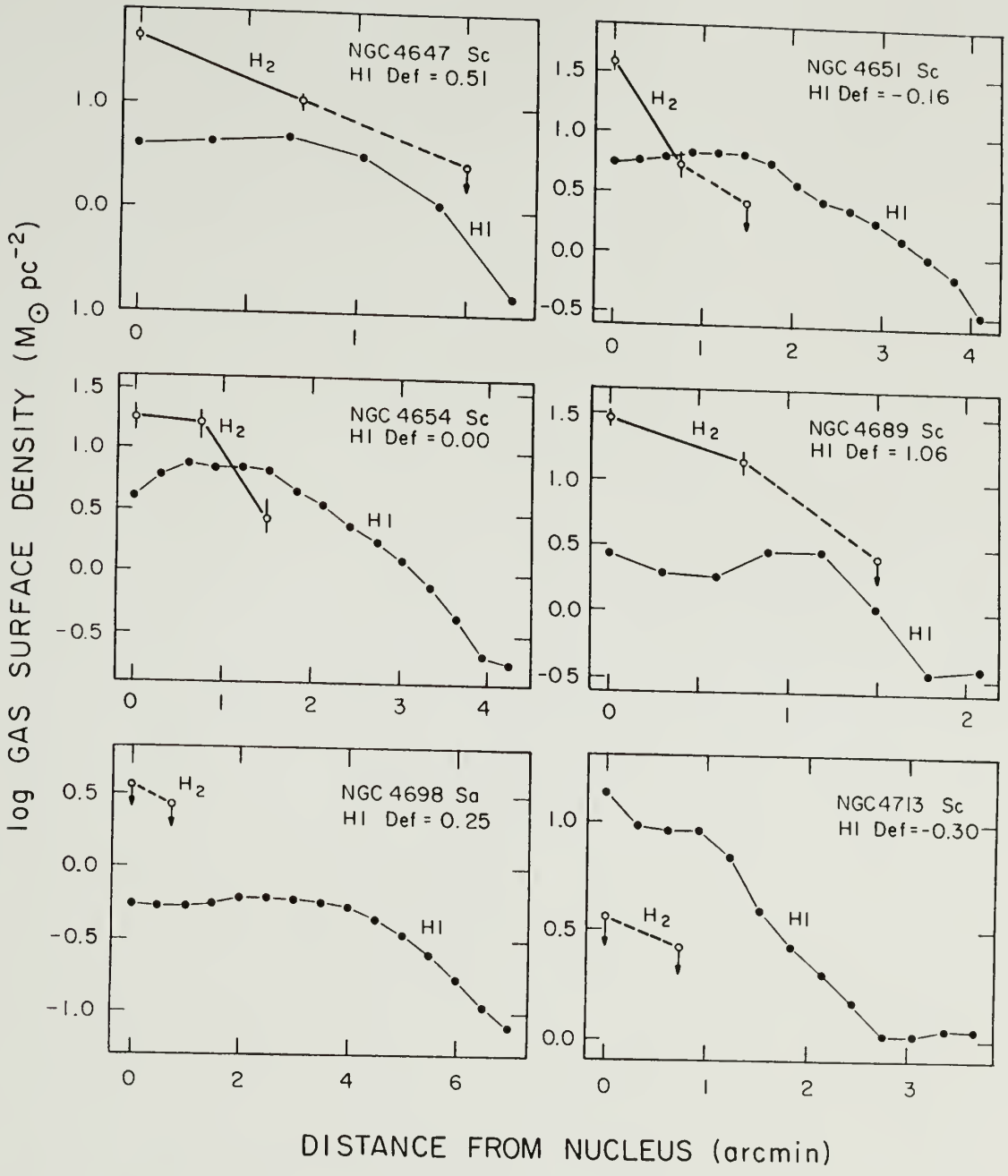

Figure 5.12 Radial distributions of HI and H_2 surface densities for 22 of the Virgo cluster galaxies. Both gas distributions have been corrected for inclination and source-beam coupling. 2σ upper limits are plotted for the H_2 distributions.

to be equal at some radius. In 6 out of the 7 systems with HI def > 0.60, $\sigma_{HI} < \sigma_{H_2}$ at all radii where CO is detected. The HI distribution in the remaining galaxy with HI def > 0.60, NGC 4388, is somewhat uncertain because the galaxy is edge-on, and the HI data are noisy, due to imperfect sidelobe removal (Warmels 1986). In the 2 HI-rich, CO-poor, low luminosity Sc's (NGC 4178, NGC 4713), $\sigma_{HI} > \sigma_{H_2}$ at all radii, except for the very center of NGC 4178, where $\sigma_{HI} \sim \sigma_{H_2}$. Furthermore, the maximum HI surface density in these 2 systems is ~13 $M_o\ pc^{-2}$, which is a factor of 2 larger than σ_{HI} in any of the other Virgo galaxies plotted here. The <u>total</u> gas surface densities ($HI+H_2$) in the inner disks of these HI-rich, CO-poor galaxies are remarkably similar to those in the Sc galaxies of the same optical luminosity with moderate HI deficiencies. A comparison of the gas distributions in NGC 4713 with those in NGC 4571 and NGC 4689 indicates that the central total gas surface densities and distributions are nearly the same, yet in NGC 4713 the central galaxy ISM is HI-dominated, while in NGC 4571 and NGC 4689 it is H_2-dominated. The difference in the gas distributions of these galaxies is either related to a possible difference in total mass, or indicates that the conversion of HI into H_2 has been assisted in low mass galaxies by an ISM-ICM interaction.

In order to place the conclusion that the central regions of the Virgo galaxies have been affected by the cluster environment on firmer quantitative ground, HI and H_2 masses within the inner half of the optical disk have been computed. Figure 5.9 shows that, on average, CO has been detected out to a radius $D_o/4$, although there is a lot of

scatter, and CO extents for early-type galaxies are generally smaller than those for late-type galaxies. The values for the fraction of HI flux within the inner half of the optical disk have been taken directly from the work of Warmels (1986). In Figure 5.13, we demonstrate that the galaxies with large global HI deficiencies have less HI in the inner disk. Plotted in Figure 5.13 is the global HI deficiency vs. the mean HI surface density σ_{HI} in the inner half of the optical disk, normalized by $\langle\sigma_{HI}(T,I)\rangle$, the average value for a more isolated galaxy of the same type (Warmels 1986). All of the Virgo galaxies in Warmels' sample have been plotted here. Although this includes several galaxies which are not in the CO survey, the slope of this relation is unaltered by omitting the galaxies which are not in common. Summarized in Table 5.3 are the results of least squares fits to the data in Figure 5.13. The slopes for all galaxy samples (with the discrepant galaxy NGC 4388 removed) are consistent with a value of -0.35 ± 0.10. This means that the galaxies which are globally HI-deficient by a factor of 10 are HI-deficient in the inner galaxy by a factor of ~2-3.

Warmels (1986) reached a different conclusion from the same data, since he plotted the normalized inner galaxy HI surface densities vs. the distance from M87. Although there is a general correlation between HI deficiency and cluster position, there is a fair amount of scatter, as we display in Figure 5.14. Scatter is expected, in part due to projection effects, and in part due to stripped galaxies whose orbits have taken them out of the core region. The amount of scatter in the HI deficiency vs. R_{M87} plane is sufficient to mask an inner galaxy HI

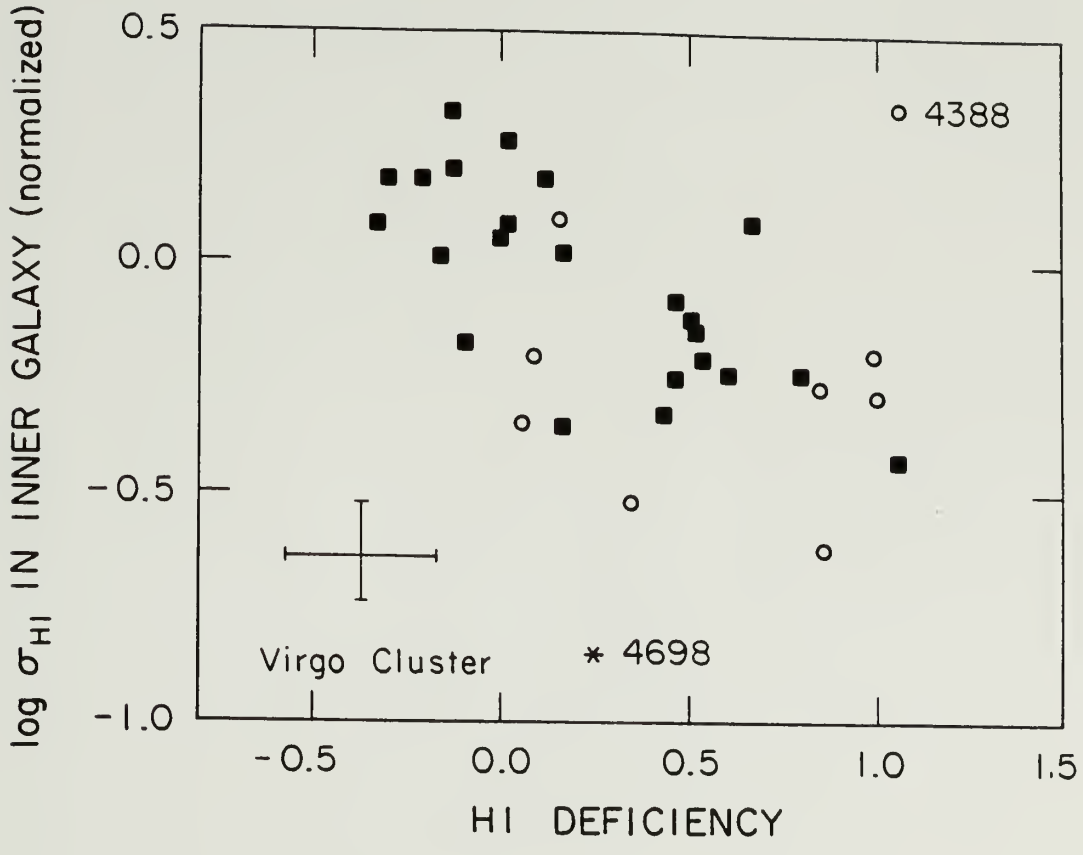

Figure 5.13 Logarithm of the mean HI surface density in the inner half of the optical disk (out to a radius $D_o/4$), normalized by the average value for a more isolated galaxy of the same type (taken from Warmels 1986) vs. HI deficiency. The 33 Virgo galaxies plotted here include 11 systems which are not in the CO survey. Their omission does not significantly affect the appearance of this figure. The 2 most discrepant galaxies in this plot, NGC 4388 and NGC 4698, are labelled. This diagram shows that even the inner regions of the globally HI-deficient galaxies are HI-deficient.

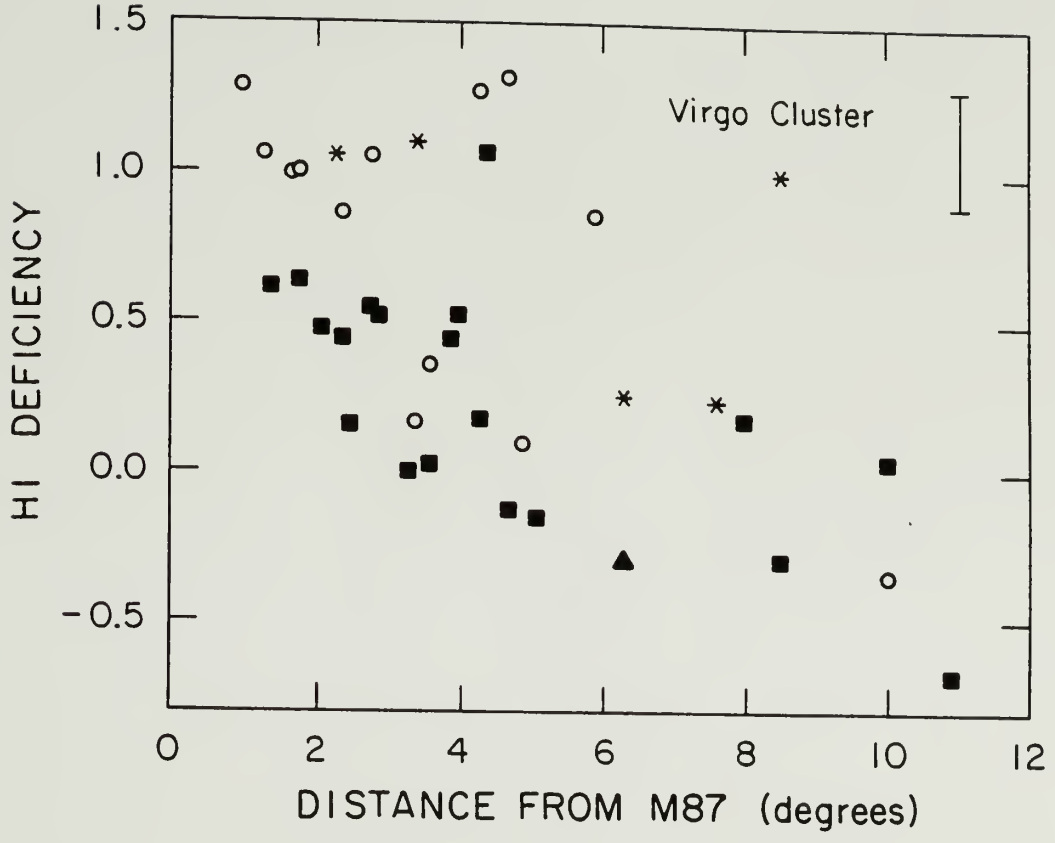

Figure 5.14 HI deficiency parameter vs. distance from M87. Although there is a good correlation between these parameters, there is also a fair amount of scatter, which is in part due to projection effects.

deficiency of a factor of 2-3. We do concur with Warmels that the outer disks of the galaxies are far more HI-deficient than the inner disks.

A moderate inner galaxy HI deficiency is required to explain a result obtained by Giovanelli and Haynes (1983). They found that the mean global HI surface density, defined as the ratio of the global HI mass to the area which contains 70% of the HI mass, is similar for HI-deficient and HI-normal Virgo spirals. This result constrains how the radial distribution of HI changes with HI deficiency. If all regions of a galaxy became equally HI-deficient, then the mean HI surface density would be smaller in HI-deficient spirals, since the area which contained 70% of the total flux would not change. If only the outer disks became HI-deficient and the inner disks remained unscathed, then the mean global HI surface density would increase in the HI-deficient galaxies, since the inner disk regions have higher HI surface densities than the outer disk regions. In order to maintain the same mean HI surface density as the HI deficiency is increased requires that most of the HI is lost from the outer galaxy, but also that some of the HI is lost from the inner galaxy. Thus the result of Giovanelli and Haynes supports our conclusion that the inner disks of galaxies with severe global HI deficiencies are moderately HI-deficient.

Given that the inner galaxy is only moderately HI-deficient with respect to the global HI deficiency, the question arises as to whether the molecular gas is also moderately deficient. In Figure 5.15, the H_2/HI mass ratio in the inner half of the optical disk is plotted vs.

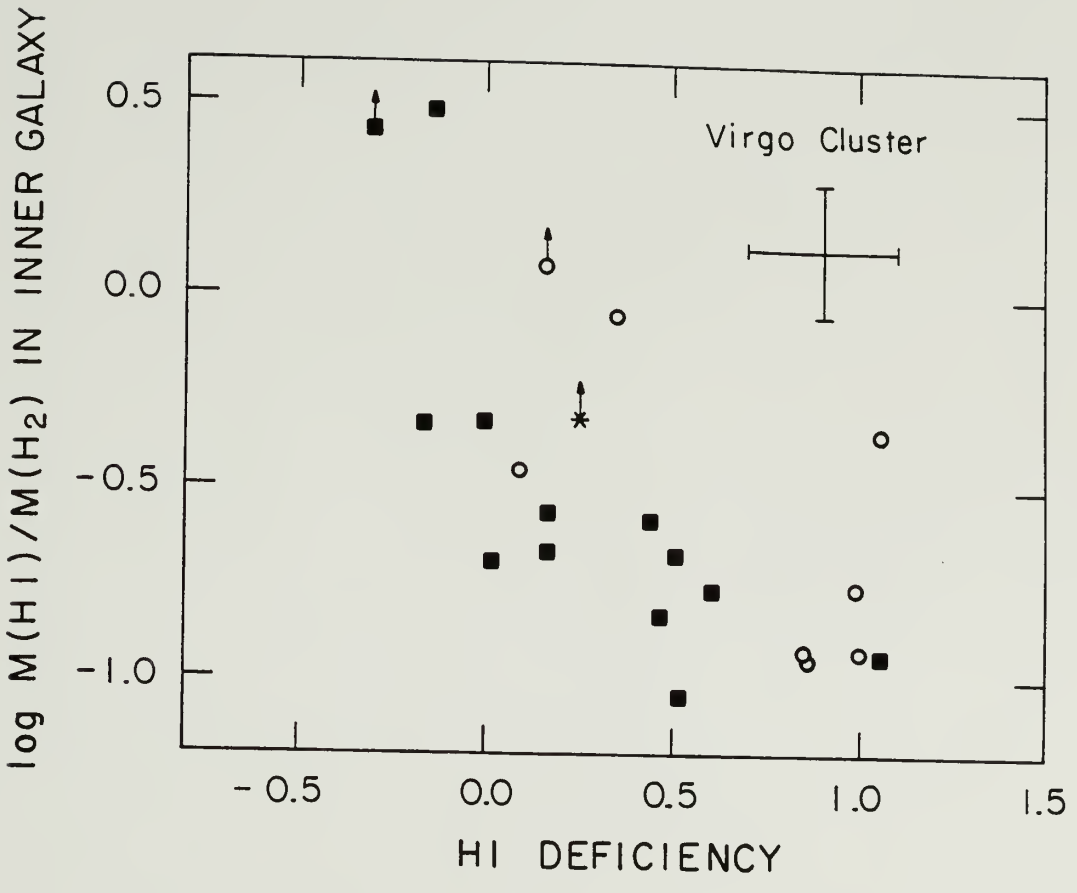

Figure 5.15 Logarithm of the HI to H_2 mass ratio in the inner half of the optical disk (out to a radius of $D_o/4$) vs. HI deficiency.

HI deficiency. While there is a lot of scatter, there is a clear trend for the HI-deficient galaxies to have larger inner galaxy H_2/HI mass ratios. This is confirmed by least squares fits to the data in Figure 5.15, which are summarized in Table 5.3. The fit for the Sab-Sb galaxies may be misleading: the one very HI-deficient Sab galaxy with an upper limit to its CO flux could not be included in this plot for lack of high resolution HI data, so the slope listed in Table 5.3 is artificially steep. For all the Sbc-Sc galaxies (which do not suffer from this problem since all the CO non-detections are for HI-rich galaxies), the slope of -0.98 ± 0.26, which is much steeper than the inner galaxy HI deficiency slope of -0.38 ± 0.09, is either the result of selection effects, or suggests that the conversion of HI into H_2 is occurring in the inner regions of at least some of the galaxies. The slope of -0.43 ± 0.14 for the Sbc-Sc galaxies with HI def > 0 is identical to the inner galaxy HI deficiency slope. Therefore the HI-deficient Virgo Sc's are not even moderately H_2 deficient in the inner galaxy. The fact that these slopes are identical does not, however mean that the hypothetical conversion of HI$\rightarrow H_2$ must cease once an HI-rich galaxy acheives HI def = 0.00. At this stage, the inner galaxy H_2 mass so dominates the HI mass that the additional conversion of HI into H_2 would not create a large fractional change in the H_2 mass. For this reason, it is not possible to tell whether the hypothetical conversion of HI$\rightarrow H_2$ might continue for HI def > 0.

§7. CO Asymmetries as a Function of HI Deficiency and Cluster Position

In view of the asymmetric HI distributions observed in many of the HI-deficient Virgo spirals (Warmels 1986), it is prudent to examine the CO distributions for similar evidence of environmentally-related modification. With one exception, there is no good evidence that the observed CO asymmetries are related to the HI deficiency or cluster position.

In Figure 5.16, the absolute value of the CO flux asymmetry parameter (see §III.7), is shown to be essentially uncorrelated with HI deficiency. Comparisons of the CO diameter asymmetry parameter vs. HI deficiency, and both CO asymmetry parameters vs. the distance from M87 (not shown) all show essentially no correlation. In Figure 5.17, the signs of the CO flux asymmetry parameter are plotted on a positional map of the Virgo cluster. The crosses represent those galaxies which have more CO emission on the side of the galaxy closest to M87, while the o's represent those with more emission away from M87. There are nearly the same number of each type, and there is no significant clustering or radial variation.

Comparisons of the CO and HI asymmetry parameters (not shown) show no correlation, yet these comparisons are plagued by differences in the regions sampled in the CO and HI surveys (see §III.7 and §V.2). Thus, no definite statement can be made on the existence or lack of existence of correlations between CO and HI asymmetry.

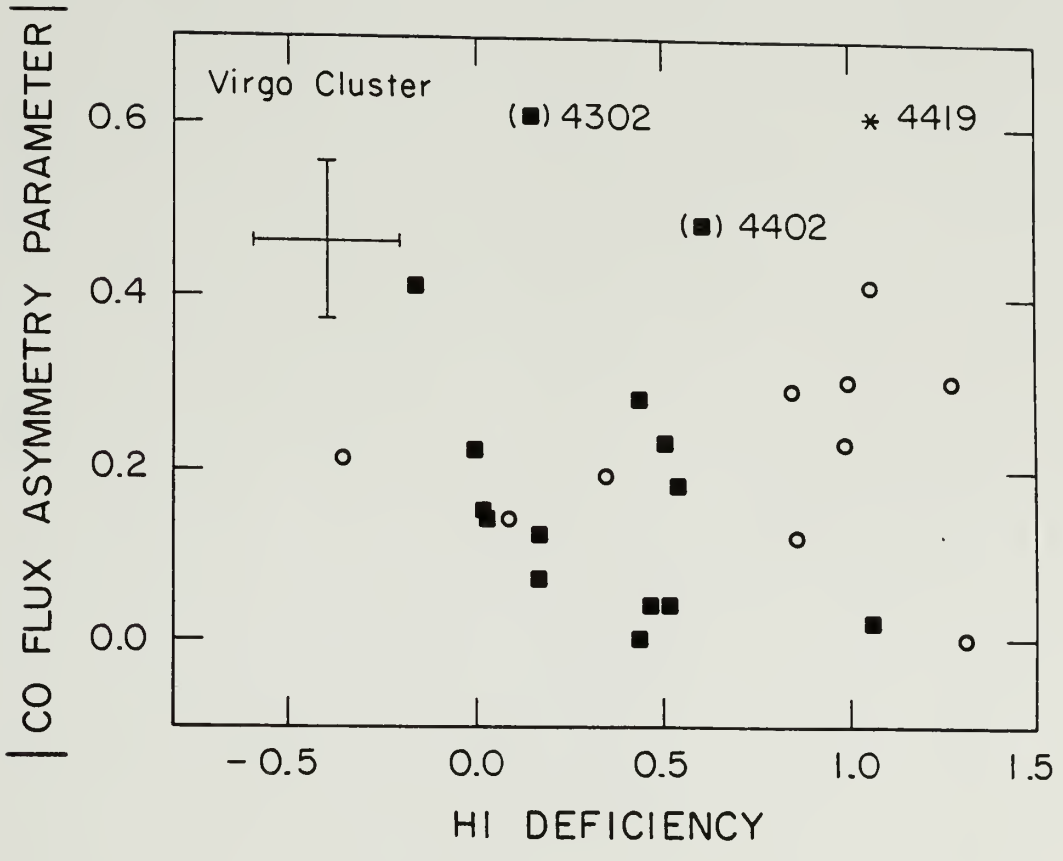

Figure 5.16 Absolute value of the CO flux asymmetry parameter vs. HI deficiency. The two galaxies in parentheses, NGC 4302 and NGC4402, are suspected of having artificially high asymmetry parameters due to the optical centers (from Dressel and Condon 1976) being offset from the true dynamical centers (see §III.7). The galaxy NGC 4419 is believed to be truly asymmetric, and moreover, has the largest S_{CO}/S_{HI} ratio in the entire Virgo sample.

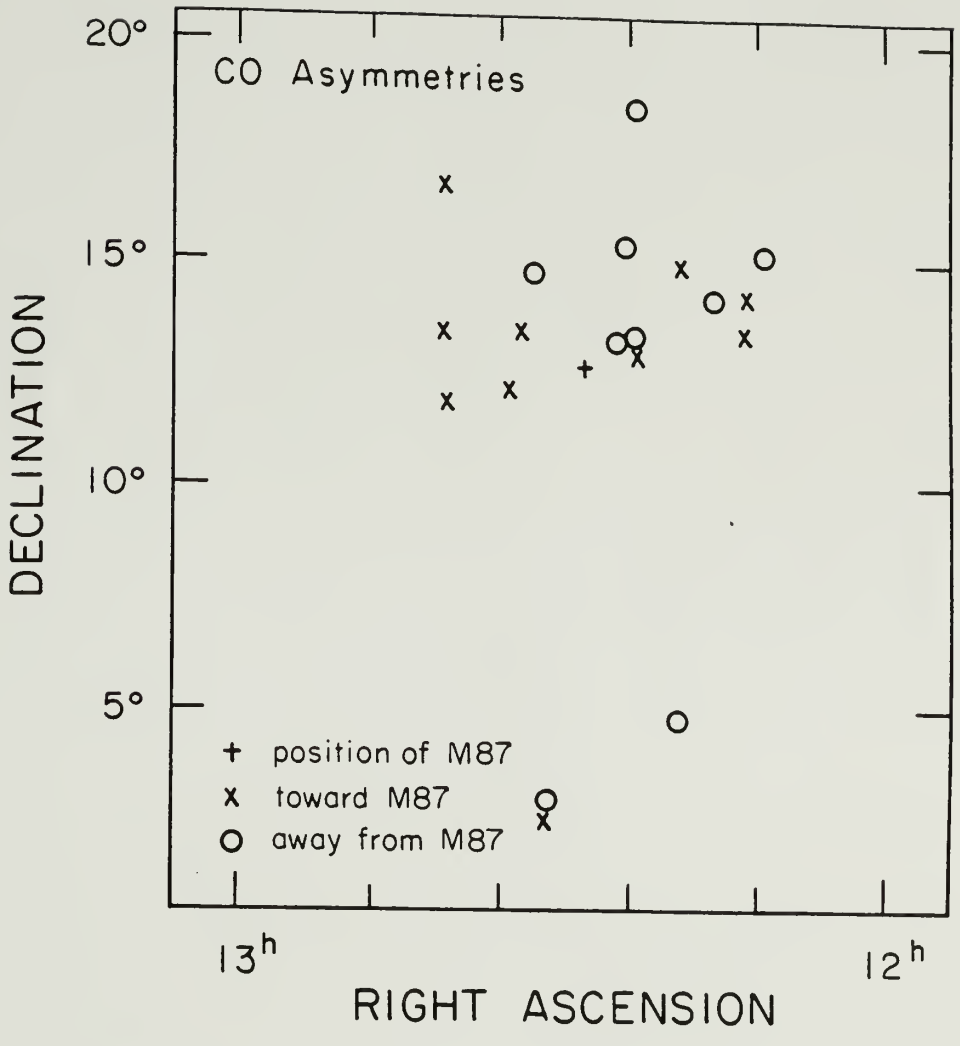

Figure 5.17 Sign of the CO flux asymmetry parameter on an RA-Dec map of the Virgo cluster. Crosses represent those galaxies with more CO emission on the side of the major axis closest to M87. Circles represent those with more CO emission on the side of the major axis away from M87. Only those galaxies with an asymmetry parameter whose absolute magnitude is greater than 0.10 have been plotted. The cross marks the location of M87.

The galaxy with the largest CO flux asymmetry, NGC 4419, is interesting because it is significantly HI deficient (HI def = 1.06), and has the largest CO/HI flux ratio in the Virgo sample (with an inferred $M(H_2)/M(HI) = 25$). Since the ISM in this galaxy has been apparently altered by cluster processes, it is likely that the large CO asymmetry is also the result of an ISM-ICM interaction. It may be that a CO asymmetry is apparent only in extreme cases of galactic modification. The sensitivity and spatial resolution of the present CO data may be insufficient to reveal intrinsic molecular gas asymmetries in galaxies whose interaction with the cluster has been less severe.

§8. The Nature of the ICM-ISM Interaction

The following conclusions can be drawn from the analyses of the CO and HI fluxes and distributions. Little or no molecular gas has been removed from the HI-deficient galaxies. While the outer disks are severely HI-deficient, the inner disks are also moderately HI-deficient. For most galaxies, it is not possible to distinguish between removal of HI in the inner galaxy, and the conversion of atomic gas into molecular gas, since molecular gas dominates the interstellar medium in the inner regions of most sample galaxies (as shown in Figure 5.15). For the lower luminosity late type galaxies, there exists an unexplained correlation in the HI and CO luminosities. One possible explanation is that low mass galaxies do not form much molecular gas, and that the HI-rich, CO-poor galaxies have systematically lower masses and were included in the sample as a result of selection effects.

Alternatively, the conversion of HI into H_2 in the inner galaxy may have been triggered by the cluster environment. In the following 2 sections, we seek to understand why molecular gas has resisted removal, and how a cluster process might facilitate the conversion of HI into H_2.

Several mechanisms have been proposed to explain the removal of HI from Virgo cluster galaxies. Most of them can be ruled out because their predictions are contradicted by the HI observations. Galaxy collisions are too infrequent to explain the large fraction of HI-deficient galaxies (Chamaraux et al. 1980). Tidal stripping is most effective in low velocity encounters, and is not a plausible mechanism in Virgo, where the 1-dimensional spiral velocity dispersion is ~800 km s^{-1} (Huchra 1985). Furthermore, the lack of tidal tails, and the difference in HI and optical radial distributions tolls the death knell for this model (Warmels 1986). Thermal evaporation (Cowie and Songaila 1977) does not predict the observed HI asymmetries or the large difference in HI-deficiency between the inner and outer galaxy, and may not occur rapidly enough to explain the large fraction of HI-deficient systems (Warmels 1986). Ram pressure stripping (Gunn and Gott 1972) is the one simple model which is consistent with most of the HI observations. We find that ram pressure stripping can also explain the basic features of the CO observations.

An objection to ram pressure stripping has been raised by Hoffman et al. (1985) and Haynes and Giovanelli (1986). Dwarf galaxies have the same range of HI deficiency values as the large spirals, despite

their lower masses and lower resistance to ram pressure stripping. The consideration of molecular gas may weaken this criticism. Molecular gas is a significant fraction of the total ISM mass in the large spirals; it resists removal, and its abundance may be enhanced in some galaxies by the conversion of HI into H_2. As a result, the total gas ($HI+H_2$) deficiency in the large spirals is only a fraction of the HI deficiency. As is shown in §V.4, large spirals which are HI-deficient by a factor of 10 have a mean total gas deficiency of only a factor of 2-3. In non-cluster dwarf irregulars, the CO to HI flux ratios are generally much lower than in large spirals, indicating that molecular gas is typically less than a few percent of the total ISM mass (e.g. Tacconi and Young 1987). Dwarf galaxies, therefore, may have total gas deficiencies equal to their HI deficiencies. Alternativley, it may be that the total gas deficiencies of dwarfs are less than their HI deficiencies, if the ICM-ISM interaction converts a large fraction of the pre-interaction HI into H_2. The weak CO signals expected from Virgo dwarfs will unfortunately keep their molecular content a mystery for years.

Turbulent viscous stripping (Nulsen 1982), which results from the Kelvin-Helmholtz instability formed near the boundary of the hot ICM and the cold ISM, compliments and in some cases is more effective than ram pressure stripping. Turbulent viscous stripping is less sensitive to a galaxy's inclination than ram pressure stripping, thus can remove gas even if the galaxy is moving edge-on through the cluster. Haynes and Giovanelli (1986) find that the mass loss predicted from turbulent

viscous stripping is consistent with the observed HI deficiencies of both spirals and dwarfs (although they did not consider the H_2 component).

The reality in the Virgo cluster is likely to encompass both effects. Here we will assess whether the predictions of ram pressure stripping are consistent with the CO observations, because of the specific predictions about the radial distribution and gas density dependence of removal susceptibility, and because of the agreement with most (if not all) of the observations. With the simple ram pressure stripping model, gas is removed if the ram pressure $\rho_{ICM} v_p^2$ exceeds the gravitational force per unit area $2\pi G \sigma_{TOT}(R) \sigma_{gas}(R)$ binding the gas to the disk. The relation for the maximum gas surface density which will be stripped is:

$$\sigma_{gas}(R)\,\sigma_{TOT}(R) < \frac{\rho_{ICM} v_p^2}{2\pi G} \quad . \qquad \text{(V-13)}$$

In this expression, ρ_{ICM} is the mass density of the ICM, v_p is the component of the galaxy's velocity with respect to the cluster ICM that is perpendicular to the disk, $\sigma_{TOT}(R)$ is the total mass surface density of the disk (including stars, gas, and dark matter), which is a function of galactocentric distance R, and $\sigma_{gas}(R)$ is the gas mass surface density ($\sigma_{gas} = \sigma_{HI} + \sigma_{H_2} + \sigma_{He}$). Since both $\sigma_{gas}(R)$ and $\sigma_{TOT}(R)$ decrease with increasing R, the ram pressure stripping susceptibility increases strongly with increasing R.

Estimates of typical values of the above parameters show that molecular clouds in spiral galaxies are resistant from ram pressure stripping. Fits to the Einstein x-ray satellite IPC surface brightness profiles (0.2-4.5 keV) out to 90' from M87 yield $n_{ICM} \sim 4 \times 10^{-4}$ cm^{-3} at a separation of 1° from M87 (Fabricant and Gorenstein 1983). An extrapolation of this surface brightness profile to 5° from M87 suggests $n_{ICM} \sim 5 \times 10^{-5}$ cm^{-3}. The line-of-sight velocity dispersion for Virgo spirals is ~800 km s^{-1} (Huchra 1985), but the strong inclination dependence means that v_p can range from 0 to 1400 km s^{-1} among Virgo spirals. Estimates of total disk surface densities in Virgo galaxies can be obtained by scaling the solar neighborhood Milky Way value of $\sigma_{TOT}(R_o) = 75\ M_o\ pc^{-2}$ (Bahcall, Schmidt and Soneira 1983) by the appropriate maximum disk rotational velocity and galactocentric distance. The mass contained within a given radius, M_R, is related to the rotational velocity V and galactocentric radius R by $M_R \sim V^2 R$, thus the mass surface density $\sigma_{TOT}(R) \sim V^2/R$. Since massive galaxies have rotation curves which flatten outside the central regions (Rubin et al. 1985), the rotational velocity at most disk positions can be estimated by the maximum rotational velocity, V_{max}, which can be inferred from the HI linewidth (equation V-2). Armed with V_{max}, the mass surface density in the disk of a galaxy can be crudely estimated from:

$$\sigma_{TOT}(R) = 75 \left\{\frac{V_{max}}{220 \text{ km s}^{-1}}\right\}^2 \left\{\frac{R}{8.5 \text{ kpc}}\right\}^{-1} M_o\ pc^{-2} \qquad (V\text{-}14)$$

where 220 km s^{-1} is the Milky Way's rotational velocity in the solar neighborhood, assumed to be 8.5 kpc from the galactic center. The least massive galaxies in the sample have $V_{max} \sim 100$ km s^{-1}, and optical radii of ~10 kpc ($D_o/2$ at a Virgo distance of 20 Mpc), which corresponds to $\sigma_{TOT}(10 \text{ kpc}) \sim 13\ M_o\ pc^{-2}$, from equation V-14. If these small spirals moved with a face-on velocity of 800 km s^{-1} through the dense intracluster gas 1° from M87, gas with a surface density less than $\sigma_{gas}(10 \text{ kpc}) = 17\ M_o\ pc^{-2}$ would be stripped. This is nearly twice the beam-averaged gas surface density of molecular clouds at the limit of detectability ($\int T_R(CO)dv = 1.5$ K km s^{-1}, where a factor of 1.36 for Helium has been included to compute the total gas surface density).

However, it is not the beam-averaged gas surface density which is relevant, but the actual gas surface density. CO surveys of the Milky Way show that the surface filling factor of molecular gas is small. Analysis of the Massachusetts-Stony Brook Galactic Plane Survey (Scoville et al. 1987) reveals that over ~80% of the Milky Way's molecular gas is contained in Giant Molecular Clouds (GMCs) with $D \geq 5$ pc and $M \geq 10^4\ M_o$. From the relationships between cloud properties given by Scoville et al., it can be inferred that the mean cloud surface density is related to the cloud size by:

$$\sigma_{gas} = 245 \left\{\frac{D}{40 \text{ pc}}\right\}^{0.1} M_o\ pc^{-2} \qquad \text{(V-15)}$$

A 'smallish' GMC with D = 5 pc has $\sigma_{gas} = 200\ M_o\ pc^{-2}$. (The masses here include the Helium contribution, and use the CO-H_2 proportionality

factor described in Chapter III which is slightly different than that used by Scoville et al.) Clouds like this would not be stripped from a galaxy moving face-on through the dense ICM gas only 1° from M87, even at the extreme velocity of 1400 km s^{-1} unless the disk mass surface density were lower than 4 M_o pc^{-2}. Disk surface densities do not become this low in any of the Virgo galaxies studied here until far beyond the optical diameters.

This example illustrates that molecular clouds are not susceptible to ram pressure stripping in the Virgo cluster environment. Kritsuk (1983) reached the same conclusion in a more detailed dynamical treatment of this problem. This is not meant to be taken as evidence that ram pressure stripping is the only (or even dominant) gas removal process operating. The properties of molecular clouds make them less susceptible than atomic gas to many removal mechanisms. Molecular clouds are colder, denser, and have a smaller scale height than HI clouds. Having atomic gas surround molecular clouds means that the atomic gas can act as a buffer layer between molecular clouds and the ICM, partially shielding the dense clouds from thermal evaporation and turbulent instabilities. Finally, the centrally peaked molecular gas distributions mean that a large fraction of the H_2 exists in the inner regions of galaxies, where it is more tightly bound. It is not surprising that molecular clouds have resisted removal.

§9. The Anti-Correlation of HI and CO in Low Luminosity Late Type Galaxies

One of the more remarkable results from §V.3 is the discovery that the HI and H_2 masses are anti-correlated in the lower luminosity late type galaxies. Interpretations of this finding must explain the following observations:

1.) The CO luminosity to optical area ratios span nearly an order of magnitude among the Virgo Sc-Sm galaxies with $11.0 < B_T^o < 12.0$. For $B_T^o < 11.0$, there is a good correlation between the CO luminosity and the optical area, with a scatter of only 0.14 dex.

2.) The CO luminosity to optical area (or blue luminosity or indicative mass) ratios in the low luminosity systems have a bimodal distribution. The CO-rich low luminosity systems have the same mean L_{CO}/D_{opt}^2 as the high luminosity systems.

3.) All of those low luminosity galaxies with low L_{CO}/D_{opt}^2 are HI-rich (i.e. HI def < 0.00). All of those low luminosity galaxies with high L_{CO}/D_{opt}^2 are HI-poor (i.e. HI def > 0.00).

4.) All of the HI-rich, CO-poor, low luminosity late type systems are in the outer cluster ($R_{M87} > 4.5°$). All of the HI-poor, CO-rich low luminosity late type systems are in the inner cluster ($R_{M87} < 4.5°$).

5.) Among those Virgo galaxies which have been mapped in both CO and HI, the inner galaxy total gas surface densities ($\sigma_{HI} + \sigma_{H_2}$) are similar for both types. In the HI-rich, CO-poor galaxies, the HI sur-

face densities in the central regions are comparable to the H_2 surface densities in the centers of the HI-poor, CO-rich galaxies.

A partial explanation for the observed anti-correlation in HI and CO luminosities among the lower luminosity late type galaxies may be that the galaxies do not have comparable masses. As explained in §II.4, our blue magnitude-limited sample suffers from an important bias. The lower luminosity end of the sample includes actively star-forming galaxies with large ratios of blue luminosity to total mass, but no galaxies of comparable mass which are not actively forming stars. It will be shown in Chapter VI (see Figure 6.2) that the B-V colors of the HI-rich, CO-poor galaxies are systematically bluer than those in the HI-poor, CO-rich galaxies. This suggests that the HI-rich, CO-poor galaxies have the lowest masses in the entire sample. If the decisive difference between these galaxy samples is one of total mass, then it is necessary to understand only why the HI-rich galaxies have not formed much H_2. If the difference in total masses turns out to be insignificant or unimportant, then it is also necessary to understand why the HI-poor, CO-rich galaxies have so much molecular gas. The existence of the systematic bias in B-V colors makes it prudent to discuss these 2 issues separately. Since the lack of CO emission from the HI-rich galaxies must be explained regardless of the bias, we will discuss this topic first.

In order for molecular gas to become the dominant phase of the ISM, at least 3 conditions must be met. 1.) The metallicity must be high enough to allow sufficient quantities of dust to form. Dust is

the principal site of H_2 formation, and it shields the CO molecules from dissociating UV radiation. 2.) The total column density of gas must be large enough to shield the H_2 molecules from dissociating radiation (Federman, Glassgold, and Kwan 1979). 3.) The gas must be suitably confined. In other words, the gas density becomes large enough a) for H_2 to form efficiently on dust grains, and b) that there are not too many ionizing sources within the column density of gas.

Clearly, the paucity of CO emission in the HI-rich low luminosity galaxies does not arise from a low total column density of gas. In the 2 HI-rich galaxies with known HI distributions, the peak HI surface density of $\sim 13\ M_\odot\ pc^{-2}$ is larger than the total gas surface density ($HI+H_2$) at which many spirals have become H_2-dominated. Apparently, a large column density of gas is a necessary but insufficient condition for the formation of an H_2-dominated ISM. Some other parameter is also important.

It is difficult to evaluate the metallicity of the systems without a detailed spectroscopic study. Since the galaxies in question all have nearly the same luminosity, a possible luminosity-metallicity relation for spiral galaxies (Bothun et al. 1984; Rubin et al. 1984) is not a factor. While lower metallicities could result from reduced star formation rates, we note that the CO-poor galaxies have comparable, and perhaps even higher massive star formation rates than the CO-rich galaxies (Chapter VI). Because of the spatial segregation of the CO-rich and CO-poor systems, an explanation based on metallicity would require that the galaxies further from M87 are younger. There is no

evidence to support or reject this idea.

A clue in this matter comes from the observation that this phenomenon is a mass-dependent (i.e. luminosity-dependent) phenomenon. The most massive Sc galaxies in Virgo have similar values of $L_{CO}/D_{opt}{}^2$, regardless of HI deficiency or cluster position. Non-Virgo dwarf systems, which are the least massive galaxies observed, all have $L_{CO}/D_{opt}{}^2$ approximately an order of magnitude lower than the luminous Sc galaxies (Tacconi and Young 1985). Another clue comes from the observation that the σ_{H_2}/σ_{HI} ratio in most galaxies increases with decreasing distance from the galactic center. Both of these observations may be explained if the local mass surface density $\sigma_{TOT}(R)$ of the disk plays a large role in determining whether the available gas remains predominantly atomic or becomes predominantly molecular. Rotation curves of galaxies over a large range of luminosities show that the local mass surface density in galactic disks decreases with increasing distance from the center, and is greater in high luminosity galaxies than in comparable locations in lower luminosity galaxies (Rubin et al. 1985). With a larger mass surface density, there is a stronger gravitational force acting to compress interstellar gas. If supporting forces are not increased in proportion to the increase in gravitational force, then the scale height of the gas will be reduced. The resulting increase in gas density might facilitate the conversion of gas from the atomic to the molecular state.

A large mean volume density of gas is insufficient, on theoretical grounds, for converting large amounts of HI into H_2. A process which

gathers the gas into large self-shielding clouds is necessary. The most efficient method for creating a large supply of H_2 is to form GMCs through the process of inelastic cloud-cloud collisions (e.g. Scoville and Hersh 1979). The random motions of clouds are thought to lead to cloud formation rates which are too small to account for the the GMCs observed in our galaxy (Elmegreen 1987). The velocity shear in the disks of massive spirals like the Milky Way may play a critical role in the formation of GMCs, in that velocity shear results in an enhanced rate of cloud-cloud collisions (Wyse 1986). Low mass galaxies have slowly rising rotation curves (Rubin et al. 1985) which results in less velocity shear, and lower cloud-cloud collision rates. Thus slowly rising rotation curves may be the explanation for the dearth of CO emission in the outer cluster low mass spirals.

If the onset of an H_2-dominated ISM is related to the shape of the rotation curve, then one would not expect any of the earlier type spirals in the present sample to lack H_2 because of a slowly rising rotation curve. The rotation curves of early type spirals rise more steeply to a higher maximum velocity than late type spirals of the same blue luminosity (Rubin et al. 1985). The lower luminosity Sc galaxies, which include the 'CO-poor' population, have an absolute magnitude of M_B=-20 (for D=20 Mpc), which corresponds to an average maximum rotation velocity of 125 km s^{-1} (Rubin et al. 1985). An average Sa (Sb) galaxy with the same-shaped rotation curve is ~2 (~1) magnitudes fainter than an Sc galaxy. The lack of an obvious 'CO-poor' population of early type galaxies in the present sample cannot be unambiguously ascribed to

this rotation curve effect, because of the unfortunate paucity of early type Virgo spirals with near-normal amounts of HI. A critical test of this hypothesis (that the formation of an H_2-dominated ISM is related to the shape of the rotation curve) will be made through the examination of the type dependence of the most luminous CO-poor galaxies among isolated galaxies.

We turn now to the question of why there is so much molecular gas in the HI-poor, CO-rich Virgo Sc's with $12 > B_T^o > 10.9$. One explanation is that these galaxies have larger masses than the HI-rich, CO-poor spirals in the same magnitude range. Their larger masses may have enabled the galaxies to convert much of their original atomic gas into molecular gas. The passage through the dense ICM in the center of the cluster caused low density HI to be stripped away, further increasing the H_2/HI ratio. Since this hypothesis can neither be proven nor disproven with the present data, we investigate another possibility. The important difference between the HI-rich, CO-poor and HI-poor, CO-rich galaxies may not be galaxy mass, but location in the cluster. In the remainder of this section, we develop this idea.

An appealing explanation is that the action of the intracluster gas has perturbed the ISM, enabling HI to become H_2. It is natural to associate the existence of these 2 populations of galaxies with an ICM-ISM process. An ICM-ISM interaction is already strongly suspected to exist, and to be the cause of the HI-deficiency in Virgo and other clusters (Giovanelli and Haynes 1985; Haynes and Giovanelli 1986). The spatial segregation of the CO-rich and CO-poor populations might result

naturally from the higher ICM density in the central few degrees of Virgo.

Without adopting a specific model for the ICM-ISM interaction, it may be argued that the strength of this interaction has the potential to enhance the conversion of HI into H_2. The fact that the interaction force is strong enough to remove gas from the outer disk implies that it is strong enough to perturb gas in the inner disk. In many locations in many Virgo galaxies, the local circumstances are such that the ICM-ISM interaction force is insufficient to overcome gravity, yet is still an appreciable fraction of the gravitational binding force. Such a large perturbation is likely to have dynamical consequences (Kritsuk 1983). One possible consequence will be a reduction in the gas scale height by the compression of low density gas in the atomic phase. In galaxies with large column densities of atomic gas, compression may aid in the conversion of HI $\rightarrow H_2$. A second possibility is that the interaction perturbs the orbits of gas clouds which are not removed from the galaxy (Kritsuk 1983). The perturbation of orbits would increase the number of cloud-cloud collisions, enabling low mass galaxies with slowly rising rotation curves to form GMCs, and thereby convert atomic gas into molecular gas. Low mass galaxies with small pre-interaction $M(H_2)/M(HI)$ ratios have the potential to convert large quantitities of HI into H_2 in an interaction, thereby significantly increasing their $M(H_2)/M(HI)$ ratios. In more massive galaxies, a cluster interaction can cause only moderate amounts

of HI to become H_2, since the galaxy has already by itself converted most of its inner galaxy gas to the molecular state.

The potential for an ICM interaction to cause the compression of individual HI clouds can be quantitatively, albeit crudely, illustrated by comparing the various supportive and compressive forces associated with interstellar gas clouds. In Table 5.5, thermal, magnetic, turbulent and gravitational energy densities are compared with ram pressure for a 'typical' HI and H_2 cloud. (Although ram pressure is used in these examples, another ICM-galaxy force may be substituted. The fact that the galaxies are gas-deficient indicates that the gas removal force has roughly the strength referred to in Table 5.5.) The HI cloud is likely to be supported by turbulent internal motions, against the pressure exerted on it by the surrounding ISM. Self-gravity plays essentially no role at such low densities. Ram pressure on this HI cloud can be comparable to the internal turbulent energy density and the external ISM pressure for a typical galaxy-ICM encounter, and thus can be expected to be dynamically important.

Contrast the situation for the HI cloud with that of a typical GMC, where gravity is nearly balanced by turbulent (and perhaps magnetic) forces. In a typical passage of a Virgo galaxy through the cluster core, the ram pressure might be an order of magnitude less than the gravitational and turbulent energy densities, meaning that ram pressure will not be dynamically important. While it is plausible for ram pressure to compress low density HI gas and somehow facilitate its

Table 5.5

Supportive and Compressive Forces in Interstellar Clouds

Supportive Forces	Formula for Energy Density or Pressure	Energy Density/Pressure (erg cm^{-3}) H_2 cloud[a]	HI cloud[b]
thermal	$\frac{3k}{4\pi\mu m_H}\rho T$	3×10^{-13}	3×10^{-14}
magnetic	$\frac{B^2}{8\pi}$	1×10^{-12}	4×10^{-14}
turbulent	$\rho\sigma_v^2$	3×10^{-11}	4×10^{-12}
Compressive Forces			
ISM pressure	-	-	-
gravitational	$\frac{3G}{20\pi}\rho^2R^2$	3×10^{-11}	3×10^{-15}
ICM ram pressure[c]	$\rho_{ICM}v_p^2$	2×10^{-12}	2×10^{-12}

a) H_2 cloud: R=10 pc, $\rho=5.2\times10^{-21}$ gm cm^{-3}, $\sigma_v=1.5$ km s^{-1}, T= 10 K, B=5 μG.

b) HI cloud: R=10 pc, $\rho=1.7\times10^{-23}$ gm cm^{-3}, $\sigma_v=5.0$ km s^{-1}, T=100 K, B=1 μG.

c) ICM ram pressure: at 2° from M87, $\rho_{ICM}=2.8\times10^{-28}$ gm cm^{-3}, $v_p=800$ km s^{-1}.

transformation to the H_2 phase, it is less plausible for ram pressure to accelerate the contraction of molecular clouds and in this manner increase the star formation rate.

§10. Morphological Type Dependence of CO Emission

The existence of a range of morphological types in the Virgo sample allows us to examine whether the CO luminosity of spiral galaxies depends upon morphological type. At issue is whether the gas mass per unit total mass is systematically lower in early type spirals. Studies of the Hα emission in samples of spiral galaxies indicate that the Hα equivalent widths, and hence star formation rates per unit total luminosity, are systematically lower in early-type galaxies (Kennicutt and Kent 1983). Is this due to less available gas?

Virgo cluster galaxies do not constitute an ideal sample to answer this question. The atomic gas contents of many of the Virgo galaxies are known to be environmentally modified. Moreover, the modification appears to be more severe for early type galaxies then for late type galaxies (e.g. Chamaraux, Balkowski, and Fontanelli 1986; see also Figures 5.7-5.8). The existence of this systematic difference raises the possibility that any difference in the CO properties of early and late type Virgo spirals may be due to the environment rather than to morphology. To the extent that it is possible, we will attempt to separate the effect of morphology from that of environment.

CO luminosities, coded by morphological types, are plotted versus

blue luminosities, blue optical diameters, and indicative masses in Figures 5.1-5.3. While the different morphological types are not well-mixed in these figures, morphology is not the only source of scatter. Among the lower luminosity Sc galaxies, there is an order of magnitude variation in the values of L_{CO}/D_{opt}^2 (see also Figure 5.6). For galaxies in this luminosity range (less than $\sim 2.5 \times 10^{10}$ L_o or 10^{11} M_o, or smaller than ~25 kpc), the variation in CO luminosity among the Sc's is greater than the difference between morphological types.

The amount of scatter in the CO luminosities within each morphological type is reduced for Virgo galaxies which have blue luminosities greater than $\sim 2.5 \times 10^{10}$ L_o, masses greater than $\sim 10^{11}$ M_o, and blue optical diameters greater than ~25 kpc. Among these galaxies, the mean value of L_{CO}/D_{opt}^2 is the greatest for Sbc-Sc galaxies, less for Sab-Sb galaxies, and lowest for S0-Sa galaxies (see Figure 5.2). The CO luminosities have been compared with the optical diameters rather than blue luminosities or indicative masses, since diameters are a disk quantity. Decomposition of galactic light profiles into bulge and disk components demonstrates that starlight at the 25th magnitude per square arc second isophote level is dominated by disk stars, except in galaxies which have very large bulge-to-disk ratios (Boronson 1981). (We note that no galaxies with very large bulge-to-disk ratios are included in the Virgo sample). Thus it appears that the CO luminosity per unit disk luminosity is higher in luminous late-type Virgo spirals than in luminous early-type Virgo spirals. It remains to be shown that this difference is due to the morphology of the galaxy, rather than the result of

systematically larger environmentally-induced alterations in the early-type galaxies.

The effect of cluster position and HI deficiency are taken into account in Figures 5.4 and 5.5. Figure 5.4 shows that within 4.5° from M87, the L_{CO}/D_{opt}^2 values of the galaxies are clearly separated by morphological type. In the outer cluster ($R_{M87}>4.5°$), there is no such separation. This is in part due to the presence of the HI-rich, CO-poor, lower luminosity Sc galaxies in the outer cluster. Figure 5.5 shows that for galaxies with HIdef>0, the Sc galaxies have higher mean values of L_{CO}/D_{opt}^2 than the S0-Sb galaxies. Unfortunately, this comparison is plagued by an uneven distribution of HI deficiency values for the early and late type galaxies. Most of the Virgo sample galaxies with 0<HI def<0.7 are classified as Sc, while all but one of the Virgo galaxies with HI def>0.7 are classified as Sa-Sb. For galaxies with HI def<0, the variation of L_{CO}/D_{opt}^2 within the Sc galaxies is greater than the difference between morphological types.

To conclude, the variation of L_{CO}/D_{opt}^2 within a given morphological type is observed to be greater than the mean difference between morphological types. However, for the largest spiral galaxies ($D_{opt}\geq 25$ kpc), Sc galaxies have the highest mean value of L_{CO}/D_{opt}^2, followed by Sb galaxies and then Sa galaxies. The existence of systematic differences in the cluster positions and HI deficiencies of the early and late type galaxies does not seem to affect this conclusion. Thus the Virgo data are consistent with the hypothesis that the Hubble sequence of Sa-Sc morphological types, at least for the largest

galaxies, is one of increasing mean molecular gas mass per unit disk luminosity. Again, it is necessary to emphasize that the presence of ISM alteration in the Virgo cluster galaxies makes it difficult to reach a firm conclusion on the effect of morphology on the molecular gas contents of galaxies. This issue should be properly addressed with a study of the CO emission in isolated galaxies of various morphological types.

§11. Effect of the CO-H(2) Proportionality Factor

The primary goal in comparing the CO, HI, and optical properties of Virgo galaxies is to assess the molecular gas contents as a function of atomic gas content. Since the CO line is not as fundamental a tracer of molecular gas mass as the HI line is a tracer of atomic gas mass, the correlations on which our conclusions are based must be examined for a dependence on possible variations in the CO-H_2 proportionality factor. The discussion in Chapter IV summarized reasons for believing that the CO-H_2 proportionality factor might depend on the mean gas temperature (at present best indicated by the $S_{60\mu m}/S_{100\mu m}$ ratio), the optical luminosity (indicated by itself), and the cloud size spectrum (not indicated by anything currently measurable). In this section, we evaluate whether a variation in the CO-H_2 proportionality factor might affect the 2 central conclusions of this chapter--the existence of an anticorrelation in the atomic and molecular gas masses of lower luminosity late type spiral galaxies; and the near-independence of the molecular and atomic gas masses for all the other sample galaxies.

Theoretically, the CO-H_2 proportionality factor is expected to be most sensitive to the mean gas temperature. It is therefore critical to determine whether the $S_{60\mu m}/S_{100\mu m}$ values, a sensitive measure of dust temperature from galaxy to galaxy, depends upon the HI deficiency parameter, since much of our analysis relies on the HI deficiency parameter. In Figure 5.18, the logarithm of the $S_{60\mu m}/S_{100\mu m}$ ratio is plotted vs. the HI deficiency parameter. The far-infrared data, which were obtained with the IRAS satellite, are more fully described in Chapter VI. Least squares fits to log $S_{60\mu m}/S_{100\mu m}$ vs. HI deficiency, which are summarized in Table 5.3, show that there is no significant correlation between HI deficiency and dust temperature. If the slope of -0.12 ± 0.06 for the Sbc-Sm galaxies is taken to be real, then galaxies which are HI-deficient by a factor of 10 have $S_{60\mu m}/S_{100\mu m}$ ratios which are 30% cooler than a galaxy with HI def=0.00. This might result if dust which is associated predominantly with HI is warmer than dust associated with H_2, and this warmer dust is absent in severely HI-deficient galaxies. Alternatively, since the mean dust temperatures are slightly cooler in HI-deficient spirals, the mean molecular gas temperatures may also be . In this case the H_2 masses inferred from the CO luminosities might be slightly underestimated in the HI-deficient systems. The magnitude of this effect is small compared to the probable uncertainty in the CO-H_2 proportionality factor, and in any case is not statistically significant. Therefore, there is no significant evidence that the gas temperatures are appreciably different in the HI-deficient and

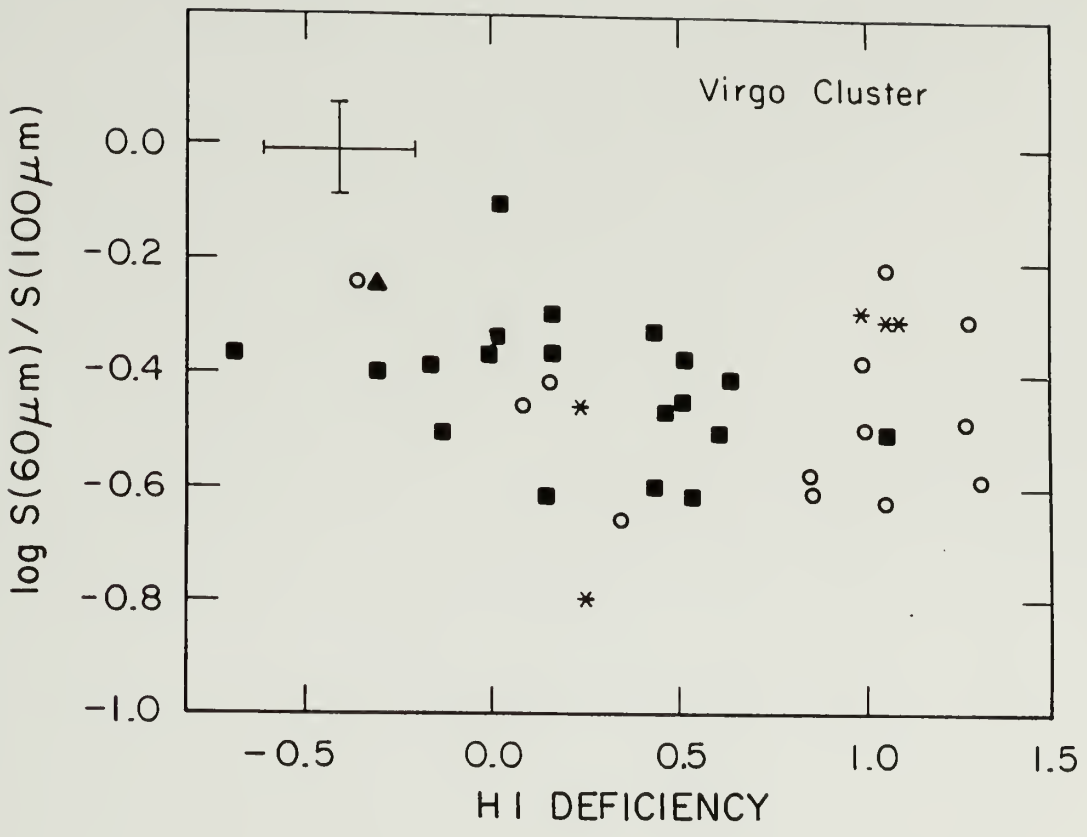

Figure 5.18 Logarithm of the 60μm to 100 μm flux density ratio vs. HI deficiency.

HI-normal galaxies. There is also no evidence for a morphological type dependence. The mean $\log(S_{60\mu m}/S_{100\mu m})$ values for several subsets of the Virgo sample are given by:

$$\text{mean } \log \frac{S_{60\mu m}}{S_{100\mu m}} = -0.44 \pm 0.14 \text{ for all 42 S0-Sm galaxies,}$$

$$-0.46 \pm 0.16 \text{ for 21 S0-Sb galaxies,}$$

$$-0.42 \pm 0.12 \text{ for 21 Sbc-Sm galaxies,}$$

$$-0.43 \pm 0.13 \text{ for 9 Sc-Sm, } B_T^o > 10.9, \text{ with HI def} > 0,$$

and

$$-0.39 \pm 0.10 \text{ for 5 Sc-Sm, } B_T^o > 10.9, \text{ with HI def} < 0.$$

Within the uncertainties, the HI-rich and HI-poor lower luminosity Sc galaxies have identical mean $S_{60\mu m}/S_{100\mu m}$ ratios.

The scatter of 0.14 dex in the $S_{60\mu m}/S_{100\mu m}$ colors corresponds to a 1σ variation of 38%, which is approximately twice the mean observational uncertainty of ~20% in the flux ratios. If the CO-H_2 proportionality factor depends linearly on the mean molecular gas temperature, and if the mean gas temperature depends linearly on the $S_{60\mu m}/S_{100\mu m}$ ratio (as might be suggested by the $^{12}CO/^{13}CO$ study of Young and Sanders 1986), then the 1σ uncertainty in the H_2 mass as inferred from the CO luminosity is 38%.

Neither of our main conclusions is changed by considering narrower ranges of galaxy luminosity. The anti-correlation between HI and CO luminosities occurs only within a narrow luminosity range. We have examined the correlations of HI deficiency vs. L_{CO}/L_B, S_{CO}/S_{HI}, and $M(HI+H_2)/D_{opt}^2$ for a luminosity dependence. The location of the Sa-Sb

galaxies in all these figures is independent of optical luminosity. The higher luminosity ($B_T^o<10.9$) Sbc-Sc galaxies lie slightly above the lower luminosity ($B_T^o>10.9$) Sbc-Sc galaxies in the S_{CO}/S_{HI} vs. HI def and $M(HI+H_2)/D_{opt}^2$ vs. HI def planes, yet these displacements are of marginal significance and in any case do not alter our conclusions.

There is no measurable parameter to serve as a probe of the cloud densities or diameters. As a result, we can make no arguments, based on empirical evidence, that the molecular cloud properties are the same in the HI-deficient and non-HI-deficient Virgo galaxies. However, the weak expected dependence of the CO-H_2 proportionality factor on cloud density ($\chi\sim\rho^{1/2}$) or cloud diameter ($\chi\sim D^{-1/2}$) would mean that in order to explain a variation in χ of a factor of 3, the mean cloud densities or diameters would have to change by a factor of 10. Such a large change seems unpalatable. Thus we believe that the S_{HI}/S_{CO} ratios in the inner galaxy, which decrease by a factor of >3 for a decrease of a factor of 10 in total HI content, cannot be explained by variations in molecular cloud properties.

§12. Summary

In this chapter, the dependence of CO luminosity on blue luminosity, optical diameter, and indicative mass have been investigated. Although there is a general correlation between the CO luminosity and the latter 3 quantities, there is a good deal of scatter. The morphological type and HI content have been identified as contributing to the scatter. For Virgo galaxies with blue optical diameters greater

than 4.3' (or 25 kpc for D=20 Mpc), Sc galaxies of a given optical diameter have the highest average CO luminosities, followed by Sb's and then Sa's. For the Sa-Sb and the largest Sc galaxies, there is no correlation between CO luminosities and HI masses. This indicates that molecular gas is not deficient in HI-deficient Virgo spirals.

For the Sc galaxies with blue magnitudes between $10.9<B_T°<12$, there is an order of magnitude variation in the ratio of CO luminosity to optical area. The Sc's in this magnitude range closer than 4.5° from M87 are all HI-poor (i.e. HI def>0) and have as much CO emission per unit area as the more luminous Sc's. Those further than 4.5° from M87 are HI-rich (i.e. HI def<0) and have on average over 5 times less CO emission per unit blue optical area than the other Sc's. An investigation of the possible systematic biases in B-V colors, blue optical diameters, and global HI linewidths between the HI-rich, CO-poor and the HI-poor, CO-rich Sc galaxies reveals that the CO luminosities in the HI-rich, CO-poor galaxies are intrinsically low; but perhaps by only a factor of 3. However, it also reveals that the HI-rich, CO-poor galaxies have bluer B-V colors on average than the HI-poor, CO-rich galaxies, indicating that the former may have somewhat lower average masses than the latter. The existence of HI-rich, CO-poor, lower luminosity late type galaxies demonstrates that large, steady-state supplies of molecular gas do not exist in (at least some) low mass spiral galaxies. Apparently in these low mass spirals, which are presumably unaffected by cluster processes, large amounts of gas do not enter or remain in the molecular state, as is the case with most

massive spirals.

Two possible explanations for the lack of CO-poor Sc galaxies in the inner cluster are discussed. One possiblity involves selection effects. Galaxies in the Virgo sample were selected by their blue magnitudes. As a result, the lower luminosity galaxies in the sample contain actively star-forming galaxies with large ratios of blue luminosity to total mass, but no galaxies of comparable mass which are not actively forming stars. Galaxies in the inner cluster are generally HI-deficient and have somewhat lower massive star formation rates, as a result of galaxy-ICM interactions. Thus inner cluster galaxies with the same total masses as the HI-rich, CO-poor, outer cluster galaxies may be too faint in the B band to have been included in the sample.

Alternatively, an ISM-ICM interaction may induce large amounts of atomic gas to enter the molecular state in the lower mass spirals which are unable to form large amounts of H_2 on their own. It is shown that the total gas contents ($HI+H_2$) are similar in the HI-poor, CO-rich, and in the HI-rich, CO-poor lower luminosity Sc's, making the cluster-induced transformation of atomic to molecular gas a viable alternative. It is pointed out that there may be sufficient energy in an ISM-ICM interaction to cause the conversion of HI into H_2, since there is enough energy to remove atomic gas from some regions of the Virgo galaxies. Consequently, when local conditions are such that the interaction force is just insufficient to remove the interstellar gas, it is still large enough to perturb the interstellar gas. Such a perturbation may result in the conversion of atomic to molecular gas.

The radial distributions of atomic and molecular gas, as well as the global CO and HI properties, have been analyzed. It is discovered that Virgo spirals which are globally HI-deficient by a factor of 10 have total ($HI+H_2$) gas deficiencies which are only a factor of 2-3. The CO distributions of the Virgo spirals are more centrally peaked than the HI distributions. The CO diameters in the HI-deficient galaxies are found to be at least as great as in the HI-normal galaxies. This provides strong evidence that molecular gas is not removed in the event which causes some of the Virgo spirals to be HI-deficient.

It is discovered that even the inner regions of the galaxies with severe global HI deficiencies are HI-deficient. In galaxies which are globally HI-deficient by a factor of 10, the inner halves of the optical disks are HI-deficient by a factor of 2-3. The inner regions of the HI-deficient galaxies are observed to be HI-deficient with respect to both the starlight and the mass of molecular gas. Since the mass of molecular gas dominates the mass of atomic gas in the inner regions of most of the Virgo sample galaxies, it is not possible to tell whether the inner galaxy HI has been removed or converted into H_2.

The observational evidence for the impact of the Virgo cluster environment on the CO properties of Virgo spirals can be summarized as follows. For the most luminous galaxies in the sample, neither the CO luminosities nor diameters are significantly affected by cluster processes. For some of the lower mass late-type galaxies, there is possible evidence that HI may be converted into H_2 by an ISM-ICM

interaction, although selections effects might also explain these observations. Finally, with one exception, there is no evidence that asymmetries in the CO distributions are larger in the HI-deficient Virgo spirals. The one exception, NGC 4419, has the most asymmetric CO distribution in the sample, is severely HI-deficient, and has the largest known ratio of CO flux to HI flux among galaxies. Its properties suggest that the large CO asymmetry may be the result of an ISM-ICM interaction.

The susceptibility of atomic and molecular gas to removal from galaxies is examined from a theoretical standpoint. One reason that molecular gas has avoided removal in severely HI-deficient galaxies is that molecular gas is more centrally confined in galaxies than is atomic gas. Therefore, a larger fraction of H_2 resides deep in the gravitationally potential well, where it is relatively difficult to remove by any external process. Yet, the fact that the HI/H_2 ratios are low in the inner regions of severely HI-deficient galaxies suggests that atomic gas may also be removed from the inner galaxy. For removal processes which act as a pressure (e.g. ram pressure stripping), the column density of material is the critical parameter which determines whether gas is removed from a particular region of a particular galaxy. It is shown that Giant Molecular Clouds in the outer disk regions of even the least massive galaxies in the sample would not be removed by ram pressure stripping, even under the extreme conditions of a face-on passage through the dense intracluster gas 1° from M87 at a velocity twice that of the cluster velocity dispersion. Under such conditions,

nearly all of a galaxy's atomic gas, much of which exists in a low column density state, would be removed.

The dynamical effects of ram pressure on interstellar gas which is not removed from a galaxy are quantitatively investigated. It is shown that the ram pressure resulting from a typical galaxy-ICM encounter is comparable to or exceeds the thermal, magnetic, and turbulent energy densities in low density HI gas. Ram pressure is therefore dynamically important for low density HI gas, and has the potential to enhance the conversion of low density atomic to high density molecular gas. Two mechanisms by which an ICM-ISM interaction might enhance the conversion of HI into H_2 are discussed. One mechanism involves the compression of low density gas. The other involves perturbing the orbits of gas clouds to increase the cloud-cloud collision rate, and thereby enhance the formation of GMCs. The effects of ram pressure on a GMC are expected to be minor. In a typical galaxy-ICM encounter, the ram pressure is estimated to be an order of magnitude less than the gravitational, turbulent, and magnetic energy densities which govern the structure and evolution of molecular clouds. Thus ram pressure is not expected to increase the star formation rate by "squeezing" GMCs.

CHAPTER VI

STAR FORMATION IN VIRGO GALAXIES AND THE EVOLUTION OF STRIPPED SPIRALS

§1. Introduction

Knowledge of both the atomic and molecular gas components of Virgo spirals permits for the first time a proper examination of the relationship between the gas contents and star formation rates in a sample of cluster galaxies. Prior investigations have found little or no correlation between the atomic gas contents and star formation properties of cluster galaxies (e.g. Bothun 1981; Kennicutt, Bothun, and Schommer 1984). A serious limitation to cluster studies like these has been the unknown role of molecular gas. Many studies in the last several years have demonstrated that tracers of star formation are fairly well correlated with CO emission, and poorly correlated with HI emission, in samples of luminous spiral galaxies (e.g. Young and Scoville 1982b; Young et al. 1986a). The importance of molecular gas in galaxies is not that it is molecular, but that it is the dominant component of the ISM in the inner regions of many spiral galaxies. Such an important ISM constituent therefore cannot safely be ignored in any study of the evolution of cluster or non-cluster galaxies.

In this chapter, various tracers of star forming activity are compared with gas properties to assess the impact of ISM-alteration on star formation. The tracers utilized in this analysis are the Hα,

radio continuum, and far-infrared (FIR) luminosities, and the B-V colors. Among these quantities, only the FIR data are previously unpublished. A brief discussion on the Hα, B-V, and radio continuum properties will consequently be followed by a description of the FIR data, a discussion on the origin of FIR emission from galaxies, and an analysis of the FIR colors and luminosities as a function of HI deficiency.

§2. Analysis of Hα and Radio Continuum Luminosities and B-V Colors

High mass star formation has been reduced in the HI-deficient Virgo spirals. This was demonstrated by Kennicutt (1983), who found a systematic difference in the Hα equivalent widths and B-V colors between Sc galaxies in the central 6° of Virgo, and those outside the center. Since Hα photons originate predominantly from the HII regions surrounding massive, short-lived, young stars, the Hα emission line luminosity is measure of the massive star formation rate. In Table 6.1, Hα fluxes and luminosities are listed for all those galaxies observed by Kennicutt and Kent (1983) in common with the CO survey. In Figure 6.1, we plot the HI deficiency parameter vs. the logarithm of the Hα luminosity, normalized by the optical area of the galaxy, for all those galaxies which our Virgo sample has in common with Kennicutt's. A least squares fit to the 14 Sbc-Sc galaxies yields a slope of -0.41 ± 0.18, which means that galaxies which are globally HI-deficient by a factor of 10 have ~2-3 times less high mass star formation.

Explanation of Columns in Table 6.1:

(1) NGC number.
(2) $(B-V)_T^o$ from RC2.
(3) Equivalent width of Hα+[NII], in angstroms, from Kennicutt and Kent (1983).
(4) Flux of Hα+[NII], in units of 10^{-13} erg cm^{-2} s^{-1}; upper limits are 3σ.
(5) Luminosity of Hα+[NII] line, in units of 10^6 L_o.
(6) 1.4 GHz continuum flux density in mJy, from Kotanyi (1980); upper limits are 3σ.
(7) 1.4 GHz continuum specific luminosity, in units of 10^{27} ergs.
(8) 2.4 GHz continuum flux density in mJy, from Dressel and Condon (1978); upper limits are 3σ.
(9) 2.4 GHz continuum specific luminosity, in units of 10^{27} ergs.
(10) 60μm to 100μm flux density ratio, uncorrected for color.
(11) Far-infrared luminosity from 40-300μm, assuming a single temperature fit to the 60μm and 100μm flux densities and a λ^{-1} emissivity law (see equation VI-2), in units of 10^8 L_o.

Table 6.1

Global Hα, B-V, Radio Continuum, and FIR Properties

NGC	B-V	EW(Hα)	$S_{H\alpha}$	$L_{H\alpha}$	$S_{1.4}$	$L_{1.4}$	$S_{2.4}$	$L_{2.4}$	$\frac{S(60\,\mu m)}{S(100\,\mu m)}$	L_{FIR}
(1)	(2)	(3)	(4)	(5)	(6)	(7)	(8)	(9)	(10)	(11)
4064	0.71				7	3	<12	<6	0.50	32
4178	0.38	23±3	19	24	<10	<5	13	6	0.38	31
4192	0.66				90	44	37	18	0.39	100
4212	0.61	20±3	20	25	<10	<5	22	11	0.47	70
4216	0.84				<10	<5	<12	<6	0.26	49
4254	0.51	32±1	123	153	516	250	186	90	0.45	395
4293		2±2	<5	<6	15	7	20	10	0.47	46
4298	0.62	11±2	5	6	20	10	19	9	} 0.29	121
4302	0.70				44	21	24	12		
4303	0.48	34±3	141	175	467	226	195	94	0.52	371
4312	0.71				18	9	<12	<6	0.33	27
4321	0.67	18±1	89	111	275	133	117	57	0.41	298
4380					<10	<5	<12	<6	0.24	12
4388	0.62				140	68	129	62	0.61	89
4394	0.76	-1±3			<10	<5	<12	<6	0.26	18
4402	0.63				60	29	50	24	0.31	67
4419	0.80				49	24	44	21	0.49	72
4424	0.60				<5	<2	13	6	0.52	27
4438	0.72				150	73	109	53	0.36	44
4450	0.74				<10	<5	<12	<6	0.26	31
4501	0.65	6±2	31	39	313	151	157	76	0.34	254
4526	0.85	0±2			<7	<3	<12	<6	0.39	64
4527	0.74				238	115	129	62	0.58	304
4532	0.27				103	50	84	41	0.56	74
4535	0.62	14±3	37	46	183	89	32	16	0.44	127
4536	0.48	18±4	33	41	160	77	136	66	0.78	251
4548	0.73	3±1	9	11	<10	<5	<12	<6	0.29	41
4567	0.67	} 14±3			63	31	54	26	} 0.40	246
4568	0.75				84	41	75	36		
4569	0.65	6±2	24	30	100	48	63	31	0.43	112
4571	0.52	10±2	9	11	<10	<5	<12	<6	0.25	25
4579	0.76	4±2	<18	<22	123	60	95	46	0.35	79
4639	0.62				<10	<5	<12	<6	0.38	21
4647	0.58				14	7	26	13	0.36	68
4651	0.50	20±2	29	36	<20	<10	<15	<7	0.40	68
4654	0.55	17±2	28	35	174	84	59	29	0.49	160
4689	0.60	13±2	14	18	<10	<5	<12	<6	0.31	39
4698	0.77				<10	<5	<12	<6	0.16	9
4710	0.70				14	7	17	8	0.46	57
4713	0.34	56±3	30	37	14	7	34	17	0.40	47
4808		43±7	23	28	45	22	34	17	0.43	67
4866	0.70	-2±3			<10	<5	<12	<6	0.35	3

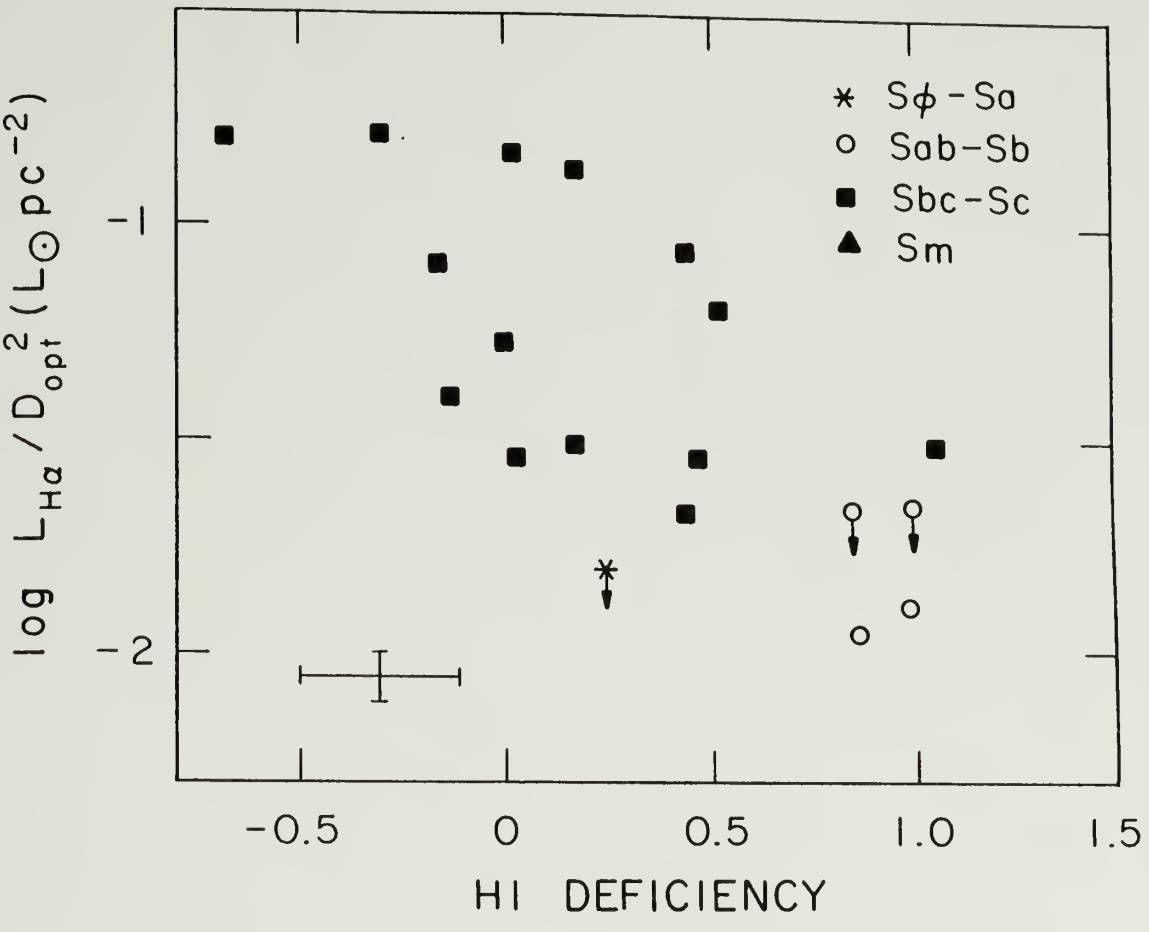

Figure 6.1 Logarithm of $L_{H\alpha}/D_{opt}^2$ vs. HI deficiency for those Virgo sample galaxies in common with the Hα sample of Kennicutt and Kent (1983).

From the 18 Sbc-Sm Virgo sample galaxies which have B-V colors available from the RC2, we find that those galaxies which are HI-deficient by a factor of 10 are redder in B-V by 0.25±0.06 magnitudes (see Figure 6.2). This large difference is more than can be explained by a change in the massive star formation rate over $\sim 10^9$ years, although this is certainly part of the reason for the difference. The other part of the difference results from the bias discussed in Chapter V: the lower luminosity end of the sample includes actively star-forming low mass galaxies, but no galaxies of similar mass which are not actively forming stars. The HI-rich galaxies include all the very blue, low mass galaxies. Since low mass galaxies can achieve bluer colors than their more massive counterparts, the difference in B-V colors between an HI-normal and a severely HI-deficient galaxy of the same mass is probably less than 0.25 magnitudes. While this bias may effect the slope of the relation, a real correlation between color and HI-deficiency is present: none of the HI-deficient Sc galaxies are very blue, and none of the HI-rich Sc galaxies are very red.

An important point raised by Kennicutt is that the HI contents, Hα equivalent widths, and B-V colors of many of the Virgo Sc's are similar to those in more isolated Sb's. In order to correctly interpret the Hα and B-V results, it is necessary to evaluate whether there is a systematic difference in morphological type classification between Virgo and isolated galaxies (or inner cluster and outer cluster Virgo galaxies). This question was addressed by Stauffer (1985), who compared the difference in nuclear and total magnitudes for Virgo and

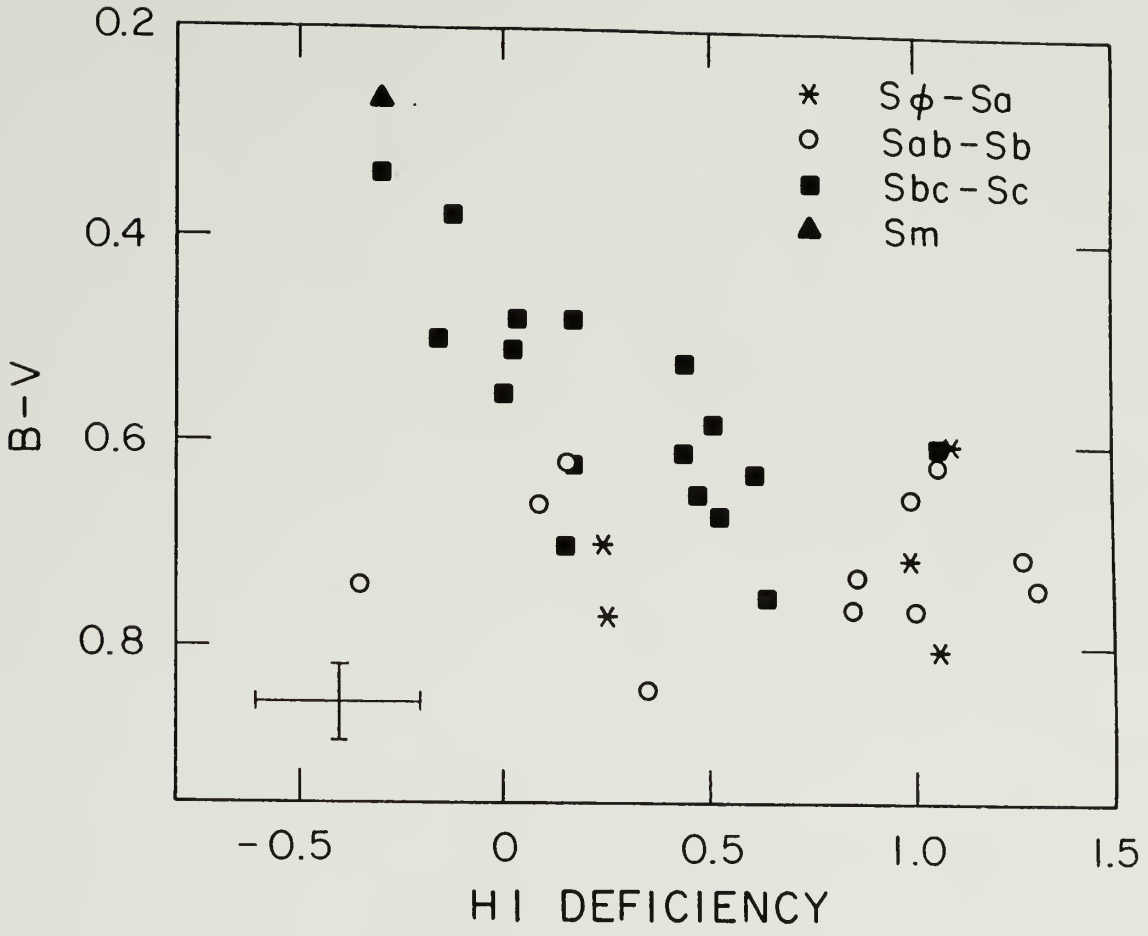

Figure 6.2 $(B-V)_T^o$ color vs. HI deficiency for Virgo sample.

non-Virgo galaxies as a measure of the degree of central concentration, and concluded that the morphological type classifications in Virgo and non-Virgo galaxies are consistent to within half a Hubble type.

Radio continuum emission from the disks of spiral galaxies is found to be correlated with Hα emission (e.g. Gavazzi and Jaffe 1985), FIR emission (e.g. Helou, Soifer, and Rowan-Robinson 1986), and other tracers of massive star formation, indicating that it, too, may be a measure of star forming activity. However, its utility as a probe of star formation is limited by the existence of non-thermal nuclear radio sources in many galaxies.

All of the Virgo cluster sample galaxies have been observed in 2 radio continuum surveys: the Dressel and Condon (1978) 2.4 GHz Arecibo bright galaxy survey, and the Kotanyi (1981) 1.4 GHz Westerbork Virgo cluster survey. Each survey detected 26 of the 42 Virgo sample galaxies. The observed fluxes from these 2 surveys are listed in Table 6.1. In Figure 6.3, the 1.4 GHz radio continuum specific luminosity, normalized by the optical area, is plotted vs. the HI deficiency parameter. A least-squares fit confirms the visual impression that there is essentially no correlation, although this conclusion is weakened by the large number of non-detections. The results for the 2.4 GHz data are similar (not shown). For the least-squares fitting, whose results are summarized in Table 6.2, we have counted 3σ upper limits as detections. Fitting only the detections yields similar results. Furthermore, we have omitted NGC 4388 and NGC 4438, which are known to have strong non-thermal nuclear components to their radio emission

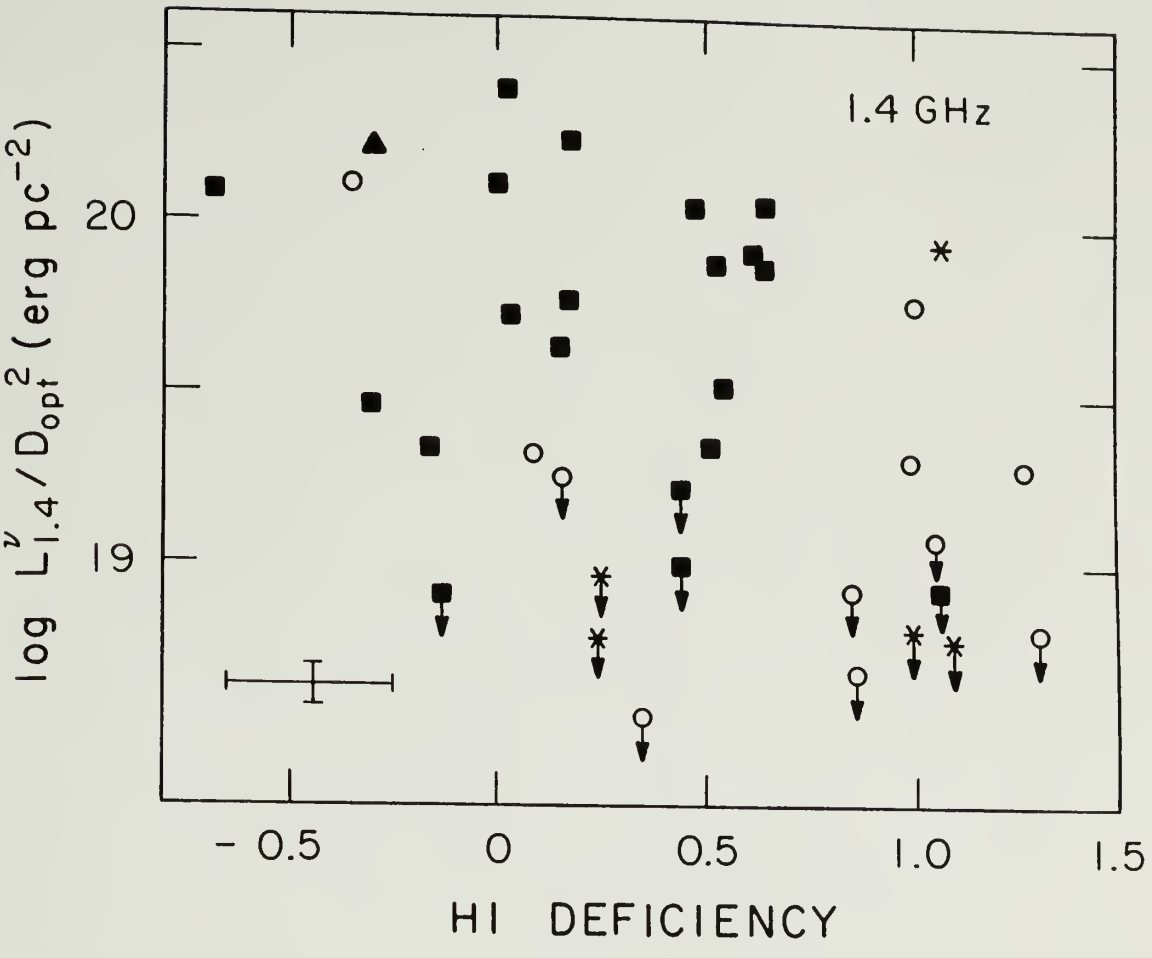

Figure 6.3 Logarithm of 1.4 GHz radio continuum specific luminosity normalized by optical area, vs. HI deficiency for Virgo sample. The radio continuum data is from Kotanyi (1981). Upper limits are 3σ.

Table 6.2

Least-Squares Fitting Results for HI Deficiency vs. Various Tracers of Gas and Star Formation

Quantity Fit vs. HI Def	Type	Number	Slope	r[a]	Comment
$\log(S_{60}/S_{100})$	Sab-Sb	12	−0.12 ±0.05	0.56	
	Sbc-Sm	21	−0.12 ±0.06	0.40	
$\log(L_{FIR}/D_{opt}^2)$	Sab-Sb	12	−0.37 ±0.13	0.66	N4388 deleted
	Sbc-Sm	17	−0.23 ±0.15	0.37	N4298/4302, N4567/ 4568 deleted
$\log(L_{H\alpha}/D_{opt}^2)$	Sbc-Sm	14	−0.41 ±0.18	0.56	
$\log(L_{1.4}/D_{opt}^2)$	Sab-Sb	11	−0.33 ±0.26	0.22	N4388, N4438 deleted
	Sbc-Sm	21	−0.28 ±0.24	0.11	includes 3 σ upper limits
$\log(L_{2.4}/D_{opt}^2)$	Sab-Sb	11	−0.18 ±0.20	0.28	same as above
	Sbc-Sm	21	−0.19 ±0.18	0.23	
$(B-V)_T^o$	Sab-Sb	12	0.00 ±0.04	0.00	
	Sbc-Sm	18	0.25 ±0.06	0.73	
$\log(L_{CO}/D_{opt}^2)$	Sab-Sb	13	−0.28 ±0.17	0.45	includes 2 σ upper
	Sbc-Sm	21	0.58 ±0.16	0.63	limits
$\log(M_{H_2}/M_{HI})$	Sab-Sb	13	0.61 ±0.16	0.75	includes 2 σ upper
	Sbc-Sm	21	1.46 ±0.18	0.88	limits
$\log(M(HI+H_2)/D_{opt}^2)$	Sab-Sb	13	−0.55 ±0.11	0.83	includes 2 σ upper
	Sbc-Sm	21	−0.33 ±0.08	0.69	limits
$\log(M_{HI}/D_{opt}^2)$ in inner galaxy	Sab-Sb	9	0.23 ±0.29	0.25	includes galaxies
	Sbc-Sm	24	−0.38 ±0.09	0.52	not in my sample
$\log(M_{H_2}/M_{HI})$ in inner galaxy	Sab-Sb	7	0.92 ±0.27	0.84	includes 2 σ upper
	Sbc-Sm	13	0.98 ±0.26	0.75	limits
$\log(M(HI+H_2)/D_{opt}^2)$ in inner galaxy	Sab-Sb	7	0.26 ±0.27	0.39	
	Sbc-Sm	13	0.14 ±0.12	0.32	

Note to Table 6.2:

a) Correlation Coefficient.

(Hummel, van Gorkom, and Kotanyi 1983). It is likely that much of the scatter in Figure 6.3 is due to nuclear components in other sample galaxies. In view of the presence of both disk and nuclear components, and the large number of non-detections, the strongest conclusion which can be drawn from the present radio continuum data about the present day massive star formation rate in Virgo galaxies is that it is consistent with the Hα observations.

§3. Far-Infrared Data

Far-infrared data from the IRAS satellite have been co-added for all the Virgo galaxies in the sample. The IRAS data were processed using the facilities of the Infrared Processing and Analysis Center (IPAC). Co-added IRAS data offer 2 advantages over the data in the IRAS Point Source Catalog (1985; hereafter PSC). 1) Many of the Virgo galaxies are extended with respect to the IRAS resolution in one or more bands, meaning that the PSC flux densities are actually lower limits. 2) The signal-to-noise ratio is increased by co-adding the data, so that many of the sources which are listed as upper limits in the PSC (especially at 12μ and 25μ) are detected by the co-adding process. Two different methods of co-adding the data have been used -- the Addscan routine for point sources and slightly extended sources, and the survey area co-add routine in intensity mode (hereafter SCI) for larger sources (c.f. IPAC User's Guide 1985).

We have taken pains to ensure that the flux density scales for the Addscan- and SCI-derived data are consistent with each other, and con-

sistent with the PSC (1985 version). This was accomplished by comparing Addscan, SCI, and PSC flux density values (for sources of the appropriate size, as described below and in Table 6.3) for a sample of 160 Virgo and non-Virgo galaxies. The analysis of the non-Virgo galaxies was carried out by S. Xie and J. Young, and kindly made available (see also Young et al. 1987). For point sources, as determined by the half-power width of emission observed in the in-scan direction (W50), which is computed by the Addscan program, the Addscan and PSC flux density values have been compared. The results of these comparisons are summarized in Table 6.3. We find that the February 1986 calibration fators used by the Addscan program significantly overestimate the flux densities at 25 μm (by 10±2%) and 100 μm (by 14±1%), relative to the PSC, while the agreement at 12 μm and 60 μm is good. There is more scatter in the Addscan vs. SCI flux density ratios, yet we find evidence that the SCI fluxes are underestimated at 12 μm (by 12±6%) and 60 μm (by 17±5%), relative to the PSC, while the agreement at 25 μm and 100 μm is good. All of our flux density values have been multiplied by the appropriate correction factor listed in Table 6.3.

Final flux density values, their associated 1 σ uncertainties, and Addscan widths W50, are tabulated in Table 6.4. Color corrections have not been made, since these are typically <5%, and in any case do not vary much among the Virgo sample galaxies because of their similar FIR colors. Uncertainties for all SCI-derived fluxes are assumed to be 20%. There are two components adding in quadrature which contribute to

Table 6.3

Results of PSC, Addscan, and Survey Co-add Comparisons[a]

Fluxes Compared	Flux Ratio[b] 12 μm	25 μm	60 μm	100 μm
S(PSC)/S(Addscan)[c]	1.00 ±0.04 (46)	0.90 ±0.02 (36)	0.97 ±0.01 (90)	0.86 ±0.01 (103)
S(SCI)/S(Addscan)[d]	0.89 ±0.03 (43)	0.89 ±0.04 (43)	0.83 ±0.03 (33)	0.89 ±0.03 (27)
S(PSC)/S(SCI)[e]	1.12 ±0.06	1.01 ±0.05	1.17 ±0.05	0.97 ±0.04

Notes to Table 6.3:

a) The February 1986 versions of Addscan and Survey Co-add are compared with the 1985 version of the Point Source Catalog.

b) Given with each flux ratio is the uncertainty in the mean. To get the dispersion, multiply this number by $\sqrt{N}$, where N is the number of galaxies used to obtain the mean flux ratio, given in parentheses.

c) Computed for sources whose Addscan width W50 $\leq$ 0.8', 0.8', 1.6', and 3.1' at 12, 25, 60, and 100 μm respectively. The IRAS instrumental resolution is 0.75', 0.75', 1.5', and 3.0' for the 4 bands. Due to the dispersion in Addscan widths for weak point sources, we counted sources with W50 values slightly greater than the instrumental resolution as point sources.

d) Computed for sources whose Addscan widths W50 $>$ 0.8', 0.8', 1.6', and 3.1' for the 4 bands, but smaller than W50 = 2.0', 2.0', 2.5', and 3.5'.

e) Computed by dividing S(PSC)/S(Addscan) by S(SCI)/S(Addscan).

Note to Table 6.4:

All flux density values come from co-added IRAS data. Addscan values are used for all galaxies whose Addscan widths W50(λ) are less than 2.0', 2.0', 2.5', and 3.5' at 12, 25, 60, and 100 μm, respectively. Survey co-add data in intensity mode are used for all galaxies whose widths are larger than these values. 3σ upper limits and 1σ uncertainties are given. All flux densities have been scaled by the appropriate correction factors listed in Table 6.3 to yield values consistent with the 1985 Point Source Catalog. No color corrections have been made.

Table 6.4

Far-Infrared Flux Densities

NGC	12 μm S(Jy)	12 μm W50(')	25 μm S(Jy)	25 μm W50(')	60 μm S(Jy)	60 μm W50(')	100 μm S(Jy)	100 μm W50(')
4064	0.21±0.05	0.75	0.29±0.07	0.75	3.47±0.39	1.45	6.99± 0.73	2.85
4178	<0.20	--	<0.45	--	2.71±0.54	3.03	7.21± 1.44	3.53
4192	1.14±0.23	1.50	1.23±0.23	1.50	9.00±1.80	1.84	23.28± 4.66	3.27
4212	0.93±0.19	1.10	0.76±0.17	1.10	7.21±0.77	1.53	15.49± 1.82	2.99
4216	0.75±0.15	3.30	1.03±0.21	4.50	3.04±0.61	4.34	11.64± 2.33	4.98
4254	4.38±0.51	1.59	5.36±0.58	1.55	39.96±4.42	2.05	87.94± 9.25	3.29
4293	0.23±0.04	0.82	0.57±0.09	0.82	4.71±0.49	1.48	10.09± 1.07	2.99
4298 } 4302	0.62±0.12	0.93	1.30±0.26	1.15	8.32±1.66	1.65	28.81± 5.76	3.15
4303	4.01±0.80	2.52	4.80±0.96	2.29	41.14±8.24	2.40	78.50± 8.66	3.29
4312	0.28±0.07	1.10	0.27±0.06	0.80	2.09±0.23	1.51	6.40± 0.68	3.09
4321	3.39±0.68	1.41	3.93±0.62	1.13	28.13±2.96	1.81	68.00± 7.06	3.29
4380	<0.22	--	<0.19	--	0.68±0.11	1.47	2.89± 0.39	2.91
4388	1.13±0.13	0.75	3.41±0.35	0.78	10.68±1.11	1.46	17.57± 1.87	2.92
4394	0.20±0.04	1.70	0.20±0.04	1.00	1.11±0.14	1.77	4.25± 0.45	3.10
4402	0.54±0.11	0.90	0.73±0.12	1.10	4.91±0.59	1.48	15.92± 1.61	3.03
4419	0.62±0.10	0.76	1.48±0.16	0.77	7.66±0.78	1.46	15.53± 1.67	2.92
4424	0.17±0.05	0.77	0.30±0.08	0.78	3.03±0.35	1.50	5.80± 0.64	2.94
4438	<0.18	--	0.21±0.06	0.80	3.77±0.41	1.54	10.39± 1.08	2.97
4450	<0.15	--	<0.13	--	1.91±0.25	1.99	7.45± 0.81	3.18
4501	2.41±0.48	1.54	2.70±0.34	1.60	20.37±2.54	1.89	59.83± 6.02	3.17
4526	0.36±0.06	0.75	0.40±0.08	0.75	5.82±0.69	1.50	14.85± 1.66	3.00
4527	2.48±0.30	1.10	3.12±0.34	1.01	35.42±3.73	1.68	61.38± 6.61	3.13
4532	0.36±0.07	0.93	1.09±0.15	0.92	8.52±0.92	1.50	15.15± 1.63	3.00
4535	2.00±0.04	2.40	2.20±0.44	1.33	12.66±1.55	2.17	28.52± 5.70	3.58
4536	1.77±0.21	0.80	4.65±0.48	0.79	33.35±3.48	1.44	42.55± 4.74	2.96
4548	0.60±0.19	1.50	<0.52	--	2.85±0.57	2.12	9.84± 1.04	3.33
4567 } 4568	1.94±0.25	1.62	2.87±0.57	1.45	22.52±2.30	1.79	56.75±11.35	3.15
4569	1.38±0.18	1.59	2.29±0.25	1.12	10.89±2.18	1.90	25.22± 5.04	3.13
4571	0.27±0.08	0.60	<0.22	--	1.50±0.22	2.22	5.96± 0.75	3.11
4579	0.68±0.12	1.55	0.71±0.13	1.22	6.49±1.30	1.87	18.56± 2.04	3.15
4639	<0.15	--	0.14±0.04	1.40	1.84±0.19	1.55	4.82± 0.60	3.03
4647	1.21±0.19	1.05	0.88±0.14	1.00	5.72±0.65	1.62	16.02± 1.64	2.91
4651	0.53±0.09	1.00	0.63±0.09	1.08	6.35±0.78	1.59	15.71± 1.71	3.02
4654	1.61±0.29	1.15	2.21±0.44	0.92	17.08±3.42	1.56	34.58± 4.16	2.96
4689	0.60±0.12	1.24	0.56±0.12	0.66	2.89±0.37	1.68	9.33± 1.06	3.11
4698	<0.22	--	<0.19	--	0.30±0.07	2.00	1.91± 0.21	3.01
4710	0.26±0.07	1.20	0.58±0.09	0.88	5.76±0.63	1.48	12.61± 1.36	2.92
4713	0.32±0.07	1.45	0.26±0.07	0.85	4.30±0.50	1.53	10.77± 1.20	3.02
4808	0.69±0.08	0.85	0.69±0.09	0.78	6.46±0.82	1.49	15.15± 1.56	3.00
4866	<0.22	--	<0.19	--	0.24±0.07	1.50	0.69± 0.16	3.00

the Addscan flux density uncertainties. One component is the larger of the signal-to-noise ratio of the final co-added scan, or the scatter in the flux density values of the individual scans. The other is a constant component, due in part to background subtraction, which we have assumed to be 10% in each of the 4 bands.

Co-adding the data has resulted in a significant number of new detections. Whereas less than half of the sample sources are listed as detections in the PSC at 12 μm and 25 μm, 33 of the 40 systems are now detected in these bands (the galaxy pairs NGC 4298/4302 and NGC 4567/4568 are unresolved by IRAS, and have been counted as one each). All of the sample are now detected at both 60 μm and 100 μm.

§4. The Origin of the FIR Emission from Normal Galaxies

Heated dust is the source of FIR emission from most galaxies, yet the heating sources and the nature of the gas associated with the dust remain somewhat controversial. Although many authors have attributed the FIR luminosity to recent and ongoing star formation, at least 2 recent papers have suggested an additional heating source for the dust. In a comparison of Hα and FIR emission in over 100 galaxies, Persson and Helou (1987) attribute much of the FIR emission from galaxies with large $L_{FIR}/L_{H\alpha}$ ratios to dust heated by non-ionizing stars. Both Persson and Helou, and Rowan-Robinson and Crawford (1986) note the spectral similarity of 'normal' galaxies with Milky Way 'cirrus' emission, and thereby associate the emission from 'normal' galaxies with 'cirrus' clouds heated by the ambient interstellar radiation

fields. Thus, there remains considerable uncertainty as to what degree the FIR emission from 'normal' galaxies is related to recent star formation. Before embarking on a discussion of the effect of HI deficiency on the FIR emission from Virgo galaxies, we use the CO and HI data sets to address the nature of the heating sources and the nature of the gas associated with 'warm' (25-50 K) dust.

As a measure of the 'total' FIR luminosity, we fit a single thermal component to the 60 μm and 100 μm flux densities, and calculate the total luminosity of this single component between 1-500 μm, using the relation given in Cataloged Galaxies in the IRAS Survey (Lonsdale et al. 1985):

$$L_{FIR} = 4\pi D^2 \; 1.26\{\Delta\nu_{60}S(60) + \Delta\nu_{100}S(100)\}\,R \qquad \text{(VI-1)}$$

where $\Delta\nu$ represents the IRAS bandwidth, the factor 1.26 corrects for the gap missed between the 60 μm and 100 μm bands, and the factor R corrects for the emission longward of 120 μm. If flux densities are given in Janskys, and the distance is given in Mpc, the FIR luminosity in L_o becomes:

$$L_{FIR} = 3.75\times10^5 \; D^2 \; \{2.58S(60) + S(100)\}\,R \;. \qquad \text{(VI-2)}$$

Values of L_{FIR} and S(60)/S(100) for the Virgo sample galaxies are tabulated in Table 6.1. In this thesis, we have adopted values for the correction factor R corresponding to a λ^{-1} dust emissivity law. Although this correction factor, which comes from Cataloged Galaxies in the IRAS Survey, yields the total FIR luminosity of this single temperature com-

ponent between 1-500μm, most of the energy of this 25-50 K component actually falls between 40-300μm. Since we are not using the actual measured 10-40μm luminosities in our estimation of L_{FIR}, we will refer to the quantities defined in equations VI-1 and VI-2 as the 40-300μm luminosity. We have not included the emission shortward of 40μm in order to facilitate comparison with galaxies which remain undetected at 12μm and 25μm. The emission in these bands exceeds that expected from a single temperature component characterized by the 60-100μm color temperature, and would contribute an additional ~20% to the FIR luminosity. This 'excess' luminosity between 10-40μm does not vary greatly among the Virgo galaxies studied here, because of their similar color temperatures. Furthermore, as a single temperature approximation of the actual FIR spectrum, equation VI-2 represents a lower limit to the true FIR luminosity between 40-300μm, as it neglects the emission from colder dust which may constitute most of the dust mass in galaxies (Young et al. 1986a).

The FIR luminosity is plotted against various gas mass quantities in Figure 6.4. The CO and FIR luminosities are shown in Figure 6.4a to be well-correlated in the Virgo sample, as shown previously for other samples (e.g. Rickard and Harvey 1984; Young et al. 1986a). However, there is an order of magnitude scatter among the galaxies with lower FIR luminosities, some of which is associated with the HI-rich, CO-poor, lower luminosity late type galaxies. Figure 6.4b shows that L_{FIR} and M_{HI} are almost completely uncorrelated. The sum of the atomic and molecular components, shown in Figure 6.4c, is as well correlated

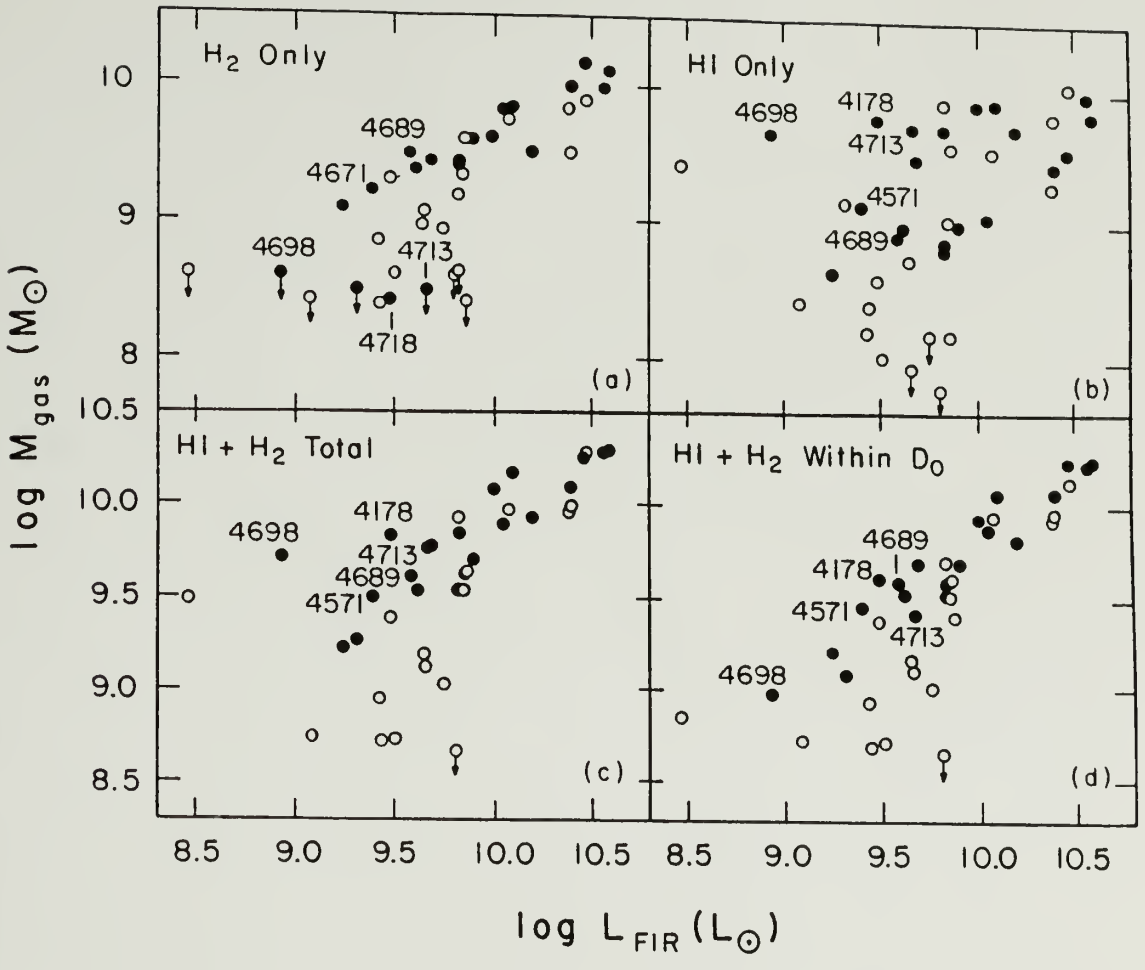

Figure 6.4 Log-log plots of 40-300μm far-infrared luminosity vs. various gas quantities. Included in these figures are the entire Virgo sample, with the exception of the unresolved (by IRAS) galaxy pairs NGC 4298/4302 and NGC 4567/4568. a) L_{FIR} vs. H_2 mass. b) L_{FIR} vs. HI mass. c) L_{FIR} vs. HI+H_2 mass. d) L_{FIR} vs. HI+H_2 mass within the optical diameter D_o (RC2). Galaxies with known HI distributions are denoted by solid circles. Those denoted by open circles have unknown HI distributions. The location in 6.4d of galaxies with unknown HI distributions is estimated as described in Table 6.5.

with L_{FIR} as is H_2 alone: the scatter among the HI-rich, CO-poor, lower luminosity late-type galaxies is reduced by considering the total gas mass, yet the large scatter in the M_{HI} vs. L_{FIR} plane carries over into the $M(HI+H_2)$ vs. L_{FIR} plane.

We find that the gas quantity which is best correlated with L_{FIR} is the total gas mass within the inner galaxy. In Figure 6.4d, the logarithm of L_{FIR} is plotted against the logarithm of the mass of $HI+H_2$ within the optical diameter D_o. The galaxies represented by filled circles in Figure 6.4 are those whose HI distributions have been given by Warmels (1986). For those galaxies which have not been mapped at high resolution in HI, we have estimated the fraction of the total HI flux which might originate within the optical diameter. Since the fraction of the total HI flux which originates within D_o is found to be well-correlated with HI deficiency for the 21 galaxies which have been mapped in HI, we have used the HI deficiency parameter as a guide in estimating the HI flux within D_o. These galaxies are represented in Figure 6.4 by open circles: the true location of these galaxies is somewhat uncertain only in Figure 6.4d. Table 6.5 summarizes the least squares fitting results for L_{FIR} vs. the various gas mass quantities, and also gives details on how the HI fluxes within D_o were estimated.

The total inner galaxy gas yields a better fit than just H_2, since FIR emission and other tracers of star formation are apparently more correlated with inner galaxy HI in the HI-rich, CO-poor galaxies (e.g. NGC 4178, NGC 4713). It yields a better fit than the total $HI+H_2$ mass, since FIR emission is apparently not associated with HI emission in the

Notes to Table 6.5:

a) The sample of 39 galaxies is composed of all Virgo sample galaxies, excluding NGC 4388 which has a large Seyfert component. The galaxy pairs NGC 4298/4302 and NGC 4567/4568 have been counted as one galaxy each. For fits, 2σ upper limits have been counted as detections.

b) The same as a, but for the 21 galaxies which have been mapped in HI with high resolution at WRST (Warmels 1986).

c) The slopes and correlation coefficients for L_{CO} are significantly affected by the presence of 8 upper limits. The result is that the actual slope is steeper than indicated here, and the true correlation coefficients are somewhat lower and probably comparable to those for log $M(HI+H_2)$ vs. log L_{FIR}.

d) For the 18 galaxies which have not been mapped in HI by Warmels, the fraction of the HI flux within $0.75D_o$ and $1.0D_o$ have been estimated as follows. It is found that the fraction of the HI flux within a given aperture is generally well-correlated with the HI deficiency parameter. For 4 galaxies with HI def$>$1.0, it is found that 0.97 ± 0.04 of the HI flux arises within $1.0D_o$, and 0.89 ± 0.13 within $0.75D_o$; for 7 galaxies with $0.4<$HI def<1.0, 0.93 ± 0.07 within $1.0D_o$, 0.69 ± 0.10 within $0.75D_o$; for 6 galaxies with $0<$HI def<0.4, 0.68 ± 0.08 within $1.0D_o$, 0.41 ± 0.07 within $0.75D_o$; for 3 galaxies with HI def<0, 0.58 ± 0.11 within $1.0D_o$, 0.37 ± 0.09 within $0.75D_o$. The only galaxy which falls well outside these general prescriptions is the Sa galaxy NGC 4698, which has 0.12 of its HI flux within $1.0D_o$, and 0.07 within $0.75D_o$. For the 18 galaxies unmapped by Warmels, the fraction of HI within each aperture has been estimated by using the above flux fractions for the appropriate HI deficiency value. The only exception is the Sa galaxy NGC 4866, which is assigned the same flux fractions as NGC 4698, on the basis of its similarly low L_{FIR}/M_{gas} ratio.

Table 6.5

Least Squares Fitting Results for log L_{FIR} vs. Various Gas Quantities

Quantity Fit vs. log(L_{FIR})	Number	Slope	Correlation Coefficient
log L_{CO}	39[a]	0.91±0.13[c]	0.76[c]
	21[b]	1.00±0.15[c]	0.84[c]
log M_{HI}	39	0.55±0.21	0.40
	21	0.38±0.20	0.41
log $M(HI+H_2)$	39	0.66±0.13	0.66
	21	0.59±0.09	0.83
log $M(HI+H_2)$ within D_o	39[d]	0.84±0.10	0.82
	21	0.78±0.06	0.95

outer disk (e.g. NGC 4698). From Figure 6.4, it can be concluded that the 25-50 K dust emission from galaxies is associated with inner galaxy gas. If most of the inner galaxy gas is molecular, then L_{FIR} is associated predominantly with molecular gas; if most of the inner galaxy gas is atomic, then L_{FIR} is associated predominantly with atomic gas.

A more quantitative estimate of how much FIR emission is associated with each gas component has been made for each galaxy. For the 21 galaxies mapped by Warmels, L_{FIR} has been correlated with the total gas mass within apertures ranging in size from $0.5D_o$ to $2.0D_o$. The best fits are for $0.75D_o$ and $1.0D_o$; $0.5D_o$ is slightly worse, and $1.5D_o$ is significantly worse. In Table 6.6, the fractions of the total gas mass within $0.75D_o$ and $1.0D_o$ in both the atomic and molecular components are tabulated. These should be good estimates of the fraction of the total FIR emission associated with each gas component. For most of the Virgo galaxies studied here, ~60-80% of the FIR luminosity is associated with molecular gas. Yet, for the HI-rich, CO-poor Virgo galaxies, as much as ~90% of the FIR emission is associated with atomic gas.

Although there is a generally good correlation between the FIR luminosity and the inner galaxy gas mass, the correlation is tightest for FIR luminosities greater than 10^{10} L_o. For galaxies with luminosities below 10^{10} L_o, there is a large amount of scatter. The analysis of CO and FIR emission for an infrared-selected sample of galaxies presented by Young et al. (1986a) demonstrated that the L_{FIR}/M_{gas} ratios were systematically higher in galaxies with higher S_{60}/S_{100} ratios. We have examined this possibility as an explanation for the scatter in

Table 6.6

Fraction of Gas Mass in HI & H_2 Phases in Inner Disks

Galaxy	f_{HI}[a]		f_{H_2}[b]	
	$0.75D_o$	$1.0D_o$	$0.75D_o$	$1.0D_o$
4178	0.89	0.93	0.11	0.07
4192	0.41	0.53	0.59	0.47
4216	0.29	0.46	0.71	0.51
4254	0.19	0.28	0.81	0.72
4303	0.32	0.42	0.68	0.58
4321	0.14	0.19	0.86	0.81
4388	0.33	0.33	0.67	0.67
4394	0.17	0.23	0.83	0.77
4402	0.18	0.20	0.82	0.80
4501	0.17	0.22	0.83	0.78
4535	0.30	0.43	0.70	0.57
4548	0.21	0.30	0.79	0.70
4569	0.15	0.15	0.85	0.85
4571	0.34	0.42	0.66	0.58
4579	0.17	0.20	0.83	0.80
4639	>0.66	>0.75	<0.25	<0.34
4647	0.18	0.22	0.82	0.78
4651	0.49	0.62	0.51	0.38
4654	0.43	0.53	0.57	0.47
4689	0.18	0.21	0.82	0.79
4698	>0.45	>0.58	<0.55	<0.42
4713	>0.83	>0.88	<0.17	<0.12

Notes to Table 6.6:

a) $f_{HI} = M(HI)/M(HI+H_2)$ within the specified aperture; where D_o is the corrected optical diameter at 25 mag arcsec^{-2} (RC2).

b) $f_{H_2} = M(H_2)/M(HI+H_2)$ within the specified aperture.

Figure 6.4d, and find that the galaxies with large L_{FIR}/M_{gas} ratios do not have systematically higher S_{60}/S_{100} ratios. Instead, we find that the scatter is associated with morphology. Figure 6.4e redisplays the data from Figure 6.4d, but coded by morphological type. It is apparent that the Virgo galaxies with the largest L_{FIR}/M_{gas} ratios are early type galaxies.

In order to help interpret these large L_{FIR}/M_{gas} ratios, it is relevant to recall that the Young et al. study found that the gas-to-warm dust (25-50 K) ratios in their infrared-selected galaxies were several times higher than the gas-to-total dust ratio in the Milky Way. This suggests that the warm dust is only ~10-40% of the total dust mass in many galaxies. All the Virgo galaxies which lie within the upper envelope of data points in Figure 6.4e have gas-to-warm dust ratios which are also several times larger than the gas-to-total dust ratio in the Milky Way. This can be taken as evidence that the bulk of the dust in most Virgo sample galaxies is too cold to radiate at 100 μm. Those early type systems with high L_{FIR}/M_{gas} ratios, but average S_{60}/S_{100} colors, either have lower gas-to-total dust ratios or have a larger fraction of their dust heated to 25-50 K. The fact that the S_{60}/S_{100} colors are no different may be explained if the heating sources in the early type galaxies differ from those in the infrared-bright sample of Young et al. In the infrared-bright galaxies, both the large L_{FIR}/M_{gas} and high S_{60}/S_{100} are attributed to efficient massive star formation, which heats a significant fraction of the dust to temperatures >50 K. In the deviant Virgo galaxies, the large

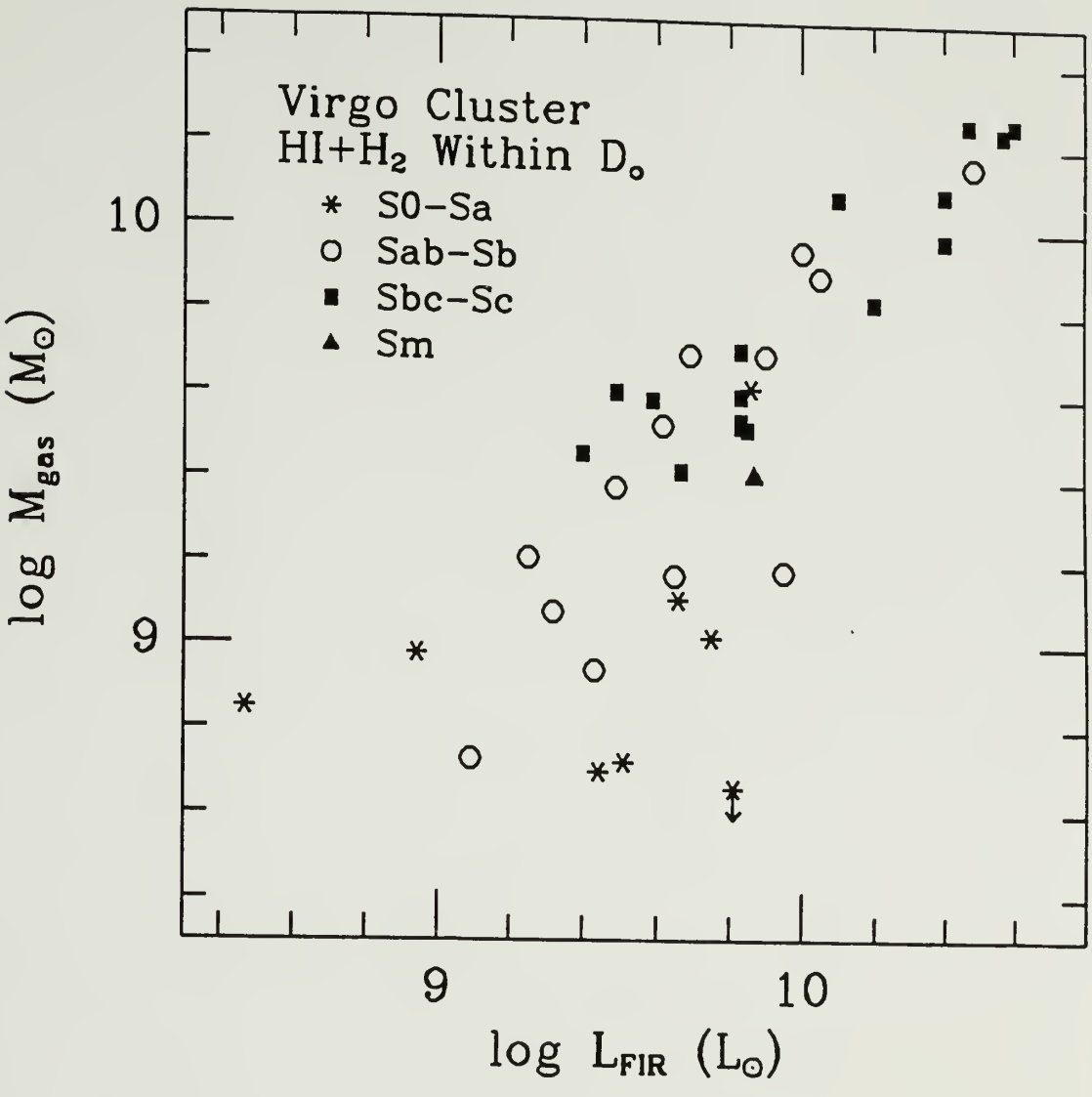

Figure 6.4e Log-log diagram of 40-300μm FIR luminosity vs. total ($HI+H_2$) gas mass within the optical diameter D_o. This diagram is identical to Figure 6.4d, except that the data are coded by morphological type. Note that all the galaxies with large ratios of L_{FIR}/M_{gas} are early type systems.

L_{FIR}/M_{gas} ratios may be simply explained by a lack of cold dust. The gas-to-warm dust ratios for these galaxies are probably comparable to the gas-to-total dust ratio in the Milky Way. If so, we predict that there are no large reservoirs of optically thick molecular clouds in these early type galaxies to shield the dust from the heating action of the interstellar radiation fields. Stars in the bulges of these galaxies could play a significant role in heating large fractions of the dust to ~25 K. Submillimeter continuum observations, which probe the coldest dust, will in principle be able to determine whether there are large reservoirs of cold dust in these early type galaxies.

The finding that both atomic and molecular gas are associated with FIR emission from Virgo galaxies is consistent with the conclusion of Persson and Helou that a significant fraction of the warm dust radiating at 40-120 μm is heated by non-ionizing stars. However, this fact and the fact that the S_{60}/S_{100} ratios of galaxies are similar to those of galactic 'cirrus' clouds, do not necessarily imply that the 40-120 μm emission from 'normal' galaxies is unrelated to star formation. We point out that 'cirrus' clouds are not unique among Milky Way interstellar clouds in having relatively small S_{60}/S_{100} ratios. Far-infrared observations of the nearby dark clouds R Coronae Australis and ρ Ophiuchi reveal that these clouds have FIR colors similar to both Milky Way 'cirrus' and 'normal' galaxies (Wilking et al. 1985). The FIR emission in each of these clouds appears to be powered by low-mass star formation, with one B star in each cloud contributing most of the luminosity. Outflow sources from young stellar objects within molecu-

lar clouds also have similar dust temperatures (Edwards et al. 1986).

It is likely that the FIR emission associated with all stars less massive than O within molecular clouds can be characterized by infrared color temperatures similar to both 'cirrus' and 'normal' galaxies. Giant molecular clouds without prodigious O star formation are found to have $S_{60}/S_{100} \sim 0.4$ (Scoville, private communication), similar to the values found for the Virgo galaxies and galactic 'cirrus' emission. The sources of heating for this dust include both young stars inside clouds, and the ambient interstellar radiation fields which heat the cloud peripheries to temperatures similar to 'cirrus' clouds. It is difficult to deconvolve the GMC FIR emission into that heated by 'young' stars and that heated by the ambient interstellar radiation field, since the color temperatures of these components are not unique. Even the interstellar radiation fields, which heat both GMC peripheries and 'cirrus-like' clouds, have a substantial contribution from O-A stars, meaning that the FIR emission from this component is a tracer of star formation on a time scale of 10^7-10^9 years (Tinsley 1980). Since different stellar populations dominate the interstellar radiation fields in different galaxies, this time scale will vary among galaxies, making it difficult to directly relate the FIR luminosity with a star formation rate.

Cosmic rays may also be an appreciable heating source for dust throughout galaxies. It is believed that the 10 K gas within molecular clouds is heated primarily by cosmic rays, which fully penetrate even the largest clouds. If so, then this is an additional 'young' heating

component, since cosmic rays are associated with events related to star formation.

The cloud dust temperature, as well as its $L_{FIR}/L_{H\alpha}$ ratio, is very sensitive to the upper end of the IMF, as pointed out by Persson and Helou. There is now evidence that the IMF varies among clouds in the Milky Way. Myers et al. (1986) and Scoville et al. (1987) both find that O stars are found exclusively in massive ($M>10^5$ M_o) GMCs, but that not all clouds with $M>10^5$ M_o contain O stars. Since the IMF is not uniform within our own galaxy, there is a precedent for IMF variations among galaxies. The massive GMCs without O stars are probably the sites of low-mass star formation, and can still contribute a significant fraction of the total galactic FIR luminosity.

§5. Analysis of FIR Colors and Luminosities

The 12-25-60 and 25-60-100 μm colors of the Virgo galaxies are compared in Figures 6.5 and 6.6. Also marked in these Figures are the locations of galaxies studied by Rowan-Robinson and Crawford (1986; hereafter RC). The sample of RC consists of all galaxies listed in the PSC with strong detections in all 4 bands, which were not flagged as extended. On the basis of FIR color-color plots and other data, RC identified 3 components which contribute to the 12-100 μm emission from galaxies: 1) a 'starburst' component (B) characterized by FIR colors similar to galactic HII regions, 2) a 'normal disk' component distinguished from the 'starburst' component by cooler S(100)/S(60) colors and warmer S(25)/S(12) colors, and 3) a Seyfert component which

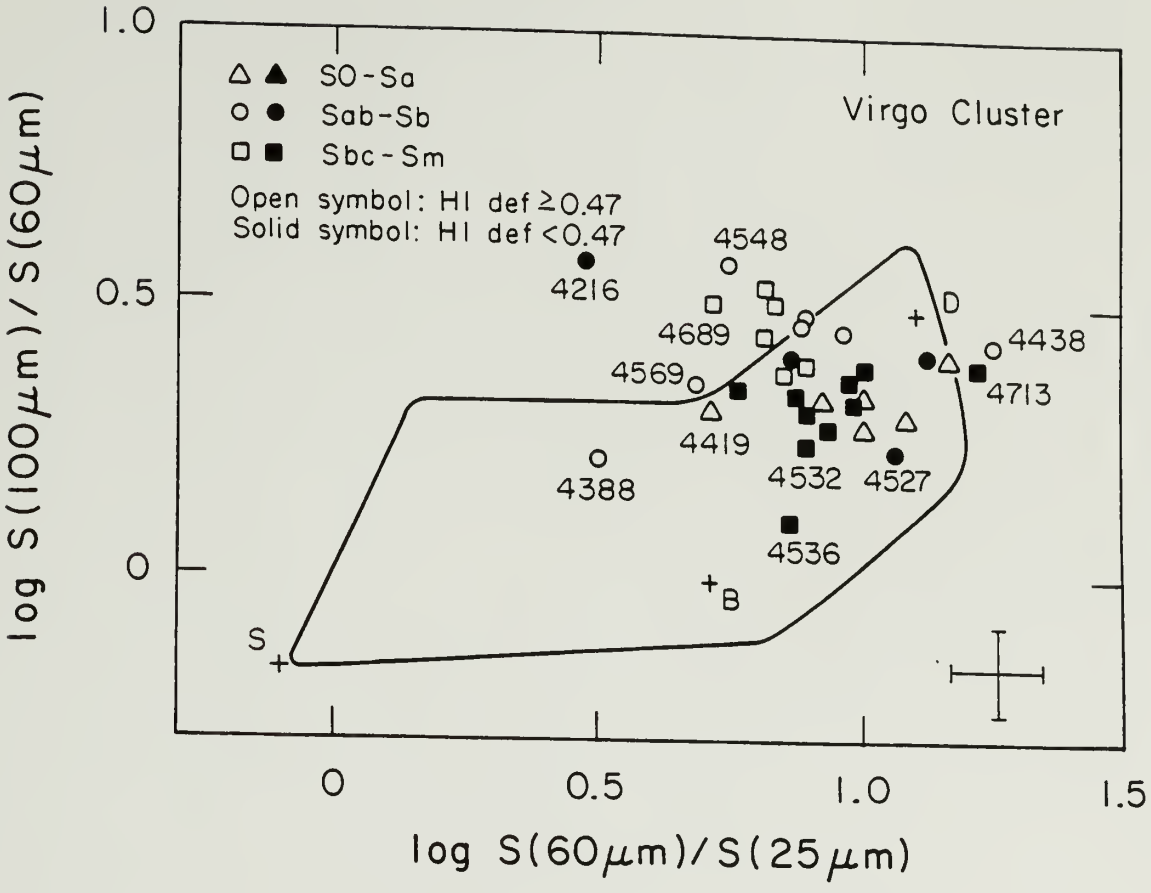

Figure 6.5 25-60-100 μm color-color diagram for Virgo sample. The enclosed region contains all the galaxies in the sample of Rowan-Robinson and Crawford (1986). The D, B, and S symbols mark the FIR colors of the 'normal disk' (D), 'starburst' (B), and Seyfert (S) components defined by RC. The galaxy NGC 4216 has much larger uncertainties in its colors than indicated by the mean errorbar, so its true colors are not well-determined. NGC 4388 is the only Virgo sample galaxy with a significant Seyfert component to its FIR emission. Non-detections have not been included in this figure. Note that most of the galaxies outside enclosed region are HI-deficient

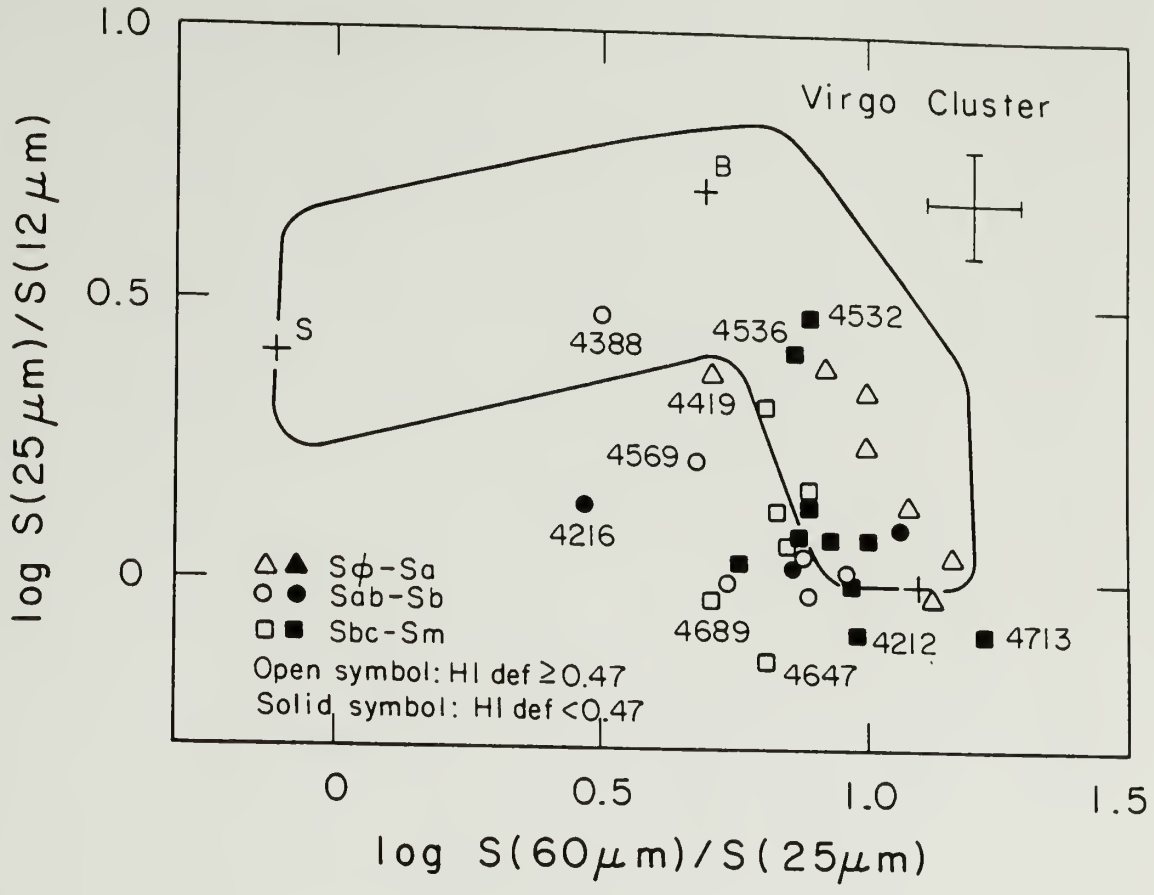

Figure 6.6 Same as Figure 6.5, but for 12-25-60 μm colors.

peaks near 25μm. Indicated in Figures 6.5 and 6.6 are the general areas in which RC find galaxies dominated by the 'normal disk', 'starburst', and Seyfert components. It is immediately clear that the Virgo and RC samples have very different FIR properties. Most of the Virgo sample is characterized by what RC term 'normal disk' FIR colors. There are no extreme 'starburst' galaxies in the Virgo sample, although there are several systems (e.g. NGC 4419, NGC 4532, NGC 4536) which have warmer S(100)/S(60) and S(60)/S(25) colors, and cooler S(25)/S(12) colors than the typical 'normal disk' galaxy. There is only one sample galaxy which has a significant Seyfert component. This galaxy, NGC 4388, is known on the basis of other observations (e.g. Hummel, van Gorkom, and Kotanyi 1983) to be a Seyfert galaxy.

The large difference between the FIR colors of the Virgo and RC samples is due predominantly to strong selection effects in the RC sample. Their requirement of large fluxes in the 12μm and 25μm bands and that no sources be extended preferentially selects Seyfert and 'starburst' galaxies at the expense of 'normal disk' galaxies. The Virgo galaxies, which form a nearly complete, blue magnitude-limited sample of galaxies all at the same distance, are therefore more representative of typical (albeit cluster) spiral galaxies.

In addition to the paucity of Seyfert and 'starburst' galaxies in the Virgo sample, there is another difference in the IR colors of the RC and Virgo samples. In the Virgo sample, there is a population of galaxies which have cooler S(100)/S(60) colors and warmer S(60)/S(25) and S(25)/S(12) colors than any of the 'normal disk' galaxies in the RC

sample. Part of this arises from the selection effects present in the RC sample. Other studies, using different selection criteria (e.g. Smith et al. 1987) also find galaxies that have cooler S(100)/S(60) and warmer S(60)/S(25) colors than the typical RC 'normal disk' galaxy. Several groups (e.g. Pajot et al. 1985; Henkel, Wouterloot, and Bally 1986; Helou 1986) have remarked on the unexpected anti-correlation of S(100)/S(60) and S(25)/S(12) colors in galaxies, which we display for the Virgo sample in Figure 6.7. This anti-correlation is thought to be due to very small grains radiating at 12μm. In weak radiation fields, the 12μm emission is dominated by very small grains heated transiently to very high temperatures by single photon absorption; while in stronger radiation fields the 12μm emission is dominated by single temperature emission from larger grains (Draine and Anderson 1985; Desert 1986). Thus it is reasonable that the selection criteria of RC would discriminate against galaxies with cooler S(100)/S(60) colors and warmer S(25)/S(12) colors.

There is evidence that the HI contents of the Virgo galaxies are correlated with their FIR colors, particularly their S(100)/S(60) and S(60)/S(25) colors. Nearly all of the galaxies which fall outside of the boundaries defined by the RC sample in Figure 6.5 are HI-deficient by more than a factor of 3. (The one galaxy which appears far outside the RC boundaries in both Figures 6.5 and 6.6, NGC 4216, has very large error bars, so its colors are not well-determined). There is a similar tendency in Figure 6.6, although the HI-deficient and non-HI-deficient galaxies are more scattered here. This may arise in part from the

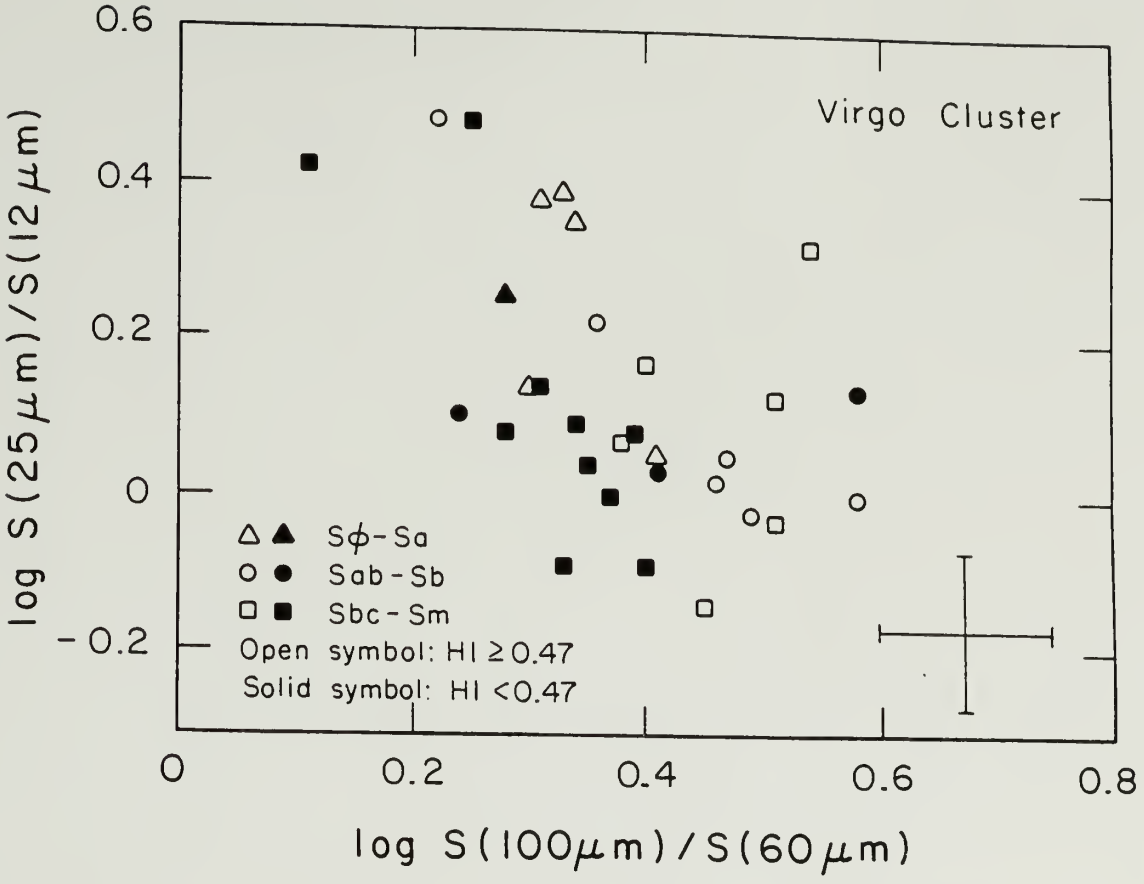

Figure 6.7 Anti-correlation between S(25)/S(12) and S(100)/S(60) colors for Virgo sample. Non-detections have not been included in this figure.

larger uncertainties in the S(25)/S(12) ratios, and in part from the tenacious 12μm emission, which exists even in weak radiation fields.

We have measured the dependency of FIR emission on HI deficiency by least-squares fitting the HI deficiency to the logarithm of the FIR flux density normalized by D_{opt}^2. The FIR emission per area is plotted vs. the HI deficiency parameter for each of the 4 bands in Figure 6.8. The results of the least squares fitting are presented in Table 6.7. Within the uncertainties, both Sab-Sb and Sbc-Sm samples exhibit the same dependence of $S(FIR)/D_{opt}^2$ on HI deficiency. For both morphological groups, the 12μm emission exhibits the weakest dependency on HI deficiency, the 60μm emission exhibits the strongest dependency, while the 25μm and 100μm emission show intermediate dependencies. The statistical significance of these differences from the fits is low, yet the fact that HI-deficient galaxies from both morphological groups show the same trend, and that the color-color diagrams of Figures 6.5 and 6.6 exhibit the same trend (i.e. warmer S(25)/S(12) and S(60)/S(25) colors, and cooler S(100)/S(60) colors) argues that the color differences are real.

In Figure 6.9, the logarithm of L_{FIR}, normalized by D_{opt}^2, is plotted vs. the HI deficiency parameter. Least squares fits have been performed separately for the Sab-Sb and Sbc-Sm galaxies, and their results are summarized in Table 6.2. For 17 Sbc-Sm galaxies the slope of -0.23 ± 0.15 indicates that the HI-deficient galaxies are only moderately deficient in FIR radiation.

Two effects related to HI deficiency may be expected to affect the

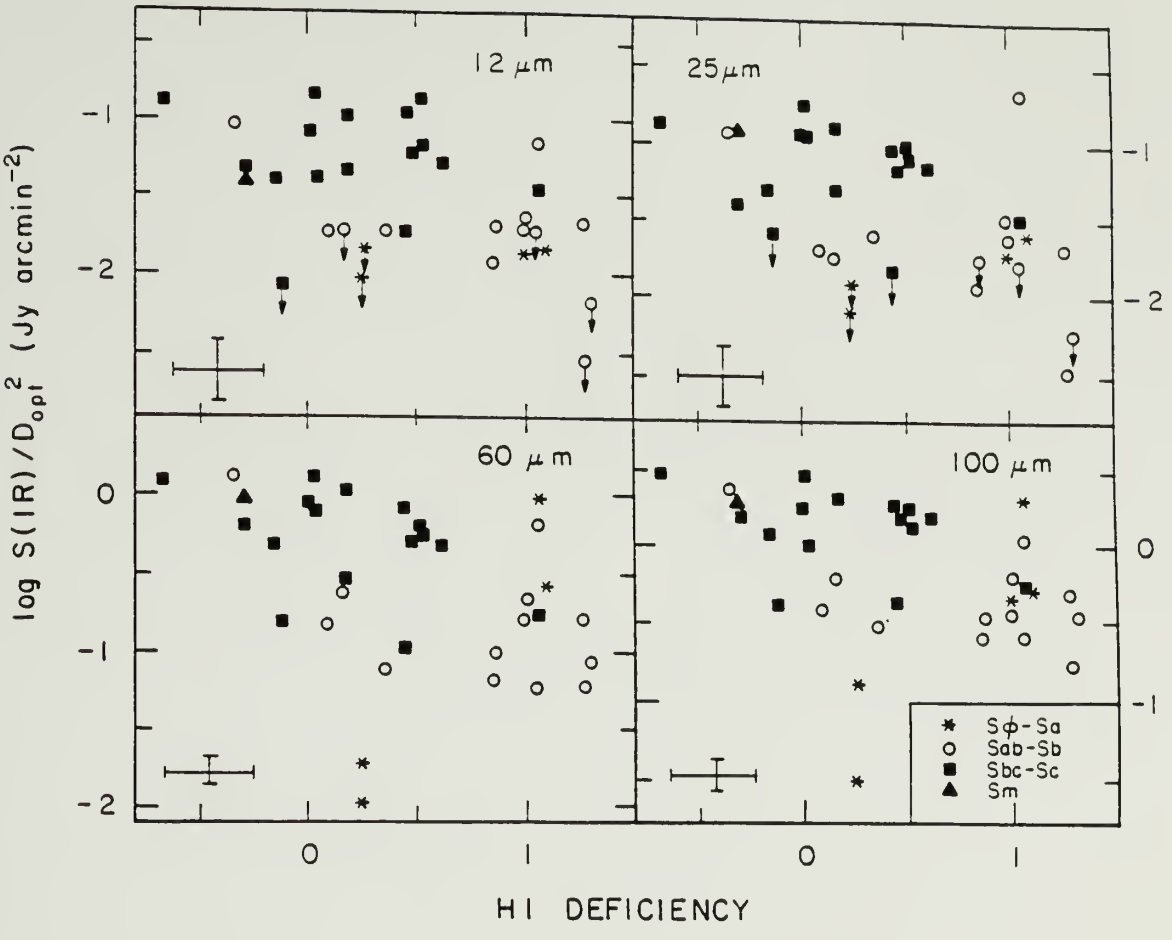

Figure 6.8 Logarithm of IR flux density normalized by optical area vs. HI deficiency, for each of the 4 IRAS bands. Upper limits are 3σ.

Table 6.7

Least-Squares Fitting Results for HI Deficiency vs. log $S(IR)/D_{opt}^2$

Morphological Type	Band	Number	Slope[a]	Correlation Coefficient[a]
Sab-Sb[b]	12 μm	8	-0.30±0.13	0.63
	25 μm	9	-0.44±0.18	0.63
	60 μm	12	-0.46±0.15	0.66
	100 μm	12	-0.34±0.12	0.65
Sbc-Sm[c]	12 μm	16	-0.11±0.14	0.19
	25 μm	15	-0.18±0.11	0.37
	60 μm	17	-0.34±0.17	0.44
	100 μm	17	-0.21±0.14	0.34

Notes to Table 6.7:

a) Slopes and correlation coefficients are given for detected galaxies only. Fits to all the galaxies, counting the 3σ upper limits of undetected galaxies as detections, result in slopes which differ by less than 1σ from the slopes given here.

b) Results for Sab-Sb galaxies heavily affected by the presence of 1 HI-rich galaxy, NGC 4527. Without this galaxy, the slopes of all 4 bands are consistent with zero. NGC 4388 has been omitted from the fits because of a significant Seyfert component to its FIR emission.

c) The galaxy pairs N4298/4302 and N4567/4568 have not been included here because IRAS fails to resolve them.

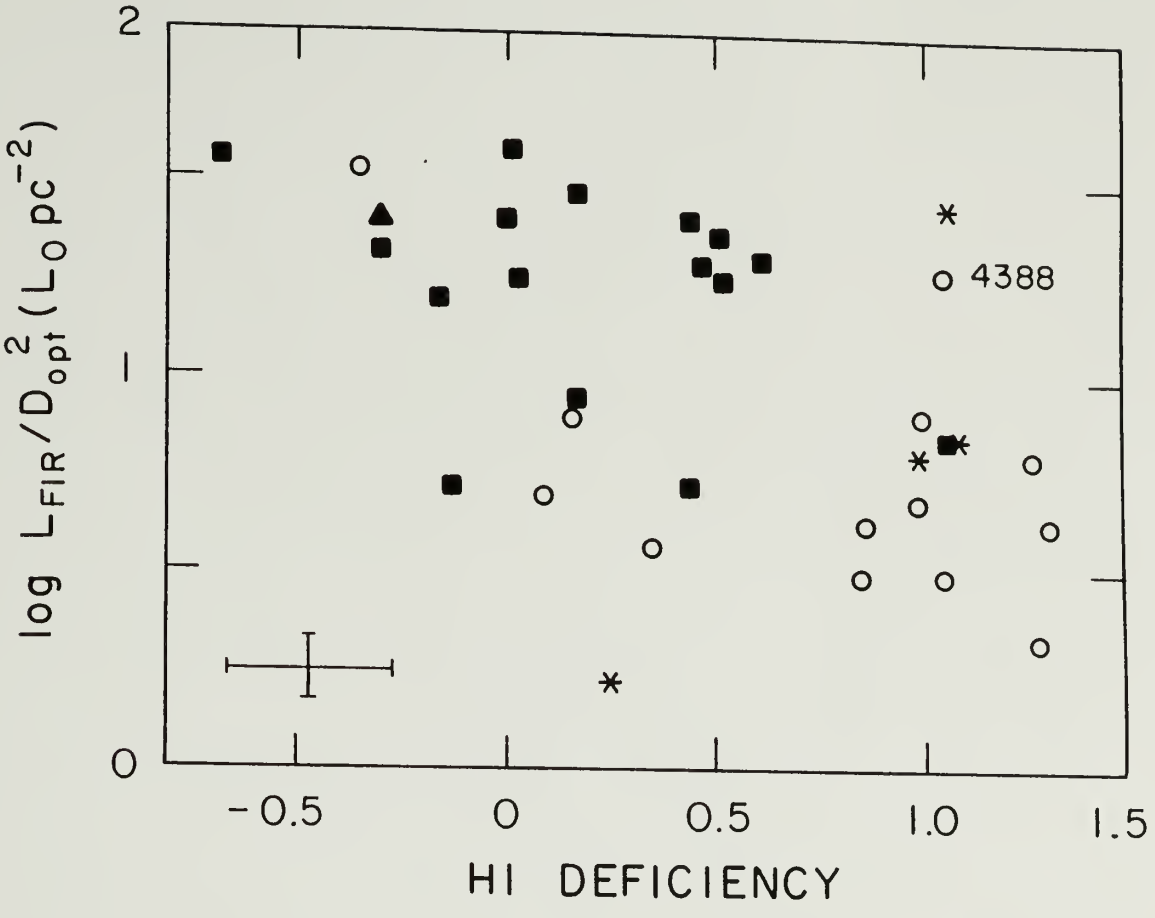

Figure 6.9 Logarithm of the 40-300μm luminosity normalized by optical area vs. HI deficiency for the Virgo sample.

infrared emission from Virgo galaxies. There is less heating from massive stars since there is less Hα emission globally (Kennicutt 1983). Secondly, there is less (warm) dust in the inner regions of HI-deficient spirals, since even the inner regions are HI-deficient. Two conclusions can be drawn from the observation that the magnitude of the 'FIR-deficiency' is no greater (and probably less than) the magnitudes of the 'Hα-deficiency' and the inner galaxy HI-deficiency. 1) The loss of dust associated with inner galaxy HI represents only a small fraction of the inner galaxy dust mass. 2) The warm dust radiating at 40-120μm is heated by more than just O stars, and these other sources have not been stifled by the HI-stripping event.

The slight change in FIR colors associated with HI deficiency, manifested by weaker emission in the 60μm band relative to the other IRAS bands, is most easily explained by less efficient massive star formation (c.f. Young et al. 1986a). This has the additional benefit of also explaining the smaller Hα fluxes in the HI-deficient systems. If the removal of 'cirrus-like' clouds (which have relatively cool S(100)/S(60) colors) were responsible for lower FIR luminosities in the HI-deficient galaxies, one would expect systematically warmer S(100)/S(60) colors in these galaxies.

§6. The Relationship Between Gas and Star Formation in Virgo Spirals

A comparison of the slopes of the fits for FIR and Hα from Table 6.2 reveals that the FIR slope is less than the Hα slope, although the

differences between the 'FIR-deficiency', the 'Hα-deficiency', and the 'radio-continuum deficiency' are not statistically significant. If the FIR and Hα slopes are taken to indicate the 'massive star formation-deficiency', we find that Virgo Sc galaxies which are HI-deficient by a factor of 10 are deficient in massive star formation, on average, by a factor of 2-3. Thus, the magnitude of the 'massive star formation deficiency' for Virgo Sc's is identical to the magnitude of the total gas deficiency, found in Chapter V.

A comparison of the radial distributions of gas and tracers of star formation, in Figure 6.10, helps to illuminate the relationship between the star formation rate and the availability of gas. In order to make these comparisons, we have assembled blue light profiles from Whitmore and Kirshner (1982) and Fraser (1977), HII region counts from Hodge and Kennicutt (1983), 1.4 GHz radio continuum distributions from Condon (1983) and Warmels (1986), and HI distributions from Warmels (1986). The HI and H_2 distributions in Figure 6.10 have been corrected for inclination as described in Chapter V, by taking into account the instrumental resolution. The radio continuum, HII region, and blue light distributions have been corrected by a factor of cos(i) to account for inclination. No attempt has been made to smooth all the data to the same resolution, so that some of the apparent differences (especially blue light) are the result of different resolutions. Although the relative scaling factors for blue light, radio continuum, and HII regions are arbitrary, they are the same for every galaxy. In most of the galaxies shown in Figure 6.10, the radial distributions of

Figure 6.10 Radial distribution of CO (H_2), HI, blue light (B), 1.4 GHz radio continuum (RC), and HII regions (HII) in Virgo sample galaxies for which RC, HII, or blue distributions exist in the literature. The vertical scale gives the HI and H_2 mass surface densities in M_o pc^{-2}, corrected for inclination. The blue light, HII region, and radio continuum data have been crudely corrected for inclination by multiplying the observed intensities by cos(i), and scaled so that their values roughly agree with the H_2 distributions in the 3 most luminous Sc galaxies. Although the scaling is arbitrary, it is the same for every galaxy. The HII region distributions are the number of HII regions per unit area (from Hodge and Kennicutt 1983) multiplied by the global Hα+[NII] flux (from Kennicutt and Kent 1983). The HII region counts may be underestimated in the inner galaxy because of plate burnout or difficulty in counting HII regions in crowded fields.

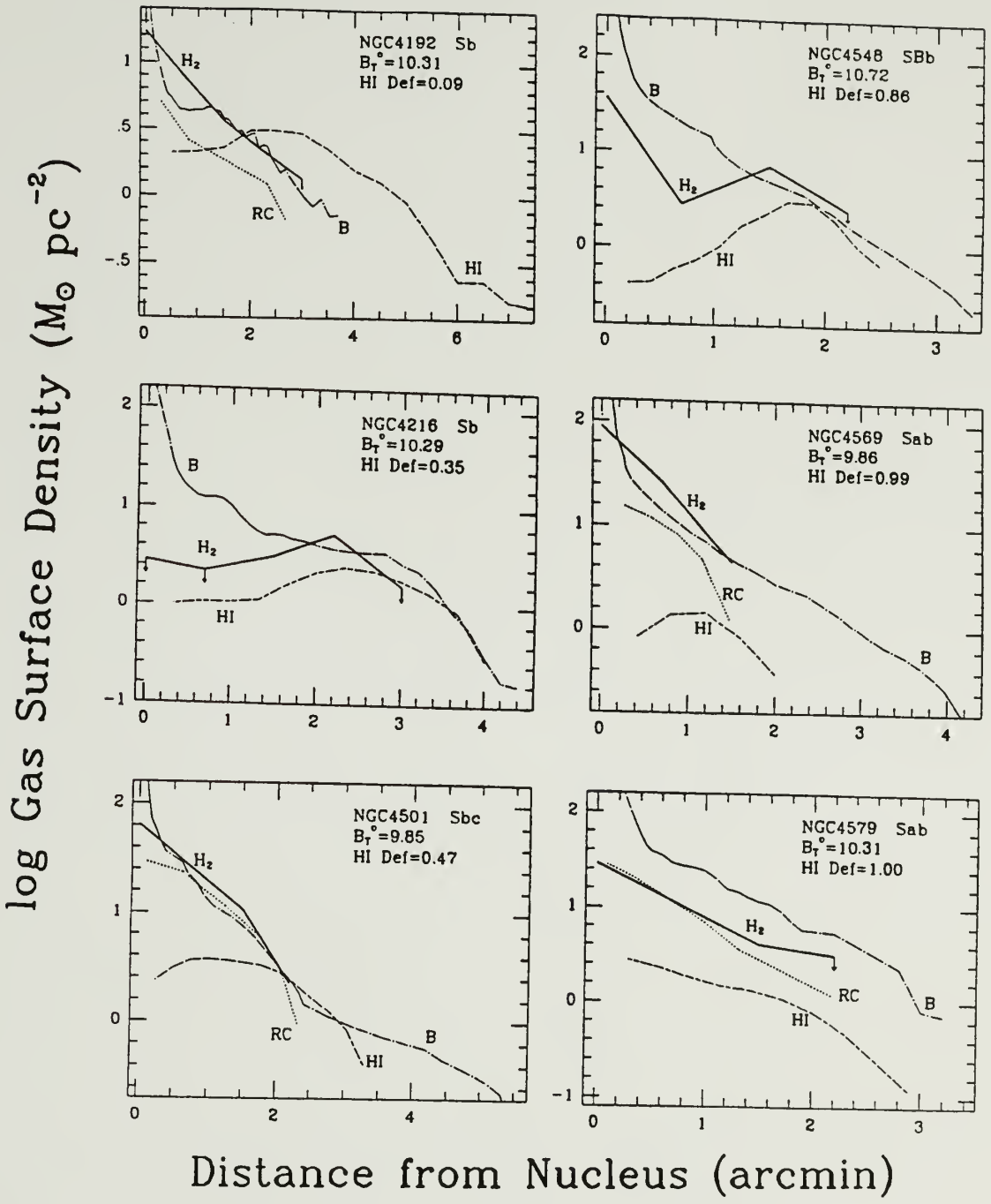
NGC4192 Sb
B_T°=10.31
HI Def=0.09
NGC4548 SBb
B_T°=10.72
HI Def=0.86
NGC4216 Sb
B_T°=10.29
HI Def=0.35
NGC4569 Sab
B_T°=9.86
HI Def=0.99
NGC4501 Sbc
B_T°=9.85
HI Def=0.47
NGC4579 Sab
B_T°=10.31
HI Def=1.00
H_2
RC
B
HI
log Gas Surface Density ($M_\odot$ pc^{-2})
Distance from Nucleus (arcmin)

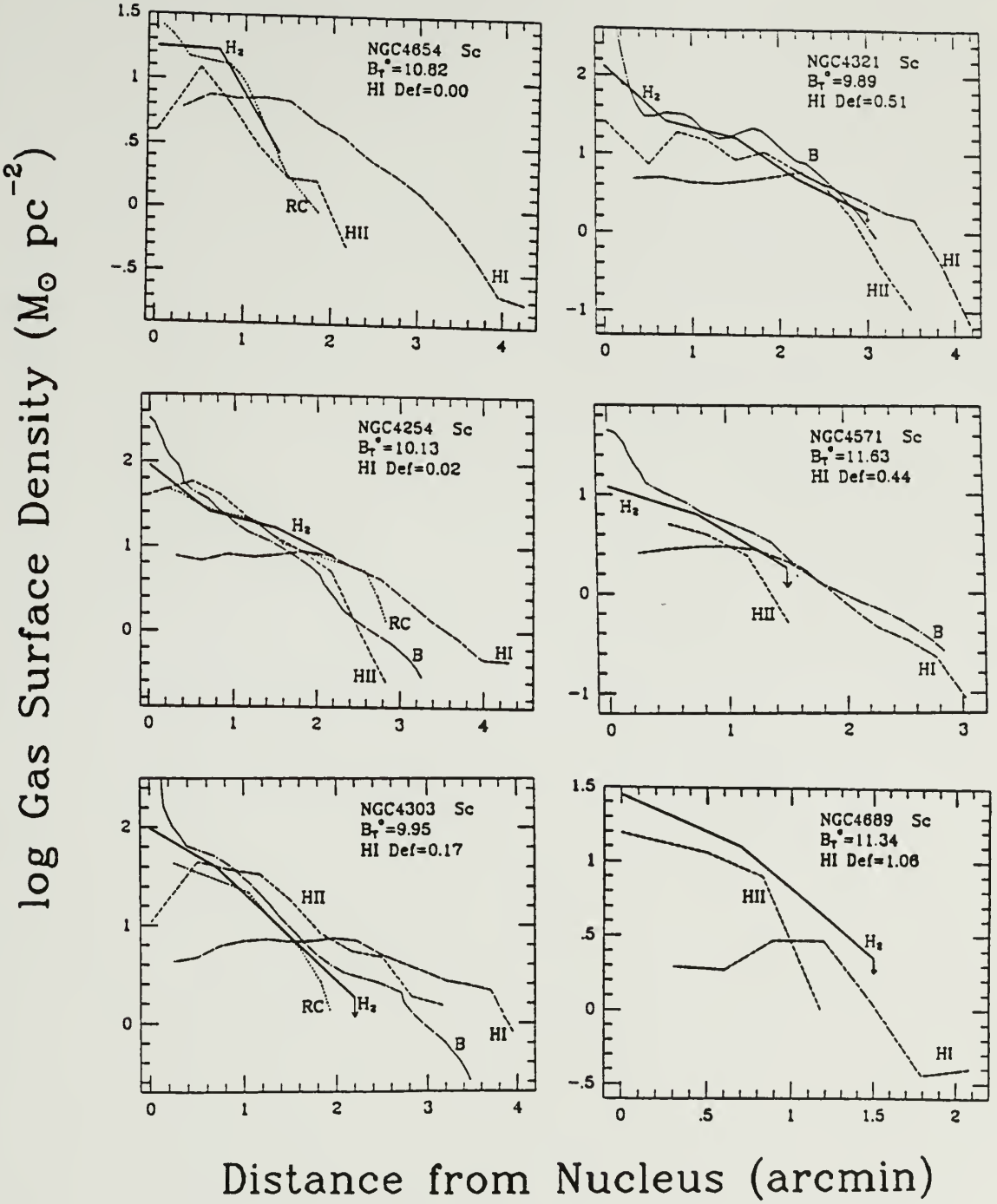

Figure 6.10 (cont.)

H_2 (CO), radio continuum, and HII regions are similar. This emphasizes that the survival (and possible enhancement) of molecular gas has played a major role in preserving the star-forming ability of HI-deficient Virgo galaxies.

It has been previously demonstrated that the distributions and total luminosities of Hα, FIR, radio continuum, and blue light in several (mostly luminous) spiral galaxies are more closely related to the molecular gas than the atomic gas (Talbot 1980; Young and Scoville 1982a; Scoville and Young 1983; deGiola-Eastwood et al. 1984; Young et al. 1986a). Yet because of the dominance of molecular gas in the inner regions of these galaxies, it was not possible to discern whether the star formation rate was more dependent upon the surface density of H_2, or more dependent upon the total gas surface density (HI+H_2). The radial distributions presented in Figure 6.10 cannot help settle this question, since all 12 galaxies displayed are H_2-dominated. Unfortunately, there is no information currently available on the Hα, radio continuum, FIR, or blue light radial distributions in the CO-poor, HI-rich galaxies. However, the global massive star formation rates of these galaxies are large, as evidenced by their Hα line, FIR, and radio continuum luminosities. A comparison of the Hα luminosities in the lower luminosity Sc galaxies is revealing. For the 4 HI-rich, CO-poor galaxies (NGC 4178, NGC 4651, NGC 4713, NGC 4808), the mean value of $\log L_{H\alpha}/D_{opt}^2 = 4.99\pm0.15$. For 3 HI-poor, CO-rich galaxies (NGC 4212, NGC 4571, NGC 4689), the mean value of the same quantity is 4.58 ± 0.18. (The reader is invited to compare these results with those

in Table 5.3, which summarizes the CO and HI properties of these 2 samples.) Uncertainties in the extinction corrections cloud the relevance of this difference. However, unless the HI-poor, CO-rich galaxies suffer twice the extinction at Hα as their HI-rich, CO-poor counterparts, it is the HI-rich, CO-poor galaxies which have slightly higher massive star formation rates.

High massive star formation rates in the CO-poor, HI-rich, spirals belie the notion that a galaxy must have a large supply of molecular gas to undergo prodigious massive star formation. Clearly, the massive star formation rate is not proportional to the H_2 surface density in these galaxies. The gas in these HI-rich galaxies undoubtedly does pass through the molecular phase on its way to forming stars (because of the high densities which gas must acheive on its way to reaching stellar densities), but apparently, the pre-existence of large quantities of gas in the molecular state is unnecessary for the star formation process to begin. These data are consistent with the hypothesis that it is the total gas surface density, more than the molecular gas surface density, which is related to the star formation rate.

Of course, it is known that the star formation rate is not simply proportional to the gas surface density in all galaxies, or even at all radii within an individual galaxy. The HI profiles in the outer regions of many galaxies (e.g. NGC 4303 among the Virgo galaxies in Figure 6.10) are shallower than the blue light and other star formation tracer profiles. Apparently, outer galaxy gas is not as efficient in forming stars as is inner galaxy gas. This could be explained by

larger scale heights and lower volume densities of gas in the outer regions of galaxies, as is observed in the Milky Way (Kulkarni, Blitz, and Heiles 1982). The volume density of gas should be more directly related to the star formation rate than the surface density of gas, meaning that the surface density would trace star forming activity only for a constant scale height.

Although the magnitude of the 'massive star formation deficiency' is equal to the magnitude of the total gas deficiency, we believe that this is partly a coincidence, because of the different radial distributions of HI and tracers of star formation. It was demonstrated in Chapter V that global gas deficiency is manifested by a deficiency of HI in the outer disks; although the inner disks are HI-deficient, they are not significantly gas-deficient because of large amounts of molecular gas. HI profiles in the outer disk regions of at least some galaxies are shallower than blue light and star formation tracer profiles, indicating that outer galaxy gas is not always as efficient in forming stars as inner galaxy gas. The region which has lost most of the gas is the region which is least efficient in forming stars, making it unlikely that the deficit of massive star formation exists solely in the outer disk. Instead, we believe that the inner regions of HI-deficient Virgo spirals may have lower efficiencies of massive star formation.

§7. Possible Variations in the IMF

All of the star formation tracers that have been discussed in this chapter are highly sensitive to the upper mass end of the main

sequence, and yield little information about the formation of low mass stars. It is entirely possible that only the formation of O and B stars has been altered in the HI-deficient Virgo spirals, and that the total star formation rate (in $M_o\ yr^{-1}$) remains unaltered due to prodigious low-mass star formation. While no quantitative examination of this important problem has yet been undertaken, Kennicutt (1985) has made the following qualitative observation from his Hα photometry: "The galaxies which are unusually gas-poor generally exhibit much smaller and fainter HII region populations. The gas deficiency seems to have altered not only the star formation rate, but also the properties of the individual star forming regions."

The physical conditions responsible for the formation of stars in different mass ranges are observationally unknown. However, as we pointed out in §VI.4, there is evidence that the formation of O stars in the Milky Way occurs only in a particular class of massive GMC (Myers et al. 1986; Scoville et al. 1987). Moreover, Scoville et al. find that the efficiencies of massive star formation in the Milky Way are a function of cloud size: the most massive GMC's ($M \sim 10^6\ M_o$) may be less efficient at forming OB stars than their smaller counterparts ($M \sim 10^5\ M_o$). The existence of both HI-dominated and H_2-dominated spirals in the cluster demonstrates that the physical conditions in the interstellar media of Virgo galaxies vary greatly. If the IMF and star forming efficiencies vary among extragalactic molecular clouds as much as the results of Scoville et al. suggest, then it would not be surprising to discover that the IMFs vary among the Virgo spirals as

well.

§8. CO in Virgo SO's and the Fate of Stripped Spirals

In the past, a number of authors (e.g. Gunn and Gott 1972) have concluded that HI-stripped cluster galaxies would quickly evolve to become inactive, featureless SO-like systems, since their reservoir of star-forming material was significantly depleted. This early conclusion was based on the erroneous assumptions that the atomic gas was the only significant component of interstellar gas mass, or that the mass of other components were simply proportional to the atomic gas mass. Both of these assumptions are false. Quantitative knowledge of the molecular gas in Virgo galaxies allows us to reevaluate the evolutionary fate of HI-deficient spirals.

An immediate conclusion from Chapters V and VI is that the survival (and possibly the enhancement) of large amounts of molecular gas mitigates the impact of HI removal on star formation and subsequent galactic evolution. We find that the total gas deficiency is equal in magnitude (within the uncertainties) to the massive star formation deficiency. The evolutionary fate of gas-deficient galaxies can be (crudely) assessed by the widely used gas-depletion timescale, which is the time it will take for a galaxy to use up its supply of gas by turning it into stars at the current rate. In order to compute the gas depletion timescale, it is necessary to estimate the total star formation rate (in M_o yr^{-1}). This is generally done by measuring a tracer of high mass stars (e.g. Hα emission, UV continuum) and assuming an

IMF. An important conclusion can be reached without specifying the star formation rates. Since the total gas deficiency in Virgo galaxies is equal to the MSF-deficiency, the formal gas depletion timescales are identical in the HI-rich and HI-deficient systems.

While this suggests that HI-deficient galaxies may evolve at the same rate as HI-rich galaxies, this does not mean that the HI-deficient galaxies undergo 'normal' evolution. We note several uncertainties which result from using the formal gas depletion timescales to predict the future evolution of cluster galaxies. 1) The IMFs may systematically differ between the HI-rich and HI-deficient galaxies, resulting in a systematic error in the gas depletion timescales. 2) The gas depletion timescales consider star formation as the only sink for interstellar gas, and do not include the continual removal of gas into the ICM by stripping. Inclusion of this gas loss mechanism decreases the true gas depletion timescales in HI-deficient galaxies.
3) Although the <u>global</u> average total gas deficiency is equivalent to the <u>global</u> average massive star formation deficiency, different regions of these galaxies may exhibit these deficiencies. It was demonstrated in Chapter V that the global gas deficiency is manifested by a deficiency of HI in the <u>outer galaxy</u>; the inner galaxy is not significantly gas deficient. We suspect that it is lower Hα emission in the inner galaxy which is largely responsible for the global "MSF-deficiency", although this has not been demonstrated. This suspicion is based on the observation that the Hα radial profiles in many galaxies exhibit much stronger central peaks than HI profiles, and on the quali-

tative impressions of Kennicutt, described in §VI.7, on the nature of the fainter star forming regions in the HI-deficient galaxies. 4) Finally, the gas depletion timescale does not uniquely describe galactic evolution. A Virgo galaxy with three times less gas, and a star formation rate three times lower will evolve and appear differently than a typical isolated galaxy, even though their gas depletion timescales are the same. As an extreme example, consider the fact that if both the gas content and the star formation rate were reduced by a factor of 1000, the gas depletion timescale would remain unaltered, although the galaxy would be declared gas-free, and devoid of star formation.

Therefore, although the survival of molecular gas lessens the impact of the HI-stripping on galaxy evolution, it does not rescue a severely stripped galaxy from an altered evolutionary path. We have identified three Virgo galaxies from among the 42 mapped which show evidence that the transformation of spirals to S0's or 'S0-like' galaxies may be occurring in the Virgo cluster. All three of these galaxies are severely HI-deficient, and have been detected in CO.

The first of these, NGC 4710, is the first S0 galaxy in which molecular gas has been detected. It is an edge-on, small B/D galaxy with a featureless outer disk, and a prominent central dust lane. Emission regions are visible within the dust lane (e.g. Hubble Atlas photo, Sandage 1961) which suggests that star formation is ocurring within the central region. NGC 4293 is similar to NGC 4710 in many respects, yet is classified as S0/a (RC2) or Sa pec (RSA). It is highly inclined,

has a featureless outer disk, and dust lanes throughout the central region (Sandage 1961). Both NGC 4710 and NGC 4293 have a source of CO emission which is unresolved in a 45" beam. Both remain undetected in HI, although sensitive searches have been carried out at Arecibo (Giovanardi, Krumm and Salpeter 1983). Each galaxy has a projected velocity comparable to the mean projected velocity of the cluster, which suggests that most of their kinetic energy is in the plane of the sky. NGC 4710 is 5.3° from M87, while NGC 4293 is 6.4° away, implying that both galaxies are beyond the 'stripping zone' of approximate radius 4.5°. The positions and projected velocities of both systems are consistent with radial orbits which carry them through the center of the cluster. If they indeed passed through the cluster core, they would take approximately 2×10^9 years to reach their observed positions from the core, assuming that they are moving with the mean cluster velocity.

These galaxies exhibit the expected aftereffects of a severe stripping event. Very little gas remains in their outer disks. The only interstellar matter remaining is dense molecular gas at the bottom of the gravitational potential wells, which are the locations least susceptible to removal. The gas contents, cluster locations, kinematics, and morphological appearances of both galaxies are consistent with the scenario that these were once later-type spirals which suffered severe stripping events approximately 2×10^9 years ago.

The third galaxy, NGC 4419, is an Sa which has been detected in CO at three positions along the major axis. It has the highest CO/HI flux

ratio of any galaxy known, with an inferred $M(H_2)/M(HI)$ ratio of 25. It also has the most asymmetric molecular gas distribution of all galaxies in the Virgo survey. With a projected velocity of -205 km s^{-1} (among the most negative of all Virgo galaxies), and a projected separation of 2.8° from M87, NGC 4419 is undoubtedly on a radial orbit which passes very close to the cluster core, ensuring a strong interaction with the intracluster gas. It is likely that the large CO/HI flux ratio, and the large CO asymmetry are the result of this interaction. Both of these properties suggest that NGC 4419 is not as evolved as either NGC 4293 or NGC 4710, so perhaps is closer to M87.

The identification of NGC 4710 and NGC 4293 as stripped spirals in the process of evolving into 'S0-like' galaxies rests largely on the untested assumption that galaxies with similar properties do not exist outside of clusters with large fractions of HI-deficient galaxies. The small amount of CO data currently available on S0 galaxies precludes any meaningful comparison of molecular gas in Virgo and non-Virgo S0's. However, the large far-infrared data base provided by the IRAS satellite allows a comparison of the HI masses and FIR luminosities of Virgo and non-Virgo S0's. Figure 6.11 displays histograms of the L_{FIR}/M_{HI} ratio for two samples of galaxies. The upper histogram exhibits the distribution of $\log(L_{FIR}/M_{HI})$ for the 42 Virgo sample galaxies. The four Virgo sample galaxies with the highest values of this ratio are NGC 4293, NGC 4419, NGC 4526, and NGC 4710.

The lower histogram exhibits the same ratio for a sample of 'S0' galaxies from the large HI compilation study of Wardle and Knapp

Figure 6.11 Histograms of L_{FIR}/M_{HI} ratio for 2 samples of galaxies. The upper histogram shows the galaxies in the Virgo sample, which include S0-Sm morphological types. The lower histogram shows the 80 E/S0-S0/a galaxies from the Wardle and Knapp (1986) study which have been observed in HI, and detected at 60μm and/or 100μm. The shaded regions of these histograms indicate lower limits (3σ) to the L_{FIR}/M_{HI} ratios. Although NGC 4293, NGC 4419, NGC 4526, and NGC 4710 are among the galaxies with the largest known L_{FIR}/M_{HI} ratios, many of the other S0 galaxies from the Wardle and Knapp study have less sensitive upper limits for their HI fluxes, and could therefore be more extreme in this ratio than these Virgo galaxies.

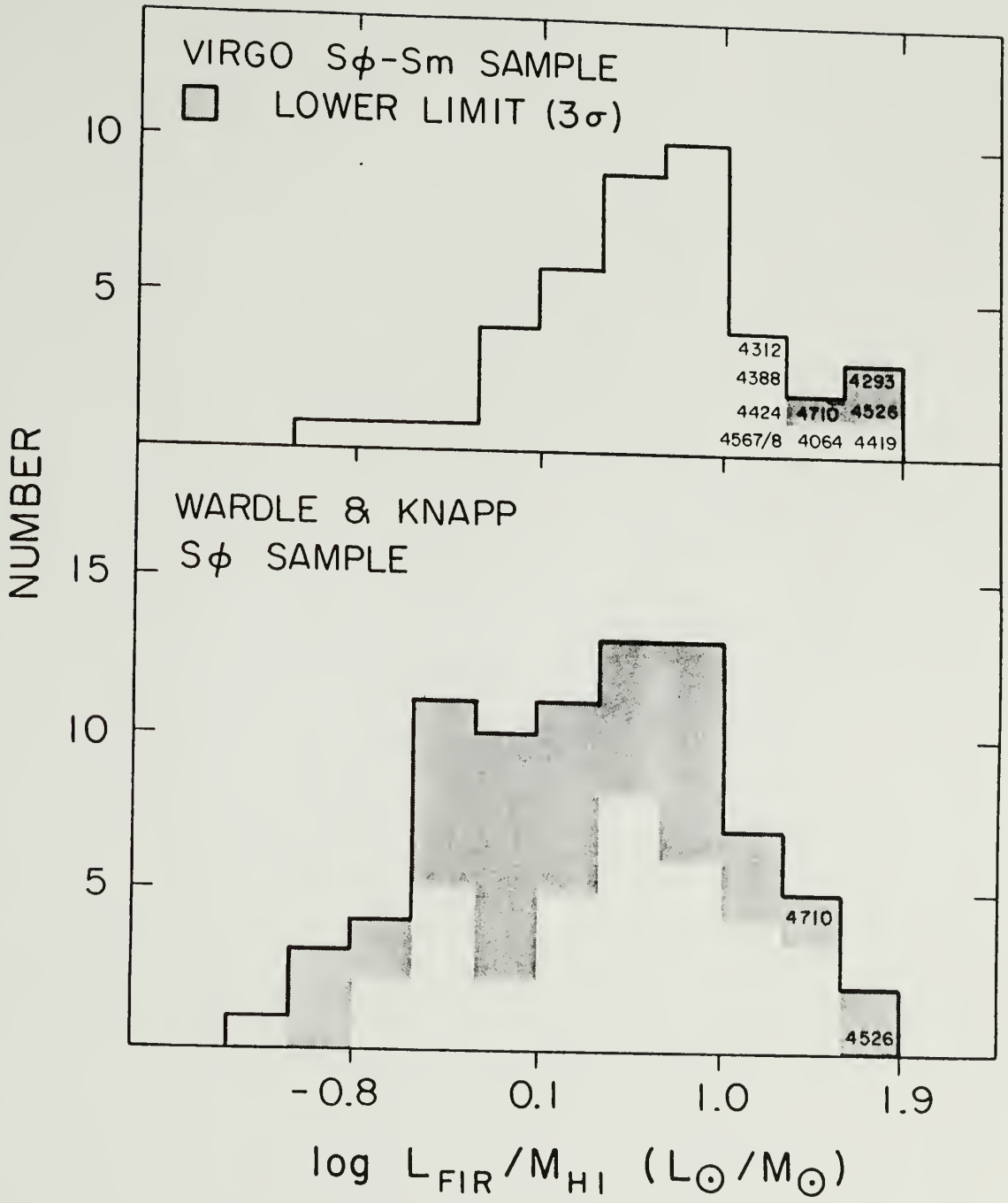
VIRGO Sϕ-Sm SAMPLE
LOWER LIMIT (3σ)
10
5
4312
4388
4293
4424
4710
4526
4567/8
4064
4419
WARDLE & KNAPP
Sϕ SAMPLE
15
10
5
4710
4526
NUMBER
-0.8
0.1
1.0
1.9
log L_FIR/M_HI (L⊙/M⊙)

(1986). For the Wardle and Knapp study, 305 HI observations of galaxies classified as E/S0, S0, S0/a, and S0pec were collected from the literature, of which 85 were detected in HI. These data originate from a variety of sources and telescopes, and are not uniformly sensitive. Of these 305 galaxies, 80 are listed in the IRAS Point Source Catalogue as a positive detection at either 60μm or 100μm or both. It is these 80 galaxies which appear in the lower histogram of Figure 6.11. Because of the non-uniform HI sensitivity, the ill-defined selection criteria, and the large number of HI non-detections, this sample is by no means an ideal sample for statistical comparisions. These histograms do, however, make the point that NGC 4293, 4419, and 4710 (and 4526) are among the early-type disk galaxies with the largest known L_{FIR}/M_{HI} ratios. It is clear that these galaxies have unusual properties for early-type systems, which makes it plausible that these properties are the products of the harsh Virgo environment.

It is of interest to identify the galaxies in these histograms which are known to have log $L_{FIR}/M_{HI}>1.0$. Of the Virgo sample, ten galaxies meet this criterion; eight of the ten are early-type galaxies which are HI-deficient by a factor of 10 or more. They are presumably recently and severly HI-stripped galaxies whose inner disk infrared emission remains strong. One of these eight, NGC 4388, has a significant Seyfert component to its FIR luminosity. The other two galaxies are members of the interacting binary Sc pair NGC 4567/4568, which are HI-deficient by a factor of 4. In this system, not only is the HI content low, but the infrared luminosity may be enhanced by an increased

efficiency of massive star formation, as is observed in strongly interacting and merging galaxies (Young et al. 1986b). Of the 14 S0 galaxies in the Wardle and Knapp sample known to have log $L_{FIR}/M_{HI} > 1$, 5 are in the Virgo cluster, 3 are in other HI-deficient clusters (A262, A1367, and A2147), one is a member of a galaxy pair, and the status of the others is uncertain.

The galaxy with the largest L_{FIR}/M_{HI} ratio in either sample is the Virgo S0 galaxy NGC 4526, which was undetected in the CO line. This galaxy, like NGC 4710 and NGC 4293, is slightly outside the Virgo core 'stripping zone', and may therefore have passed through the core region $\sim 2 \times 10^9$ years ago. This galaxy is more luminous, and therefore more massive, than either NGC 4710 or NGC 4293, and as a result is more difficult to detect because of its larger expected linewidth. Its large L_{FIR}/M_{HI} ratio suggests that NGC 4526 may also be a severely stripped spiral in the process of becoming an S0 galaxy.

While the preceeding analysis presents a convincing case that these galaxies were stripped $\sim 2 \times 10^9$ years ago, the evidence that they were later-type spirals immediately prior to the stripping events is only circumstantial. The following points suggest that this may be the case: 1) These galaxies exhibit the expected characteristics of severely stripped Sa-Sb galaxies. 2) At some time in their past, these galaxies underwent prodigious star formation in their disks, and during that time would have been classified as spirals. Prior to being stripped, these galaxies had gas in their disks, and therefore could have been forming stars, creating a stronger 'spiral' appearance. 3)

There are very few HI-deficient later-type spiral galaxies in the outer cluster. In the present sample of 42 galaxies, there are 6 galaxies with $R_{M87}>4.5°$ and HI def>0.4. Four of these (NGC 4064, NGC 4293, NGC 4526, and NGC 4710) are classified as S0-Sa. The other galaxies are NGC 4450, an Sab, and NGC 4394, an SBb in close proximity to the elliptical galaxy NGC 4382. This morphological segregation could also be due to selection effects. If all late-type spirals have predominantly circular orbits (Dressler 1986), then one would not expect to find stripped late-type spirals outside the 'stripping zone'.

While the preceeding analysis presents a convincing case that these galaxies were stripped $\sim 2 \times 10^9$ years ago, the evidence that they were later-type spirals immediately prior to the stripping events is only circumstantial. The following points suggest that this may be the case: 1) These galaxies exhibit the expected characteristics of severely stripped Sa-Sb galaxies. 2) At some time in their past, these galaxies underwent prodigious star formation in their disks, and during that time would have been classified as spirals. Prior to being stripped, these galaxies had gas in their disks, and therefore could have been forming stars, creating a stronger 'spiral' appearance. 3) There are very few HI-deficient later-type spiral galaxies in the outer cluster. In the present sample of 42 galaxies, there are 6 galaxies with $R_{M87}>4.5°$ and HI def>0.4. Four of these (NGC 4064, NGC 4293, NGC 4526, and NGC 4710) are classified as S0-Sa. The other galaxies are NGC 4450, an Sab, and NGC 4394, an SBb in close proximity to the elliptical galaxy NGC 4382. This morphological segregation could also be

due to selection effects. If all late-type spirals have predominantly circular orbits (Dressler 1986), then one would not expect to find stripped late-type spirals outside the 'stripping zone'.

§9. Summary

In this chapter, various traces of star formation in Virgo spirals are compared with their gas properties. The major conclusion drawn is that the massive star formation rate in HI-deficient spirals is reduced by an amount comparable to the total gas ($HI+H_2$) deficiency.

Comparisons of the radial distributions of HI and CO with Hα line and radio continuum emission reveal that the survival of molecular gas plays a prominent role in preserving the star forming ability of HI-deficient galaxies. However, galaxies do not need a large steady-state supply of molecular gas to form stars. There are several low mass Sc-Sm galaxies in the cluster which are rich in atomic gas, but have little or no CO emission. The 2 HI-rich, CO-poor galaxies which have been mapped at high resolution in HI have HI surface densities greater than those observed in any CO-rich galaxy. Despite the lack of molecular gas, these galaxies are strong sources of Hα line, far-infrared, and radio continuum emission. The massive star formation rates per unit area in these galaxies are comparable to those in the more luminous, CO-rich, Virgo Sc galaxies.

Infrared data at 12-100μm are used to discuss the nature of the heating sources for the dust, the phase of the gas associated with the dust, and the dependence of FIR emission on morphology and HI defi-

ciency. It is found that the gas quantity which exhibits the best correlation with FIR luminosity is the mass of HI+H_2 within the optical isophotal diameter D_o. The correlation between these quantities is tight for Sc galaxies. However, there is an order of magnitude variation in the L_{FIR}/M_{gas} ratio for S0-Sb galaxies. The L_{FIR}/M_{gas} ratio among these galaxies is not correlated with the $S_{60\mu m}/S_{100\mu m}$ ratio, indicating that heating by massive stars is not the cause of L_{FIR}/M_{gas} variations. Either the gas-to-dust ratios in some early type Virgo spirals are lower than that in the Milky Way, or the fraction of dust which exists at ~10 K is small.

Virgo spirals which are HI-deficient by a factor of 10 have 40-120μm luminosities which are lower by a factor of ~2-3. Of the 4 IRAS bands, the emission at 60μm is most affected by HI deficiency. This effect, although small in magnitude, is consistent with less heating from massive stars.

Although the survival of molecular gas mitigates the impact of HI deficiency on star formation and subsequent galactic evolution, it does not spare severely stripped galaxies from altered evolutionary paths. We have identified 3 early type Virgo galaxies whose properties suggest that the transformation from spirals to S0-like galaxies may occur as the result of stripping. CO emission has been detected in the center of NGC 4710 and NGC 4293, 2 S0-S0/a galaxies which remain undetected in HI. The morphologies and orbital constraints on these galaxies suggest that they are the evolved remnants of early type spirals which suffered severe stripping events ~2×10^9 years ago. A third galaxy, classified

as an Sa, has the largest known ratio of CO to HI flux, and has the most asymmetric CO distribution in the Virgo sample. NGC 4419's extreme negative velocity and its projected location close to M87 ensure a strong interaction with the intracluster medium. Its gas properties suggest that NGC 4419 may be less evolved than either NGC 4293 or NGC 4710, so perhaps it is still close to the cluster core.

A comparison has been made of the L_{FIR}/M_{HI} ratios of the Virgo sample and the Wardle and Knapp (1986) sample of S0 galaxies. HI-deficient S0-Sa Virgo galaxies have the highest values of this ratio among the 2 samples, which provides strong evidence that these galaxies have been modified by the Virgo environment. Several reasons are given which support our contention that the galaxies exhibited a later-type morphology prior to the environmentally induced modification.

CHAPTER VII

THE ROLES OF ATOMIC AND MOLECULAR GAS IN STAR FORMATION

§1. The Lifetime of the Molecular Phase in Galaxies

The existence and persistence of large ratios of molecular-to-atomic gas in the inner regions of HI-deficient spirals not only has important implications for the long-term evolution of these galaxies, but may also constrain the rate at which gas cycles between the atomic and molecular phases in these galaxies. Before proceeding, two relevant facts are recalled: 1) In HI-deficient Virgo galaxies, the HI surface density within the inner half of the optical disk is low with respect to both starlight and the surface density of molecular gas. 2) The large fraction of HI-deficient galaxies with large σ_{H_2}/σ_{HI} ratios implies that these large ratios endure for a period of order a cluster crossing time, which is $\sim 2 \times 10^9$ years. The first implication of these facts, which has already been discussed, is that the long-term survival of molecular gas minimizes the impact of HI deficiency on star formation and subsequent galactic evolution (particularly in the inner galaxy).

The enduring nature of the large σ_{H_2}/σ_{HI} ratios is also relevant to the lifetime of the molecular phase in the galaxies. It is necessary to define what is meant by the lifetime of the molecular phase. We do not mean the lifetime of an individual molecular cloud. We also do not mean the average amount of time a typical nucleon spends

in the molecular phase. The large H_2/HI ratios in the central regions of both Virgo and isolated high luminosity galaxies indicate that a typical nucleon in these regions spends most of its existence in the molecular phase. What we do mean by the lifetime of the molecular phase is the average length of time a nucleon spends between molecular formation and dissociation. The rate at which interstellar gas cycles between the ionized, atomic, and molecular phases is important in theories of star formation and the evolution of the interstellar medium. Prior estimates of molecular phase lifetimes in the inner disk of the Milky Way have ranged from $\sim 10^7$ years (Blitz and Shu 1980) to $\sim 10^9$ years (Scoville and Hersh 1979). An independent assessment of the molecular phase lifetime in galaxies can be made from the Virgo cluster observations.

The original conclusion of Kenney and Young (1985, 1986) and Stark et al. (1986) that the molecular phase in galaxies is long-lived was based on the unstated assumption that the large σ_{H_2}/σ_{HI} ratios were due only to HI removal. If the large σ_{H_2}/σ_{HI} ratios were due to the conversion of atomic to molecular gas by a cluster-galaxy interaction process, then the possibility exists that the galaxy-ICM interaction might limit the use of Virgo spirals as probes of typical ISM behavior. The idea here is that if gas in molecular clouds were rapidly returned to the atomic phase, a continuing HI$\rightarrow H_2$ process might maintain large σ_{H_2}/σ_{HI} ratios. However, such a scenario could not explain the large inner disk σ_{H_2}/σ_{HI} ratios in HI-deficient galaxies which are outside the active "stripping zone" (e.g. NGC 4293). Beyond the 4.5° radius

"stripping zone", the hypothetical HI→H_2 process would no longer operate. Yet large σ_{H_2}/σ_{HI} ratios persist in galaxies which appear to have passed through the densest regions of the core over 10^9 years ago. The existence of these galaxies makes it unlikely that large σ_{H_2}/σ_{HI} ratios are "maintained" by an ICM-ISM interaction.

Even if the low HI surface densities in the inner regions of the HI-deficient spirals are due to HI removal, one could imagine a scenario where only low column density HI not associated with GMC's was removed from the galaxy. The surviving HI in the HI-deficient galaxies may be predominantly associated with GMC's. GMC's are massive enough to be gravitationally bound, and therefore could act as harbors from the intracluster storm. Within this gravitationally bound complex, nucleons might pass through atomic, ionized, and molecular phases any number of times during the 2×10^9 year cluster crossing time. In order for this scheme to be tenable, roughly half of the inner disk HI in an HI-normal luminous Sc galaxy must be associated with gravitationally bound GMC's, a typical 'GMC complex' must be composed of ~10-30% neutral hydrogen (see Figure 5.15), and the HI must remain associated with its GMC for $\sim2\times10^9$ years. While this scenario permits gas within a 'GMC complex' to cycle between phases on short timescales, it requires that the individual 'GMC complexes' survive for $\sim2\times10^9$ years.

Thus the persistence of large σ_{H_2}/σ_{HI} ratios in the inner regions of Virgo spirals appears to require that either the molecular phase lifetime, or the lifetime of individual GMC complexes is $\sim2\times10^9$ years. If H_2 were rapidly cycled through the atomic phase, then one would

expect H_2 to become rapidly depleted to achieve the value of σ_{H_2}/σ_{HI} which was present prior to HI removal.

It should be emphasized that the term 'molecular phase lifetime' does not have physical meaning for an entire galaxy, but may have meaning for separate regions within a galaxy (e.g. within annuli). In the outer disks of galaxies, and even the inner regions of HI-dominated galaxies, the small ratios of σ_{H_2}/σ_{HI} imply that a typical nucleon spends most of its life in the atomic phase. Yet in the inner regions of H_2-dominated galaxies, a typical nucleon may spend long uninterrupted periods of time in the molecular state, particularly if most of the H_2 mass exists in hard-to-destroy GMCs.

§2. The Roles of Atomic and Molecular Gas in Star Formation

Stars form from molecular gas, but molecular gas forms from atomic gas. In the simplest terms, the evolution of galaxies can be understood as HI→H_2→stars. At present, little is known about the roles that atomic and molecular gas each play, on a global scale, in the star formation process. The relative amounts of HI and H_2, and the relationship between the star formation rate and the amounts of HI and H_2 can be utilized to constrain the manner in which gas in galaxies is transformed into stars.

Since Schmidt's (1959) original suggestion that the star formation rate (SFR) is proportional to some power n of the gas density, a myriad of papers have discussed this idea. Since the volume density of gas, ρ_{gas}, is difficult to observationally determine, the Schmidt law is

commonly expressed in terms of the gas surface density, σ_{gas}, which is observationally measured, and the scale height of the gas, z_{gas}. Thus the Schmidt law can be written

$$SFR \propto \rho_{gas}{}^{n} \propto \left\{\frac{\sigma_{gas}}{z_{gas}}\right\}^{n} \quad . \qquad \text{(VII-1)}$$

For several reasons, it is convenient to express a Schmidt-type relation for the star formation rate in terms of the surface gas density to the first power, or:

$$SFR(R) = \sigma_{gas}(R)\ SFE \qquad \text{(VII-2)}$$

where the total gas surface density σ_{gas} (in $M_{\odot}\ pc^{-2}$) and the star formation rate SFR (in $M_{\odot}\ yr^{-1}\ pc^{-2}$) are functions of galactocentric radius R, and the proportionality factor is called the star formation efficiency SFE (in yr^{-1}).

Equation VII-2 is convenient because the quantity $\sigma_{gas}(R)$ is directly observed in other galaxies. Moreover, a direct proportionality between SFR(R) and $\sigma_{gas}(R)$ have been observed in several luminous spiral galaxies (e.g. Scoville and Young 1983; Chapter VI). Equation VII-2 separates the star formation rate into the amount of raw material available, and a term which depends on physics. (As such, equation VII-2 is not a physical law, as is equation VII-1. A variation in z_{gas}, or a power of n different from 1 in equation VII-1 would be incorporated into the SFE term in equation VII-2). The pre-

sent gas distribution $\sigma_{gas}(R)$ depends on the initial gas distribution, determined by the collapse of the protogalaxy, and by the amount of gas already used up to form stars. (This simple picture thus ignores significant radial transport of gas, and gas accretion after galaxy formation.) All the physics of star formation, which is inherently a local process, are included in the SFE term. Magnetic fields and turbulence support molecular clouds from rapid gravitational collapse severely limiting the SFE and prolonging cloud lifetimes. Various processes may increase the SFE over the quiescent value. These include passages through spiral arms and barlike potentials, cloud-cloud collisions, and shocks from nearby star forming regions. Evidence for increased SFE's has been presented for the spiral arms of M51 and the bar of M83 (Lord 1987), and in interacting and merging galaxies (Young et al. 1986b). In all these cases, the increased SFE can be considered as an enhancement not depending on global galaxy properties, but due to the local environment.

In the Schmidt-law description of star formation, it is not a priori obvious whether it is more physically meaningful to consider all the gas, or just the densest star-forming clouds in the gas surface density term. Equation VII-I does not distinguish between different physical states of gas. Yet, we seek an explanation for the large range of σ_{H_2}/σ_{HI} ratios in galaxies, and this explanation may or may not directly involve star formation.

Qualitatively, the decreasing σ_{H_2}/σ_{HI} ratios with increasing radius in a galaxy might be easy to understand. The total mean gas

surface density decreases strongly with radius, and for a constant (or increasing) scale height, the total mean gas volume density also decreases strongly with radius. With a lower mean volume density at large radii, less gas exists at high densities (e.g. H_2), and more exists at low densities (e.g. HI). This simple geometric argument encounters difficulty in explaining large σ_{HI}/σ_{H_2} ratios when the total gas surface density is large. At the location where the HI surface density peaks in the HI-rich, CO-poor galaxies, NGC 4178 and NGC 4713, $\sigma_{HI}=13\ M_o\ pc^{-2}$ and $\sigma_{HI}/\sigma_{H_2}>5$. At the location in NGC 4254 which has $\sigma_{HI+H_2}=13\ M_o\ pc^{-2}$, $\sigma_{HI}/\sigma_{H_2}\simeq 0.8$. Thus, in order for a lower volume density to account for these different σ_{HI}/σ_{H_2} ratios, the gas scale heights must differ by a factor of ~6. If the effects of magnetic fields and cosmic rays are ignored, then the scale height of the gas, z_{gas}, is related to the total disk mass surface density σ_{TOT} by $z_{gas} \propto \Delta v \sigma_{TOT}^{1/2}$ (Spitzer 1978), where Δv is the gas velocity dispersion. For constant velocity dispersions, the disk mass surface density must be 36 times greater to reduce the scale height by a factor of 6. This is roughly an order of magnitude greater than the difference between the estimated disk mass surface densities of NGC 4178 and NGC 4254 1.5' from their nuclei, using equation V-22 and numbers from Table 5.2. Even if a lower mean volume density is invoked to explain the large σ_{HI}/σ_{H_2} ratios in the HI-rich, CO-poor galaxies, then one has difficulty understanding the large star formation rates in these galaxies.

One explanation for the large range of σ_{H_2}/σ_{HI} ratios in galaxies is that the HI$\rightarrow H_2$ and $H_2\rightarrow$stars processes are somewhat independent, and

occur at different rates (Tacconi and Young 1986). In this approach, the H_2 is considered to exist exclusively in 'star-forming clouds' and the HI in 'clouds that form the star-forming clouds'. Thus the gas surface density which determines the SFR in equation VII-I is only the H_2 surface density. An equation similar to VII-I is written for the rate at which HI$\rightarrow H_2$. This approach encounters serious problems in explaining galaxies with large surface densities of atomic gas, small surface densities of molecular gas, and high star formation rates. A comparison of Hα luminosities and total gas masses in the lower luminosity Virgo Sc galaxies is revealing. For the 4 HI-rich, CO-poor galaxies (NGC 4178, NGC 4651, NGC 4713, NGC 4808), the mean value of $\log L_{H\alpha}/M_{HI+H_2} = -2.34 \pm 0.07$. For 3 HI-poor, CO-rich galaxies (NGC 4212, NGC 4571, NGC 4689) the mean value of the same quantity is -2.31 ± 0.09. Despite the fact that the mean ratio of atomic to molecular gas in these 2 samples differs by a factor of 40 (see Table 5.3), their mean global massive star formation efficiencies (using the total gas mass) are identical. This strongly suggests that it is the total gas surface density, and not the H_2 surface density, which helps determine the massive star formation rate. The distinction between H_2 and HI as 'star-forming clouds' and 'clouds which form the star-forming clouds' is somewhat artificial, since galaxies appear to form massive stars at a rate which is independent of the HI/H_2 ratio.

Under this interpretation, the relative amounts of HI and H_2 indicate different mean physical and/or chemical conditions in the interstellar media, which are directly or indirectly related to the

total disk mass surface densities. Whether gas exists in the atomic or molecular phase depends on the balance between the rates of molecular formation and destruction (Hollenbach, Werner, and Salpeter 1971). Molecular hydrogen is destroyed mainly by a 2-step process, involving the absorption of a Lyman-band photon, followed by a radiative decay which results, in some fraction of cases, in dissociation. The dissociation rate therefore depends upon the intensity of the Lyman-band radiation field. Since dissociation is initiated by absorption of line radiation, this dissociating field becomes too weak to support the process after a certain column density of H_2 is built up. The most efficient formation mechanism under typical Milky Way interstellar cloud conditions is recombination on dust grain surfaces. The formation rate is linearly proportional to both the number density of hydrogen atoms and dust grains.

Most of the HI emission in the Milky Way arises from gas with densities ranging from 0.1 cm^{-3} to 50 cm^{-3} (Kulkarni and Heiles 1987), although a small amount of HI, in dark clouds, exists at densities as large as 10^3 cm^{-3} (Myers 1978). Galactic CO emission arises from gas with densities greater than 10^2 cm^{-3} (Myers 1978). The densities at which atoms and molecules exist depend, among other things, on the dust-to-gas ratio. If the dust-to-gas ratio is varied, and all other variables are held constant, the gas density at which H_2 will begin to dominate will depend linearly on the dust-to-gas ratio. One could imagine a giant gas complex, similar in many respects to Milky Way GMC's, yet with an order of magnitude less dust. In such a dust-poor cloud, a

large fraction of gas in the $\sim 10^2$-10^3 cm^{-3} density range would exist in the atomic phase, whereas in nearby Milky Way clouds, it is predominantly in the molecular phase. The densest regions of the cloud would still be molecular, but most of the cloud mass might exist in the atomic phase. The exact fraction of the cloud mass in the atomic phase depends upon the critical density at which H_2 begins to dominate, and the fraction of cloud mass existing at densities greater than the critical density, which are both relatively uncertain quantities.

There is evidence that the Magellanic Clouds have low dust-to-gas ratios. Dust-to-gas ratios have been estimated to be 4 times lower in the LMC than in the Milky Way, and 17 times lower in the SMC (Koornneef 1982; Koornneef 1984; Lequeux et al. 1984). CO emission is very weak in both galaxies. While the CO-H_2 proportionality factor may be systematically different from the Milky Way value in the Magellanic Clouds (Israel et al. 1986), the low dust contents also suggest that the H_2/HI ratios in their star-forming clouds are systematically low.

Dust-to-gas ratios are expected to be correlated with metallicities. Evidence for systematically lower metallicities in low mass galaxies has been presented by Pagel and Edmunds (1981) and Bothun et al. (1984). If low dust-to-gas ratios are the correct explanation for the HI-dominated galaxies, then actively star-forming HI-dominated galaxies are predicted to have systematically lower dust-to-gas ratios and metallicities than actively star-forming H_2-dominated galaxies. This can be tested with submillimeter continuum observations, to measure dust masses, in a suitable sample of HI-dominated and

H_2-dominated galaxies. Metallicities can be assessed with optical spectrophotometry of HII regions.

Metallicities and dust-to-gas ratios are not the only quantities which vary systematically with galaxy mass. The shapes of rotation curves also vary with galaxy mass, and may contribute to the formation of GMC complexes. The most efficient way to form GMCs is through an agglomeration of smaller clouds by cloud-cloud collisions (e.g. Scoville and Hersh 1979). However, random cloud motions are thought to be too small to efficiently form 10^5-10^6 GMCs (e.g. Elmegreen 1987). It has been suggested that the velocity shear in the disks of luminous spirals plays an important role in the growth of GMCs, since velocity shear results in more cloud-cloud interactions (Wyse 1986). While massive galaxies have flat rotation curves, and hence significant velocity shear over a large fraction of their disks, diminutive galaxies have slowly rising rotation curves, and very little velocity shear (Rubin et al. 1985). In this scenario, the paucity of molecular gas in low mass galaxies with large HI column densities is due their inability to concentrate a large self-shielding mass of gas in a small volume. The major reason that GMCs are predominantly molecular is that they have built up enormous column densities of gas, which shield the interior of the cloud from dissociating UV radiation. If a GMC were to be broken up into many smaller clumps, and distributed throughout the galaxy, a larger fraction of its total mass would become atomic, since dissociating photons from the interstellar radiation field would penetrate a larger fraction of the total mass. Thus a galaxy without

GMCs could still have a significant amount of high density gas--it could exist in smaller clouds, with a larger fraction of the total gas mass in the atomic state.

The efficiency of star formation, on large scales, does not appear to strongly depend on whether gas exists predominantly in the atomic or molecular phase. Yet, many aspects of star formation are likely to be different in HI-dominated and H_2-dominated environments. Our understanding of galactic evolution will be greatly improved if we can discover the answer to these two questions: What determines the dominant phase of the interstellar medium? How does star formation (the process and the product) differ in HI-dominated and H_2-dominated environments?

§3. Summary

Two important results are discussed in this chapter. The first section describes how the large H_2/HI ratios in the inner regions of HI-deficient Virgo spirals constrain the rate at which gas cycles between the atomic and molecular phases. It is argued that either the lifetime of the molecular phase, or the lifetime of individual GMC complexes must be $\sim 2 \times 10^9$ years in the H_2-dominated central regions of galaxies.

The last section focusses on the roles of atomic and molecular gas in star formation. A comparison of the HI-rich, CO-poor and HI-poor, CO-rich lower luminosity late type galaxies provides one of the most interesting conclusions of this thesis. Despite the fact that the

mean ratio of atomic to molecular gas in these 2 samples differs by a factor of 40, their mean global massive star formation efficiencies (using the total HI+H_2 mass) are identical. This strongly suggests that it is the total gas surface density which helps determine the massive star formation rate.

This conclusion raises an important issue: what determines the dominant phase of the ISM? Many HI-rich, CO-poor galaxies apparently have enough high density gas to form stars, yet very little of this gas exists in the molecular phase. A parameter related to the low mass of these HI-rich galaxies is likely to be responsible for their small amounts of H_2. The dust-to-gas ratio and the shape of the rotation curve are discussed as parameters which probably play significant roles in determining whether a gas-rich galaxy forms a significant amount of molecular gas.

APPENDIX A

THE CALIBRATION OF POINT SOURCES AT 115 GHZ

§1. Point Source Calibration and Correction to the Chopper Wheel Method

The calibration of CO(J=1→0) data is made difficult by the significant atmospheric opacity at 115 GHz. There is an elevation dependence to the calibration which is due not only to gain changes, but also to time-variable atmospheric effects. The chopper wheel method, which is the calibration technique commonly used at millimeter wavelengths (and at FCRAO) to compensate for atmospheric absorption and emission (Penzias and Burris 1973), is inadequate at frequencies near the atmospheric O_2 line at 118 GHz. The wings of this O_2 line enhance the opacity enough at 115 GHz to create significant errors in the chopper wheel calibration method, especially at lower elevations. This error arises because the chopper wheel calibration temperature, which is measured several times an hour, is used as an estimate of the total (i.e. atmosphere-corrected) system temperature. The chopper wheel calibration temperature is equal to the total system temperature only when the temperature of the ambient load (i.e. chopper wheel) is equal to the effective temperature of the absorbing regions of the atmosphere. In general, the atmosphere is colder than the ambient load, which necessitates a correction to the chopper wheel calibration temperature to get the true total system temperature.

This correction, pointed out by Davis and Vanden Bout (1973), and

described in Schloerb and Snell (1980), is appreciable when both the opacity and the temperature difference (ΔT) between the ambient load (T_{AMB}) and the atmosphere (T_{ATM}) are large. The magnitude of this elevation-dependent correction is given to first order by

$$C_{FAC} = 1 + \frac{\Delta T}{T_{AMB}} (e^{\tau_o A} - 1) \qquad (A\text{-}1)$$

(Snell and Schloerb 1983), where τ_o is the zenith opacity, and $A=1/\sin(\text{elevation})$ is the airmass. In principle, it is possible to determine C_{FAC} if τ_o and ΔT can be measured. In practice, however, neither τ_o nor ΔT are easy to accurately determine.

Because of the difficulty in estimating τ_o and ΔT, a different approach is taken in this thesis. In order to determine both the elevation dependence of the calibration and an absolute calibration scale (in Janskys K^{-1}), we have analyzed 193 measurements of the planets, IRC+10216, and OrionHV at 115 GHz, taken from the FCRAO pointing logs during 1983-86. The only measurements used here are those taken after the observer checked to make sure that the telescope was properly focussed and pointed on the source. A mean elevation dependence of the calibration between 20° and 65°, and a mean absolute constant for converting antenna temperature (T_A^*) to Janskys for point sources at 60° have been determined from these data. Observations on the same day of a small source (IRC+10216) and a large source (the Moon) from transit to setting have been used to estimate the fraction of the elevation

dependence associated with gain changes, and the fraction associated with atmospheric effects. From fits to the elevation dependence of the small source and large source calibration data, mean values of τ_o and ΔT have been inferred, which allow the observed antenna temperatures to be corrected for all atmospheric effects.

The only strong astronomical sources which can be used as flux density standards at millimeter wavelengths are the planets. Since the angular sizes of the planets range from a few arcseconds to over 60" (which is slightly larger than the HPBW of the FCRAO 14-meter telescope at 115 GHz), both the beam efficiency and the aperture efficiency can be determined from planetary observations, if the appropriate size corrections are made. Point source calibration factors (Jy K^{-1}), or calibration 'constants' (CC), for 115 GHz have been determined for each of 63 measurements of Jupiter, Saturn, and Venus. Since there are no published determinations of planet brightness temperatures (T_B) at 115 GHz, the values used, which are presented in Table A.1, are based on interpolations between the 90 GHz and 150 GHz values of Ulich (1981). The equation used to calculate the flux densities of the planets is:

$$S_\nu(\mathrm{Jy}) = \frac{1.0888\times10^{-7}\ \nu^3(\mathrm{GHz})\ \langle SD" \rangle^2}{\exp\{\ 0.047994\ \nu(\mathrm{GHz})/T_B(K)\ \} - 1} \qquad (A\text{-}2)$$

(Ulich 1980), where $\langle SD \rangle = 1/2(D_{eq}D_{pol})^{1/2}$ is the semidiameter of the planet in arcseconds, and D_{eq} and D_{pol} represent the apparent equatorial and polar diameters of the planet. This is a general expression which

Table A.1

Calibration Results for 115 GHz

All Pointed and Focussed Measurements 1983-86

Source	Number of Obs.	T_B (K)[1]	Calibration constant corrected to 60°[2]
Venus	23	337	43.4 ± 2.9 Jy K^{-1}
Jupiter	37	174	43.9 ± 3.2
Saturn	3	144	45.1 ± 3.6
OrionHV[3]	29	-	44.3 ± 3.9
IRC+10216[4]	101	-	43.8 ± 3.3
All Planets	63	-	43.8 ± 3.3 Jy K^{-1}

[1]Brightness temperature values for planets at 115 GHz are interpolations of 90 and 150 GHz values of Ulich (1981).

[2]All data fit to equation A-7 with a=0.18, b=0.5.

[3]All OrionHV $^{12}CO(J=1\rightarrow0)$ line data scaled such that at 60° elevation, T_A^*(peak) = 49.6 K

[4]All IRC+10216 $^{12}CO(J=1\rightarrow0)$ line data scaled so that at 60° elevation, $\int T_A^* dv$ = 131.0 K km s^{-1}

holds for any uniform disk source of known brightness temperature, and thus ignores any possible limb brightening or darkening, or longitudinal brightness differences. Calibration 'constants' are given by:

$$CC = \frac{C_s S_\nu}{T_A^*} \qquad (A-3)$$

The size correction factor

$$C_s = \frac{x^2}{1-e^{-x^2}} \qquad (A-4)$$

where,

$$x^2 = \ln 2 \frac{D_{eq}\ D_{pol}}{HPBW^2} \qquad (A-5)$$

compensates for the Gaussian beam-weighting of the planetary disk emission.

The planetary calibration factors have been plotted in Figure A.1 as a function of elevation. Also plotted in Figure A.1 are 130 measurements of the CO emission line in the strong galactic sources IRC+10216 and OrionHV, to help establish the mean elevation dependence of the calibration. Since the absolute fluxes of these 2 sources are not known a priori, their values have been scaled to match the plane-

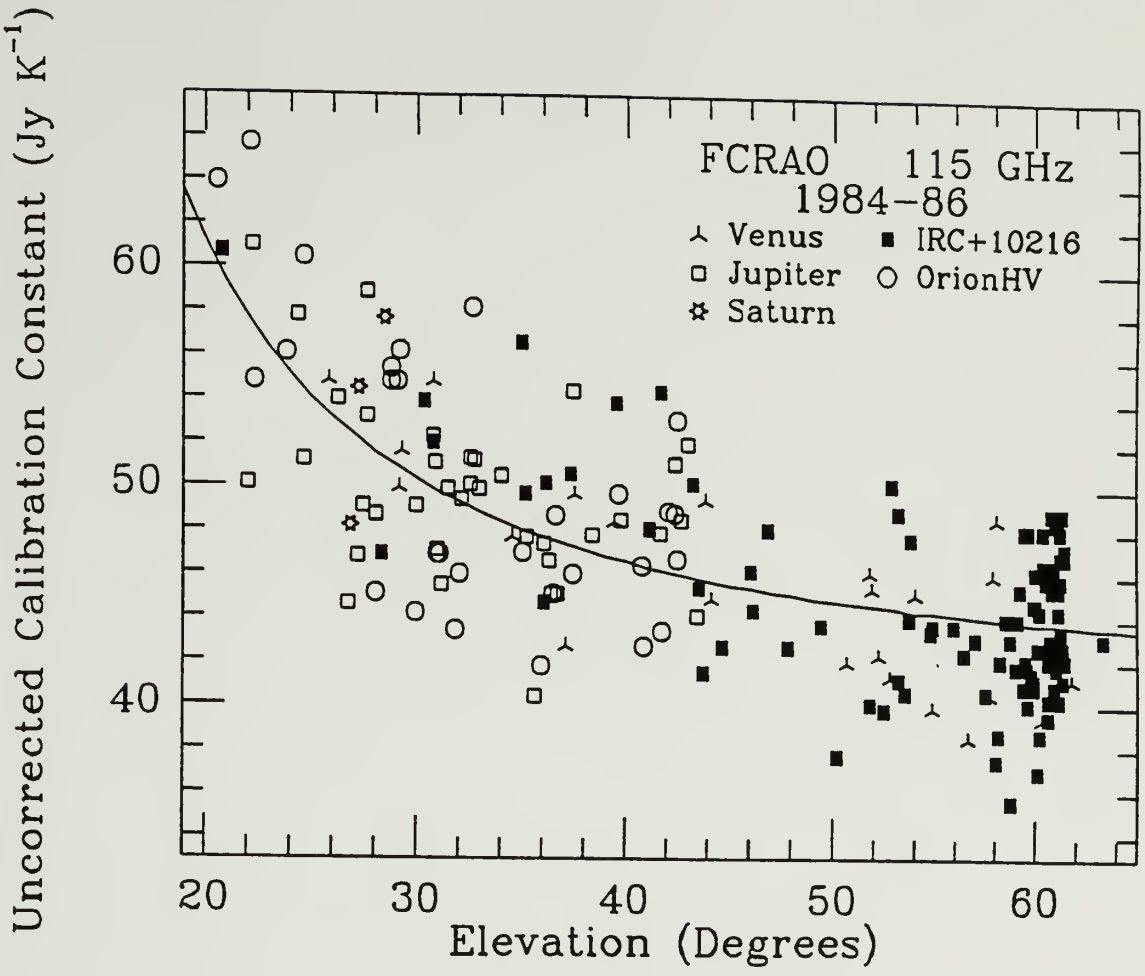

Figure A.1 Uncorrected calibration constant vs. elevation for all 115 GHz observations obtained during 1984-86. The line represents a least squares solution to the elevation dependence using equation A-7 with a = 0.18, b = 0.5.

tary calibration values.

The strong elevation dependence of the calibration shown in Figure A.1 can be represented by a function of the form

$$C_{EL} = \frac{C_{FAC}(EL)}{C_{FAC}(60°)} + C_{GAIN}(EL) \qquad \text{(A-6)}$$

where C_{FAC} is given by equation A-1, and $C_{GAIN}(EL)$ is an unknown function. For the purpose of correcting the data for the mean elevation dependence, it is largely irrelevant whether gain changes or atmospheric effects are responsible. Therefore, we initially assume $C_{GAIN}(EL) = 0$, and fit the elevation dependence to the following equation, which has the same functional form as C_{FAC}:

$$C_{EL} = c \{ 1 + a (e^{bA} - 1) \} \qquad \text{(A-7)}$$

where

$$c^{-1} = 1 + a (e^{b/\sin 60°} - 1) \qquad \text{(A-8)}$$

There is no unique least squares solution for a and b. Several solutions for a and b yield equally good fits to the data. One such solution is a = 0.18, b = 0.5. The lack of a unique solution has no bearing on the primary goal of establishing an expression for the mean elevation dependence of the calibration. Figure A.2 displays the calibration data with the elevation dependence removed, and Table A.1 lists the calibration constants separately for each source. From the

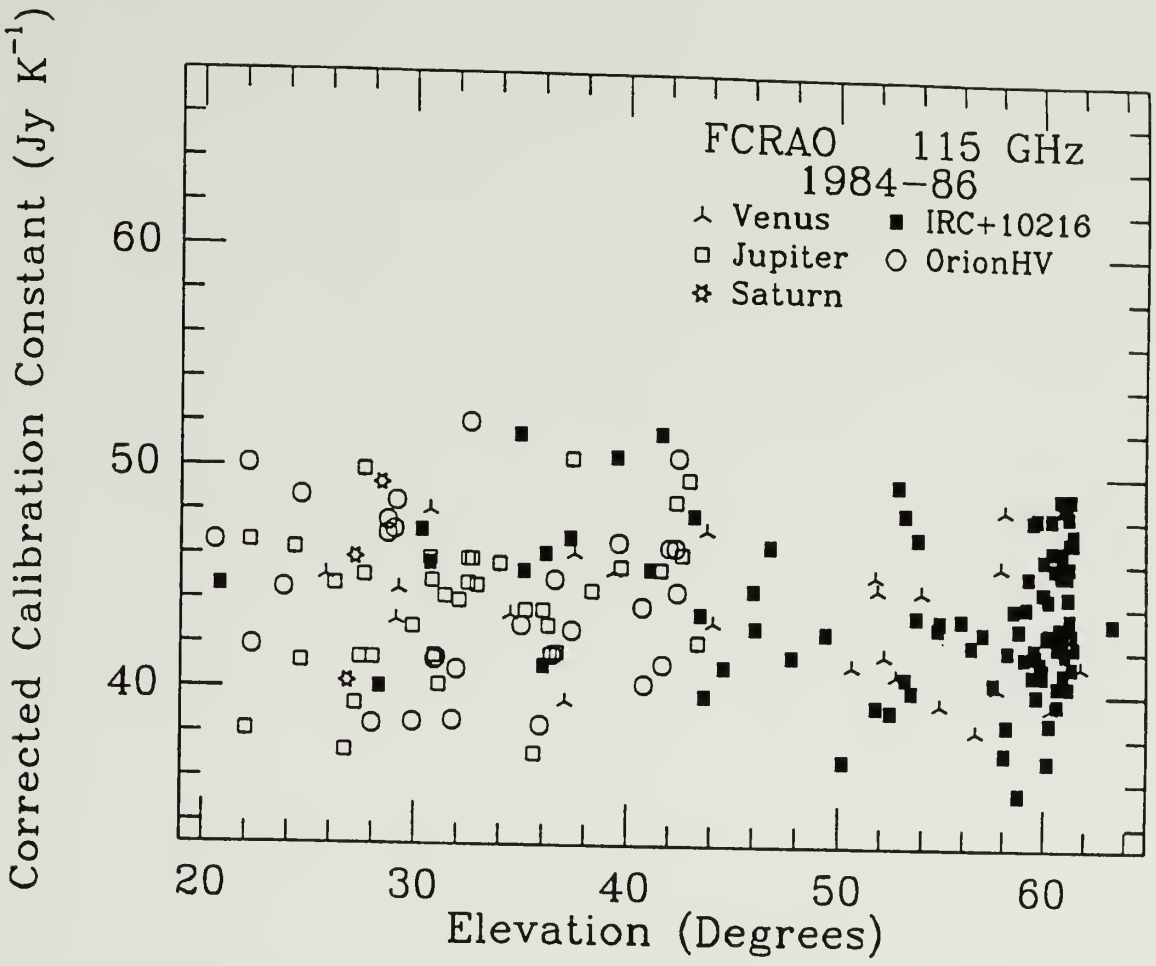

Figure A.2 Same as Figure A.1, but with elevation dependence removed.

planet data, the mean calibration constant at 60° elevation is found to be 43.8±3.3 Jy/K(T_A^*). At other elevations, the calibration constant is given by this number multiplied by C_{EL} in equation A-7, with a = 0.18 and b = 0.5. This calibration constant is found to apply to each of the 3 observing seasons (1983-84, 1984-85, and 1985-86), as shown in Figure A.3.

§2. Correcting the Data to Outer Space

Some observers like to fully correct their data for all atmospheric effects. The procedure outlined in §A.1, which goes only as far as correcting the data to an elevation of 60°, is adequate for many purposes. However, for comparison with data at other frequencies and at other telescopes, it is often useful to estimate the line strength which would be observed by the telescope if it were in outer space, above all the earth's atmosphere. In this section, we estimate mean telescope efficiencies for 115 GHz which are fully corrected for atmospheric effects.

There are at least 2 components contributing to the elevation dependence of the data displayed in Figure 1a. This is evident from Figure A.4, which displays the antenna temperatures (normalized to 1.00 at 60° elevation) as a function of elevation for IRC+10216 (whose CO J=I→0 emission is extended over a region ~3' in diameter, Kwan and Linke 1982) and the Moon (~30' in diameter). Since these data were taken on the same day at the same time (both IRC+10216 and the Moon transitted at the same time), the large difference in their elevation

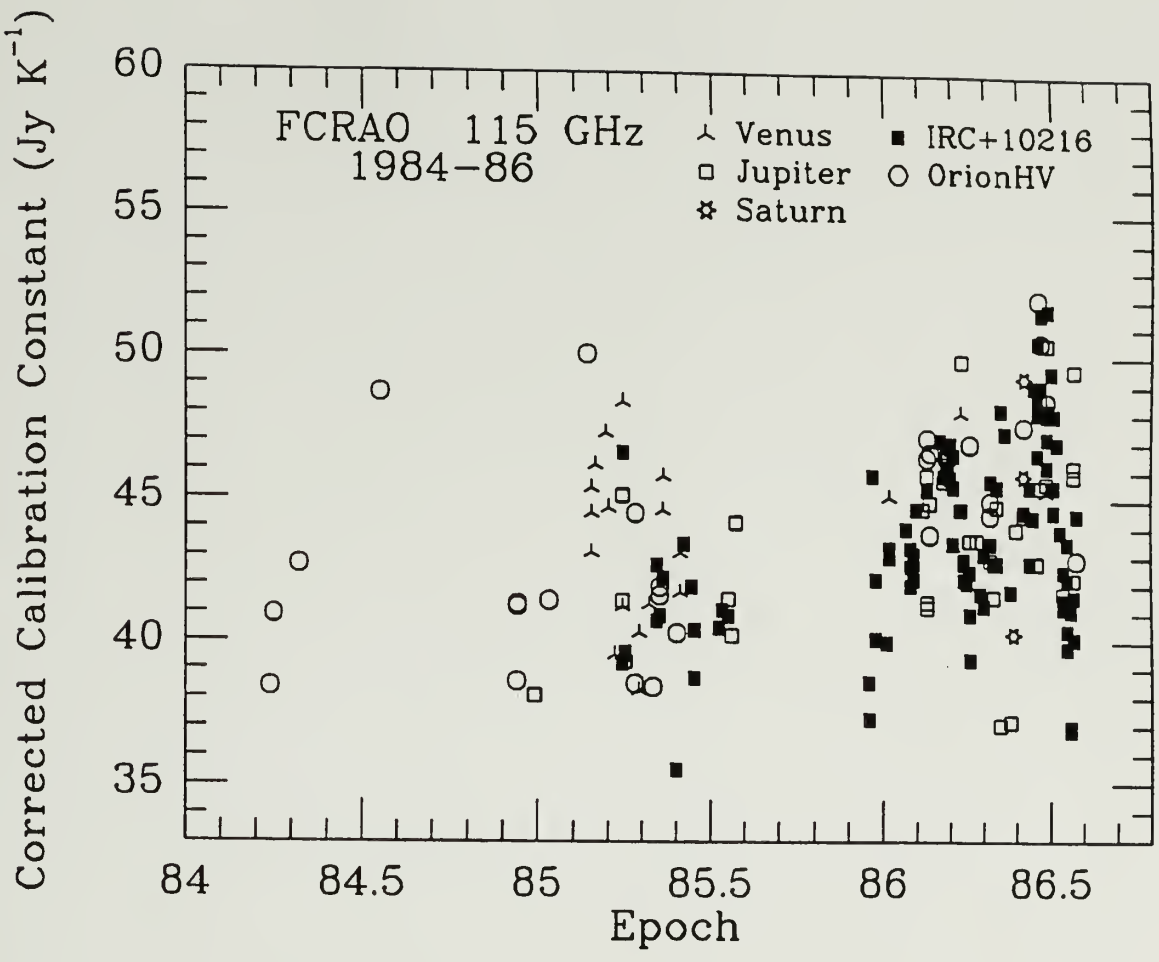

Figure A.3 Elevation-corrected calibration constant vs. epoch for 115 GHz data. The range in calibration constants is similar for each of the 3 observing seasons.

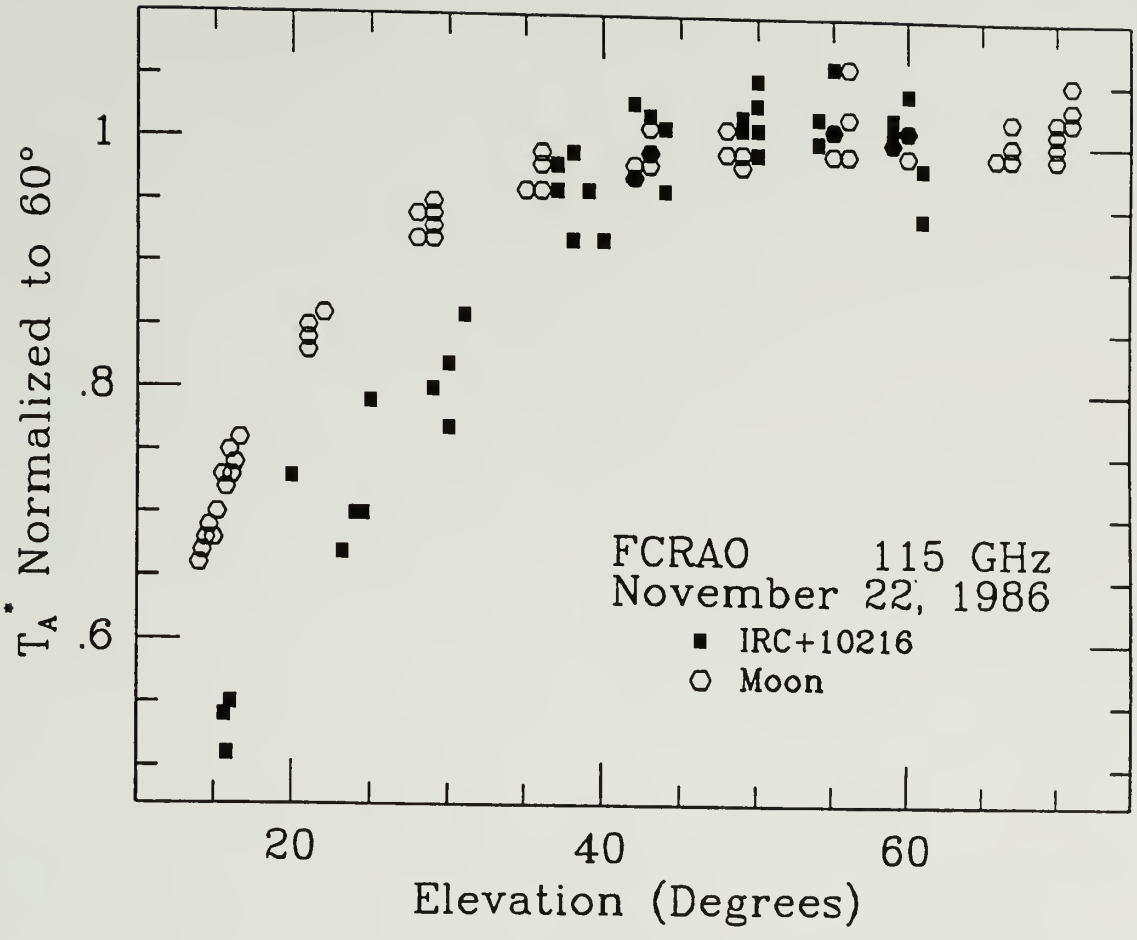

Figure A.4 Elevation dependence of antenna temperatures for the Moon and IRC+10216 on 11-22-86. The antenna temperatures have been normalized to 1.00 at 60° elevation. The different elevation dependences for the Moon and IRC+10216 indicate that there is a significant gain variation for small sources at lower elevations.

dependence must be due to their size. Gain variation is a likely size-dependent effect. At lower elevations, the dish deforms, changing the distribution of power on the sky. The difference between IRC+10216 and the Moon can be understood if dish deformation at lower elevations redistributes power from the main beam to near sidelobes. The elevation dependence of the Moon's antenna temperatures indicates an upper limit to the magnitude of the atmospheric component of the calibration. In fact, we find that the Moon's elevation dependence is consistent with being entirely the result of atmospheric effects. FCRAO's DIP routine (Schloerb and Snell 1980) estimated that the zenith atmospheric opacity was $\tau_o = 0.38$ on that particular day. Given $\tau_o = 0.38$, the elevation dependence of the Moon's antenna temperatures could be fully explained if $\Delta T = 30$ K, which is reasonable for a cold clear November day.

A fit to all the 'small source' data in Figure A.1 indicates that on a typical observing day, antenna temperatures at 115 GHz for small sources are 28% lower at 20° elevation than they are at 60° elevation. Assuming that the atmosphere is entirely responsible for the Moon's elevation dependence, then approximately half of the 28% at 20° is due to the atmosphere, and half is due to gain changes. A difference of 14% between 20° and 60° in the atmospheric component of the elevation dependence implies that $C_{FAC} = 1.05 \pm 0.01$ at 60° elevation. All the data in this thesis have therefore been corrected to 60° elevation by multiplying by equation A-7 to compensate for the mean elevation dependence displayed in Figure A.1, and then corrected to outside the

atmosphere by multiplying by a factor of 1.05. The calibration constant, corrected to outside the atmosphere, is 41.7 ±3.2 Jy/K(T_A*).

APPENDIX B

THE CALIBRATION OF EXTENDED SOURCES

§1. Relating Observed Line Intensities to Global Fluxes

In order to calculate the flux of the CO line observed in galaxies, it is necessary to account for the extended nature and undersampling of the emission. The basic expression relating the total CO line flux S_{CO} to the brightness temperature distribution $T_R(\Omega, v)$ of a source is:

$$S_{CO} = \frac{2k}{\lambda^2} \int\int T_R(\Omega, v)\, d\Omega\, dv \qquad \text{(B-1)}$$

where Ω is the relevant solid angle, v is the velocity, λ is the wavelength of the observation, and k is Boltzmann's constant. It is desirable to relate S_{CO} to the quantity actually observed, which is called in this thesis the integrated intensity $\int T_A^* dv$. In the millimeter wave radio astronomy terminology proposed by Kutner and Ulich (1981), T_A^* is related to the average brightness temperature within the main beam T_{Ravg} by:

$$T_{Ravg}(v) = \frac{T_A^*(v)}{\eta_c(v)\,\eta_{fss}} \qquad \text{(B-2)}$$

where η_{fss} is the forward scattering and spillover efficiency, and $\eta_c(v)$ is the source-beam coupling efficiency. For emission at velocity

v, $\eta_c(v)$ is given by:

$$\eta_c(v) = \frac{\int_0^{2\pi} T_R(\Omega,v)\, B(\Omega)\, d\Omega}{T_{Ravg}(v) \int_0^{\Omega_{norm}} B(\Omega)\, d\Omega} \qquad (B-3)$$

where $B(\Omega)$ is the antenna beam pattern, and Ω_{norm} is the solid angle chosen to normalize this definition. The normalization solid angle chosen here, because it is convenient, is 30' in diameter, so that a uniform source of that size (e.g. the moon) has a coupling efficiency of 1.0. T_{Ravg}, which appears in equation B-3, can be represented as:

$$T_{Ravg} = \frac{\int_0^{\Omega_{MB}} T_R(\Omega,v)\, B(\Omega)\, d\Omega}{\int_0^{\Omega_{MB}} B(\Omega)\, d\Omega} \qquad (B-4)$$

where Ω_{MB} is the main beam solid angle. In practice, $\eta_c(v)$ is estimated from equations B-3 and B-4 by finding a model $T_R(\Omega,v)$ which fits the data.

To be completely rigorous, one should consider the source-beam coupling for each velocity channel separately. This requires a well-known velocity field for each galaxy, which is generally not available. Furthermore, the calculation of coupling for separate channels would needlessly complicate the procedure for estimating total fluxes. For simplicity, we will assume that all velocity components are distributed uniformly throughout the galaxy. The error caused by making this assumption is partially offset by the assumption of a purely gaussian

beam pattern with no sidelobes (for a fuller discussion, see §B.2). From this point on in Appendix B, all explicit references to velocity will be dropped. The following equations will be formally correct for each velocity channel separately, and will be assumed to hold when integrated over velocity.

The beam pattern $B(\Omega)$, as defined here, is equivalent to the effective area function commonly used in radio astronomy (e.g. Kraus 1966), normalized by its value at beam center, or

$$B(\Omega) = \frac{A_e(\Omega)}{A_e(0)} = \frac{A_e(\Omega)}{\eta_A A_{phys}} \qquad \text{(B-5)}$$

where η_A is the aperture efficiency, and A_{phys} is the physical area of the antenna. This normalization is convenient since $B(0) = 1$.

For sources which uniformly fill the main beam, the coupling efficiency $\eta_c = \eta_B/\eta_{fss}$, where η_B is the main beam efficiency, so that

$$T_{Ravg} = \frac{T_A^*}{\eta_B} \qquad \text{(B-6)}$$

For most of the Virgo cluster galaxy CO spectra described in this thesis, this expression gives a good rough estimate of the average main beam brightness temperature.

More rigorously, an expression relating T_A^* and $T_R(\Omega)$ is obtained by substituting equation B-3 into equation B-2, and reorganizing to

yield:

$$T_A^* = \eta_{fss} \frac{\int_0^{2\pi} T_R(\Omega)\, B(\Omega)\, d\Omega}{\int_0^{\Omega_{norm}} B(\Omega)\, d\Omega} \qquad (B\text{-}7)$$

To solve for the $T_R(\Omega)$ needed in equation B-1, one should properly deconvolve $T_R(\Omega)$ and $B(\Omega)$. Unfortunately, this requires both high signal-to-noise spectra and many map points, and therefore is impossible for the purposes of this thesis.

What can be done, instead, is to model the source distribution, approximate the beam pattern, and weight the model source distibution by the beam pattern at each of the observed positions. If good agreement can be found between the observed T_A^*'s and the beam-weighted $T_R(\Omega)$'s for a particular model $T_R(\Omega)$, then that model $T_R(\Omega)$ can be used in equation B-1 to estimate the total flux. A potential disadvantage of this method is that if no simple functional form can be found which fits the data well, S_{CO} is very uncertain. For this reason, the following hybrid method is used to estimate CO fluxes in this thesis.

To justify this method, the expression for S_{CO} which will be used is derived from equations B-1 and B-7. Integrating equation B-7 over velocity, then dividing both sides by $\int T_A^* dv$, and multiplying the result by equation B-1 yields:

$$S_{CO} = \frac{2k \int_0^{\Omega_{norm}} B(\Omega)\, d\Omega}{\eta_{fss}\, \lambda^2} \int T_A^* dv \frac{\int_0^{2\pi} T_R(\Omega)\, d\Omega}{\int_0^{2\pi} T_R(\Omega)\, B(\Omega)\, d\Omega} . \qquad (B\text{-}8)$$

The first term on the RHS of this expression is the calibration constant (CC) for converting antenna temperature (T_A^*) to Janskys for point sources. To make this apparent, the integral in the numerator can be evaluated, using equation B-5, as follows:

$$\int_0^{\Omega_{norm}} B(\Omega)\, d\Omega = \frac{1}{\eta_A A_{phys}} \int_0^{\Omega_{norm}} A_e(\Omega)\, d\Omega$$

$$= \frac{\eta_{fss}}{\eta_A A_{phys}} \int_0^{2\pi} A_e(\Omega)\, d\Omega \qquad \text{(B-9)}$$

$$= \frac{\eta_{fss}\ \lambda^2}{\eta_A A_{phys}}$$

Thus the first term in equation B.8 is equivalent to

$$CC = \frac{2k}{\eta_A A_{phys}} \qquad \text{(B-10)}$$

which is the standard definition of the point source calibration constant. The mean calibration constant corrected to outside the atmosphere for the FCRAO telescope at 115 GHz during 1983-1986 is determined in Appendix A to be 41.7±3.2 Jy/K(T_A^*).

The second term in equation B-8 is the integrated intensity, $\int T_A^* dv$, which is the quantity that is directly observed, times the elevation-dependent correction factor described in Appendix A.

The third term on the RHS of equation B-8 is the inverse of what will be called 'the fraction of emission observed', or simply f, where

$$f = \frac{\int_0^{2\pi} T_R(\Omega)\, B(\Omega)\, d\Omega}{\int_0^{2\pi} T_R(\Omega)\, d\Omega} \quad . \qquad \text{(B-11)}$$

This is the term which contains the all-important correction for source-beam coupling. Note that this implicitly corrects for the inclination of a galaxy, and for over- or under-sampling of emission, regardless of the distribution of observed points, provided that a model $T_R(\Omega)$ can be found which fits the data reasonably well.

The description of this quantity as 'the fraction of emission observed' is appropriate with respect to point sources. For a point source centered on the beam, f = 1. For a source which is extended with respect to the main beam, f<1, since the emission away from the beam center suffers the Gaussian weighting of the beam pattern. Consequently it does not contribute as much to the observed line as does an area of equivalent brightness temperature at the beam center. In this sense, not all of its emission is being 'observed'. If the same extended flux were squooshed into an area much smaller than the width of the main beam, the observed line intensity would become greater, and all of its emission would be 'observed'.

Rewriting equation B-8 in terms of the newly-defined abbreviations,

$$S_{CO} = CC \; (\int T_A^* dv) \; f^{-1} \quad . \qquad (B\text{-}12)$$

This formulation is preferable to equation B-1 because it explicitly includes the observable $\int T_A^* dv$, and is not as dependent on the model $T_R(\Omega)$ as is equation B-1. The quantity f contains $T_R(\Omega)$ in both the numerator and denominator, so that errors in S_{CO} due to differences between the actual and model source distributions do not cause as large an error in equation B-12 as in equation B-1.

While equation B-12 is formally correct even for only one observation, it is not very useful since the source distribution $T_R(\Omega)$ cannot be suitably constrained from only one observation. In practice, to determine S_{CO} with a reasonably small uncertainty, it is necessary to observe enough positions to suitably constrain $T_R(\Omega)$. When more than one position is observed, equation B-12 is modifed to include sums over f and $\int T_A^* dv$:

$$S_{CO} = CC \; (\Sigma \int T_A^* dv) \; (\Sigma f)^{-1} \quad . \qquad (B\text{-}13)$$

This relation is used in Chapter III to derive global CO fluxes.

§2. The Beam Pattern

In order to calibrate extended sources, it is necessary to know both the source brightness distribution and the beam pattern. For the purposes of estimating CO fluxes, a purely gaussian beam pattern has been assumed. In this section, the current knowledge on the actual beam pattern is summarized, and the uncertainties introduced by our

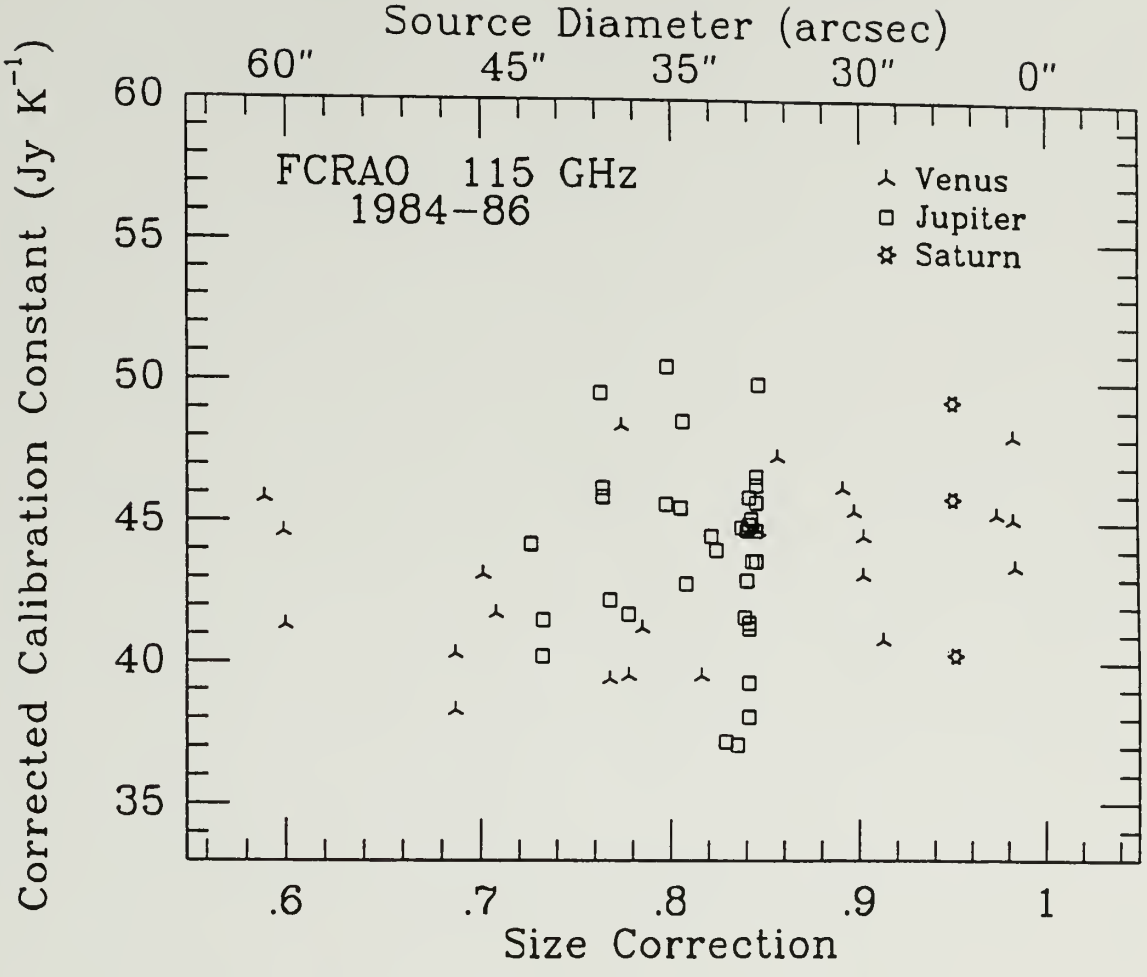

Figure B.1 Elevation-corrected calibration constant vs. source size correction (equation A-4) for 115 GHz planetary data. The upper horizontal axis indicates the planet diameter. No discernable trend is evident out to a source diameter of 60", which means that the beam can be represented by an azimuthally symmetric gaussian to an accuracy of ~5% out to a radius of 30".

assumption are discussed.

Since the planets range in size from a few arcseconds to more than 60" (i.e. Venus near inferior conjunction), the calibration data presented in Appendix A can be used to quantitatively assess how well the inner beam is described by an azimuthally-symmetric gaussian. Figure B.1 displays the elevation-corrected calibration constant for 115 GHz plotted against the source size correction (equation A-4). There is no significant correlation. From the 115 GHz data, we can set a limit of ~5% out to a radius of 30" on the maximum error resulting from the assumption of a perfect, azimuthally-symmetric gaussian beam. This holds for data taken above an elevation of ~30°. Below 30°, dish deformation causes power to be redistributed from the main beam to nearby sidelobes (see Appendix A). The distibution of power in the main beam is not known below 30°, but its effect on the Virgo cluster CO data is minimal, since nearly all the data were taken at elevations greater than 35°.

The distribution of beam power beyond a radius of ~60" is not that well-known, although some estimates of it from Sun scans are presented in Predmore (1982) and Snell (1985). The planet azimuth and elevation scans of Snell (1985) indicate that there are no sidelobes greater than 2% of the peak (17dB) along these directions within 4' from beam center at elevations ≥30°. However, even a 2% sidelobe can result in uncertainties of as much as ~10% in the total flux of a source which is a couple of arcminutes in diameter. We note that the KPNO 11-meter telescope (before the resurfacing in 1982) contained ~16% of its power

in near sidelobes at 91 GHz (Kutner, Mundy, and Howard 1984). A proper full map of a strong planet with a sensitivity of ~1% can be made in a few hours, and would enable small extended sources at Quabbin to be calibrated more accurately.

While the presence of sidelobes affects the calibration of small (few arcminutes) extended continuum sources and galactic molecular clouds, their effect on small galaxies (like all the Virgo galaxies) is not as great. The ordered velocity fields of galaxies act to minimize the importance of sidelobes. Emission from a region of the sky where a sidelobe is located will only contribute to the line if the velocity of the gas in the sidelobe is the same as the velocity of gas in the main beam. Disk galaxies rotate, so that an inclined disk galaxy has different velocity components originating from different parts of the galaxy. As a result, if the telescope is pointed somewhere along the eastern part of the major axis, emission from the western half of the galaxy will not contribute to the observed line because of the velocity difference between the eastern and western halves.

BIBLIOGRAPHY

Aaronson, M., et al. 1982, Ap.J.Suppl., 50, 241.

Allen, C.W. 1973, Astrophysical Quantities (London: Athlone).

Allen, R.J., and Goss, W. M. 1979, A.A.Suppl., 36, 135.

Allsopp, N.J. 1979, M.N.R.A.S., 188, 765.

Bahcall, J.N., Schmidt, M., and Soneira, R.M. 1983, Ap.J., 265, 730.

Bevington, P.R. 1969, Data Reduction and Error Analysis for the Physical Sciences, (New York: McGraw Hill, Inc.).

Binggeli, B., Sandage, A., and Tammann, G.A. 1985, A.J., 90, 1681.

Bloemen, J.B.G.L. 1985, Ph.D. thesis, University of Leiden.

Bloemen, J.B.G.L., et al. 1986, A.A., 154, 25.

Blitz, L., Bloemen, J.B.G.M., Hermsen, W., and Bania, T.M. 1985, A.A., 143, 267.

Blitz, L., and Shu, F.H. 1980, Ap.J., 238, 148.

Boroson, T. 1981, Ap.J.Suppl., 46, 177.

Bosma, A. 1978, Ph. D. Thesis, Groningen.

Bosma, A., van der Hulst, J.M., and Sullivan, W.T., III 1977, A.A., 57, 373.

Bosma, A. 1985, in ESO Workshop on the Virgo Cluster of Galaxies, eds. O.-G. Richter and B. Binggeli (Garching: ESO), p. 425.

Bothun, G.D. 1981, Ph.D. thesis, University of Washington.

Bothun, G.D., Romanshin, W., Strom, S.E., and Strom, K.M. 1984, A.J., 89, 1300.

Catalogued Galaxies and Quasars Observed in the IRAS Survey 1985, prepared by Lonsdale, C.J., Helou, G., Good, J.C., and Rice, W. (Jet Propulsion Laboratory).

Chamaraux, P., Balkowski, C., and Gerard, E. 1980, A.A., 83, 38.

Chamaraux, P., Balkowski, C., and Fontanelli, P. 1986, A.A., 165, 15.

Chincarini, G., and de Souza, R. 1985, A.A., 153, 218.

Cohen, R.S., Dame, T.M., and Thaddeus, P. 1986, Ap.J.Suppl., 60, 695.

Combes, F., Gottesman, S.T., and Weliachew, L. 1977, A.A., 59, 181.

Condon, J.J. 1983, Ap.J.Supp., 53, 459.

Cottrell, G.A. 1977, M.N.R.A.S., 178, 577.

Cowie, L.L., and Songalia, A. 1977, Nature, 266, 501.

Cram, T.R., Roberts, M.S., and Whitehurst, R.N. 1980, A.A.Suppl., 40, 215.

Davies, R.D., and Lewis, B.M. 1973, M.N.R.A.S., 165, 231.

Davis, J.H., and Vanden Bout, P. 1973, Ap.Letters, 15, 43.

Dickman, R.L. 1978, Ap.J.Suppl., 37, 407.

Dickman, R.L. 1986, private communication.

Dickman, R.L., Snell, R.L., and Schloerb, F.P. 1986, Ap.J., 309, 326 (DSS).

Desert, F.X. 1986, in Light On Dark Matter, ed. F.P. Israel (Dordrecht: Reidel).

de Giola-Eastwood, K., Grasdalen, G.L., Strom, S.E., and Strom, K.M. 1984, Ap.J., 278, 564.

de Vaucouleurs, G. 1961, Ap.J.Suppl., 6, 218.

de Vaucouleurs, G., de Vaucouleurs, A.,and Corwin, H.G. 1976, Second Reference Catalogue of Bright Galaxies (Austin: University of Texas Press) (RC2).

de Vaucouleurs, G., and Corwin, H.G. 1986, A.J., 92, 722.

de Vaucouleurs, G., and Pence, W.D. 1979, Ap.J.Suppl., 40, 425.

Draine, B.T., and Anderson, N. 1985, Ap.J., 292, 494.

Dressler, A. 1986, Ap.J., 301, 35.

Dressel, L.L., and Condon, J.J. 1976, Ap.J.Suppl., 31, 187.

Dressel, L.L., and Condon, J.J. 1978, Ap.J.Suppl., 36, 53.

Edwards, S., Strom, S.E., Snell, R.L., Jarrett, T.H., Beichman, C.A., and Strom, K.M. 1986, Ap.J.(Letters), 307, L65.

Elmegreen, B.G. 1987, in Interstellar Processes, eds. D. Hollenbach and H. Thronson (Dordrecht: Reidel), in press.

Elmegreen, B.G., Elmegreen, D.M., and Morris, M. 1980, Ap.J., 240, 455.

Faber, S.M., and Gallagher, J.S. 1976, Ap.J., 204, 365.

Federman, S.R., Glassgold, A.E., and Kwan, J. 1979, Ap.J., 227, 466.

Ftaclas, C., Fanelli, M.N., and Struble, M.F. 1984, Ap.J., 282, 19.

Forman, W., Schwarz, J., Jones, C., Liller, W., and Fabian, A.C. 1979, Ap.J.(Letters), 234, L27.

Fraser, C.W. 1977, Astr.Ap.Supp., 29, 161.

Gavazzi, G., and Jaffe, W. 1985, Ap.J.(Letters), 294, L89.

Gerola, H., and Seiden, P.E. 1978, Ap.J., 223, 129.

Giovanardi, C., Helou, G., Salpeter, E.E., and Krumm, N. 1983, Ap.J., 267, 35.

Giovanardi, C., Krumm, N., and Salpeter, E.E. 1983, A.J., 88, 1719.

Giovanelli, R., and Haynes, M.P. 1983, A.J., 88, 881 (GH83).

Giovanelli, R., and Haynes, M.P. 1985, Ap.J., 292, 404 (GH85).

Glassgold, A.E., Huggins, P.J., and Langer, W.D. 1985, Ap.J., 290, 615.

Gorenstein, P., Fabricant, D., Topka, K., Tucker, W., and Harnden, F.R., Jr. 1977, Ap.J.(Letters), 216, L95.

Gunn, J.E., and Gott, J.R. 1972, Ap.J., 176, 1.

Haynes, M.P., Giovanelli, R., and Roberts, M. 1979, Ap.J., 229, 83.

Haynes, M.P., and Giovanelli, R. 1984, A.J., 89, 758 (HG84).

Haynes, M.P., Giovanelli, R., and Chincarini, G.L. 1984, Ann.Rev.Astr. Astr., 22, 445.

Haynes, M.P., and Giovanelli, R. 1986, Ap.J., 306, 466.

Heckman, T.M., Balick, B., and Sullivan, W.T., III 1978, Ap.J., 224, 745.

Helou, G. 1986, Ap.J., 311, L33.

Helou, G., Giovanardi, C., Salpeter, E.E., and Krumm, N. 1981, Ap.J. Suppl., 46, 267.

Helou, G., Hoffman, G.L., and Salpeter, E.E. 1979, Ap.J.(Letters), 228, L1.

Helou, G., Hoffman, G.L., and Salpeter, E.E. 1984, Ap.J.Suppl., 55, 433 (HHS).

Helou, G., Soifer, B.T., and Rowan-Robinson, M. 1985, Ap.J.(Letters), 298, L7.

Henkel, C., Wouterloot, G.A., and Bally, J. 1986, A.A., 155, 193.

Heyer, M.C. 1986, Ph.D. thesis, University of Massachusetts.

Hodge, P.W., and Kennicutt, R.C. 1983, A.J., 88, 296.

Hoffman, G.L., Helou, G., Salpeter, E.E., and Sandage, A. 1985, Ap.J. (Letters), 287, L15.

Hollenbach, D.J., Werner, M.W., and Salpeter, E.E. 1971, Ap.J., 163, 165.

Huchra, J.P. 1985, private communication.

Huchra, J.P. 1985, in ESO Workshop on the Virgo Cluster of Galaxies, eds. O.-G. Richter and B. Binggeli (Garching: ESO), p. 181.

Huchtmeier, W.K., Tammann, G.A., and Wendker, H.J. 1976, A.A., 46, 381.

Hummel, E., van Gorkom, J.H., and Kotanyi, C.G. 1983, Ap.J.(Letters), 267, L5.

Hunter, D.A., Gallagher, V.S., and Rausenkrantz, D. 1982, Ap.J.Suppl., 49, 53.

IPAC Users Guide 1985, (Jet Propulsion Laboratory).

IRAS Point Source Catalog 1985, Joint IRAS Science Working Group, (Washington D.C.: U.S. Government Printing Office).

Israel, F.P., de Graauw, T., van de Stadt, H., and de Vries, C.P. 1986, Ap.J., 303, 186.

Johnson, H.L. 1966, Ann.Rev.Astr.Ap., 4, 193.

Kenney, J.D., and Young, J.S. 1985, in ESO Workshop on the Virgo Cluster of Galaxies, eds. O.-G. Richter and B. Binggeli (Garching: ESO), p. 165.

Kenney, J.D., and Young, J.S. 1986, Ap.J.(Letters), 301, L13.

Kennicutt, R.C. 1983, A.J., 88, 483.

Kennicutt, R.C., Bothun, G.D., and Schommer, R.A. 1984, A.J., 89, 1279.

Kennicutt, R.C. 1985, in ESO Workshop on the Virgo Cluster of Galaxies, eds. O.-G. Richter and B. Binggeli (Garching: ESO), p. 227.

Kennicutt, R.C., and Kent, S.M. 1983, A.J., 88, 1094.

Koornneef, J. 1982, A.A., 107, 247.

Koornneef, N. 1984, in I.A.U. Symposium 108, Structure and Evolution of the Magellanic Clouds, eds. S. van den Bergh and K.S. de Boer (Dordrecht: Reidel).

Kotanyi, C.G. 1980, Astr.Ap.Supp., 41, 421.

Kotanyi, C.G. 1981, Ph.D. thesis, University of Groningen.

Kraus, J.D. 1966, Radio Astronomy (New York: McGraw-Hill, Inc.).

Kulkarni, S.R., Blitz, L., and Heiles, C. 1982, Ap.J.(Letters), 259, L63.

Kulkarni, S.R., and Heiles, C. 1987, in Galactic and Extragalactic Radio Astronomy, eds. K.I. Kellerman and G.L. Verschuur, in press.

Kutner, M.L., Mundy, L., and Howard, R.J. 1984, Ap.J., 283, 890.

Kutner, M.L., and Ulich, B.L. 1981, Ap.J., 250, 341.

Kwan, J. 1979, Ap.J., 229, 567.

Kwan, J., and Linke, R.A. 1982, Ap.J., 254, 587.

Larson, R.B. 1981, M.N.R.A.S., 194, 809.

Lequeux, J., Maurice, E., Prevot, C., Prevot-Burnichon, M.L., and Rocca-Volmerange, B. 1984, in I.A.U. Symposium 108, Structure and Evolution of the Magellanic Clouds, eds. S. van den Bergh and K.S. de Boer (Dordrecht: Reidel).

Lord, S. 1987, Ph.D. Thesis, University of Massachusetts.

Lord, S., Young, J.S., and Kinzel, W. 1985, FCRAO Memo.

Mould, J., Aaronson, M., and Huchra, J. 1980, Ap.J., 238, 458.

Myers, P.C. 1978, Ap.J., 225, 380.

Myers, P.C., Dame, T.M., Thaddeux, P., Cohen, R., Silverberg, R.F., Dwek, E., and Hauser, M.G. 1986, Ap.J., 301, 398.

Nilson, P. 1973, Uppsala General Catalouge of Galaxies (Uppsala) (UGC).

Nulsen, P.E.J. 1982, M.N.R.A.S, 198, 1007.

Pagel, B.E.J., and Edmunds, M.G. 1981, 18, 77.

Pajot, F., Boisse, P., Gispert, R., Lamarre, J.M., Puget, J.L., and Serra, G. 1986, A.A., 157, 393.

Penzias, A.A., and Burrus, C.A. 1973, Ann.Rev.Astr.Ap., 11, 51.

Persson, C.J., and Helou, G. 1987, Ap.J., in press.

Peterson, Strom, S.E., and Strom, K.M. 1979, A.J., 84, 735.

Predmore, R. 1982, FCRAO Memo.

Rickard, L.J., and Harvey, P.M. 1984, A.J., 89, 1520.

Rickard, L.J., and Blitz, L. 1985, Ap.J.(Letters), 292, L57.

Rogstad, D.H., and Shostak, G.S. 1972, Ap.J., 176, 315.

Rogstad, D.H., and Shostak, G.S. 1973, A.A., 22, 111.

Rowan-Robinson, M., and Crawford, J. 1986, in Light On Dark Matter, ed. F.P. Israel (Dordrecht:Reidel) (RC).

Rubin, V.C., Burstein, D., Ford, W.K., Jr., and Thonnard, N. 1985, Ap.J., 289, 81.

Rubin, V.C., Ford, W.K., Jr., Strom, K.M., Strom, S.E., and Romanishin, W. 1978, Ap.J., 224, 782.

Sandage, A., 1961, The Hubble Atlas of Galaxies (Washington D.C.: Carnegie Institute of Washington).

Sandage, A., Binggeli, B., and Tammann, G.A. 1985, A.J., 90, 395.

Sandage, A., Binggeli, B., and Tammann, G.A. 1985b, A.J., 90, 1759.

Sandage, A., and Tammann, G.A. 1976, Ap.J.(Letters), 207, L1.

Sandage, A., and Tammann, G.A. 1981, A Revised Shapley-Ames Catalog of Bright Galaxies (Washington, D.C.: Carnegie Institution of Washington) (RSA).

Sanders, D.B., Scoville, N.Z., and Solomon, P.M. 1985, Ap.J., 289, 373.

Sanders, D.B., Solomon, P.M., and Scoville, N.Z. 1984, Ap.J., 276, 182.

Sancisi, R., and Allen, R. J. 1979, A.A., 74, 73.

Schmidt, M. 1959, Ap.J., 129, 243.

Schweizer, F. 1976, Ap.J.Suppl., 31, 313.

Scoville, N.Z., private communication 1987.

Scoville, N.Z., and Hersh, K. 1979, Ap.J., 229, 578.

Scoville, N.Z., Sanders, D.B., Clemens, D.P. 1986, Ap.J.(Letters), 310, L77.

Scoville, N.Z., and Solomon, P.M. 1975, Ap.J.(Letters), 199, L105.

Scoville, N.Z., and Young, J.S. 1983, Ap.J., 265, 148.

Scoville, N.Z., Young, J.S., and Lucy, L.B. 1983, Ap.J., 270, 443.

Scoville, N.Z., Yun, M.S., Clemens, D.P., Sanders, D.B., and Waller, W.H. 1987, Ap.J.Suppl., in press.

Schloerb, F.P., and Snell, R.L. 1980, FCRAO Report # 150.

Shane, W. W., 1975, in Les Dynamiques des Galaxies Spirales, ed. L. Weliachew (CNRS Colloque No. 241), p. 217.

Shostak, G.S. 1978, A.A., 68, 321.

Smith, B.J., Kleinmann, S.G., Huchra, J.P., and Low, F.J. 1987, Ap.J., in press.

Snell, R.L. 1985, FCRAO Memo.

Snell, R.L., and Schloerb, F.P. 1983, FCRAO Report # 220.

Solomon, P.M., Scoville, N.Z., and Sanders, D.B. 1979, Ap.J.(Letters), 232, L89.

Solomon, P.M., Barrett, J., Sanders, D.B., and de Zafra, R. 1983, Ap.J (Letters), 266, L103.

Stark, A.A. 1979, Ph. D. Thesis, Princeton University.

Stark, A.A., Penzias, A.A., and Beckman, B. 1983, in Surveys of the Southern Galaxy, ed. W.B. Burton and F.P. Israel (Dordrecht: Reidel).

Stark, A.A., Knapp, G.R., Bally, J., Wilson, R.W., Penzias, A.A., and Rowe, H.E. 1986, Ap.J., 310, 660.

Stauffer, J.R. 1981, Ph.D. thesis, University of California, Berkeley.

Stauffer, J.R. 1985, in ESO Workshop on the Virgo Cluster of Galaxies, eds. O.-G. Richter and B. Binggeli (Garching: ESO), p. 301.

Stauffer, J.R., Kenney, J.D., and Young, J.S. 1986, A.J., 91, 1286.

Sulentic, J.W. 1977, Ap.J.(Letters), 211, L59.

Tacconi, L.J. 1987, Ph.D. Thesis, University of Massachusetts.

Tacconi, L.J., and Young, J.S. 1985, Ap.J., 290, 602.

Tacconi, L.J., and Young, J.S. 1986, Ap.J., 308, 600.

Tacconi, L.J., and Young, J.S. 1987, Ap.J. (submitted).

Talbot, R.J., Jr. 1980, Ap.J., 235, 821.

Tinsley, B.M. 1980, Fundmentals Cosmic Phys., 5, 287.

Trimble, V. 1975, Rev.Mod.Phys., 47, 877.

Tully, R.B. and Fisher, J.R. 1977, A.A., 54, 661.

Tully, R.B. 1985, in ESO Workshop on the Virgo Cluster of Galaxies, eds. O.-G. Richter and B. Binggeli (Garching: ESO). p. 385.

Tully, R.B., and Shaya, E. 1984, Ap.J., 281, 31.

Ulich, B.L. 1981, A.J., 86, 1619.

van Gorkom, J. and Kotanyi, C. 1986, private communication.

van Gorkom, J., and Kotanyi, C. 1985, in ESO Workshop on Virgo Cluster Galaxies, eds. O.-G. Richter and B. Binggeli (Garching: ESO), p. 61.

Verter, F. 1985, Ap.J.Supp., 57, 261.

Wardle, M., and Knapp, G.R. 1986, A.J., 91, 23.

Warmels, R.H. 1985, in ESO Workshop on the Virgo Cluster of Galaxies, eds. O.-G. Richter, and B. Binggeli (Garching: ESO), p. 51.

Warmels, R.H. 1986, Ph.D. thesis, Groningen.

Whitmore, B.C., and Kirshner, R.P. 1982, A.J., 87, 500.

Wilking, B.A., Harvey, P.M., Joy, M., Hyland, A.R., and Jones, T.J. 1985, Ap.J., 293, 165.

Wyse, R.F.G., 1986, Ap.J.(Letters), 311, L41.

Young, J.S. 1986, I.A.U. Symposium 115, Star Forming Regions, eds. M. Peimbert, and J. Jugaku.

Young, J.S., Gallagher, J.S., and Hunter, D.A. 1984, Ap.J., 276, 476.

Young, J.S., and Sanders, D.B. 1986, Ap.J., 302, 680.

Young, J.S., Schloerb, F.P., Kenney, J.D., and Lord, S.D. 1986a, Ap.J., 304, 443.

Young, J.S., and Scoville, N.Z. 1982a, Ap.J., 258, 467.

Young, J.S., and Scoville, N.Z. 1982b, Ap.J.(Letters), 260, L11.

Young, J.S., and Scoville, N.Z. 1982c, Ap.J.(Letters), 260, L41.

Young, J.S., and Scoville, N.Z. 1984, Ap.J., 284, 153.

Young, J.S., Scoville, N.Z., and Brady, E. 1985, Ap.J., 288, 487 (YSB).

Young, J.S., Tacconi, L.J., and Scoville, N.Z. 1983, Ap. J., 269, 136.

Young, J.S., Kenney, J.D., Tacconi, L., Claussen, M.J., Huang, Y.-L., Tacconi-Garman, L., Xie, S., and Schloerb, F.P. 1986b, Ap.J.(Letters), 311, L17.

Young, J.S., Xie, S., Kenney, J.D., and Rice, W. 1987, in preparation.